Controlling light-matter interactions with two-dimensional semiconductors at cryogenic temperatures

Samarth Vadia

München 2021

Controlling light-matter interactions with two-dimensional semiconductors at cryogenic temperatures

Samarth Vadia

Dissertation
an der Fakultät für Physik
der Ludwig-Maximilians-Universität
München

vorgelegt von
Samarth Vadia
aus Una, Indien

München, den 21. Mai 2021

Erstgutachter: Prof. Dr. Alexander Högele
Zweitgutachter: Prof. Dr. Khaled Karraï

Tag der mündlichen Prüfung: 02. Juli 2021

Zusammenfassung

Effiziente Wechselwirkungen zwischen Festkörpersystemen und Photonen bilden die Grundlage für die aufstrebenden Quantentechnologien. Die zentrale Herausforderung bei der Kontrolle von Wechselwirkungen zwischen Licht und Materie kann durch die Verwendung eines optischen Resonators gelöst werden. Durch Einfangen der Photonen in einem kleinen Volumen wird die Wechselwirkungszeit mit dem Festkörpersystem in solchen quantenoptischen Experimenten erhöht.

Diese Arbeit konzentriert sich auf Wechselwirkungen zwischen Licht und Materie in zweidimensionalen halbleitenden Übergangsmetalldichalkogeniden. Stark gebundene Elektron-Loch-Paare (Exzitonen) in Übergangsmetalldichalkogeniden weisen eine große Oszillatorstärke auf und bieten einen weiteren Pseudospin-Freiheitsgrad in der Bandstruktur, der mit spezifischer Polarisation des Lichts interagiert. In dieser Arbeit realisieren wir in zwei Experimenten Licht-Materie-Wechselwirkungen mit monolagigem Wolframdiselenid mit unterschiedlichen optischen Resonatoren.

Im ersten Experiment untersuchten wir ein Hybridsystem, das lokalisierte Plasmonen auf der Oberfläche von Goldnanoscheiben mit monolagigem Wolframdiselenid kombiniert. Kohärente Interferenz von Exzitonen mit Plasmonen ergibt eine asymmetrische spektrale Antwort - als Fano-Linienform bekannt - im Grenzfall schwacher Licht-Materie-Kopplung. Diese optische Antwort des Hybridsystems wird durch ein Drei-Niveau-Modell bestätigt. Zusätzlich wird die magnetfeldinduzierte Energieaufspaltung der Exzitonen genutzt, um chirale Reflexion zu ermitteln.

Das zweite Experiment entwickelt einen modular abstimmbaren optischen Resonator bei kryogenen Temperaturen. Eine große technologische Herausforderung bei skalierbaren kryogenen Experimenten sind mechanische Schwingungen. Basierend auf einem gründlichen Verständnis der Funktionalität eines Kryostaten mit geschlossenem Kreislauf wurden verschiedene Techniken zur Schwingungsreduzierung implementiert, um einen Aufbau mit offenen optischen Resonatoren zu entwickeln. Im Vergleich zu Vibrationen des Standardsystems wurde eine 50-fache Verminderung erreicht, und somit über den gesamten Zeitraum eines Kühlzyklus eine mittlere Stabilität von weniger als 100 pm gewährleistet. Dies ermöglicht den Betrieb eines optischen Resonators mit hoher Finesse bei niedrigen Temperaturen. Anschließend wurde die Vielseitigkeit des Systems in einem kontrollierten Experiment mit monolagigem Wolframdiselenid demonstriert. Exziton-Polaritonen wurden im Regime starker Kopplung mit hoher Kooperativität beobachtet.

Abstract

Efficient interactions between solid-state systems and photons are the basis for the emerging quantum technologies. An outstanding challenge in facilitating light-matter interactions can be solved by the introduction of an optical resonator. By trapping the photons in a small volume, the interaction time with the solid-state system is increased in such quantum optics experiments.

This thesis focuses on light-matter interactions with two-dimensional semiconductor transition-metal dichalcogenides. Strongly bound electron-hole pairs (excitons) in transition-metal dichalcogenides exhibit large oscillator strength and offer a valley degree-of-freedom in the band structure that interacts with specific polarization of light, this makes them an excellent prospect for quantum optics experiments. In this work, we realize light-matter interactions with monolayer tungsten diselenide in two experiments using different optical resonators.

In the first experiment, we investigated a hybrid system combining localized plasmons, on the surface of gold nanodisks, with a monolayer tungsten diselenide. The coherent interference of excitons with plasmons yield an asymmetric optical response, known as Fano line-shape, in the limit of weak light-matter coupling. This optical response of the hybrid system is corroborated with a three-level model. In addition, magnetic field-induced valley-dependent exciton energy splitting is harnessed to achieve chiral reflection.

The second experiment develops a modular tunable cavity at cryogenic temperatures. A major technological challenge involving scalable cryogenic experiments is mechanical vibrations. After a thorough understanding of the functionality of a closed-cycle cryostat, a variety of vibration-reduction techniques were applied to develop an open cavity setup. In comparison to the vibrations on the standard closed-cycle cryostat, we attain 50-fold reduction to reach the root-mean-square stability of less than 100 pm over the entire period of a cooling cycle. This enables the operation of a high-finesse cavity at low temperatures. Subsequently, the versatility of the platform was demonstrated in a controlled experiment with monolayer tungsten diselenide. Exciton-polaritons were observed in the high cooperativity strong-coupling regime.

Contents

1 Introduction

The second quantum revolution is taking shape right now. The development of the theory of quantum mechanics about a century ago has been one of the most remarkable achievement of humankind, not just for the better understanding of the underlying mechanisms but also in technological advancements [1–3]. In the so-called first quantum revolution, the knowledge of quantum physics has led to the development of lasers, transistors and magnetic resonance imaging (MRI) devices amongst others [3]. Further technological progress in the second quantum revolution has enabled rapid success in the field of quantum science and technology [1, 2, 4–6].

This plethora of recent advances promises to improve or even upheaval the fields of communication, computing, metrology and simulation [2]. Long distance transfer of quantum information is essential for implementing quantum cryptography which will lead to more secure communication protocols. Photons are the fundamental ingredient for such protocols involving the quantum random number generation and the quantum key distribution (QKD), as they are the natural and excellent carrier of information over short and long distances. Thus, photons are commonly referred to as flying qubits [2, 7–9].

Quantum computing can outperform the classical computers in several computational problems such as factoring and unstructured search [10–12]. While the number of qubits is still small and the error rates are high, the current Noisy Intermediate-Scale Quantum (NISQ) era has garnered a lot of attention. There has been a remarkable progress in proving quantum advantage in several practical use-cases, e.g. in optimization tasks and quantum chemistry [13–16]. At present, several architectures are being developed such as superconducting qubits [17, 18], trapped ions [19, 20], spin qubits in silicon and other defects such as color centers and rare-earth ions [21–24] as well as photonic states [25–27]. It is clear that photons are integral for quantum computing, either as controllable qubits or for coherent control and measurement of matter-based qubits [19, 26, 27].

Sensitive sensors and measurement devices are crucial for navigation, material analysis for chemistry and biology, as well as for quantifying fundamental units of nature. Quantum-

enhanced sensing and imaging promises to increase the precision and the sensitivity to detect magnetic field in materials and biological applications, detect gravitational waves and improve atomic clocks [2, 28]. The electromagnetic field plays a vital role as a tool to probe and detect sensor signals. One famous example is the use of squeezed light to enhance the sensitivity of gravitational wave detection in the Laser Interferometer Gravitational-Wave Observatory (LIGO) experiment [29].

Another important avenue for quantum technologies is to simulate a complex quantum system by engineering another controlled quantum system [2]. In the last two decades, an extraordinary progress has been achieved using neutral atoms in optical lattices, trapped ions, and more recently, spin-defects in solid-state and photonic systems to simulate classically intractable problems in the area of condensed-matter physics, topological phenomena and high-energy physics [30, 31]. Optical control of matter again plays a key part in controlling the dynamics of such systems.

Thus, it is quite obvious that photons play an indispensable role in the development of next generation quantum technologies. This leads to a prerequisite for the development of an efficient and a deterministic control of light and matter, and their interaction. In the latter part of the last century, the understanding of the quantum theory of optical coherence and technological advances spurred the development of the field of cavity quantum-electrodynamics (cavity QED), in which interacting photons are confined in some form of an optical resonator or a cavity [32–35]. The focus of this work was on cavity QED experiments with solid-state matter. First experimental realizations in the area of quantum optics were achieved in the atomic physics community, such as the enhancement of the spontaneous emission rate of a single atom [36–39] as predicted by Purcell [40] as well as strong coupling of a single atom [41–44]. This was quickly followed by advances in solid-state physics, where excitons were coupled to photons in the strong coupling regime [45–48].

An exciton is a bound state of an electron-hole pair which can be treated as an *atom-like* two-level system. There has been a surge of two-dimensional materials after the discovery of graphene [49–51]. An interesting avenue has emerged with the discovery of atomically thin semiconductors called transition-metal dichalcogenides (TMDs), based on transition-metals (tungsten or molybdenum) and chalcogens (sulphur or selenium)[52–54]. Excitons in monolayer TMDs have a high oscillator strength, making them an excellent candidate to couple with photons. The broken inversion symmetry due to the two-atom basis in combination with a strong spin-orbit coupling leads to a valley degree-of-freedom that can be utilized for optoelectronic applications [55–57].

In this work, two platforms are presented to study the interaction between excitons in TMDs and photons in an optical resonator. One approach involves a fiber-based open Fabry-Pérot cavity at cryogenic temperatures. The setup design allows for in-situ positioning of the cavity mirrors enabling a modular platform to precisely control the interaction between photons and a variety of solid-state materials [58, 59]. A detailed analysis of technical chal-

lenges and the development of the platform is presented, followed by the demonstration of controlled exciton-photon coupling. The second approach involves localized plasmons that confine electromagnetic field in an extremely small volume and enable on-chip integration of quantum optical devices. A proof-of-principle experiment showing a non-reciprocal chiral reflectivity, based on Fano interference in weak coherent coupling, is presented.

1.1. Overview

The structure of this thesis is the following: Chapter 2 covers the fundamentals of TMDs, optical resonators and light-matter interaction. We start with introducing the basic properties of two-dimensional TMDs and explain why they are an attractive solid-state material for quantum optics research and applications. Then, the basic principles of two optical resonators used in this work, i.e. plasmons and Fabry-Pérot cavities, are discussed. Finally, the theoretical tool-box for light-matter interaction in the semi-classical and quantum regime is introduced. In the semi-classical regime, the quantized energy levels in matter interact with a classical electromagnetic field. A full quantum picture describes the formalism of the solid-state system coupled with single photons. Furthermore, the light-matter coupling is discussed in an open quantum system in the context of coupled exciton-plasmon system, where the dissipation and decay dynamics are included. The optical response is developed in the Lindblad formalism.

In chapter 3, the attention is on experimental techniques, especially on the performance of a closed-cycle cryostat, a crucial component for the development of an open Fabry-Pérot cavity at low temperatures. First, we introduce the principle and importance of a closed-cycle cryocooler for cryogenic experiments. Next, the thermal and mechanical properties of a specific closed-cycle cryostat (attoDRY800) are discussed. The heat load and temperature budget of the cryostat were studied in detail, followed by the demonstration of the reduction of temperature fluctuations at cryogenic temperatures. The characterization of the mechanical vibrations of the cold sample space on an optical table was performed, along with the suitability of the cryostat to perform optical microscopy experiments is demonstrated. Furthermore, an introduction to various vibration isolation techniques is discussed in chapter 3 that are then later implemented in chapter 5. Appendix A discusses an emerging area of research of the acoustic and elastic metamaterials for vibration-isolation.

Chapter 4 focuses on coherent interference between a neutral exciton in tungsten diselenide (WSe_2) monolayer and a localized plasmon in the gold nanodisk. The hybrid system shows a coherent interference in the form of Fano spectra in confocal microscopy. The agreement between the experimental data and the coupled system model, developed in chapter 2, is illustrated. Furthermore, the valley-Zeeman effect is exploited in the presence of an external magnetic field to demonstrate chiral reflectivity. The experimental chiral interference

complimented with the theoretical model paves the path towards using a non-reciprocal light-matter coupled system as a component for future quantum optical networks.

Chapter 5 discusses the open tunable Fabry-Pérot cavity platform at low temperatures. First, the motivation to utilize this platform is described. Then, the step-by-step development and characterization of the cavity platform is presented with a focus on the mechanical stability. Subsequently, WSe_2 is introduced in the cavity platform to study the light-matter interaction. The interaction between photons and excitons is tuned to be in the strong coupling regime with the observation of exciton-polaritons.

Chapter 6 provides a concise summary of the work highlighting the main achievements. To conclude, a discussion on future research and a perspective on quantum optics experiments with transition-metal dichalcogenides is presented.

2 Basics of monolayer semiconductors and optical resonators

An accurate description of the light-matter interaction, introduced earlier, is required to understand the cavity-QED experiments using TMDs. The experiments in solid-state quantum optics are performed in the presence of dissipation and external excitation that are treated as an open quantum system coupled with an external system commonly referred as reservoir or bath. This chapter provides an introduction to TMDs and two optical resonators used in this thesis. This is followed by a theoretical foundation of cavity QED.

First, the novel two-dimensional semiconductors are introduced with a discussion on their unique optoelectronic properties and their applications, especially in the context of quantum optics. Second, the fundamentals of two optical resonator platforms is provided. These are localized plasmons hosted by metallic nanodisks, that are used in chapter 4, and Fabry-Pérot cavity, that is used in chapter 5. Finally, I introduce the theoretical model of interaction between light and matter. A semi-classical and fully quantum treatment of interaction is given. While this is textbook theory, the goal here is to provide an overview of basic concepts that are used to describe experiments later. It is supplemented with appropriate references to ensure completeness and serve as a guide to the reader. A driven-dissipative quantum system description based on the master equation was also developed for a three-level system combining plasmons and excitons, discussed experimentally in chapter 4.

2.1. Introduction to layered semiconductors

The interest in layered semiconductors called transition metal dichalcogenides (TMDs) has exploded in a little over the last decade and half after the breakthrough experiments on graphene [49, 50, 52–54, 60, 61]. While the first investigations of bulk TMD crystal were done over half a century ago [62], the recent advances in fabrication made it possible to achieve few- to monolayer TMD samples. In particular, group VI TMD material of the form MX_2, where M is the transition metal (tungsten or molybdenum) and X is the chalcogen atom

(sulphur, selenium or tellurium), were found to be semiconducting in the monolayer limit [52, 53].

The massive attention to the family of semiconducting TMDs is due to their electronic and optical properties [55–57]. The exciton formed upon excitation of an electron to conduction band and generation of a hole in valence band has almost-ideal 2-dimensional confinement and low dielectric screening from the environment resulting in massive binding energy in the order of ~ 300–500 meV [57, 63–66].

In the bulk TMD crystals, the indirect band gap is formed in Γ-K direction, where the electronic states of Γ point (center of Brillouin zone) in valence band maximum consists of the p_z orbital of chalcogen atom while the K point in the conduction band minimum consists of the d_{z^2} orbital of transition atom [57]. Due to the broken inversion symmetry, the Brillouin zone in the monolayer TMD has two degenerate pairs of vertices K and K' which has energy band extrema (referred to K and K' valley) leading to a direct band gap where the electronic states are strongly localized in d orbital of transition metal in both conduction and valence band [57]. This leads to a strong spin-orbit coupling in both valence and conduction bands leading to valley-dependent lifting of spin degeneracy. The splitting of spin sub-bands in the valence band is in the order of few hundred meV, in the conduction band, however, the spin splitting is much smaller. In addition, there is opposite magnetic moment in two valleys due to broken inversion symmetry which leads to chiral optical selection rules [57]. A particular circularly polarized light (σ^+ or σ^-) leads to a transition in only one of the valley, K or K'. This enables valley- and spin-dependent optical and electronic properties [67]. Figure 2.1 shows an overview of properties of monolayer TMDs.

In this work, the monolayer of WSe_2 is used for the experiments. In contrast to the the molybdenum-based monolayer, the tungsten-based TMDs have a spin-forbidden ground state, called dark exciton, due to the sign reversal of spin-orbit splitting in conduction band. In addition, the monolayer WSe_2 hosts momentum-indirect Q-K excitons, biexcitonic species and charged trion or polaron species that leads to a rich and intricate photoluminescence (PL) spectrum of WSe_2 that has been a subject of intense studies in the recent years [64, 65, 68–77]. The presence of spin-forbidden dark exciton in WSe_2 has been experimentally confirmed with prospective on using long valley-lifetime for information storage and processing [65, 78–83].

The applications of two-dimensional materials, and also in particular of TMDs, are far-reaching, from electronics and optoelectronics to photonics, computing and quantum technologies [54–56, 60, 84–91]. Here, I provide a short overview of the emerging use-cases of TMDs in various fields and particularly provide a short overview on quantum optics experiments with TMDs. In electronics, the advent of bendable 2D materials are promising for flexible and wearable electronics. TMD-based devices have been shown with charge mobility similar to traditional thin-film transistors and single-crystal silicon, while showing higher strain limit, promising for a new generation of atomically thin transistors [92–94]. TMDs also

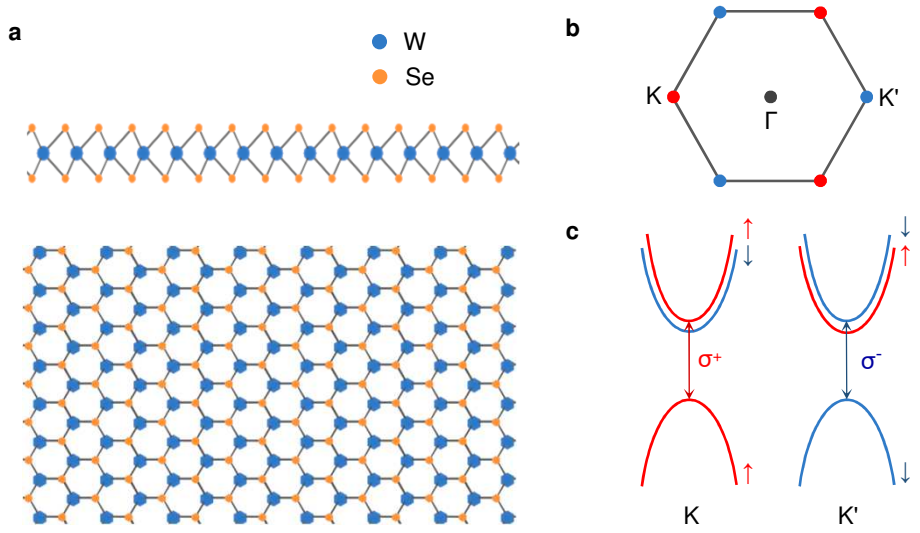

Figure 2.1.: **a**, A schematic of monolayer WSe_2 from the side and top view. The monolayer limit has a layer of tungsten atom with selenium atom on either side which forms a hexagonal lattice similar to graphene in top view. **b**, The Brillouin zone of the TMD with two distinct groups of symmetry points K and K'. **c**, The sketch of the conduction and valence band at symmetry points showing the spin-valley locking and the optical selection rules for the WSe_2.

offers an attractive platform for optoelectronics applications. Exciton-based light-emitting diodes (LEDs) have been demonstrated [95–98]. Due to the valley-dependent optical selection rules, LEDs based on WSe_2 were also shown to have a polarization-controlled emission [99]. The photo-detectors based on atomically thin semiconductors have also been realized using either photo-current or photo conduction effect [96, 100–104]. In addition, unique degree of freedom presented by valley-dependent optical absorption can be leveraged to generate valley- and spin-dependent photo-current [105, 106].

Due to their interesting optical properties, the TMD monolayer and van der Waals heterostructures are also highly promising material for photonics and optical quantum technologies. Both monolayer and more recently, heterostructures have shown to serve as a host for quantum dots which emit single photons [107–110]. The single-photon sources based on quantum dots in TMDs possess tunability and have been demonstrated to be deterministically generated via strain-tuning, ion irradiation, etc. [109–114]. Upon combining the two-dimensional materials with photonic resonators, it is possible to achieve Purcell-effect in the weak-coupling regime that can enhance (or in general modify) the spontaneous emission rate of the excitons and provides a path to control emission properties. The Purcell-enhancement has been first demonstrated with MoS_2 in a photonic crystal

cavity [115] followed by experiments with other monolayer and bilayer TMDs in various optical resonators [116–125].

The excitons in TMDs have large oscillator strength apart from high binding energy which makes them excellent candidates not just for Purcell enhancement but also in the strongly-coupled regime of light-matter interaction. In a solid-state system interacting with light, when the interaction becomes stronger than the individual decay rates, it leads to formation of the dressed-state quasiparticles called polaritons. The first signature of the strong-coupling regime was already shown with MoS_2 in a dielectric monolithic microcavity [126]. Subsequently, it has also been shown in an open tunable Fabry-Pérot cavity with $MoSe_2$ where cavity detuning is actively controlled to demonstrate avoided-crossing behavior of this regime [127]. Following the first experiments, it has also been demonstrated in different TMD monolayers: WSe_2 [128–130], WS_2 [131–134], MoS_2 [135] and charged excitonic species in $MoSe_2$ [136].

The polaritonic systems are promising way to study a variety of fundamental phenomena, including non-equilibrium condensation and superfluidity and polariton lasing [137–139], non-linear interactions [140–143]. Similar to the cold-atom BECs in optical lattices, the polariton condensates have also emerged as a platform to perform simulations of complex quantum systems [144–147].

2.2. Optical resonators

Optical resonators confines light in a small volume for an extended period of time to enhance the interaction between light and solid-state matter. In this thesis, we employ two different kind of resonators to enhance light-matter interactions. First were the collective oscillations of the electrons inside metals known as plasmons. Second was the fiber-based Fabry-Pérot microcavity in which an electromagnetic field is confined between two mirrors facing each other. Here we provide an introduction to the fundamentals of plasmonics and Fabry-Pérot cavities.

2.2.1. Introduction to plasmonics

Plasmonics enables confinement of an electromagnetic field on a sub-wavelength scale. While the classical framework for plasmonics was first developed and understood over hundred years ago, it continues to be a very attractive and active research area within the broader field of photonics [148–152]. In this section, I will introduce the basic concepts of the field.

The high density of free carriers in a metal leads to tiny energy level spacings in comparison to thermal excitations at room temperature energy $k_B T$, thus, it is sufficient to

determine their response to an electromagnetic field with classical Maxwell equations. The Drude model explains the interaction of free electrons in a metal with an electromagnetic field. The equation of motion for the electrons in the external electric field $\vec{E}$ takes the shape of a harmonic oscillator equation:

$$m\ddot{\vec{x}} + m\gamma\dot{\vec{x}} = -e\vec{E} \tag{2.1}$$

where m and e are the electron mass and charge respectively. For the harmonic electric field $\vec{E} = E_0 \exp^{-i\omega t}$, we solve equation 2.1 for the electron motion with the ansatz $\vec{x} = x_0 \exp^{-i\omega t}$. Using the relation for polarization $\vec{P} = Ne\vec{x}$, the dielectric displacement can be written as:

$$D = \epsilon_r \epsilon_0 E = \epsilon_0 E + P = \epsilon_0 E - \frac{Ne^2 E}{m(\omega^2 + i\gamma\omega)} = \epsilon_0 E\left(1 - \frac{\omega_p^2}{\omega^2 + i\gamma\omega}\right) \tag{2.2}$$

where $\omega_p = (Ne^2/\epsilon_0 m)$ is the plasma frequency. The relative permittivity is thus given by:

$$\epsilon_r = 1 - \frac{\omega_p^2}{\omega^2 + \gamma^2} + i\frac{\gamma\omega_p^2}{\omega(\omega^2 + \gamma^2)} \tag{2.3}$$

In the limit of small damping (γ=0), the permittivity ϵ_r is real and negative for $\omega < \omega_p$. The refractive index $n = \sqrt{\epsilon_r}$ in this spectral range is therefore imaginary, leading to the high reflectivity of metals in the visible range.

The quantum of the free electron plasma oscillations is called a plasmon. There are two type of commonly studied plasmon systems. The first type is the electromagnetic excitations at the interface of a dielectric and a conductor called surface plasmons. Surface plasmons are evanescently confined in one direction but are free to propagate in other directions, they also interact strongly with light to form polaritons known as surface plasmon polaritons. The second type are known as localized surface plasmon resonances, they are the collective excitations of the electronic cloud in metallic nanostructures which is confined in all dimensions [153, 154].

The localized surface plasmon resonances are the topic of study in this work (referred from here on as localized plasmons or for simplicity just plasmons). The localized plasmons lead to electromagnetic field amplification both inside and near-field outside of metallic nanostructures and are directly excitable with an external light source. The plasmon resonance for metals such as gold (Au) and silver (Ag) lies in the visible wavelength range providing enhanced absorption and scattering, making them an interesting platform as an optical resonator to study light-matter interaction.

The properties of plasmons depend on the material, size and shape of the nanostructures. The scattering of light by a particle depends on the relative size of the particle to wavelength

of light and can be defined with the size parameter $x = 2\pi r/\lambda$ where r is the radius of particle and λ is the wavelength. In the limit of nanostructures with a size much smaller than the wavelength of electromagnetic field ($r << \lambda$), the quasi-static approximation can be used i.e. the phase of the electromagnetic field is assumed constant over the particle size. The polarizability α of a sphere can be derived to be [154]:

$$\alpha = 4\pi r^3 \frac{\epsilon - \epsilon_m}{\epsilon + 2\epsilon_m} \tag{2.4}$$

where ϵ and ϵ_m are the dielectric functions of the sphere and of the surrounding environment respectively. The resonance condition is met when $|\epsilon + 2\epsilon_m|$ is minimum, leading to an enhancement of scattering and absorption of the electromagnetic field. The polarizability can also be analytically calculated for more complex shapes [154, 155]. When the size parameter gets closer to one ($r \approx \lambda$), the phase change of the electromagnetic field can't be assumed to be constant over the particle. The theory of scattering and absorption of a large particle was developed by Mie by expanding electromagnetic fields into a set of normal modes [156]. The polarizability of a sphere of volume V is [154]:

$$\alpha = \frac{1 - \frac{1}{10}(\epsilon + \epsilon_m)x^2 + O(x^4)}{\left(\frac{1}{3} + \frac{\epsilon_m}{\epsilon - \epsilon_m}\right) - \frac{1}{30}(\epsilon + 10\epsilon_m)x^2 - i\frac{4\pi^2\epsilon_m^{3/2}V}{3\lambda^3} + O(x^4)} V \tag{2.5}$$

While for vanishingly small size parameter x, the polarizability is the same as the one obtained with the quasi-static approximation, as the size of the sphere increases, the plasmon resonance shifts to lower energy due to the quadratic terms for Drude and noble metals. The imaginary term in the denominator accounts for the radiative damping channel. The discussion on various damping channels in plasmons and their relative contribution can be found in references [157, 158]. The analytical solution can be complemented by numerical simulation for more complex geometries of nanostructures, the details of finite-difference time domain (FDTD) simulation for the gold nanodisk lattice studied in this work can be found in reference [155].

2.2.2. Introduction to cavity

The most basic and straight-forward optical interferometer is a set of two mirror facing each other as first developed by Charles Fabry and Alfred Pérot in 1899 [159, 160], now commonly referred to as Fabry-Pérot cavity. The development of miniaturized Fabry-Pérot cavity based on the fiber tip with curvature makes it attractive for light-matter interaction in solid-state emitter. Here, I will introduce some basic properties of such cavities.

In a textbook description of a Fabry-Pérot cavity, the mirror i (i = 1 or 2) is characterized by its transmission T_i, scattering S_i and absorption A_i. The loss of each mirror is given by

$L_i = S_i + A_i$ and thus, the reflection of a mirror is $R_i = 1 - T_i - L_i$. The cavity linewidth in the units of frequency is given by [59]:

$$\kappa = \frac{cL_{tot}}{4\ l_c} = 2\pi\delta\nu \tag{2.6}$$

where c is the speed of light, l_c is the length of the cavity, $L_{tot} = T_1 + T_2 + L_1 + L_2$ i.e. total loss plus transmission through both ends of the cavity. The cavity linewidth term κ is related to the experimentally measured linewidth (full-width at half-maximum, FWHM) $\delta\nu$ by the second term in the equation above.

For our purpose, the most relevant property of a Fabry-Pérot cavity is the finesse. The finesse of the cavity is defined as [59]:

$$\mathcal{F} = \frac{FSR}{\kappa} = \frac{2\pi}{L_{tot}} \tag{2.7}$$

where FSR is the free spectral range given by $FSR = c/2\nu$. The finesse signifies the loss of stored photon energy in the cavity per round-trip, and thus, it is independent of the length of the cavity and is defined only by the mirrors' properties. Therefore, a high finesse is possible by reducing the scattering and absorption losses of the reflective coating on mirror. On the other hand, the Q-factor of the cavity is dependent on the length by definition as finesse times the mode number of the cavity:

$$Q = \frac{\nu}{\delta\nu} = \mathcal{F}\frac{l_c}{\lambda/2} \tag{2.8}$$

where ν and λ are the resonance frequency and wavelength, respectively. Therefore, the Q-factor is related to the photon energy decay time in the cavity. The second important parameter after the finesse for coherent coupling with matter is the cavity waist, or volume. In the case of an asymmetric concave-fiber plane-mirror configuration as implemented in this work, the cavity mode waist is given by [59, 161]:

$$w_m = \sqrt{\frac{\lambda}{\pi}}(l_c ROC)^{1/4} \tag{2.9}$$

where ROC is the radius of curvature of the concave profile. Subsequently, the mode volume at the minimum waist is:

$$V_m = \frac{\pi}{4} w_m^2 l_c \tag{2.10}$$

The light in- and out-coupling in fiber-based Fabry-Pérot cavity is efficient because the fiber, functioning as a micromirror, can at the same time be used for the coupling of light. In this case, the coupling efficiency is only limited by mode-matching between the cavity mode

and the mode of the single-mode fiber (in case of a multi-mode fiber, it can essentially be loss-less). The coupling efficiency can be derived to be [59]:

$$\epsilon = \frac{4}{(\frac{w_f}{w_m} + \frac{w_m}{w_f})^2 + (\frac{\pi\, n_f\, w_f\, w_m}{\lambda\, R})^2} \tag{2.11}$$

where w_f is the radius of the Gaussian transverse mode in the fiber and n_f is refractive index of the fiber. It can be shown that a maximum efficiency ($\epsilon \approx 1$) can be achieved even for single-mode fiber when the cavity mode waist is equal to the waist of Gaussian mode in the fiber [59].

The important parameter with respect to the coupling of the quantum emitter to the Fabry-Pérot cavity is the coherent coupling rate g. At maximum field intensity, it is given by:

$$g = \sqrt{\frac{3\lambda^2\, c\, \gamma}{2\pi V_m}} \tag{2.12}$$

where γ is the linewidth (FWHM) of the excited state of a quantum emitter in units of wavelength. The mode volume is minimized for the highly curved mirror (small radius of curvature) and smallest cavity length. The coherent coupling rate can be maximized by lowering the mode volume, for instance by reducing the cavity length for a fixed radius of curvature. However, this also leads to larger cavity linewidth as becomes evident from equation 2.6. Therefore, the ratio of coherent coupling to cavity decay rate is crucial. A figure of merit to characterize the coupling in the emitter-cavity system is the cooperativity, C, given by:

$$C = \frac{2g^2}{\kappa\gamma} = \frac{3\lambda^2}{\pi^3}\,\frac{\mathcal{F}}{w_m^2} \tag{2.13}$$

The cooperativity in the coupled system depends on the wavelength, the finesse and the mode waist of the cavity. In most cases, higher finesse and, therefore, higher cooperativity leads to more efficient light-matter interaction. The cooperativity higher than one indicates strong light-matter coupling regime.

2.3. Description of light-matter interaction

The subject of a coupled-system involving light and atom or atom-like object with discrete energy levels is under investigation for several decades. First description of interaction between a light field and matter was a fully classical model provided by Hendrik Lorentz [162]. In the classical model, the light is described with Maxwell's equations while the atom is

considered as a mechanical system with two masses i.e. a nucleus and an electron connected with a spring. The electron is excited when the light field interacts with the atom, the equation of motion of the electron can be written as a simple harmonic oscillator:

$$m_0\ddot{x} + m_0 2\gamma\dot{x} + m_0\omega_0^2 x = -eE(t) \tag{2.14}$$

where $x(t)$ and m_0 are the position and the mass of the electron, e is the electronic charge, $E(t)$ is the electric field, ω_0 and γ is the resonance frequency of the oscillator and the loss term from an oscillating dipole emitting energy. The solution to the position for a given electric field $E(t) = E_0 \exp^{i\omega t}$ is given by:

$$x(\omega) = \frac{e/m_0}{\omega^2 - \omega_0^2 - 2i\omega\gamma} E(\omega) \tag{2.15}$$

Thus, the motion of an electron is determined, in this model for a given electric field, to be a well-known Lorentzian response. It is now well-known that the simple classical model is incomplete and quantum theory is required to fully describe the light-matter interaction. Next, we will discuss an accurate treatment of the light-matter interaction.

In the first place, a semi-classical model is considered. Here, the atom or matter is quantized into discrete energy levels and their interaction with classical electromagnetic field is considered. This classical treatment of light is enough to describe many current experiments. Afterwards, we discuss a fully-quantum model where the electromagnetic field is also quantized into photons and the Jaynes-Cummings model is introduced. Finally, we introduce a method to consider dissipation and decoherence that is omnipresent in solid-state quantum systems using the master equation approach. In particular, we discuss a three-level system interacting with an electromagnetic field that is used to derive optical response in chapter 4.

Semi-classical system

The simplest approximation of an atom or exciton in two-dimensional semiconductor TMD is a two-level system, i.e. two discrete energy levels commonly referred as ground state denoted by $|g\rangle$ and excited state denoted by $|e\rangle$ with frequency difference between two states ω_{eg}. In the semi-classical picture, the interaction is between a two-level system and a classical electromagnetic field. The Hamiltonian for such a coupled system is:

$$H = \hbar\omega_{eg}|e\rangle\langle e| - \vec{d}\vec{E}(t) \tag{2.16}$$

where the last term is the interaction terms where $\vec{d} = e\vec{r}$ is the dipole moment of the transition between two levels and $\vec{E}(t) = E_0 cos(\omega t)\vec{\epsilon}$ is the time-dependent electric field. To obtain the solution, we start with the following ansatz for the wavefunction $|\psi(t)\rangle$ =

$c_g(t)|g\rangle + c_e(t)\exp^{-i\omega_{eg}t}|e\rangle$. Using the time-dependent Schrödinger equation, we get following:

$$\begin{aligned} \dot{c_g}(t) &= i\Omega_0 \exp^{-i\omega_{eg}t}\cos(\omega t)c_e(t) \\ \dot{c_e}(t) &= i\Omega_0 \exp^{i\omega_{eg}t}\cos(\omega t)c_g(t) \end{aligned} \tag{2.17}$$

Here, we introduce the Rabi frequency $\Omega_0 = dE_0/\hbar$. After the rotating-wave approximation and transformation of coefficients of wavefunction as $\widetilde{c}_g(t) = c_g(t)\exp^{-i\delta t/2}, \widetilde{c}_e(t) = c_e(t)\exp^{i\delta t/2}$ where $\delta = \omega - \omega_{eg}$, the above solution can be re-written as:

$$\frac{d}{dt}\begin{pmatrix} \widetilde{c}_g(t) \\ \widetilde{c}_e(t) \end{pmatrix} = \frac{i}{2}\begin{pmatrix} -\delta & \Omega_0 \\ \Omega_0 & \delta \end{pmatrix}\begin{pmatrix} \widetilde{c}_g(t) \\ \widetilde{c}_e(t) \end{pmatrix} \tag{2.18}$$

The probability to find the system in the excited state at time t is given by:

$$P_e(t) = \left|\widetilde{c}_e(t)^2\right| = \left(\frac{\Omega_0}{\Omega}\right)^2 \sin^2\left(\frac{\Omega t}{2}\right) \tag{2.19}$$

where $\Omega = \sqrt{\Omega_0^2 + \delta^2}$ is the effective Rabi frequency. To estimate the optical response, let us empirically add a spontaneous emission term in the form of radiative decay rate Γ to the excited state $|e\rangle$ such that:

$$\frac{d\widetilde{c}_e(t)}{dt} = \frac{i}{2}\left(\Omega_0\widetilde{c}_g(t) + \delta\widetilde{c}_e(t)\right) - \frac{\Gamma}{2}\widetilde{c}_e(t) \tag{2.20}$$

where the spontaneous emission decay rate can be quantitatively derived from the Wigner-Weisskopf theory to be $\Gamma = d_{eg}^2\omega_{eg}^3/3\pi\epsilon_0\hbar c^3$ [163, 164]. The net dipole moment of the transition is:

$$d(t) = -e\left(c_g * c_e d_{eg}\exp^{-i\omega_{eg}t} + c_e * c_g d_{ge}\exp^{i\omega_{eg}t}\right) \tag{2.21}$$

The polarization due to the ensemble of a two-level system in a sinusoidal electric field is given by:

$$P(t) = \frac{\epsilon_0 E_0}{2}\left(\chi(\omega)\exp^{-i\omega t} + \chi(-\omega)\exp^{i\omega t}\right) \tag{2.22}$$

where $\chi(\omega)$ is the linear susceptibility. The polarization is also related to the net dipole moment of the transition by:

$$P(t) = Nd(t)/V \tag{2.23}$$

where N is the number in ensemble and V is the volume of interaction. By comparing the polarization from equations 2.22, 2.23 and combining the result of equations 2.21, 2.18, 2.20, the linear susceptibility can be obtained. The real and imaginary part of the linear susceptibility are:

$$\begin{aligned}\chi'(\omega) &= \frac{Nd^2}{3\varepsilon_0\hbar V}\left(\frac{\omega_{eg}-\omega}{\left(\omega_{eg}-\omega\right)^2+\Gamma^2/4}\right)\\ \chi''(\omega) &= \frac{Nd^2}{3\varepsilon_0\hbar V}\left(\frac{\Gamma/2}{\left(\omega_{eg}-\omega\right)^2+\Gamma^2/4}\right)\end{aligned} \tag{2.24}$$

The imaginary part χ'' of the susceptibility is related to the absorption due to the two-level system which leads to an absorption of Lorentzian line-shape with the linewidth Γ. The real part of the susceptibility has a dispersive line-shape. The linear susceptibility obtained here holds for single or low density limit of two-level systems where dipole-dipole coherent interactions and super-radiant effects can be neglected.

Before further discussion on a three-level system and introduction of dissipation terms in details, we switch to the formalism of density matrix ρ. The density matrix is a more general form of describing the state required for a mixed state [163]. The density matrix elements for the two-level system are:

$$\rho_{gg} = |c_g^2|, \rho_{ee} = |c_e^2|, \rho_{ge} = c_g c_e*, \rho_{eg} = c_e c_g* = \rho_{ge}* \tag{2.25}$$

The diagonal matrix elements ρ_{ii} are the populations of the state $|i\rangle$, and the off-diagonal matrix elements ρ_{ij} (with $i \neq j$) are the coherences between the state $|i\rangle$ and $|j\rangle$. The equations of motion for density matrix elements can be written from equation 2.18 as:

$$\begin{aligned}\frac{d\widetilde{\rho}_{gg}}{dt} &= -\frac{d\widetilde{\rho}_{ee}}{dt} = \gamma\widetilde{\rho}_{ee}\frac{i\Omega_0}{2}(\widetilde{\rho}_{eg}-\widetilde{\rho}_{ge})\\ \frac{d\widetilde{\rho}_{ge}}{dt} &= -\frac{\gamma}{2}\widetilde{\rho}_{ge}+i\delta\widetilde{\rho}_{ge}+\frac{i\Omega_0}{2}(\widetilde{\rho}_{ee}-\widetilde{\rho}_{gg})\\ \frac{d\widetilde{\rho}_{eg}}{dt} &= -\frac{\gamma}{2}\widetilde{\rho}_{eg}+i\delta\widetilde{\rho}_{eg}+\frac{i\Omega_0}{2}(\widetilde{\rho}_{gg}-\widetilde{\rho}_{ee})\end{aligned} \tag{2.26}$$

The above set of equations are known as Maxwell-Bloch equations or optical Bloch equations [163, 165]. A more general description of the time-dependent evolution of the density matrix in the form of master equation is introduced later in the section.

Fully quantized system

Now we switch to the full quantum-mechanical description of the coupled system where electromagnetic field is also quantized. The quantization of the electromagnetic field $\vec{E}$ in the second quantization results in:

$$\vec{E} = \sum_{\vec{k}} \hat{\mathcal{E}}_{\mathbf{k}} \sqrt{\frac{\hbar\omega_k}{2\epsilon_0 V}} \left(a_{\vec{k}} e^{i(\vec{k}\cdot\vec{r}-\omega t)} + a^{\dagger}_{\vec{k}} e^{-i(\vec{k}\cdot\vec{r}-\omega t)} \right) \tag{2.27}$$

where $\vec{k}$ is the wave-vector, V is the volume of electromagnetic field, $a_{\vec{k}}(a^{\dagger}_{\vec{k}})$ are the photon annihilation (excitation) operator with the following canonical relation: $a^{\dagger}|n\rangle = \sqrt{n}|n+1\rangle$ and $a|n+1\rangle = \sqrt{n+1}|n\rangle$ where $|n\rangle$ is the state with n photons. The photons are the excitation quantum of the harmonic oscillator associated with a single field-mode with wave vector $\vec{k}$. The interaction Hamiltonian of an 'atom' described by a two-level system coupled with an electromagnetic field is:

$$H = \hbar\omega_k a^{\dagger} a + \hbar\omega_{eg} x^{\dagger} x + \sum_{\vec{k}} \hbar g_{\vec{k}} \left(x^{\dagger} + x \right) \left(a^{\dagger} + a \right) \tag{2.28}$$

where the first term is the electromagnetic radiation and the subscript denoting mode k is dropped from photon operators for simplicity. The second term is the two-level 'atomic' system, same as equation 2.16 but represented in second quantization where $x(x^{\dagger})$ are the exciton annihilation (excitation) operator with relation: $x^{\dagger}|g\rangle = |e\rangle$ and $x|e\rangle = |g\rangle$. The last term represents the interaction between an electromagnetic radiation field and a two-level system with coupling constant $g_{\vec{k}}$ given by:

$$\hbar g_{\vec{k}} = \sqrt{\frac{\hbar\omega_k}{2\epsilon_0 k V}} d_{\mathrm{eg}} \tag{2.29}$$

The general interaction Hamiltonian shown in equation 2.28 can be simplified to describe an interaction between a two-level exciton with a single mode of electromagnetic radiation, e.g. a photonic mode trapped in a cavity, in rotating-wave approximation with the Jaynes-Cummings hamiltonian of an interacting system:

$$H = E_C a^{\dagger} a + E_X x^{\dagger} x + \hbar g \left(a^{\dagger} x + a x^{\dagger} \right) \tag{2.30}$$

where $E_C = \hbar\omega_k$ is the energy of radiation mode, $E_X = \hbar\omega_{eg}$ is the energy of exciton. Similar to the inclusion of a spontaneous decay term in the semi-classical picture, we can phenomenologically introduce the decay terms: exciton decay rate Γ and cavity photon decay rate κ. The solution to the Jaynes-Cummings Hamiltonian leads to two new eigenstates referred to dressed states in the atomic physics community while in the solid-state quantum

optics, these new eigenstates results in new quasiparticles called exciton-photon polaritons [139, 166]. The new eigenstates are:

$$\begin{aligned} |+\rangle &= \cos(\theta/2)|e\rangle|n\rangle + \sin(\theta/2)|g\rangle|n+1\rangle \\ |-\rangle &= \cos(\theta/2)|g\rangle|n+1\rangle - \sin(\theta/2)|e\rangle|n\rangle \end{aligned} \tag{2.31}$$

with respective eigenenergies:

$$E_{\pm} = \frac{E_C + E_X}{2} - \frac{i}{2}\left(\hbar\kappa + \hbar\gamma\right) \pm \hbar\Omega_c \tag{2.32}$$

where $\theta = \arctan(-\Omega_c/\Delta E)$ is the mixing angle, $\Delta E = E_C - E_X$ is the energy detuning and Ω_c is the complex coupling Rabi frequency given by:

$$\hbar\Omega_c = \sqrt{g^2 + \left((\Delta E - i\left(\hbar\kappa - \hbar\gamma\right)\right)/2\right)^2} \tag{2.33}$$

In the solid-state matter, the excitonic ($\mathcal{X}$) and photonic ($\mathcal{C}$) fraction in the polariton is given by the Hopfield coefficients [139, 166]:

$$\begin{aligned} \left|\mathcal{C}^2\right| &= \frac{1}{2}\left(1 + \frac{\Delta E}{\sqrt{\Delta E^2 + \Omega_c^2}}\right) \\ \left|\mathcal{X}^2\right| &= \frac{1}{2}\left(1 - \frac{\Delta E}{\sqrt{\Delta E^2 + \Omega_c^2}}\right) \end{aligned} \tag{2.34}$$

Here, we introduced the fully quantum-mechanical model of a two-level system coupled to an electromagnetic mode. The experimental results of a monolayer exciton coupled to a photonic mode in a cavity, in chapter 5, are analyzed within this framework. The observation of polariton is shown and the coherent coupling rate is determined using equation 2.33. In the next section, we switch the attention to a description of an open system in presence of dissipation and discuss it in the context of a three-level system.

Open Quantum System

Any practical quantum system will have dissipation of the constituents as it interacts with the environment. In both pictures discussed above, we have introduced the dissipation in a phenomenological way. However, a proper way to introduce dissipative processes without losing the quantum nature of the system is by describing the interaction of a system with a reservoir [166]. In this way, the system is also coupled to a reservoir with which it can

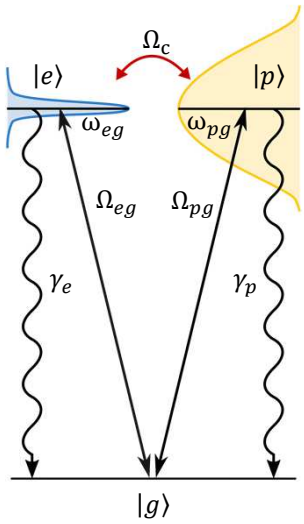

Figure 2.2.: Energy level schematic of the coupled three-level system. $|e\rangle$ represents the WSe_2 neutral exciton, $|p\rangle$ the plasmon in a Au nanodisk. Ω_{eg}/Ω_{pg} are the Rabi frequencies of light coupling the ground state $|g\rangle$ to the two excited states, Ω_c is the coupling between $|e\rangle$ and $|p\rangle$, γ_e/γ_p are the decay rates of the two respective states.

exchange energy. The system has high probability to lose the energy to one of the states in reservoir but the likelihood of the energy returning to system is vanishingly small as system size is insignificant compared to reservoir.

The general dynamics of the Hamiltonian including dissipation can be described by the master equation approach in the Lindblad form [163]:

$$\dot{\rho} = -\frac{i}{\hbar}\left[H, \rho\right] + L\rho, \tag{2.35}$$

where the first term is the Schrödinger equation for the density matrix ρ with matrix elements ρ_{ij} describing the statistical state of the system. The diagonal matrix elements ρ_{ij} (with $i = j$) are the populations of the states, with $i = g$, e or p, and the off-diagonal matrix elements ρ_{ij} (with $i \neq j$) are the coherences between the states i and j with complex conjugate $\bar{\rho}_{ij} = \rho_{ji}$. The second term in the equation, $L\rho$, accounts for the dissipation in the Lindblad form.The second term in the equation, $L\rho$, accounts for the dissipation. The system here is assumed to be under Markovian evolution with no memory of the past. In addition, there is a relatively weak coupling of the system with reservoir i.e. the Born approximation and the rotating wave approximation that removes the fast oscillating terms.

Here, the master equation is used to develop a model of three-level system. The model represents a coherently coupled system of exciton in monolayer WSe_2 and localized surface plasmon in a gold nanodisk interacting with a light field which is experimentally studied in chapter 4. The discussion that follows here is done with the convention suitable for describing the physical system shown in figure 2.2. We consider three-level system comprising

$|g\rangle$, $|e\rangle$ and $|p\rangle$ as the ground, exciton and plasmon state, respectively coupled with classical light field with frequency ω. The energy separation between the states $|g\rangle$ and $|e\rangle$ and the states $|g\rangle$ and $|p\rangle$ is $\hbar\omega_{eg}$ and $\hbar\omega_{pg}$, respectively. The Rabi frequencies for the respective transitions are Ω_{eg} and Ω_{pg}. In addition, the coherent coupling between the states $|e\rangle$ and $|p\rangle$ is denoted by Ω_c. The Hamiltonian of the system is written as:

$$H = \hbar \begin{pmatrix} 0 & \frac{1}{2}\Omega_{eg}e^{i\omega t} & \frac{1}{2}\Omega_{pg}e^{i\omega t} \\ \frac{1}{2}\Omega_{eg}e^{-i\omega t} & \omega_{eg} & \frac{1}{2}\Omega_c \\ \frac{1}{2}\Omega_{pg}e^{-i\omega t} & \frac{1}{2}\Omega_c & \omega_{pg} \end{pmatrix}. \tag{2.36}$$

First, we apply the rotating-wave approximation (RWA) to remove the time-dependent terms in the Hamiltonian of Eq. 2.36. Using $\rho_{ii} = \widetilde{\rho}_{ii}$, $\rho_{eg} = \widetilde{\rho}_{eg}e^{-i\omega t}$, $\rho_{pg} = \widetilde{\rho}_{pg}e^{-i\omega t}$, and $\rho_{ep} = \widetilde{\rho}_{ep}$, the Hamiltonian in RWA modifies to:

$$\widetilde{H} = \hbar \begin{pmatrix} 0 & \frac{1}{2}\Omega_{eg} & \frac{1}{2}\Omega_{pg} \\ \frac{1}{2}\Omega_{eg} & \Delta_{eg} & \frac{1}{2}\Omega_c \\ \frac{1}{2}\Omega_{pg} & \frac{1}{2}\Omega_c & \Delta_{pg} \end{pmatrix}, \tag{2.37}$$

where $\Delta_{eg} = \omega_{eg} - \omega$ and $\Delta_{pg} = \omega_{pg} - \omega$ are the respective detunings between the transition frequencies ω_{eg} and ω_{pg} and the laser frequency ω. Omitting the tilde superscript in the following for simplicity, we describe the dynamic evolution of the density matrix elements by the master equation (eq. 2.35) in the Lindblad form as:

$$\begin{aligned}
\dot{\rho}_{gg} &= -i\left[\frac{\Omega_{eg}}{2}\left(\rho_{ge}-\rho_{eg}\right)+\frac{\Omega_{pg}}{2}\left(\rho_{pg}-\rho_{gp}\right)\right]+\Gamma_{ee}\rho_{ee}+\Gamma_{pp}\rho_{pp} \\
\dot{\rho}_{ee} &= -i\left[\frac{\Omega_{eg}}{2}\left(\rho_{eg}-\rho_{ge}\right)+\frac{\Omega_c}{2}\left(\rho_{pg}-\rho_{gp}\right)\right]-\Gamma_{ee}\rho_{ee} \\
\dot{\rho}_{pp} &= -i\left[\frac{\Omega_{pg}}{2}\left(\rho_{gp}-\rho_{pg}\right)+\frac{\Omega_c}{2}\left(\rho_{ep}-\rho_{pe}\right)\right]-\Gamma_{pp}\rho_{pp} \\
\dot{\rho}_{ge} &= -i\left[\frac{\Omega_{eg}}{2}(\rho_{ee}-\rho_{gg})-\Delta_{eg}\rho_{ge}+\frac{\Omega_{pg}}{2}\rho_{pe}-\frac{\Omega_c}{2}\rho_{gp}\right]-\Gamma_{eg}\rho_{ge} \\
\dot{\rho}_{gp} &= -i\left[\frac{\Omega_{pg}}{2}\left(\rho_{pp}-\rho_{gg}\right)+\frac{\Omega_{eg}}{2}\rho_{ep}-\frac{\Omega_c}{2}\rho_{ge}-\Delta_{pg}\rho_{gp}\right]-\Gamma_{pg}\rho_{gp} \\
\dot{\rho}_{ep} &= -i\left[\frac{\Omega_{eg}}{2}\rho_{gp}-\frac{\Omega_{pg}}{2}\rho_{eg}+\Delta_{eg}\rho_{ep}+\frac{\Omega_c}{2}\left(\rho_{pp}-\rho_{ee}\right)-\Delta_{pg}\rho_{ep}\right].
\end{aligned} \tag{2.38}$$

Dissipation is introduced in the above master equation via population decay rates, Γ_{ee} and Γ_{pp}, and the decoherence rates, Γ_{eg} and Γ_{pg} [167]. The population decay rate includes contributions from radiative and non-radiative decay channels, $\Gamma_{ii} = \Gamma_{ii}^{r} + \Gamma_{ii}^{nr}$. The decoherence rate is related to the population decay rate as $\Gamma_{ig} = \Gamma_{ii}/2 + \Gamma_{ig,coll}$ where $\Gamma_{ig,coll}$ is the decay

rate for elastic phase-loss processes. The Rabi frequency Ω_{ig} between the excited state $|i\rangle$ ($|i\rangle = |e\rangle$ or $|p\rangle$) and the ground state $|g\rangle$ is given by:

$$\Omega_{ig} = \frac{\mu_{ig} E_{ig}}{\hbar} = \sqrt{\frac{6\pi c^2 \Gamma_{ii} P}{\hbar n \omega_{ig}^3 A}} \tag{2.39}$$

where μ_{ig} is the dipole moment of the transition, E_{ig} is the electric field, c is the speed of light, Γ_{ii} is the population decay rate of the state $|i\rangle$, P is the illumination laser power, n is the refractive index, ω_{ig} is the transition frequency from the excited state $|i\rangle$ to the ground state $|g\rangle$, and A is the illumination area. For the transition between the exciton state $|e\rangle$ and the ground state $|g\rangle$, there are two distinct Rabi frequencies, the Rabi frequency for the excitons in the vicinity of the Au nanodisk that are affected by the plasmonic enhancement of the electric field, i.e. the coupled Rabi frequency $\Omega_{ig,c}$ and the Rabi frequency of the excitons not coupled to the plasmon but still excited within the optical focal spot $\Omega_{ig,uncoupled}$. The Rabi frequency for coupled exciton fraction is related to the Rabi frequency for the uncoupled fraction as $\Omega_{eg,c} = \sqrt{F}\, A_c\, \Omega_{eg,uncoupled} / A_{uc}$, where A_c is the overlap area between the ML and the nanodisk where plasmonic enhancement is present, A_{uc} is the area of uncoupled excitons within the optical focal spot, and EF is the enhancement factor of the electric field obtained from the FDTD calculation.

Solving the set of coupled equations for steady state where $\dot{\rho}_{ij} = 0$, and using population conservation in the three-level system as $\rho_{gg} + \rho_{ee} + \rho_{pp} = 1$, we obtain analytical expressions for the populations and coherences in the coupled system as a function of experimental parameters. The optical response is obtained from the imaginary part of the coherence matrix elements [168]. In the device studied in chapter 4, the focal spot consists of an exciton-plasmon hybrid region showing coherent interference and also a region with uncoupled excitons in ML spatially far from the nanodisk. Therefore, we obtain the extinction $\mathcal{E}$ in the optical response as the sum of the coherence matrix elements of two coupled states and the uncoupled exciton state as following:

$$\mathcal{E} \propto \alpha_e \frac{\Omega_{eg,c}\Gamma^r_{ee}}{\Omega^2_{eg,c} + \Omega^2_{pg}} \mathrm{Im}(\rho_{ge}) + \alpha_p \frac{\Omega_{pg}\Gamma^r_{pp}}{\Omega^2_{eg,c} + \Omega^2_{pg}} \mathrm{Im}(\rho_{gp}) + \alpha_e \frac{\Gamma^r_{ee}}{\Omega_{eg,uc}} \mathrm{Im}(\rho_{ge,uncoupled}), \tag{2.40}$$

where α_e and α_p correspond to the maximum on-resonance scattering contrast of the exciton and plasmon transition with radiative decay rates Γ^r_{ee} and Γ^r_{pp}. The respective contrasts α_i are obtained as [169]:

$$\alpha_i = \frac{3}{2\pi} \frac{c^2}{n^2 \omega_{ig}^2 A}. \tag{2.41}$$

We note here that the extinction is not quantitative as we don't take into account all reflecting surfaces of the device to calculate the Rayleigh scattering field based on the procedure

detailed in [169]. However, the response spectrum is proportional to the imaginary part of the coupled coherences ρ_{eg} and ρ_{pg}, and the uncoupled exciton coherence $\rho_{eg,uncoupled}$ as a function of frequency, and we obtain correct qualitative description of differential reflection.

3 Experimental techniques

A very important part of enabling a high finesse Fabry-Pérot cavity in a closed-cycle cryostat is the technical challenges regarding operating a cryostat in optimum conditions. This chapter describes the fundamental properties of the cryostat. In particular, the thermal and mechanical performance of the chosen cryostat i.e. the attoDRY800 for the tunable cavity experiments was studied. The attoDRY800 is a cryostat integrated within the optical table such that it provides a flexible optical access to free-space components on the optical table, and simultaneously it can fit a large and complex positioning setup with the sample and cool it down to cryogenic temperature.

We begin with the introduction to closed-cycle cryostats, the motivation of using a helium-free system and the basic working principle in section 3.1. The focus is then switched to the thermal properties of the attoDRY800 in section 3.2. First, we present the analysis of different components of the cryostat and their contribution to thermal properties. Second, we discuss the issue of temperature fluctuations at low temperature and present a method to increase temperature stability. Section 3.3 is dedicated to the mechanical properties of the attoDRY800. The vibration performance of the cryostat are presented, followed by the introduction to various techniques for vibration reduction that are later implemented in chapter 5 for the tunable cavity setup.

3.1. Introduction to closed-cycle cryostat

While the first time humans were able to have a controlled generation of heat with fire at least a few hundred thousand years ago [170], our ability to generate colder temperature has took off only in the last two centuries. The concentrated effort to go to lower temperature began with the development of a better understanding of thermodynamics as well as a demand for controlled refrigeration by the food and beverage industry, one of the path-breaking achievements in 1908, Heike Kamerlingh Onnes achieved the first liquefaction of Helium

and reached down to 1.5 K, the coldest temperature reached at the time, which he followed 3 year later with the discovery of superconductivity [171, 172].

In the last decades, helium has found use in a variety of applications from coolant in magnetic resonance imaging (MRI) machines to balloons for weather and festivities. It has also become a work-horse coolant in many science laboratories, for example in solid-state and quantum physics experiments at cryogenic temperature. However, helium is a scarce and non-renewable resource, it is not possible to retrieve gaseous helium lost in the atmosphere as gravity does not hold helium on earth and it is also not possible to generate new helium with a chemical process [173].

The development of closed-cycle cryocoolers starting in the late 1950s provides a comprehensive solution to reach cryogenic temperature without needing constant supply of liquid helium. There are primarily two types of cryocoolers used to reach temperatures of liquid helium, i.e. 4 Kelvin: Gifford-McMahon (GM) cryocoolers and pulsed-tube (PT) cryocoolers. While a detailed comparison of characteristics and performance parameters of both types is out of the scope of this work, the PT cryocoolers offers lower mechanical vibration, higher up-time before maintenance. On the other hand, GM cryocoolers have higher efficiency and most importantly they can work in any orientation while PT coolers can only work with their cold end facing down or with small angles with respect to the gravity. The reason for this is that gravity leads to convection in the pulse tube opposing the flow generated to create the cooling power, making the cryocooler lose efficiency when operated at an orientation other than cold end pointing towards gravity [173, 174]. Due to the design requirement of attoDRY800 integrated in the optical table with complete optical access, the choice of cryocooler for the attoDRY800 is the GM cryocooler.

The GM cryocooler can be divided into two parts: compressor and cold head. The compressor provides a high pressure and a low pressure helium gas line. The cold head is the main body which contains a regenerator and displacer unit as well as compression and expansion space. In a typical thermodynamic cycle, first the high-pressure gas builds up in the compression space towards room temperature side of the cold head. In the next step, displacer move towards the room temperature side as the gas passes through the regenerator which absorbs the heat from the gas leaving it at low temperature on the cold side of cold head in expansion space. Now the valve to the high-pressure side of the compressor is closed and towards the low-pressure side is opened to create a suction. The gas in the expansion space now expands generating the cooling power next to the cold side. In the final step, the displacer moves back from room temperature to the cold side as gas passes back through the regenerator, adsorbs heat from it and leaves at ambient temperature towards the compressor. The cooling cycle is typically repeated at 1 Hz while the gas compressor can independently maintain the gas at about 16 bars at the import side of the cryocooler, with normal electric-supply frequency of 50 Hz. The two primary characteristics of a GM cryocooler are: first, the primary function to reach the low temperature by producing cool-

ing power and second, generation of undesirable mechanical vibrations due to moving displacer/regenerator part inside the cold head. Both characteristics are introduced and analyzed in detail in the next sections.

3.2. Thermal properties

The most crucial parameter for a closed-cycle cryostat is its thermal performance, as the primary function of a cryostat is to cool down an object to the temperature of few Kelvin and maintain that temperature. The base temperature and cooling power a cryostat can achieve defines the usability of such a device for isolating a physical system under study from environmental disturbances. In this section, I will describe some aspects of the thermal performance of the attoDRY800.

The attoDRY800 is a GM-cooler based closed-cycle cryostat integrated within an optical table. It was the choice of cryostat to perform stable cavity experiment presented in chapter 5. A huge advantage for this choice was the excellent starting point in terms of the mechanical vibrations of the cryostat, which is discussed in detail in section 3.3.1.

In section 3.2.1, the base temperature and thermal performance of the cryostat is studied. This study was prompted by irregularities in reaching the specified temperature for several attoDRY800 cryostats in late 2016. A series of experiments were performed to identify all the heat loads with the goal to understand the thermal budget of the cryostat. The improved understanding of the mechanisms at play enabled us to reduce the base temperature from 4.40 K to 3.63 K in this particular cryostat by removing unnecessary heat loss channels. The potential problems that could lead to higher than designed temperature were also identified. At present, we achieve base temperature in the range of 3.3 K for attoDRY800 cryostats.

Section 3.2.2 discusses the issue of base temperature fluctuations. The temperature fluctuate during a period of the cooling cycle. It may also fluctuate over longer time period if the cooling power of the cryocooler is not constant. This fluctuations can change the material properties as well as the accuracy of cavity stability and scanning-probe techniques depending on the magnitude of such fluctuations. We studied the fluctuations and we devise a way to reduce the temperature fluctuations by introducing a thin stainless steel layer. To this end, the theory of heat diffusion is briefly discussed and an analytical solution is derived, then the results of measurement with metal pieces of various thickness are presented and compared with an analytical model of heat conduction. This study paves the path towards improving the temperature stability of a sample in a cryogenic instrument.

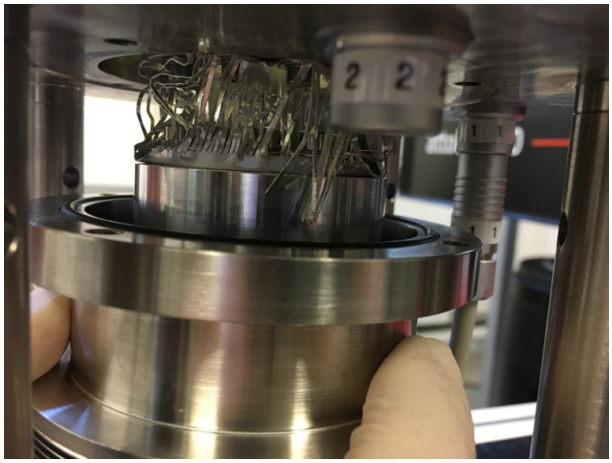

Figure 3.1.: A picture of broken 40 K link. The visual confirmation of fragile thermal link connecting the first stage of cold head to the cold shield on optical table was broken.

3.2.1. Thermal budget

In this section, I will discuss the systematic study of the heat source and thermal performance of the attoDRY800. The standard specified temperature of the attoDRY800 is 3.80 K based on the base temperature and the cooling power of the cold head combined with our understanding of the thermal heat load of the cryostat.

This study was motivated by irregularities in achieved base temperature observed for different attoDRY800 cryostats manufactured in late 2016. For example, one cryostat (project 208197) reached the base temperature of 4.40 K as produced, which was higher than the expected base temperature by 0.6 K. We decided to undertake a detailed analysis with two goals: One, to solve the higher than specified base temperature in this particular system and second, to reach the long-term goal to have a consistent and expected base temperature in all produced attoDRY800 cryostat by understanding different sources to the heat load.

The tests shown in this section are all performed on the cryostat for project 208197 and temperature has been measured with a calibrated Cernox temperature sensor and monitored with either an internal attoDRY controller or an external temperature controller (Lakeshore 335 Temperature Controller). As mentioned above, the base temperature achieved for the first cool-down of the attoDRY800 is 4.40 K. This was few hundred mK higher than the temperature routinely achieved with previous attoDRY800 cryostats. One potential cause for the unexpected high base temperature in the attoDRY800 system is the thermal links that connects the cryocooler to the cold plate on the optical table. There are two thermal connections that link the GM cryocooler's first and second stage to the cold shield part and the cold plate part of the sample, respectively, and are conventionally referred as '40 K link' and '4 K link' due to the typical temperature reached in these areas.

The purpose of the thermal link is to provide an optimum thermal connection between

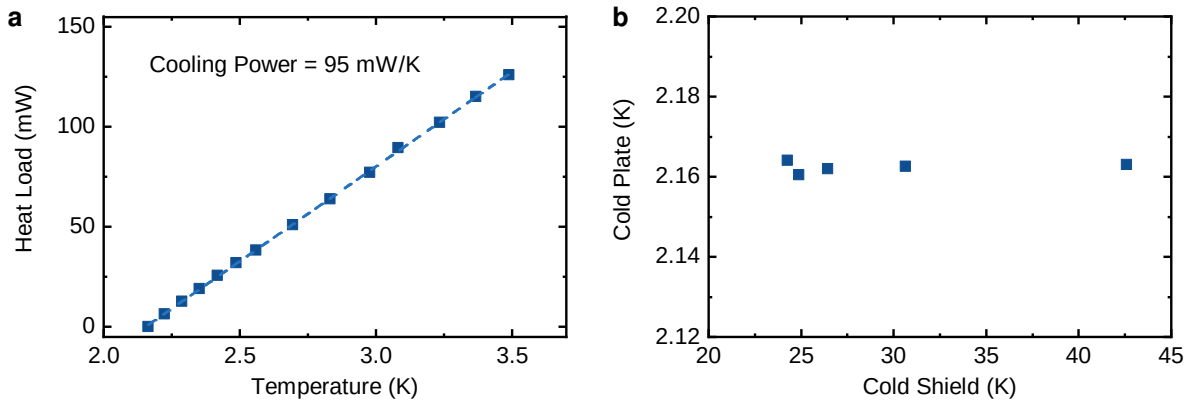

Figure 3.2.: Cooling power and heat load of cold head. **a** Cooling power measurement results of the bare cold head. **b** Relation between first and second stage cold head temperature.

the cold head and the respective cold part of the sample space, to maintain a high cooling power while minimizing the transfer of mechanical vibration between the cryocooler and the sample space which is connected to the floating optical table [175, 176]. The geometric design at the time to fulfill this requirement led to the thermal link being fragile, and thus rendering it as a potential problem source. In this system, we removed the cryostat from the optical table and upon visual inspection, it was found that the 40 K link was damaged as shown in figure 3.1. The link used in here was a new design with a smaller width of the stripes than the previous generation link. Also, this new generation link was fabricated with a new laser cutting method compared to the previous links which were fabricated by the hand cutting technique.

We replaced the broken link with a new hand-cut link, with same width as the previous generation link, and the base temperature reached 4.20 K. It was later verified that the laser-cut link performs as good as the hand-cut link. Therefore, the first issue was the change in design towards a reduced width that presumably made the link more likely to break when mechanically strained at low temperature.

In further investigation, we first test the performance of only the cold head (GM cryocooler RDK-101DL) that is used in the attoDRY800 to quantify its performance. The cryocooler cold head second stage reaches the base temperature of 2.16 K and first stage reaches 24.3 K which meets the specification of the supplier. The cooling power is also measured by applying a heat load via a calibrated heater on the cold plate and monitoring the change in temperature, as shown in figure 3.2a. The cooling power is linear as a function of temperature in this case and the value is determined to be 95 mW/K. In addition, the dependency of the second stage temperature as a function of heat load on first stage of the cold head was measured. Figure 3.2b shows that while the first stage temperature is increased from 25 K to 45 K by

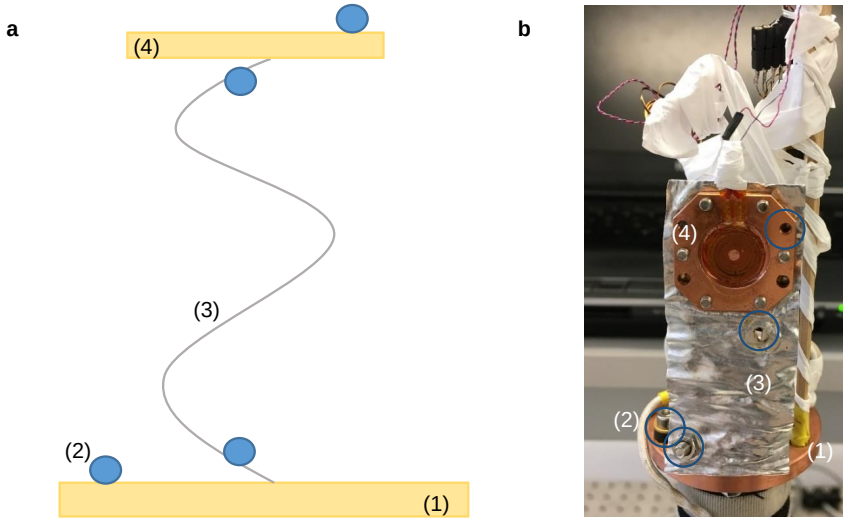

Figure 3.3.: The setup used to measure the temperature conductivity of thermal link of the cryostat. a) Schematic and b) Picture of the setup with components: 1) 4 K plate of the cold head, 2) Temperature sensor, 3) Aluminum thermal link and 4) Top plate emulating cold plate.

applying thermal load with a heater, the second stage temperature stays at 2.16 K and the cooling power of the second stage stays unaffected. This confirms that the first stage has high cooling power and the high heat load on the first stage should not affect the performance of the second stage thermal performance. Therefore, the design of the attoDRY800 should minimize the heat load on the second stage by thermalizing unnecessary heat loads to the first stage.

In the next set of tests, the thermal conductivity of aluminum, which is the material used for the thermal link, and the thermal conductivity through the interface was measured. The setup is demonstrated in figure 3.3. There are two interfaces for the thermal link, one with the cold plate and second with the the cold head. The extrapolation of the thermal conductivity of the interfaces was done by scaling the effective contact area from the setup here to the actual interfaces in the attoDRY800. The results of the thermal conductivity measurements for the material and the interfaces are summarized in Table 3.1. The effective cooling power can be deduced to be 74 mW/K. We also measured the thermal conductivity of the same material that was standing in air for more than 3 years and confirmed that there is no age-based material property change that hampers the thermal performance.

Thereafter, the heat load of different components of the cryostat is determined, either through a direct measurement or by inferring their contribution to the total load by removing that specific component. First, the heat load of the electrical wires accessible at the sample area is studied. In total, there are 40 brass, 8 manganin and 2 copper wires running from

Test Description	Result
Measure the thermal conductivity of the interface cold head second stage/Apiezon/Al/6xM4 screws	756 mW/K
Measure the thermal conductivity of the interface cold Cu Plate/Apiezon/Al/10x M2.5 screws	1200 mW/K
Measure the thermal conductivity of Aluminium	1.5 - 2 x 10^4 W/m/K
Effective cooling power of the system calculated (cold finger+Al link+Cu plate+interfaces)	74 mW/K
Measure the thermal conductivity of the first batch of Al material from Fall 2014	Althermal conductivity does not age

Table 3.1.: Summary of thermal conductivity tests of Aluminum link and interfaces

300 K to the 4 K cold plate via the 40 K plate. We removed all the brass wires and measured the base temperature with only 8 manganin and 2 copper wires which are needed for the temperature sensor and the heater. The base temperature reached is 3.90 K, compared to 4.20 K before the removal of brass wires, which infer a heat load due to the brass wires of 22 mW.

In the second test, the contribution of thermal radiation to the 4 K region coming through the free space in 40 K thermal link is inferred. This thermal radiation is due to the stripe geometry of the 40 K thermal link that exposes the 4 K region to the room temperature. This was temporarily covered with an aluminum foil to remove any exposure while increasing mechanical vibrations by introducing a rigid connection of the foil. The base temperature reached was 3.63 K (still without brass wires), compared to 3.90 K previously. Therefore, the above thermal radiation has 20 mW of heat load that can be possibly reduced with a future re-design of the 40 K link.

In the next step, the gold coating of the cold plate area that has an interface with thermal link was removed to directly establish a contact of the thermal link to the cold plate (shaded area in figure 3.4). This change in interface conductivity due to the removal of gold coating leads to reduction of heat load by 16 mW, as the system reaches a lower base temperature of 3.42 K. Next, we remove the cold plate and directly measured the base temperature achieved at the end of 4 K thermal link, the temperature is 3.15 K, lower by 0.27 K as compared to the temperature on the cold plate. Compared to the base temperature of the cold head second stage of 2.16 K, the temperature at the end of thermal link is almost 1 K higher, this increase in temperature infers to the heat load of 75 mW.

This heat load was quite surprising as there were no obvious sources between cold head and the top end of 4 K thermal link with such significant contribution to the heat load. Upon closer look at the cryostat design, four apertures are found in the thermal shield designed to protect the second stage of cold head from the room temperature (see figure 3.5), these

Test Description	Result
The cryostat as produced (40x brass + 8x manganin + 2x copper contacts)	T = 4.40 K
The cryostat was opened and a broken 40 K thermal link was replaced & T = 4.20 K	
GM cooler was tested separately	T = 2.16 K
Thermal conductivity of the thermal link material and interface was measured separately	$1.5-210^4$ W/m/K for aluminum, 756 mW/K for 6x M4 interface and 1200 mW/K for 10x M2.5 interface
All brass contacts were removed	T = 3.90 K -> 22 mW for all brass contacts
Thermal load from radiation through opening in 40 K thermal link was eliminated	T = 3.63 K -> 20 mW radiation through gaps in the link
The gold coating on the cold plate interface was removed for effective interface between 4 K thermal link and cold plate	T = 3.42 K -> 16 mW heat load due to additional resistance from the coating
The base temperature at the top of 4 K thermal link connected to only to the cold head second stage	T = 3.15 K -> 75 mW unknown heat load is present in the system
Four apertures on the shield on cold head are identified as potential heat source and blocked	T = 2.27 K -> major heat loss channel explained (8 mW heat load left)
Full cryostat system but with the above four apertures blocked	T = 3.63 K

Table 3.2.: Overview of thermal tests and heat loads of attoDRY800

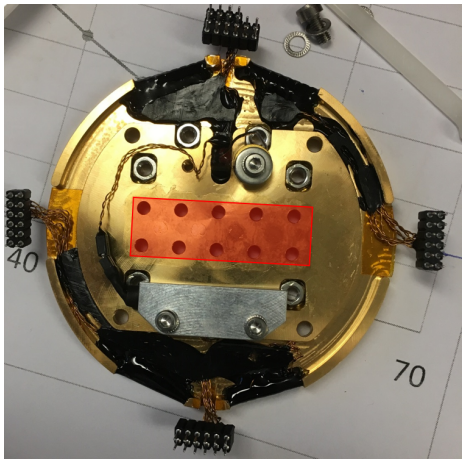

Figure 3.4.: The picture of bottom side of the cold plate. The red shaded box shows the interface area with thermal link where the gold coating was removed to create more efficient thermal interface.

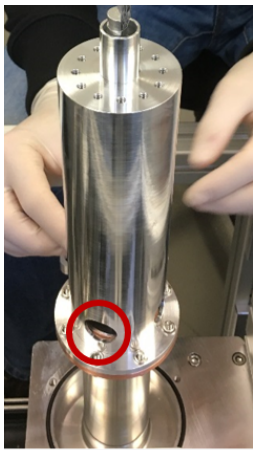

Figure 3.5.: Original design of shield for the cold head with four round apertures (circa 2 cm diameter) at the base (highlighted in red) for efficient pumping.

apertures were originally introduced to ensure an effective pumping to reach vacuum. In the next test, these apertures were closed with aluminum tape. In the subsequent cool-down, the top end of the thermal link reached base temperature of 2.27 K instead of 3.15 K. We also observe no obvious increase in the pumping time, an increased base pressure or any other negative consequences for the cryostat performance. Therefore, an unnecessary heat source of 67 mW was found, and the apertures were removed in the subsequent design of the cryostat.

With the major undesired heat source found and removed in the form of apertures, the cryostat with all components removed in previous steps was able to reach the base temperature of 3.63 K. The results of the thermal tests are summarized in Table 3.2. In addition,

other necessary components and their thermal contribution were understood.

3.2.2. Thermal oscillation damping

The oscillation of base temperature and the method to reduce such oscillations are discussed in this section. Due to the nature of the cooling cycle of a closed-cycle cryostat, the cooling power is not constant. Hence, the temperature undergoes an oscillation with the same period as the cryocooler. These temperature fluctuations are as high as 150 mK in a standard attoDRY800, as shown below. This undesired oscillations can be an issue, especially in experiments where small temperature change leads to either a change in the property of a material under study such as a phase transition or in sensitive experiments like high-finesse cavity or atomic-force microscopy where temperature change can lead to additional mechanical vibration.

One way to tackle the temperature oscillation is to introduce an additional spacer layer of a low diffusivity material that leads to the damping of temperature oscillation. First, I will briefly discuss the principal of thermal oscillation damping based on classical Fourier heat diffusion theory. Second, the results based on stainless steel as a spacer layer in the attoDRY800 are presented.

The classical heat diffusion dynamics are based on the following equation:

$$\nabla^2\psi = \left(1/a^2\right)\left(\partial\psi/\partial t\right) \tag{3.1}$$

where ψ is the temperature as a function of spatial and time coordinates, $a^2 = \kappa/\rho C$ is the diffusivity coefficient, κ is the heat conductivity, ρ is the material density and C is the heat capacity per unit mass. For a simple one-dimensional system, the heat diffusion dynamics in frequency space turns to the following equation:

$$d^2\psi/dz^2 + \left(i\omega/a^2\right)\psi = 0 \tag{3.2}$$

The general solution to the above equation is:

$$\psi(z,t) = A\exp-\left[(1-i)\frac{z}{\ell_0}\right] + B\exp\left[(1-i)\frac{z}{\ell_0}\right] \tag{3.3}$$

where an effective heat diffusion depth $l_0 = \sqrt{2a^2/\omega}$ is defined based on the material properties. The constants A and B can be determined depending on the boundary conditions. The heat energy flow per unit area is given by:

$$\vec{J}(z,t) = -\kappa\vec{\nabla}\psi \tag{3.4}$$

which is flowing perpendicular to the layer direction. The general expression for the heat flow is:

$$J(z,t) = \sqrt{2\kappa\rho C\pi f}\left\{A\exp-\frac{(1-i)z}{\ell_0} - B\exp\frac{(1-i)z}{\ell_0}\right\}\exp(-i\pi/4) \tag{3.5}$$

Now with the general solution for the temperature and the heat flow obtained, let us look at the boundary conditions for the temperature oscillation reducing material spacer. We consider a spacer layer of finite thickness l attached to the cold plate at the plane at $z = 0$ and the layer is not connected to any additional heat bath at $z = l$. The first boundary condition at $z = 0$ dictates that the temperature is driven by the cold plate temperature:

$$\psi(z=0,t) = A + B = \psi_0\exp(-i\omega t) \tag{3.6}$$

The second boundary condition means that there is no heat density flow at this face i.e. at $z = l$:

$$\nabla\psi(l) = A\exp-\frac{(1-i)\ell}{\ell_0} - B\exp+\frac{(1-i)\ell}{\ell_0} = 0 \tag{3.7}$$

Combining both equations of the boundary conditions, we get the following solution for A and B:

$$\begin{aligned} A &= \frac{\exp(1-i)\ell/\ell_0}{\exp\ell/\ell_0(1-i)+\exp-\ell/\ell_0(1-i)}\psi_0\exp(-i\omega t) \\ B &= \frac{\exp-(1-i)\ell/\ell_0}{\exp(1-t)\ell/\ell_0+\exp-(1-i)\ell/\ell_0}\psi_0\exp(-i\omega t) \end{aligned} \tag{3.8}$$

The temperature at $z = l$ will be:

$$\psi(\ell,t) = \frac{2}{\exp(1-t)\,(\ell/\ell_0)+\exp-(1-t)\,(\ell/\ell_0)}\psi_0\exp(-i\omega t) \tag{3.9}$$

The general solution to the equation 3.9 can be solved for the phase lag and temperature oscillation amplitude. The temperature oscillation amplitude is given by:

$$\psi_{maximum} = A\cos\left(\phi-\phi'\right) + B\cos\left(\phi+\phi'\right) \tag{3.10}$$

where $\phi = l/l_0$, A and B are respectively given by $A = \exp(+\ell/\ell_0)\,/\,\{\cosh(2\ell/\ell_0)+1\}$ and $B = \exp(-\ell/\ell_0)\,/\,\{\cosh(2\ell/\ell_0)+1\}$. The phase lag is given by:

$$\phi' = \arctan\left(\tanh(\phi)\ \tan\phi\right) \tag{3.11}$$

The damping factor and phase lag based on equation 3.10 and 3.11 are shown in figure 3.8. The dynamic thermal penetration depth for our damping slab at 4 K is $l_0 = 2.44$ mm for $\omega/2\pi = 1$ Hz, based on its thermal properties [177]. This means that with a reasonable

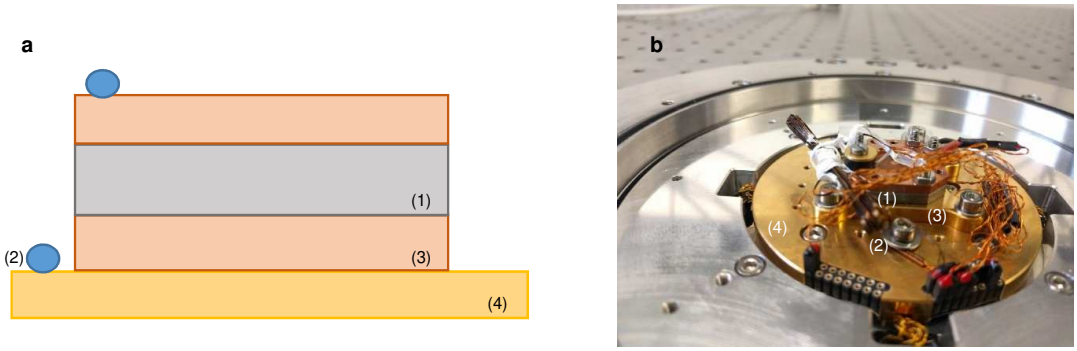

Figure 3.6.: The setup used to measure the temperature oscillations. a) Schematic and b) Picture of the setup with components: 1) Thermal damping layer, 2) Temperature sensor, 3) Copper mounting plate and 4) Cold plate.

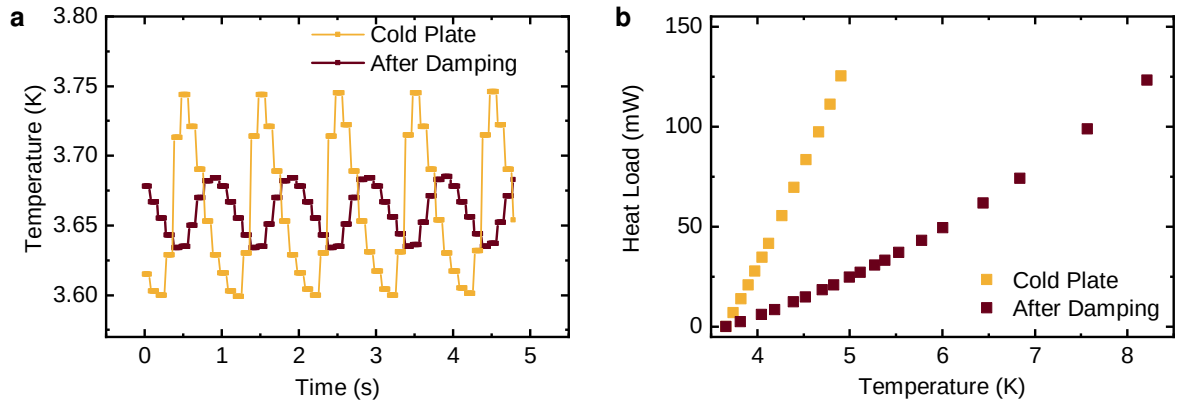

Figure 3.7.: Result of introducing 3 mm stainless steel thermal damper on temperature oscillation and cooling power. **a** Thermal oscillation at cold plate and after 3 mm thermal damper. **b** Cooling power measured on the cold plate and after the thermal damper.

thickness of few millimeters, the slab can provide a significant damping in temperature fluctuations.

After the analytical analysis of introducing a stainless steel spacer as a thermal damper, we performed experiments to verify their effectiveness. The experimental setup is sketched in figure 3.6. A damping layer is mounted on the cold plate of the attoDRY800 with help of a copper mounting plate (copper has the dynamic penetration length of $l_0 = 2.7$ m at low temperature so it can be considered a perfect conductor and neglected for small thickness) and a Cernox temperature sensor and a heater are mounted on another copper piece on top of the damping layer that allows perfect thermalization at the top side.

We begin with a spacer of 3 mm thickness. The temperature oscillations are plotted in

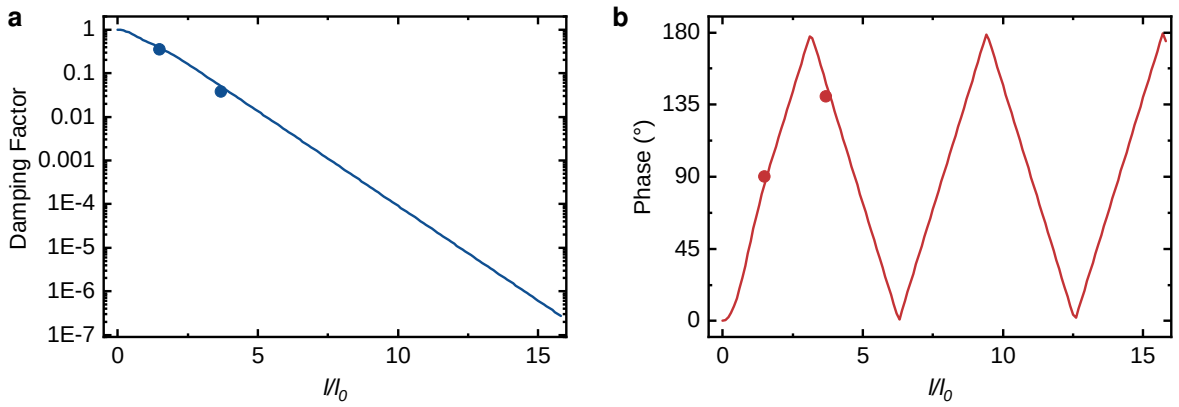

Figure 3.8.: Temperature oscillation damping. **a** Damping factor and **b** phase as a function of thermal damper thickness. Solid lines represents the damping factor and phase of the oscillations determined by the analytical model for our damping slab. Solid dots represents experimental data for two damping slabs with thickness of 3 mm and 7 mm. Dynamic thermal penetration depth is $l_0 = 2.44$ mm.

figure 3.7a. The temperature oscillations go from 145 mK on the cold plate to 50 mK after the damper at the base temperature of 3.6 K. This shows the damping factor of 0.34. The phase of the fluctuations can be noted to be approximately 90 degrees shifted with respect to the cold plate temperature oscillations measured at the same time. The cooling power measured after the damping layer is shown in figure 3.7b. It is linearly approximated at 3.7 K to be 20.2 mW/K, so, temperature oscillation damping comes at the cost of cooling power.

Then, we perform the same measurement with the damping spacer of 7 mm thickness (results not shown). The temperature oscillation after damper is 6 mK, which yields a damping factor of 0.04. The phase in the oscillation cycle is shifted by approximately 135 degrees. The linearly-approximated cooling power is 8.5 mW/K after the damper. The damping factor and phase lag of oscillation for both thickness are compared with the analytical results in figure 3.8 and show excellent agreement.

This set of results shows the possibility to improve temperature stability at cryogenic temperature, however it comes at the price of reduction of the cooling power through the damping layer.

3.3. Mechanical properties

Another crucial parameter next to thermal performance is mechanical vibration in a closed-cycle cryostat. In a Gifford-McMahon (GM) cryo-cooler, the cooling is done in the cold head which includes a moving regenerator/displacer whose cycle is synchronized with a working

gas (helium) supplied by the compressor. This moving displacer generates the mechanical vibration. The amplitude of vibration induced by GM cryo-cooler is of the order of 10 μm [178].

This level of vibration is too high for even the most basic optical spectroscopy experiments e.g. confocal microscopy where depth-of-field of an objective is less than 1 μm. This puts the upper-limit on vibration amplitude. For more sensitive scanning-probe experiments such as an atomic-force microscopy (AFM), the limit becomes more severe as vibration amplitude has to be (much) smaller than the resolution desired, setting the required vibration amplitude to be less than 1 nm.

A fiber-based Fabry-Perot optical cavity is one of the most mechanically-sensitive experiments. The stability required depends on the desired Finesse of the cavity for a given wavelength. The linewidth of the cavity is given by the free-spectral range (FSR) divided by the Finesse (see section 2.2.2). Therefore, in a high-Finesse optical cavity i.e. for $\mathcal{F} = 10^4$ and wavelength $\lambda = 780$ nm, the linewidth will be 39 pm. For a moderate Signal-to-Noise ratio (SNR) of 100, the required stability of the system already reaches sub-pm regime.

It becomes quite clear that a significant work is required to go from the inherent vibration of a GM cryo-cooler of 10 μm to sub-pm regime requiring over 7 orders of magnitude improvement. In this section, we quantify the mechanical performance of the attoDRY800 and then discuss various vibration damping techniques that could be used to improve it further. The design of the closed-cycle cryostat attoDRY800 provides an improvement to the vibration of the cryocooler. The sub-section 3.3.1 discusses the vibration improvement achieved due to the design of the closed-cycle cryostat. In the sub-section 3.3.2, the common mechanical vibration isolation or damping methods are described, particularly the ones that were practically implemented during the work on this thesis.

3.3.1. Mechanical vibration analysis

The method used for measuring the displacement of the cold plate is an interferometric sensor. Typically, an interferometric sensor can detect displacement using change in phase of an interference pattern generated with light reflected off a target with respect to the light reflected off a reference. In a Fabry-Pérot interferometer, the reflected light coming from two parallel surfaces, i.e. a cavity, is interfered such that the displacement of one surface is measured with respect to other surface as a reference.

The Fabry-Pérot interferometer as a displacement sensor offers several advantages over other methods. The optical interferometric sensing offers high resolution, high accuracy as well as the ability to measure over long distance compared to other common distance measurement techniques such as capacitive or resistive readout, linear encoders and linear variable differential transformers (LVDT) [179–181]. It is also suitable to work in ultra-high vacuum and cryogenic environments. Compared to the other optical technique using a

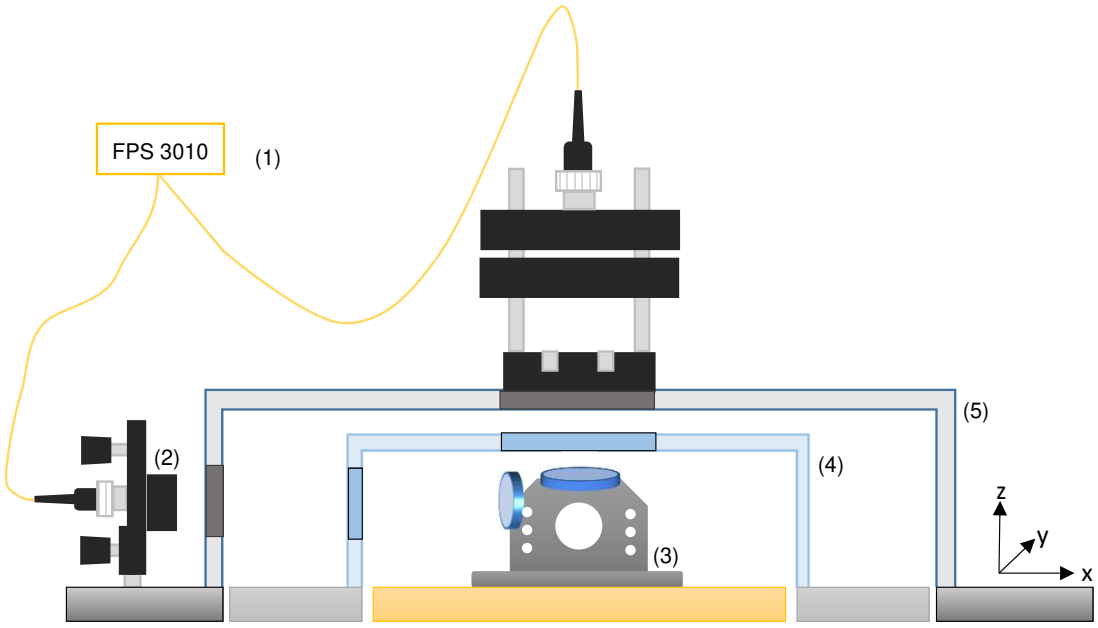

Figure 3.9.: The setup used to measure the mechanical vibrations of the cold plate using optical interferometer displacement sensor. The components of the setup: 1) FPS Displacement sensor, 2) Optomechanics mount for fiber coupler, 3) The mount holds mirror in all dimensions whose displacement is measured, 4) 40 K shield with optical windows, 5) Room temperature pressure shield with optical windows, 6) Cold plate, 7) 40 K plate, 8) Optical table. The measurement of mechanical vibration of positioners or other components is measured by mounting them on cold plate (6) and fixing holder (3) with a mirror on the top.

Michelson interferometer where light is split with a beam-splitter and one part is sent to a target surface while other is to a reference surface, Fabry-Pérot interferometer doesn't need an additional reference surface. This is advantageous as it is difficult to have a reference surface with absolutely zero displacement. Moreover, the relative disturbances in two optical path can also create additional phase change [182–184].

The measurements shown in this section are done with a commercial displacement sensor (attocube FPS3010). FPS3010 is a miniaturized Fabry-Pérot interferometric sensor with a built-in laser diode, detector and other optical and electronic components. The laser beam (laser wavelength = 1550 nm) from the diode is first divided with a 2x2 fiber beam-splitter, one fiber arm is guided to a free-space coupler (referred to as sensor head), a few percent of light gets reflected back from the sensor head, thus serving as the reference beam. The free-space beam is reflected from the target surface and is guided back through the sensor head to the photodiode together with reference beam. The phase fluctuations in the intereference signal is then converted to the displacement fluctuations of the target surface [179, 182, 183].

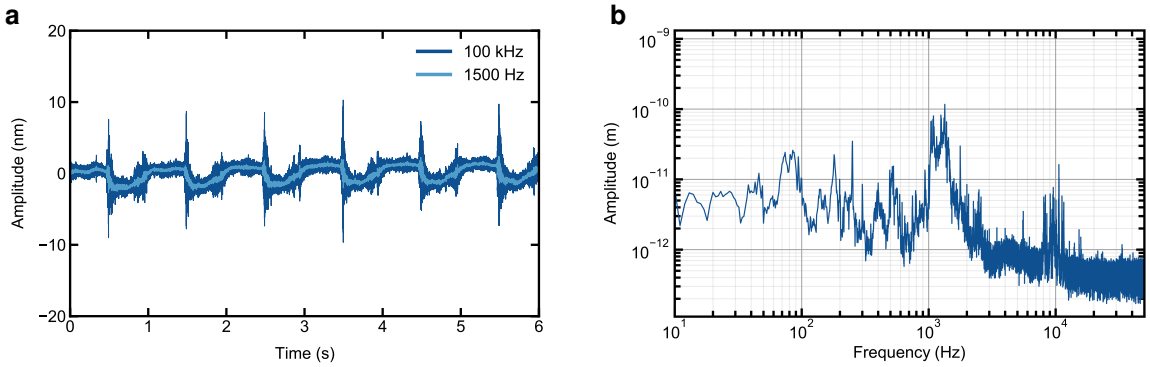

Figure 3.10.: Mechanical vibration spectra of cold plate in vertical direction as a function of **a** time and **b** frequency.

The measurement setup used for vibration measurement is sketched in figure 3.9. The sensor head is a collimating lens mounted on the vacuum shroud facing downwards for vertical measurement and on the optical table for lateral measurement. Both sensor heads are mounted on optomechanic mounts (ThorLabs Kinematic mount) for alignment. The target surface has a small mirror (R > 95%) glued on it such that the FPS3010 is operating in double-pass configuration for the measurements shown below. The measurements are done at lowest sampling time possible in the FPS3010 of 10.24 μs, leading to the measurement bandwidth of $\approx$ 100 kHz.

The first set of measurements shown here are the vibration measurements, performed between January-March 2017, of the cold surface at the optical table of the attoDRY800 (referred to as cold plate) and a set of nanopositioners on top of the cold plate. All the measurements shown here are done at cryogenic temperature (T = 4 K).

All vibration measurements are also performed at room temperature. We see that the peak-to-peak displacement at the full bandwidth at room temperature is similar to the cryogenic temperature, but the resonance frequencies of the system changes at different temperature. So a complete analysis of the mechanical properties of the setup requires the measurement at cryogenic temperature. However, room temperature measurements are a useful method to quickly verify the vibration performance without requiring a complete cool-down.

First, the vibration of the cold plate is measured in vertical and lateral direction with respect to the surface of optical table. The vertical vibrations in time are shown in figure 3.10a. Most strikingly, we see that the cold plate exhibits a motion with a characteristic square-like wave shape. This behavior is induced during the cycle of the cryostat when the rotating valve switches the pressure inside the cold head from high to low and back again. As the cryostat cycle repeats with a frequency of 1 Hz, the square-like shape repeats

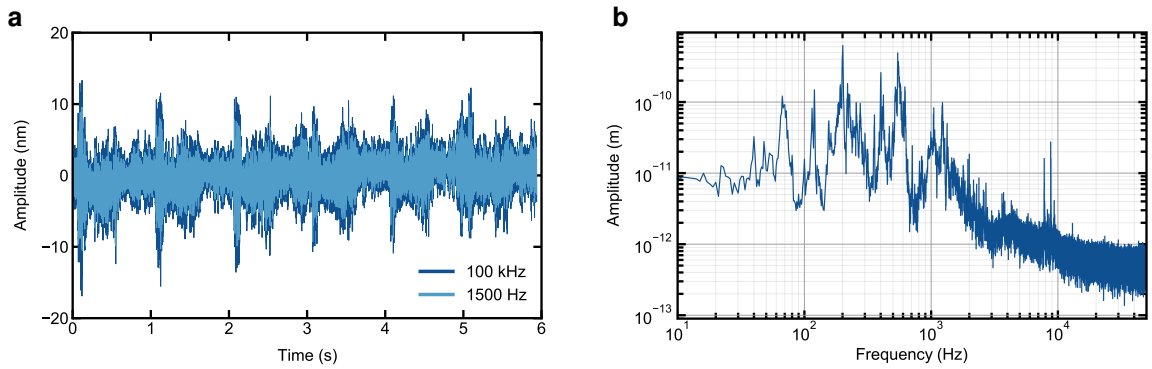

Figure 3.11.: Mechanical vibration spectra of the cold plate in horizontal direction as a function of **a** time and **b** frequency.

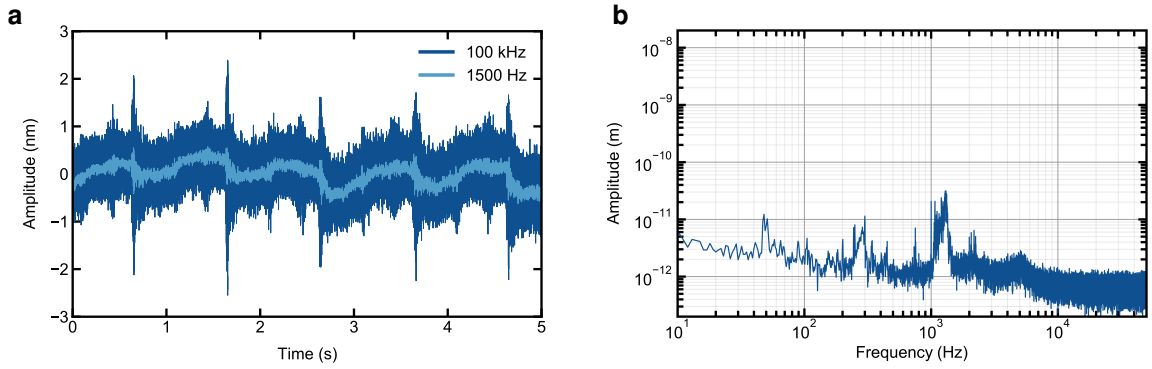

Figure 3.12.: Mechanical vibration spectra of cold plate measured in 2020 in vertical direction as a function of **a** time and **b** frequency.

itself after 1 second. On top of the low frequency square-like step behavior, we observe an additional fluctuation in the time trace due to high frequency contributions to the cold plate motion. The peak-to-peak vibration is ≈ 12 nm (root-mean-square fluctuations is 1.3 nm) at bandwidth of 100 kHz while the step size of the square wave is roughly 2.6 nm as can be seen from smaller bandwidth e.g. 1.5 kHz. The fast Fourier transform (FFT) is calculated from the raw data to analyze the mechanical properties of the cold plate at higher frequencies and to identify the major mechanical resonance. The FFT resolution is set to 1 Hz. The FFT for the vertical vibration is shown in figure 3.10b. There are several resonances visible, the most significant resonance is at approximately 1.2 kHz with a magnitude several times higher compared to the other resonances. In the sub-100 Hz range, there are several peaks that stems from the mechanical and electronic resonances of ground, cryocooler and optical table, however, an exact identification of the source for each resonance is difficult.

The lateral vibration of the cold plate are also measured and shown along with the FFT in

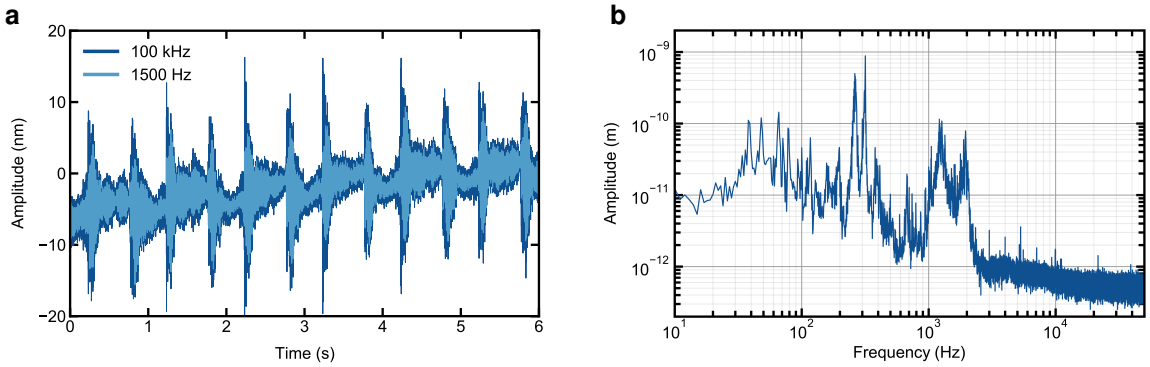

Figure 3.13.: Mechanical vibration spectra of ANP xyz positioner stack (2 x ANPx101, ANPz102) on top of the cold plate in the vertical direction as a function of **a** time and **b** frequency.

figure 3.11. The peak-to-peak vibration is around 20 nm at the bandwidth of 100 kHz and around 16 nm at the bandwidth of 1.5 kHz. The dominant frequencies are 200 Hz and 550 Hz. We note here that the vibration in two lateral direction were independently checked and they are similar in magnitude even though the frequency response vary. For the sake of simplicity, only one lateral direction is reported here.

As a side note, the usual vibrations of the cold plate in recent cryostats (measured in 2020) are shown in figure 3.12. Due to design improvements, the cold plate displacement in vertical direction is now much smaller. At full bandwidth, the peak-to-peak displacement is 4 nm and the FFT spectrum shows fewer resonance frequencies.

An introduction of nanopositioners is necessary to in-situ control the sample position in any experiment. However, this positioners also introduces additional mechanical vibrations as they are not mechanically rigid objects. Next, the vibrations on top of an ANP 100 stack (1x ANPz102, 2x ANPx101) were measured. The time trace and the FFT are shown in figure 3.13. The peak-to-peak vibration in vertical direction is 30 nm (15 nm) at bandwidth 100 kHz (1.5 kHz). The dominant frequencies are 270 Hz and 310 Hz which are presumably the resonance frequency of ANP 100 stack, as suggested by the eigenmode simulation of the mechanical design by the finite element analysis software. In the lateral direction, the vibrations are higher than the vertical direction, same as on the cold plate. The result are shown in figure 3.14. The peak-to-peak vibration is 150 nm (140 nm) at bandwidth 100 kHz (1.5 kHz). The dominant frequencies are 250 Hz and 300 Hz.

In conclusion, we have shown that the inherent vibrations of the cryostat are of the order of 10 nm in all directions, indicating that the attoDRY800 design achieves ~ 3 orders of magnitude improvement on the cold plate compared to the base vibration on the cold head. We note here that for microscopy applications such as confocal or wide-field imaging, the bandwidth of measurement is typically lower than 1 kHz and the vibration amplitude at the

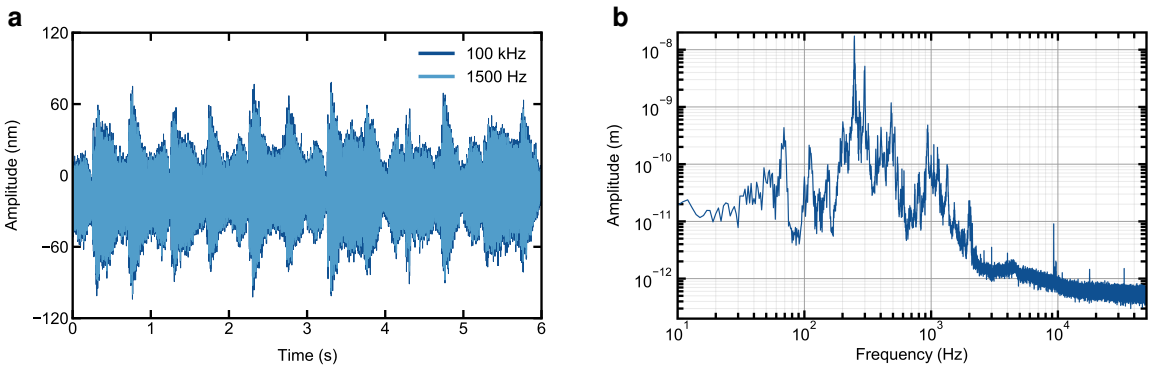

Figure 3.14.: Mechanical vibration spectra of ANP xyz positioner stack (2 x ANPx101, ANPz102) on top of the cold plate in the horizontal direction as a function of **a** time and **b** frequency.

highest measurement bandwidth of the order of 10 nm is much smaller than the depth of field of a high-NA objective which is in order of 500 nm. Next, we briefly demonstrate the suitability of the attoDRY800 for the imaging applications. However, the mechanical stability requirement for sensitive experiment such as a high-Finesse cavity, as discussed previously, is still far away.

Wide-field optical microscope

An optical microscopy is a powerful tool to study and understand novel materials and systems. For optical microscopy at low temperatures, an obvious pre-requisite is the spatial stability, scarce optical signals such as single photons from quantum emitters in TMDs imply efficient signal extraction over long time period. Here, we studied the suitability of attoDRY800 to perform such optical measurements by implementing a wide-field optical microscope.

The stability of the cryogenic imaging setup was measured with two standard configurations available for wide-field or confocal imaging in the cryostat. First is LT-APO (low temperature apochromatic objective) configuration. This configuration uses attocube LT-APO objectives that are developed for the use at low temperature. Second is HV-RT (high-vacuum room temperature objective) configuration. This configuration allows any objective compatible in vacuum to be used for imaging. As a sample, we used a test pattern with various shapes in dimensions ranging from 300 nm to 10 µm in both configurations.

We being with quantifying the impact of mechanical vibration during the operation of the cryocooler in wide-field measurements. For this, we use the HV-RT configuration (Olympus MPLANAPON 50x NA = 0.95). The optical resolution of the setup is ~ 353 nm. Figure 3.15 shows the wide-field image of the 300 nm pattern with the cryocooler off and cryocooler on.

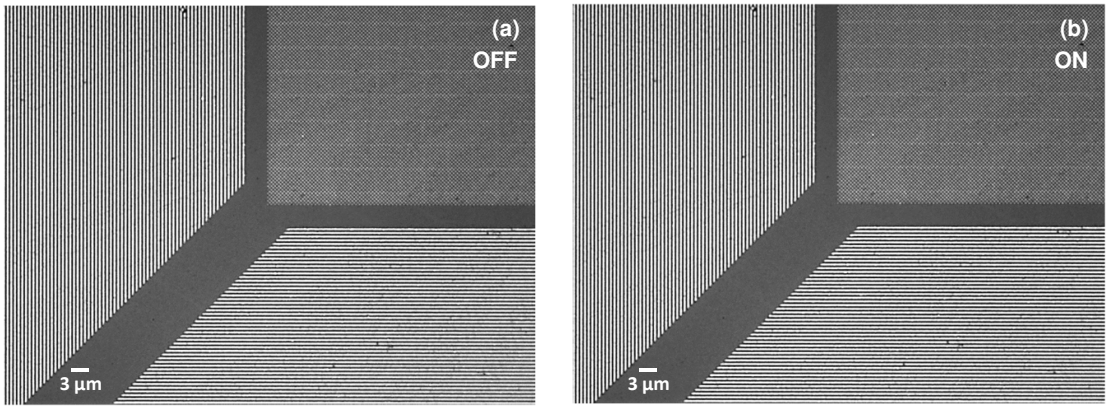

Figure 3.15.: Wide-field imaging with and without the operation of the cryocooler. The two images shows no difference up to the pixel size due to the mechanical vibrations of the cryostat.

There are no measurable differences down to the pixel level between the images acquired with cryocooler on and off. Thus, we conclude that the use of attoDRY800 with a diffraction limited wide-field microscope, up to high resolution of 350 nm, is not influenced by the operation of the closed-cycle cryostat.

Next, we investigate the stability of the wide-field microscope over time and temperature range. For this set of measurements, LT-APO configuration with LT-APO/VISIR objective (NA = 0.82, Working Distance = 0.65 mm) was used. The optical resolution of our microscope is ~ 409 nm and the pixel size on the sample plan is ~ 53 nm. The attocube LT-APO objectives have been developed for the use at low temperature and in vacuum. Therefore, they are mounted directly into the cryogenic space and thermally coupled with the cold plate providing a better stability over time and temperature range.

The long-term mechanical stability was checked by acquiring an image of the 500 nm pattern at 3.9 K, as shown in figure 3.16. In agreement with the theoretical resolution of 409 nm provided by our setup, the wide-field image in figure 3.16a clearly resolves the 500 nm checkerboard pattern on the sample. We acquired a wide-field image after 41 hours, shown in figure 3.16b. The two images are identical up to the pixel level. This means that the sample stays in the focus of LT-APO objective over this time period. It also demonstrates that the spatial movement in horizontal plane is lower than the pixel size of 53.5 nm over the entire time period.

Furthermore, we evaluated the spatial response of wide-field image to sample temperature. As a reference, we monitor the spatial position of a defect on the 500 nm checkerboard pattern. Figure 3.17a shows the wide-field image acquired at 5 K. We performed a step-wise sample temperature increase and measured the spatial position change once the sample was thermally stabilized at each temperature. The results of the measurements of the lateral

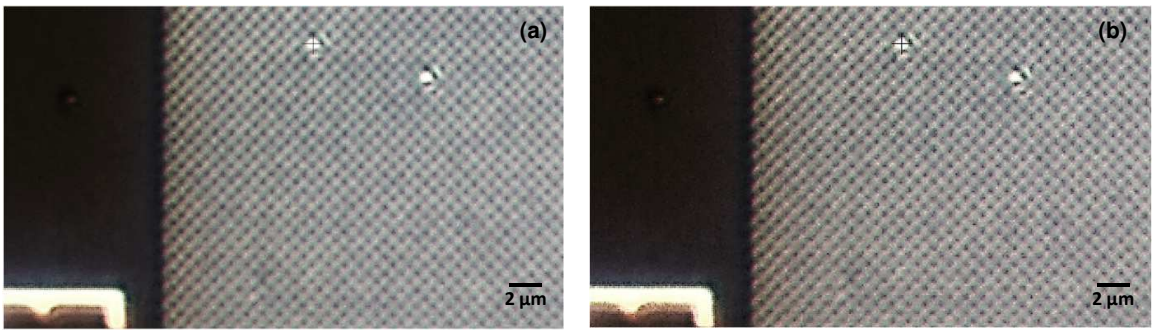

Figure 3.16.: Stability over time of wide-field imaging in the closed-cycle cryostat. The two images are acquired at the period of 40 hours without changing any parameter, it shows that the long-term drift is smaller than the pixel size in the cryostat.

Temperature Range	Total Lateral drift	Average Drift
0 - 30 K	less than a pixel	negligible
30 - 60 K	0.5 µm	9 nm/K
60 - 100 K	1.5 µm	16 nm/K
100 - 150 K	3.8 µm	26 nm/K
150 - 200 K	7.7 µm	40 nm/K
200 - 250 K	12 µm	49 nm/K
250 - 300 K	17 µm	58 nm/K

Table 3.3.: Lateral drift and average drift per degree as a function of the sample temperature range

drift and the corresponding average drift per change in temperature are summarized in Table 3.3 as a function of sample temperature range. The drift from base temperature to 30 K is negligible, meaning it is smaller than a single pixel on horizontal plane while staying in objective focus. At higher temperature, the horizontal drift increases, from 9 nm/K until 60 K, up to 58 nm/K for the full range from base to room temperature.

Figure 3.17 shows the image acquired at base temperature and room temperature. The dashed line highlights the drift path. The lateral drift at 300 K is about 17 µm, while it also requires realigning the focus again in z-direction. Therefore, the displacement over the full temperature range is within the wide-field view of the microscope.

In this section, we showed that attoDRY800 is ideal to perform optical spectroscopy measurements without being limited by the mechanical vibration. In addition, the long-term position stability of the imaging setup at base temperature is remarkable (smaller than one pixel size, < 53.5 nm). It is also suitable to perform temperature-dependent measurements upto room temperature with small lateral and vertical drift due to heating. Next, we

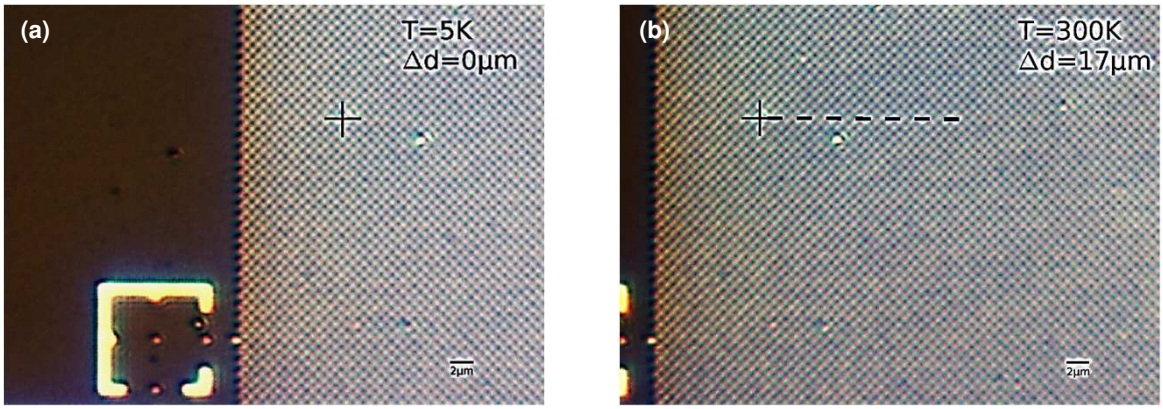

Figure 3.17.: Temperature dependence of the wide-field microscope. The sample shifts in the xy-plane with respect to the objective by 17 µm over the whole range of temperature.

discuss some vibration reduction techniques to implement more sensitive experiments in the attoDRY800 cryostat. Some of these techniques are used in chapter 5 to implement high-Finesse optical cavity.

3.3.2. Vibration reduction methods

Vibration reduction is an important requirement across many scientific and engineering disciplines, ranging from an everyday suspension system in a car to an extremely sensitive interferometric gravitational wave detector LIGO experiment [29, 185, 186].

The high-Finesse cavity puts one of the most stringent requirements in terms of mechanical stability along with the likes of scanning probe microscopes and interferometric detectors. Even with a promising starting point provided by the base vibration level of the cryostat in the nanometer scale, we need to achieve an improvement of at least 2-3 orders of magnitude. The nature of excitation frequencies was determined in the previous section. The main mechanical excitation starts from the mechanical and electronic resonances of ground, cryocooler and optical table in sub-100 Hz range to mechanical resonance of nanopositioners upto few kHz. Therefore, vibration reduction from near-zero to around 10 kHz needs to be implemented.

The area of vibration reduction is already quite mature with decades of work and continues to be an active area of research in both engineering and science [187–189]. Broadly, the vibration reduction techniques can be divided into two categories: first, passive vibration reduction. In this category, a vibration reduction system usually isolates the target from the incoming vibrations. Second, active vibration cancellation techniques. Here, the target object motion is tracked and an external element feedback on this motion to reduce or eliminate the motion.

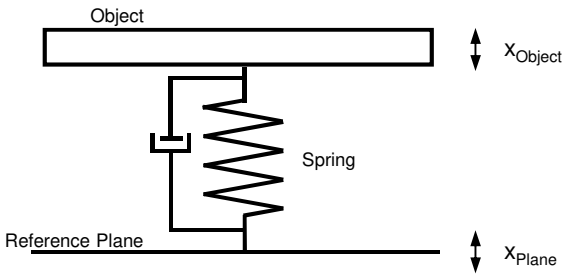

Figure 3.18.: Harmonic oscillator setup where an object with mass m is attached via a spring with stiffness k to a reference plane

Both techniques have advantages and disadvantages. The passive techniques are typically simple in implementation and can be used in the 'set-and-forget' mode compared to the active techniques. On the other hand, active techniques provides much more flexibility in terms of their operation frequency range. In this section, I will introduce some common vibration reduction techniques of both kinds that are implemented in chapter 5.

It is important to first clarify the nomenclature of various vibration related terms that are often interchangeably used. For the rest of this work, we make a distinction between the terms in the following way. 'Vibration isolation' is referred to isolating an object that has to be stabilized from the vibration source, for example using elastic spring or other harmonic oscillator. 'Vibration damping' refers to a process that involves energy dissipation coming from the source leading to vibration reduction on the target object, e.g. viscous damping. 'Vibration cancellation' refers to those processes where vibrations of the target object are measured and external energy is provided to cancel the vibrations in a feedback or feed-forward loop. We use 'vibration reduction' as the general term that involves any of the above to decrease the mechanical displacement of the target object.

Passive Vibration Isolation

One simple yet classic method to reduce vibration is to introduce a harmonic oscillator such as a pendulum or a spring between a moving object and a stable (or required to be stable) object. The harmonic oscillator is a well-known concept studied in classical mechanics where a system applies a restoration force upon disturbance from its equilibrium position.

We start with looking at the response of a simple harmonic oscillator. The system we consider is a spring connecting an object with mass m to a reference plane as shown in figure 3.18. The governing equation of motion is:

$$m\ddot{x} + m\gamma\dot{x} + k(x - x_0) = 0 \tag{3.12}$$

where x and x_0 are the displacement of the object and reference plane respectively, m is the

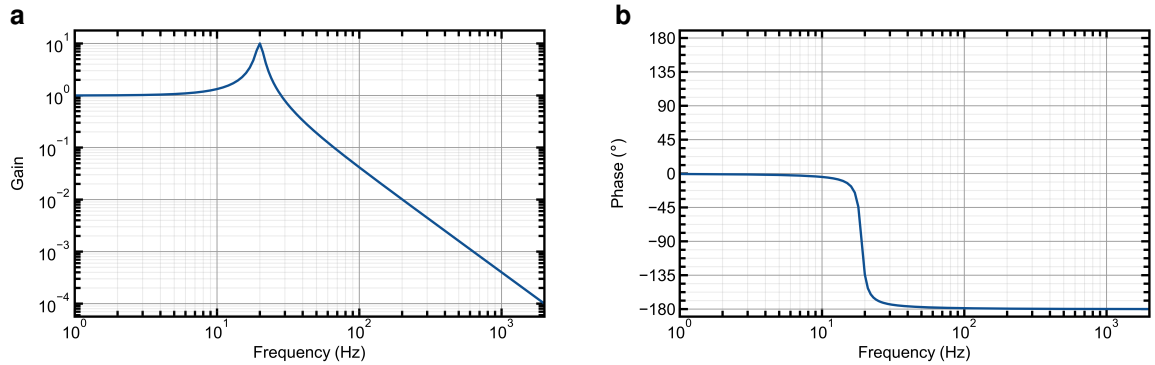

Figure 3.19.: Transfer function showing **a** amplitude and **b** phase of a simple harmonic oscillator as function of frequency. The values are set to ω_0 = 20 Hz and the Q=10. Amplitude gain response shows an enhancement of displacement at resonance frequency followed by the isolation at higher frequencies as the function of squared-frequency, Phase response shows the shift of -180° at the resonance frequency. Parameters are chosen such that resonance frequency of the oscillator is 20 Hz and Q-factor is 10.

mass of the object, γ is the damping coefficient, k is the spring constant/stiffness of spring. With the Fourier transform, the response can be written in the frequency space:

$$m(-\omega^2 + i\omega\gamma + \omega_0^2)x = m\omega_0^2 x_0 \tag{3.13}$$

where $\omega_0 = \sqrt{k/m}$ is the resonance frequency of the harmonic oscillator. We define the ratio of displacement of object with respect to the reference plane as the transfer function. The transfer function will be:

$$\frac{x}{x_0} = \frac{1}{1 - u^2 + iu/Q} \tag{3.14}$$

where $u = \omega/\omega_0$ is the relative frequency and $Q = \omega_0/\gamma$ is the Q-factor of the oscillator. The transfer function as a function of frequency is shown in figure 3.19. The transfer function amplitude (referred to as gain) response is flat i.e. displacement of the object x will be same as the reference plane x_0 below the resonance frequency ω_0. At the resonance frequency, the object's displacement is enhanced by the Q-factor which is followed by a frequency dependent reduction of displacement at higher frequencies. The phase response of the transfer function shifts by $\pi/2$ or 90° degrees at the resonance frequency and shows a shift of π over the entire resonance.

Based on the harmonic oscillator response, let us consider a toy model of a tunable cavity, as shown in figure 3.20. One mirror of the cavity is mounted on a damping stage and the other mirror is on a positioner for tuning. Both damping stage and positioner are modeled as spring with different resonance frequency and the relative displacement of the two mirrors

is analyzed. The overall response of the model will be a product of the transfer function response of damping stage and a relative response induced by the positioner between two mirrors. The individual responses and the total transfer function are plotted in 3.21.

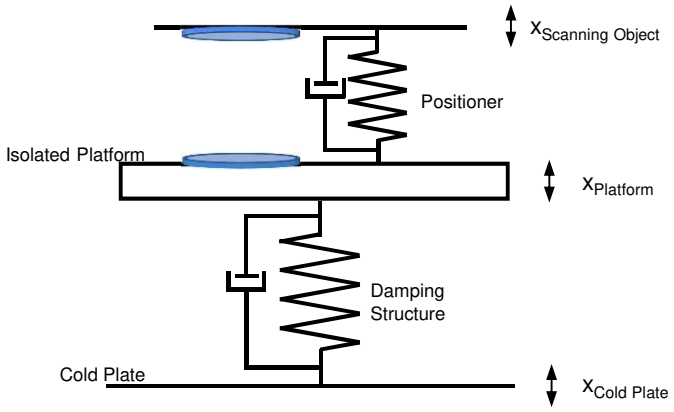

Figure 3.20.: Toy model of cavity setup where one mirror is on a set of positioners modeled as a spring, both mirrors are mounted on a spring-based vibration isolation stage.

The response of the damping stage is the same as the one of the harmonic oscillator discussed above. The relative response induced by the positioner $((x_{Platform} - x_{ScanningObject})/\ x_{Platform})$ is "flipped" in frequency i.e. it is small at low frequencies and increases as a function of frequency-squared upto resonance frequency of the positioner and becomes constant afterwards. This is because we are looking at the relative displacement of the mirror on the positioner with respect to the mirror on the platform. The total response $((x_{Platform} - x_{ScanningObject})/\ x_{ColdPlate})$ shows a vibration reduction over the entire frequency range. The magnitude of displacement reduction depends on resonance frequencies of two components: the resonance frequency of the damping stage should be as low as possible while the positioner should be stiff i.e. have as high mechanical resonance as possible. This set of information obtained from a straight forward analysis of the toy model serves as a guide during the mechanical design process. The phase of the total transfer function demonstrates two sharp changes at the two resonance frequencies with a π shift at the damping stage and around $3\pi/4$ shift at the resonance frequency of the positioner. An understanding of the phase response between two mirrors is crucial to apply feedback and active cancellation of the motion between two mirrors of the cavity.

While the toy model is important to provide a design guide for vibration isolation stage and the positioners that are used for moving the cavity mirrors, let us consider a more extensive version of the cavity stage where both mirrors of the Fabry-Pérot cavity are on separate positioner stacks. The model is shown in figure 3.22. There are two motivation to analyze a detailed version of the setup designed in chapter 5. One, the complete setup has more tuning knobs due to more positioners so this can provide additional insight on controlling

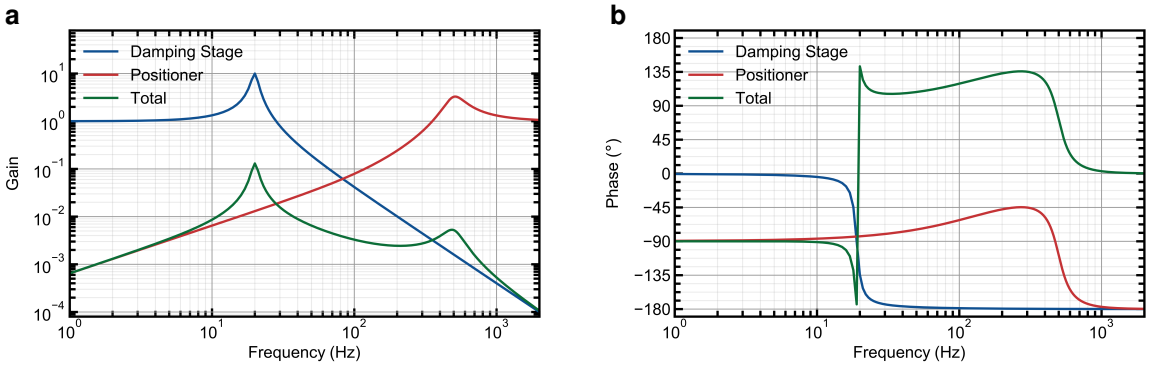

Figure 3.21.: Transfer function of the toy model as function of frequency. **a** Amplitude gain response shows two resonance, the one of the spring isolation stage and the positioner, **b** phase response also shows a shift at both resonance frequency. Parameters are chosen such that damping stage has resonance frequency of 20 Hz and Q-factor of 10 while the positioner has resonance frequency of 500 Hz and Q-factor of 3.

the vibration isolation properties via this knobs. Second, we can introduce an additional link between the two mirrors that provides another channel to reduce the differential motion between the mirrors. Here, we introduce this link in form of another spring in the model. The full cavity model is essentially two coupled-oscillator system with a vibration isolation stage at the bottom. The experimental implementation of such link to reduce differential motion is discussed in detail in chapter 5, we focus here on the transfer function to gain insight on the design of such a link.

First, we look at the transfer function $((x_{MacroscopicMirror} - x_{FiberMirror})/x_{ColdPlate})$ of the cavity model shown above but without any link (shown in figure 3.23 in blue). The resonance frequencies are set to realistic values based on the experimental setup discussed in chapter 5. The resonance of the vibration isolation stage is at ~ 20 Hz. The resonance of both positioner set is at ~ 250 Hz. The isolation is achieved over the entire frequency range. Least isolation occurs at the two resonance frequencies. Upon introducing a link to couple the two mirrors, the attenuation can be modified. There are two parameters that can be tuned for the link: stiffness and the damping coefficient. Next, we take two limiting example cases to provide a guideline on reducing differential motion by changing parameters of the coupled model, however, the goal is not to be quantitatively accurate. First, we take the case of a link which is a high stiffness spring with a small damping coefficient. The transfer function (figure 3.23a) shows the decrease in gain over the entire frequency range. An extreme limit would be an infinitely stiff link where the differential motion between two mirror should go to zero at all frequencies. Second, we consider the case of link which is highly damped, the response is shown in figure 3.23b. Addition of high damping between the mirrors leads to a decrease in amplitude of the resonance of the positioners. This shows that

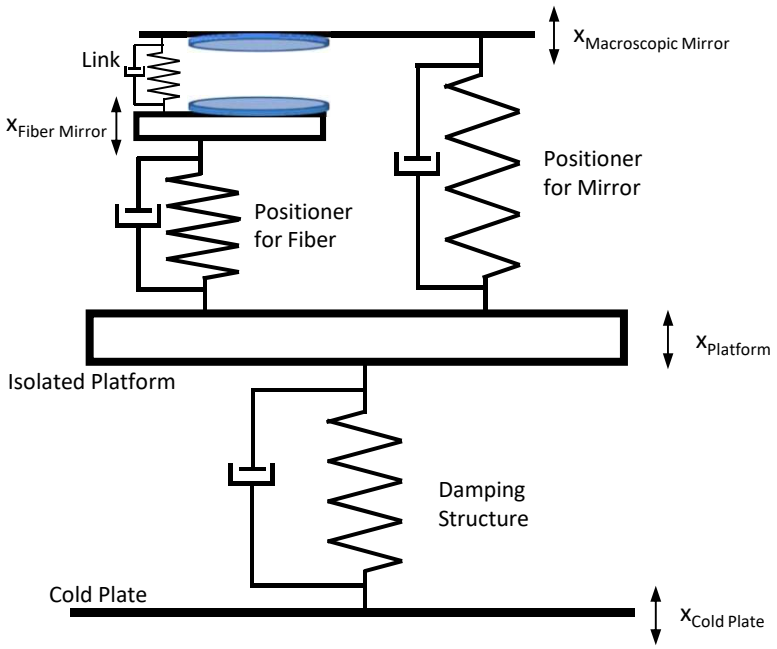

Figure 3.22.: Complete model of cavity setup where both mirrors are on their individual set of positioners, the additional connection between two mirrors is denoted as link, this entire coupled-oscillator system is on a spring-based vibration isolation stage.

a link with high stiffness can bring vibration isolation over the entire range of low frequencies and damping can reduce the motion induced by the set of positioner. The immense practical challenge is to introduce coupling which is stiff and damped but still provides a modularity to tune the cavity mirrors with respect to each other, an experimental implementation showing that is discussed in the section 5.2.

Viscous damping based on Eddy Current

The harmonic oscillator provides a frequency-dependent vibration isolation response that is suitable for high frequency noise as the vibration isolation factor scales with the square of frequency after the resonance of the oscillator. The down-side of a harmonic oscillator based isolation system is the enhancement of vibrations at the resonance frequency by the Q-factor. As the typical resonance frequency of a spring isolation stage is in the range 1 - 100 Hz, a particular care has to be taken to avoid the overlap of the resonance with several seismic and cryocooler's mechanical and electronic resonance present in this frequency range. In addition, the Q-factor of a spring stage could be quite high i.e. in the range of 10 to 100 due to a small inherent damping coefficient of the spring. Here, we explore a method to engineer the damping coefficient γ using viscous damping based on Eddy currents.

When a conductor is passed through a stationary magnetic field or a conductor is in

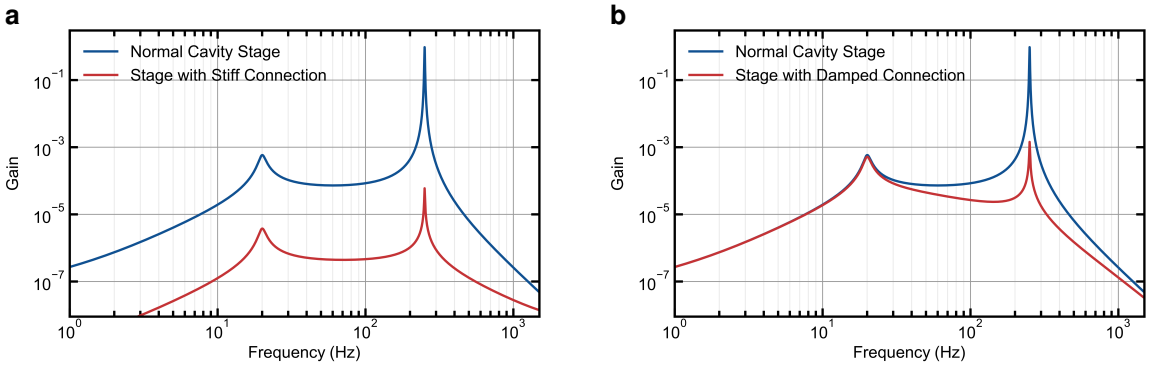

Figure 3.23.: Transfer function of the complete model with link as function of frequency. **a** Response of the cavity model with a highly stiff link and compared to the cavity without a link. **b** Response of the cavity model with a highly damped link and compared to the cavity without a link. Parameters are chosen such that damping stage has resonance frequency of 20 Hz and Q-factor of 10 while the positioner stages has resonance frequency of 250 Hz and Q-factor of 1000. For the response in **a**, stiffness of link is set to 10^7 with damping coefficient is set to 10, while for the response in **b**, stiffness of link is set to 10 with damping coefficient is set to 10^5.

vicinity to a changing magnetic field, it induces eddy current within the conductor. Lenz's law states that the direction of the induced current is such that it creates a magnetic field that opposes the changing magnetic flux that induces this current. The magnitude of the eddy current depends on the strength and the rate of change of the magnetic flux, the exposed surface area and the resistivity of the conductor. As the eddy currents decreases due to Joule heating through the resistivity of material, the vibrational energy of the system is dissipated, thus providing a method to achieve a controlled viscous damping. The magnet-conductor system based damping is a popular method for various applications, e.g. magnetic braking system in the automobile industry.

The dissipated power (P) due to the eddy currents in a high conductivity metal slab given by [190]:

$$P = \frac{1}{2}\sigma\delta B_z^2 A v^2 \tag{3.15}$$

where σ is the electrical bulk conductivity of the metal, δ is the thickness of the slab, B_z is the magnetic field perpendicular to the slab, A is the surface area of the slab and v is the velocity of the conductor moving perpendicular to the magnetic field. From the dissipated power, we can calculate the force $F = P/v$ acting on the conductor:

$$F = \frac{1}{2}\sigma\delta B_z^2 A v \tag{3.16}$$

The force due to eddy currents is proportional to the velocity with which the conductor is moving in the magnetic field, similar to any sort of a viscous or drag force. Based on the equation 3.12, the viscous force can be written as $F = -m\gamma v$. Hence, the damping coefficient using eddy current damping is:

$$\gamma = \frac{\sigma \delta B_z^2 A}{2m} \tag{3.17}$$

This enables one to control the damping coefficient in a spring-based vibration isolation by introducing a magnetic field and an appropriate conductor. In chapter 5, we will experimentally implement this with pairs of permanent magnets mounted on the cold plate, and a metal piece fixed to the spring stage. To consider effectiveness of viscous damping using numbers, let's say the metal piece is made of high-purity aluminum. The conductivity is $\sigma \approx 1.25x10^9$ S/m at cryogenic temperature [177]. The design of the spring stage enables 8 pair of magnets in series arranged in a circular geometry. The magnet diameter is 10 mm and the gap between each pair is 5 mm, the surface area is A = $\pi/25$ cm^2, the thickness of the metal piece is δ = 3 mm, the magnetic field B_z = 0.3 T (two Neodymium split magnets) and the mass of the spring isolation stage is m ≈ 0.5 kg. The damping rate will be $\gamma/2\pi \approx 24$ Hz using the equation 3.17. The normalized damping rate is $\gamma/\omega_0 = 1.2$ for $\omega_0/2\pi = 20$ Hz, which will give the Q-factor ≈ 1. While, a Q-factor below one is not desired as it leads to stiff coupling to the base vibration. In principle, the Q-factor can further be reduced by using the high-purity copper instead of aluminum (increase in conductivity by factor of ≈ 10 with Cu-RRR 300) leading to the Q-factor much smaller than one in the above configuration.

Other Passive Techniques

During the course of this work, several other techniques were also explored for the implementation in cryogenic system. Here, I briefly describe some of the techniques that were explored, with a description of their working principle and their strengths and weaknesses in context of our application.

Apart from spring based vibration isolation, it is also possible to use elastomer materials such as rubber for the isolation, however their suitability across temperature and pressure range is an open question. There are also methods to reduce the fundamental resonance frequency to near-zero values via negative stiffness design or to design resonance frequency independent of the mass on top via magnetic levitation, both of which are discussed shortly in the rest of this section.

Before that, I shortly introduce a fundamentally different way for vibration reduction using the emerging field of mechanical metamaterial. While analog to it's photonic counterpart, it is possible to design phononic crystals which can reflect an elastic wave of a certain frequency due to the Bragg scattering [191–193]. Although the problem with Bragg

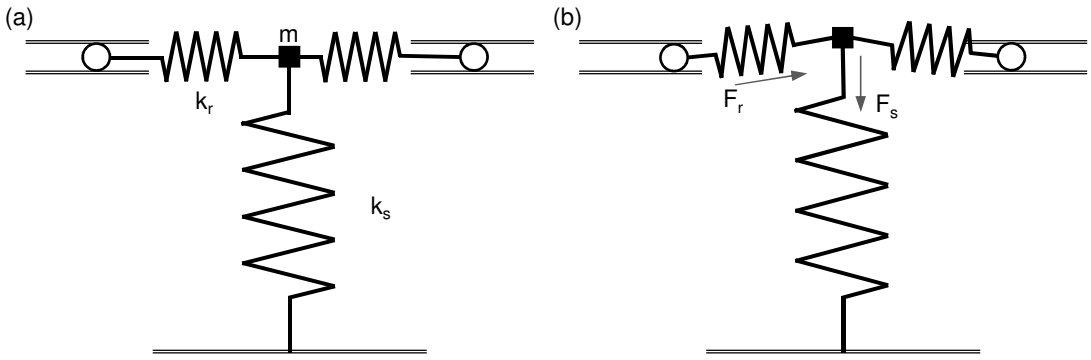

Figure 3.24.: The one-dimensional sketch of negative-stiffness model. The mass is connected to a spring with a finite stiffness and loaded with another spring that cancels out the motion of mass by applying force in opposite direction.

scattering is that the dimensions of unit cell of such phononic crystal has to be in the order of wavelength of the phononic wave, making it too large (in the range of meters) for the low frequency range (less than 10 kHz) that we intend to tackle and thus, impractical for the cryogenic application. More recently, metamaterial based on locally resonant structure have been demonstrated which can have a unit cell much smaller than the wavelength. Thus, it is feasible to have a compact metamaterial design that can reduce vibrations at low frequencies [194, 195]. Furthermore, phonon-based metamaterial provides an interesting platform to study topological effects [196–199]. This method was theoretically investigated in some detail during the work on this thesis, see Appendix A for a detailed discussion on this technique.

Negative stiffness mechanism

To revisit the idea of using a simple harmonic oscillator such as spring for vibration isolation discussed in previous section, the ideal property of such a system is to have a minimum resonance frequency such that the vibration isolation begins at smaller frequency and provides more isolation at high excitable frequencies. However, with a normal spring, there is a trade-off between lowering the stiffness to reduce resonance frequency and the total mass that can be supported by low-stiffness springs. The idea of 'negative stiffness mechanism' is to design a mechanical system where the stiffness is reduced to almost zero or a negligible value to have an effective vibration isolation system.

A simple one-dimension example is sketched in figure 3.24. The system consists of a spring (denoted as s) with stiffness k_s in z-direction connected to the mass m. Two springs (denoted as r) with stiffness k_r in horizontal plane are connected to the mass, the other end of horizontal spring is supported by a groove which allows that end to move only in x-direction. A rest position (figure 3.24a) has two springs r pre-loaded with a certain external

force F at the groove end facing towards mass m. When the mass is slightly displaced towards top (figure 3.24b), the spring s will apply a force F_s towards bottom as it is elongated. On the other hand, pre-loaded springs r still applies an outward force due to external force F that leads to a total upward force due to two springs r. Thus, an overall force is canceled out by springs s and r resulting in an overall effective stiffness $k = k_s - k_r$ which can be lowered to small or even zero net stiffness.

The idea can be extended to all 6 spatial degrees-of-freedom and it provides a pathway to vibration isolation starting from very small frequencies [200, 201]. It is a very promising approach as, let's say, changing the resonance frequency of the stage from 20 Hz to 2 Hz leads to 100 times more isolation at 200 Hz and four orders more isolation at 2 kHz. Nevertheless, there are a few factors to keep in mind for the experimental implementation. First, the design of an effective negative stiffness is much more complex than a simple spring, which makes the geometry harder to implement and operate at cryogenic temperature. Second, it must also be noted that the frequency of the cryocooler cycle is 1 Hz so the resonance frequency of the isolation stage should be kept as far apart from 1 Hz as possible.

Magnetic Levitation

Another approach towards passive vibration isolation is using magnets instead of mechanical springs. The technique, referred to as magnetic levitation vibration isolation, involves a pair of magnets that are in an equilibrium position such that they act as springs for any displacement. The ideas for implementation includes inclined permanent magnet pairs [202], quasi-zero stiffness systems combining with a normal mechanical spring similar to the negative stiffness described above [203, 204] and an active feedback using an electromagnetic coil and a magnet [205].

An advantage of a 'magnetic spring' is that it is independent of the load mass on the system. However, there are still several unknowns that needs to be investigated before the implementation. For example, the range of displacement around the equilibrium position that has enough restoring force needs to be determined. The design is also more complex than a simple spring isolation and requires further investigation for operation at cryogenic temperature.

Active Vibration Reduction

The idea of controlling a dynamic system to a desired value in an automated way already exists for more than 2000 years with the first application in hydraulic systems [206, 207]. The research and applications have grown remarkably over the last centuries into the field of control theory.

Closed-loop systems have two primary components: sensor and actuator. The sensor determines the error signal that needs to be eliminated, e.g. displacement of a mirror with

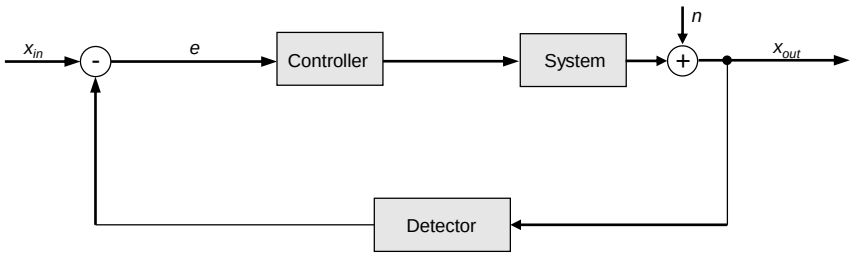

Figure 3.25.: The closed-loop feedback scheme demonstrating major components: controller, system (e.g. cavity) and detector. The noise n is the mechanical vibrations added to the system due to external disturbance

respect to a reference object or another mirror in a cavity experiment, or the deviation of temperature in a room around a fixed set-point. The actuator is provided with the feedback signal and acts upon it to reduce the error signal, e.g. a piezo moving an object in a certain direction or a heater increasing the temperature of the room. Feedback systems have a limited frequency range, commonly referred to as bandwidth, within which the actuator has a well-defined amplitude and phase behavior that reduces the error signal.

Feedback-based control systems are ubiquitous in mechanical vibration-sensitive experiments, particularly because they are well-suited to reduce noise at low frequencies where passive isolation systems are not effective. The key challenge in practical implementation of active feedback is to find the sensor and actuator with appropriate specifications. A common element for a displacement actuator is a piezoelectric element. The range of piezo elements are typically within few microns and the resolution of actuation is usually limited by the electronic noise of the signal input and not the element itself. There exists a variety of sensors such as velocity sensors, piezo-based force sensor, accelerometers and optical interferometers [180, 181]. However, it is a non-trivial task to have a sensor with sufficient resolution in a range below 10^{-9} m [179].

There are interesting proposals to implement a general purpose active isolation system, such as a piezo-based sensor and actuator hexapod to reduce vibrations in all 6 degrees-of-freedom [208]. The other approach would be to implement an active feedback at the final stage that needs to be stabilized. This is well suited for optical cavity experiments (and scanning-probe microscopes) where the relative displacement between two objects is the primary concern. The sensor in this case would be the signal from the cavity itself, which provides enough resolution to derive the error signal. In addition, active feedback at the final stage can be combined with passive reduction techniques on earlier stages, enabling high amplitude reduction over a large bandwidth. This will be experimentally implemented in chapter 5.

The typical signal flow in a closed-loop system is sketched in figure 3.25. The main com-

ponents from a control theory viewpoint are the controller, the system and the detector. The controller gets the error signal and then provides a dynamic output based on a user-defined algorithm denoted by the transfer function K. The controller is often referred to as servomechanism/servo and can be digital or analog. The system or *plant* is the part to which feedback is applied. It usually includes the actuator. The detector or sensor performs the measurement and closes the loop to determine the error signal. The transfer function of a system is denoted S and for the detector D. Let us further consider the mechanical noise induced in the system, n, separate from it's response function S that depends on the input from the controller. The output of the feedback loop in the frequency domain can then be written as:

$$x_{out} = \frac{KS}{1+KSD} x_{in} + \frac{1}{1+KSD} n \tag{3.18}$$

The goal of the feedback loop is to reduce the contribution of noise n to the output. The factor $1/(1+KSD)$ by which the noise is suppressed is called Sensitivity. The feedback bandwidth is defined as the frequency that leads to a unity gain of the whole loop $|KSD| = 1$. One special condition is when $KSD \approx -1$ i.e the loop has a unity gain with π phase shift, it leads to an instability condition where the controller gain actually is negative instead of positive such that the system starts to show an uncontrolled spontaneous oscillation that can damage the piezo actuator.

Probably the most common and simplest controller technique is the PID (proportional-integral-derivative) controller, for which the output function depends on the input error function $e(t)$ as:

$$o(t) = K_\mathrm{p} e(t) + K_\mathrm{i} \int_0^t e\left(t'\right) dt' + K_\mathrm{d} \frac{de(t)}{dt} \tag{3.19}$$

where $K_\mathrm{p}, K_\mathrm{i}, K_\mathrm{d}$ are the respective gain for the proportional, the integral and the derivative part. The PID controller can be quite easily combined with passive electronic filters such as low-pass and notch filters. To tackle a more complex system response, a sophisticated controller design is required. A good starting place for controller design are refs. [209–212]. With the advent of programmable ICs such as FPGAs, the controller transfer function can also be altered to account for mechanical resonances in the system and increase feedback bandwidth [213, 214].

It is important to understand the system response accurately to optimize the gain amplitude and feedback bandwidth. Here, I briefly describe the technique to measure the open loop transfer function while still being in the closed loop configuration using a network analyzer. This virtual breaking of the loop is important in sensitive experiments such as high-Finesse cavities, where the transfer function can only be measured within a small dynamic range of the signal.

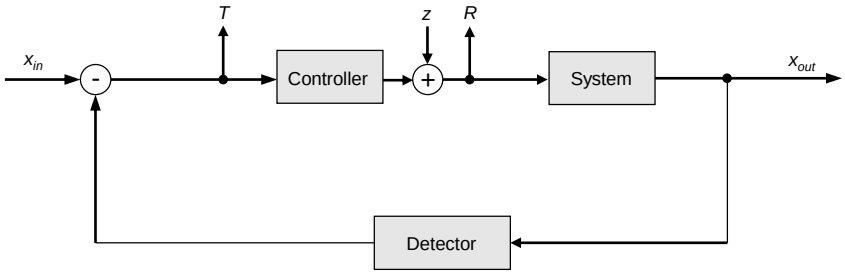

Figure 3.26.: The measurement of 'system-detector' transfer function in a closed-loop feedback is done by picking up the input at points T and$R$ and introducing a controlled frequency-dependent disturbance z to actuator signal to system as shown

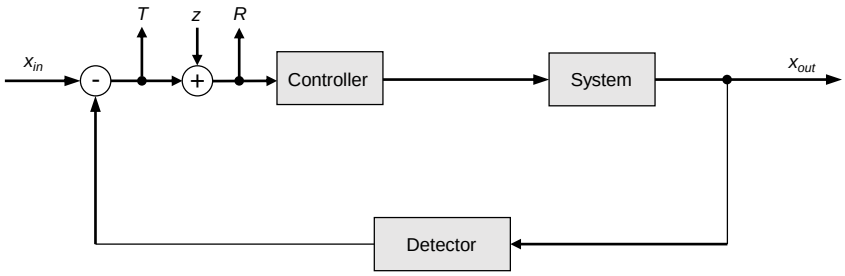

Figure 3.27.: The measurement of 'system-detector' transfer function in a closed-loop feedback is done by picking up the input at points T and$R$ and introducing a controlled frequency-dependent disturbance z before the controller as shown

First, we look at the signal flow of the closed loop system during measurement of the transfer function of the system-detector, shown in figure 3.26. Apart from the closed loop system shown above, an additional disturbance z is introduced in the circuit after the controller. This disturbance summed up with servo output is then feed into the system. The two inputs of the network analyzer marked as T and R can be written as:

$$\begin{aligned} x_T &= x_{in} - SDz - Dx_{out} \\ x_R &= x_{in} + z - KDx_{out} \end{aligned} \tag{3.20}$$

The ratio of the two inputs $x_T/x_R \approx SD$ gives the transfer function of system-detector combined at the locked point when input and output contribution can be neglected. Usually the response of the detector is well understood so it provides insight into the cavity's resonance frequencies and the respective phase response.

By changing the probe method as shown in figure 3.27, the transfer function of the whole feedback loop can be determined. The disturbance is now added to the error signal and the probes of the analyzer are placed just before and after the disturbance. The input at the

nodes will be:

$$\begin{aligned} x_T &= x_{in} - KSDz - Dx_{out} \\ x_R &= x_{in} + z - Dx_{out} \end{aligned} \tag{3.21}$$

The ratio here is given by $x_T/x_R \approx KSD$, corresponding to the transfer function of the whole loop while it is locked. Thus, it is possible to measure both the system-detector transfer function as well as complete feedback loop i.e. of the controller-system-detector transfer function.

4 Chiral Fano interference of exciton-plasmon system

This chapter describes an interesting platform combining a localized plasmon resonance in a Au nanodisk lattice with a TMD monolayer that exhibits a coherent interference. This interference manifests in the form of a Fano resonance, a hallmark of weak coupling between plasmons and excitons. We also demonstrate the chiral nature of this Fano interference that can be exploited to get an energy-dependent reflection or transmission band for different chirality within a broadband absorption window.

In section 4.1, we provide the motivation to use a plasmonic platform as an optical resonator and possibilities when combining them with the 2D excitons in TMDs. In section 4.2, we discuss the confocal spectroscopy results on a proof-of-principle device demonstrating the Fano resonance. Then, we introduced the magnetic field to exhibit the chiral behavior of the coupled system due to Zeeman splitting of the neutral exciton resonance in a WSe_2 monolayer in section 4.3.

4.1. Motivation

The control of interaction between light and a quantum emitter that depends on a specific attribute e.g. propagation-direction or polarization of light has garnered a lot of attention in recent years. Chiral light-matter interfaces can serve as a useful component such as a non-reciprocal optical isolator in photonic integrated circuits and complex quantum networks as well as a basic unit to perform quantum computational tasks [215–220]. The directional coupling is also proposed to create entanglement between several quantum emitters and to study many-body quantum dynamics [221–223]. An excellent review on this emerging field of chiral quantum optics is reference [224].

Plasmonic nanostructures can localize and enhance electromagnetic fields at a sub-wavelength scale, which makes them a promising platform for applications in the area of bio-sensing and bio-imaging [225–227], solar cells [228–230], surface-enhanced Raman

scattering (SERS) [231–233] and as optical resonators in quantum optics experiments [148, 149, 234–238]. The interaction of plasmonic structures with excitons in TMDs has been under increasing investigation [239, 240]. In recent years, there have been several works showing enhancement of photoluminescence (PL), brightening of dark excitons and strong coupling in hybrid TMD-plasmonic devices [120–125, 130, 241–246]. The unique valley properties of TMDs have also been explored in combination with plasmonic metamaterials, for example to separate the valley-based PL emission [247–249] or for the enhancement of valley polarization with a chiral metasurface [250].

Here, we propose an approach to achieve a non-reciprocal chiral reflectivity by combining a monolayer semiconductor with valley degree and plasmonic nanodisk lattice. We demonstrate coherent interference between valley excitons and plasmons. The interaction strength stochastically varies across our device due to imperfections of the nanodisk shapes leading to local variations in the plasmonic resonance energy, this coherent interference is explained in the framework of Fano resonance [251–253]. In presence of an external magnetic field, our device shows the chiral reflection dip in a wide-band absorption. Next, we introduce the basics of the metal-based localized plasmons.

4.2. Coherent interference in exciton-plasmon coupled system

The hybrid plasmon-TMD system consists of a monolayer WSe_2 encapsulated in hexagonal boron nitride (hBN) and a gold nanodisk lattice. Individual Au nanodisks support localized plasmons which together with the neutral excitons in WSe_2 show a coherent interference to create a complex Fano optical response.

The method of inspection for the device is confocal spectroscopy at cryogenic temperature, the optical setup is shown in figure 4.1. The measurements were either performed in a liquid helium bath cryostat (T = 4.2 K) or in a closed-cycle cryostat attoDRY1000 (T = 3.5 K). White-light reflection spectroscopy was performed using a home-built confocal microscope. A Halogen lamp or NKT Supercontinuum Extreme laser were used as a broadband excitation source with illumination focus area ~ 1 µm (attocube LT-APO objective, NA = 0.82/0.68). The reflected light was spectrally dispersed and detected by a CCD. For polarization-resolved measurements, a linear polarizer was used in the excitation arm and a combination of quarter-wave plate and linear polarizer were introduced in the detection arm to select either σ^+ or σ^- polarization.

Before looking at the optical response of the hybrid system, we begin with characterizing individual areas where either only excitons or plasmons are within the optical spot. The exfoliated and hBN encapsulated WSe_2 monolayer is placed on a SiO_2 substrate such that a part of monolayer is overlapping with the Au nanodisk lattice while the other part is directly lying on the substrate, as shown in illustration in figure 4.2a. This enables the study of

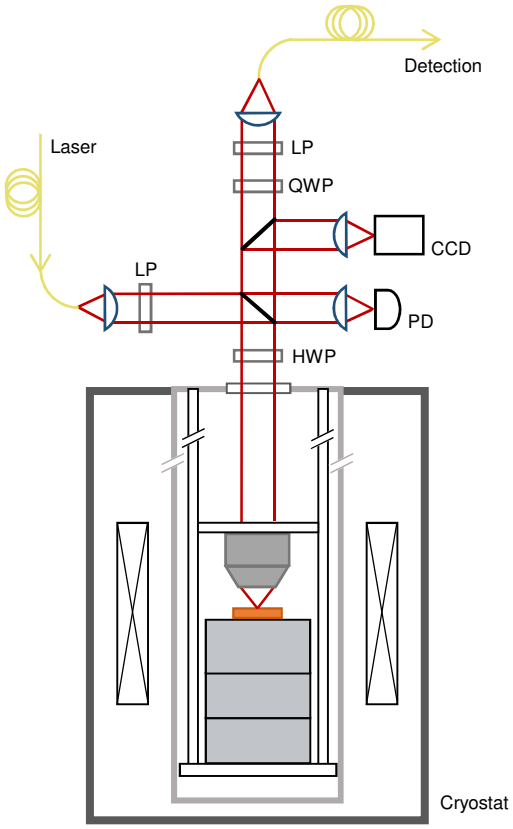

Figure 4.1.: The confocal microscope used for the measurements presented in this chapter. The sample is placed on top of xyz-nanopositioner inside a cryostat. The excitation comes from a fiber which is focused onto the sample via an objective, the reflected light is guided straight through a beamsplitter via a detection fiber to a spectrometer coupled CCD. The polarization of excitation and detection signal is changed via linear polarizer and a combination of $\lambda/4$ and $\lambda/2$ wave plates mounted on an automated rotator (ANR240). Assignment of abbreviations: quarter waveplate (QWP), half waveplate (HWP), linear polarizer (LP), beamsplitter (BS), fiber beamsplitter (FBS), photodiode (PD), objective (OB), piezo nanopositioner (PZ), camera (CCD).

excitons in monolayer TMD and plasmons in Au nanodisks independently of each other as well as a coupled system where excitons in TMD interact with plasmons in an Au nanodisk within the optical illumination spot. The differential reflection response of a stand-alone WSe_2 monolayer region is shown in figure 4.2b. There is one peak which is attributed to the neutral exciton X^0 at the resonance energy of $\omega eg = 1.723$ eV with a linewidth (half-width at half maximum, HWHM) of $\Gamma_{eg} \simeq 4$ meV, slightly higher than the reported radiative-limited linewidth of ~ 1 meV [254, 255].

Figure 4.2c shows a typical differential reflection spectrum in the region of the Au nanodisk lattice, here we observe a broad plasmon resonance with resonance energy ~ 1.7 eV and

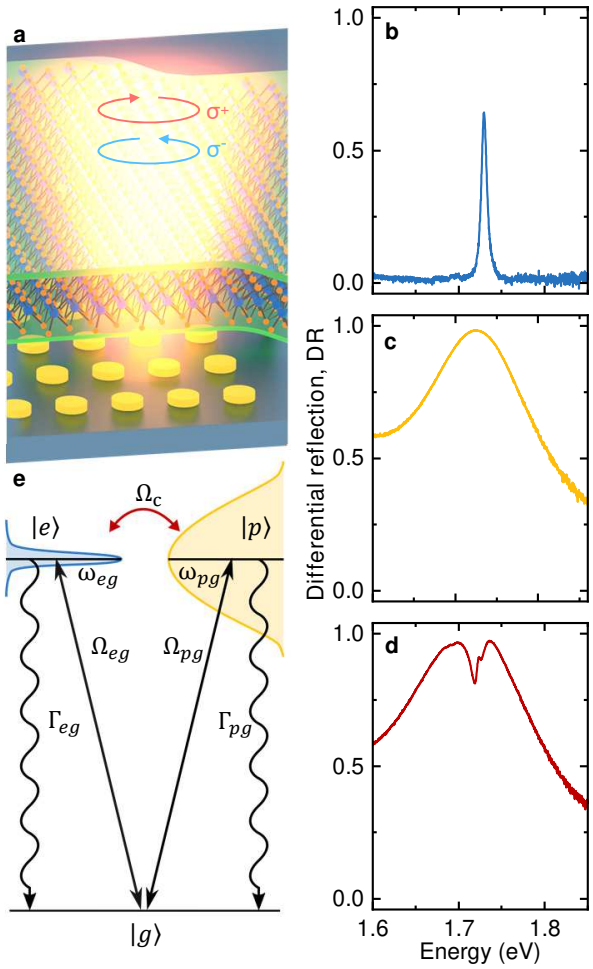

Figure 4.2.: **a** An illustration of the device. The three-atom thick monolayer WSe_2 is shown encapsulated in hBN (in green). The Au nanodisks (in gold) are arranged in a periodic lattice. The monolayer is exfoliated on the substrate such that a part of it is overlapping with Au nanodisks to enable coherent interference between excitons and plasmons. Differential reflection optical spectra in the region of **b** Au nanodisk, **c** monolayer and **d** the coupled system.

linewidth of ~ 180 meV. The individual metallic nanoparticles support plasmon resonances localized to the size of the particle. They are characterized by the enhanced electric field in their direct proximity under optical excitation, which we use to coherently couple exciton and plasmon resonance.

The spectral position of the plasmon resonance depends on the shape and size of the particles and on their dielectric environment. The development of the Au nanodisk arrays follows some basic considerations. First, the plasmon resonance of the Au nanodisks has to match the energy of the exciton transition in WSe_2 to enable near-resonance coherent coupling. Second, the TMD monolayer has to be placed in direct proximity to the Au nan-

odisks to use the plasmonic near-field for enhanced exciton plasmon interaction. Third, the height of the Au disks should be as small as possible to avoid exciton localization in the form of quantum dots due to the variation in lateral strain in the TMD monolayer [112, 256]. And fourth, finally, the number of nanodisks within the focal spot under optical excitation should be large to increase the coupling strength of excitons and plasmons.

Following these considerations, we performed finite-difference time-domain (FDTD) simulations with a commercial software (Lumerical) to find the optimal geometrical parameters for our system [155]. A SiO_2 coated silver mirror was used as substrate for the nanostructure both in simulations and in actual samples. A thin layer with refractive index $n = 1.76$ simulates the hBN interface at the top surface of the nanodisks. The defining geometrical parameters for tuning the plasmon resonance of the disks are their diameter and height. With the consideration to minimize the nanodisk height in mind, we fixed the height at ~ 15 nm where evaporated gold is expected to form smooth surfaces. The plasmon resonance can be shifted to smaller energies by increasing the disk diameter, while a blue-shift accompanies diameter reduction. Figure 4.3a shows this behavior when simulating the extinction of an optical plane wave propagating through gold nanodisks with different diameters. To enhance the near-field effect, we used a 6 nm thin bottom hBN layer in our van der Waals heterostack defining the distance between the TMD monolayer and the Au nanodisk array. To estimate the magnitude of near-field enhancement at the monolayer position, we tracked the intensity of the electric field during the FDTD simulation in the monolayer plane as plotted in figure 4.4a. The mean intensity value across the entire area of a nanodisk is shown as dashed line in the intensity line profile in figure 4.4b and gives the input parameter for the model of the coupled exciton-plasmon system. The plasmonic response in differential reflection varies within a range of 100 meV across the WSe_2-plasmon metasurface. We take advantage of this variation to explore the coupled system at different spectral detunings. The shift of the plasmonic resonance is significant only in the region where the array is covered by hBN, so we ascribe this effect to the variation of dielectric environment induced by the inhomogeneity in the distance of hBN to the plasmonic structure.

Using the simulation results as input parameters, we fabricated gold nanodisk arrays via electron beam lithography. Figure 4.3c shows a scanning electron microscope image of the Au-nanodisk array used for the structure discussed in this work. The optimized interparticle distance for a maximum density of nanodisks within the periodic array is a = 300 nm. Smaller array spacing complicate the lift-off process for nanodisk diameters larger than 100 nm. The resolution of the electron beam lithography process is dependent on the e-beam voltage and has a limit at ~ 10 nm. This limited resolution determines the range of variation in disk diameter in an array of otherwise conformly chosen fabrication parameters. The variation of individual nanodisk diameters causes inhomogeneous broadening of the plasmon resonances measured in differential reflection (see figure 4.3b) as compared to the results of corresponding FDTD simulations shown in figure 4.3a. The experimental HWHM linewidth

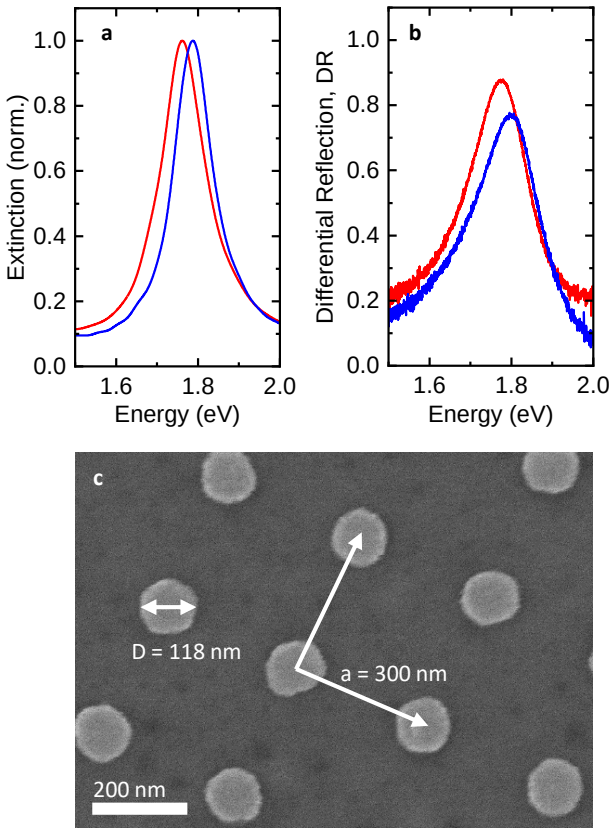

Figure 4.3.: **a**, Extinction spectra of two different gold nanodisk arrays on a silver/SiO_2 substrate obtained from FDTD simulation. The intensities of reflected (R) and transmitted (T) fields are extracted at both ends of the computational cell of the simulation and normalized to the signal of the plane wave source. The extinction is defined as the $1-R-T$. Both arrays have a lattice constant a of 300 nm and height h of 15 nm. The red and blue curve correspond to a diameter D of 114 nm and 106 nm, respectively. **b**, Differential reflection spectra of two gold nanodisk arrays fabricated via e-beam lithography on a silver/SiO_2 substrate. The geometrical parameters correspond to the ones used for the simulation in **a**. **c**, Scanning electron micrograph of an array section of the sample investigated in the main text with mean targeted nanodisk diameter D of 118 nm.

of the plasmon resonances is $\Gamma_{pg} \simeq 90$ meV which is used as the decoherence rate in the model used later.

Now we study a region where WSe_2 is overlapping with Au nanodisks which allows interference between excitons and plasmons. The differential reflection spectrum is shown in figure 4.2e. The optical response displays a complex shape with three peaks, two on either sides with large linewidth and a central narrow peak. Due to the highly dissipative nature

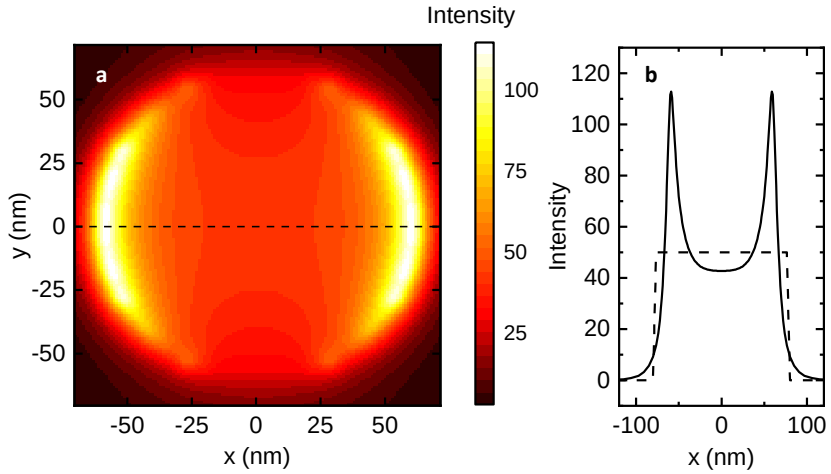

Figure 4.4.: **a**, Intensity of the cross-section area ~ 6 nm above the Au nanodisk (at the position of the monolayer) obtained from FDTD simulation at the plasmon resonance. The intensity is normalized to the intensity of the excitation plane wave source; hence, it effectively determines the intensity enhancement factor for the near-field of the plasmonic nanodisk. **b**, One-dimensional cut (dashed line in **a**) of the intensity cross-section area shown in **a**. The dashed line at intensity 50 represents the approximation of the intensity within a circle with radius 80 nm.

of the plasmon resonance indicated by a large linewidth, we deduce that the coherent interference is not in the strong-coupling regime. However, we expect it to manifest as a Fano interference between two competing channels of excitation in three-level system (figure 4.2e) which should result in a narrow transmission dip in a broad absorption profile in differential reflection [251, 253].

To understand the optical response, we analyzed a coupled oscillator model with three-level system, as illustrated in figure 4.2e. There is a ground state (denoted as state $|g\rangle$) and two competing excited levels $|e\rangle$ and $|p\rangle$ that show coherent interference. The resonance energy of the exciton state $|e\rangle$ is denoted as ω_{eg} and the plasmon state $|p\rangle$ is denoted as ω_{pg}. The Hamiltonian of this system is written as:

$$H = \hbar \begin{pmatrix} 0 & \frac{1}{2}\Omega_{eg}\exp^{i\omega t} & \frac{1}{2}\Omega_{pg}\exp^{i\omega t} \\ \frac{1}{2}\Omega_{eg}\exp^{-i\omega t} & \omega_{eg} & \frac{1}{2}\Omega_{c} \\ \frac{1}{2}\Omega_{pg}\exp^{-i\omega t} & \frac{1}{2}\Omega_{c} & \omega_{pg} \end{pmatrix} \tag{4.1}$$

The optical response of the system is developed in chapter 2. The extinction is obtained in equation 2.40 as:

$$\mathcal{E} \propto \alpha_e \frac{\Omega_{eg,c}\Gamma^r_{ee}}{\Omega^2_{eg,c}+\Omega^2_{pg}}\mathrm{Im}(\rho_{ge}) + \alpha_p \frac{\Omega_{pg}\Gamma^r_{pp}}{\Omega^2_{eg,c}+\Omega^2_{pg}}\mathrm{Im}(\rho_{gp}) + \alpha_e \frac{\Gamma^r_{ee}}{\Omega_{eg,uc}}\mathrm{Im}(\rho_{ge,uncoupled}). \tag{4.2}$$

The key fact in obtaining the above expression for extinction is that the optical illumination spot consists of an exciton-plasmon hybrid region showing coherent interference and also a region with uncoupled excitons in monolyaer spatially far from the nanodisk. Therefore, we obtain the extinction $\mathcal{E}$ in the optical response as the sum of the coherence matrix elements of two coupled states for excitons and plasmons as well as the matrix element for the uncoupled exciton state. Based on the understanding of the coupled model, we systematically study the optical response of our system in detail. The tuning parameter, that is inherently available in our system, is the detuning energy Δ given by the difference of resonance energy of the exciton state $|e\rangle$ and the plasmon state $|p\rangle$ as $\Delta = \omega_{pg} - \omega_{eg}$ that varies with the spatial position of measurement due to the variation in the plasmon resonance energy. The differential reflection optical response from two positions in our device with negative (positive) Δ are shown in figure 4.5a (4.5b). Now, to calculate the extinction from the model for the coupled system, all variables are either experimental parameters or known from literature. For the state $|e\rangle$, the population decay due to radiative recombination is known from literature: $\Gamma_{ee} = \Gamma_{ee}^{rad} \simeq 1$ meV [257, 258]. The experimental linewidth (half-width at half maximum, HWHM) is measured from the monolayer TMD region (figure 4.2c) to be $\Gamma_{eg} \simeq 4$ meV. We interpret the additional linewidth broadening in our sample as homogeneous broadening by pure dephasing. For the plasmon state $|p\rangle$, the experimental HWHM linewidth is found to be $\Gamma_{pg} \simeq 90$ meV. We neglect any pure dephasing process such that $\Gamma_{pg} = \Gamma_{pp}/2$ [158]. The radiative contribution in the plasmonic state $|p\rangle$ for the gold nanodisk is estimated to be $\simeq 46$ % such that $\Gamma_{pp}^{rad} \simeq 18$ meV [158]. The Rabi frequencies $\Omega_{eg,uncoupled}$ and Ω_{pg} are calculated using an illumination laser power $P = 1$ nW, illumination area $A \simeq 1\mu m^2$, and the corresponding linewidth and resonance frequency. The Rabi frequency of excitons coupled to the plasmons $\Omega_{eg,c}$ is calculated using the enhancement factor, $F = 50$, and the coupled and uncoupled areas, $A_{coupled}$ and $A_{uncoupled}$, determined from the FDTD simulation shown in figure 4.4.

The coupling strength is derived by plotting the energy positions of two broad peaks in the complex optical response as a function of detuning as shown in figure 4.5e. Here, the detuning is determined by assuming a fixed exciton resonance energy $\omega eg = 1.723$ eV and obtaining the plasmon resonance energy ωpg by fitting a bare plasmon response (Lorentzian) to the coherent optical response. The coupling constant is then estimated from the experiment to be $\Omega_c \simeq 28$ meV. Figure 4.5c,d show the optical response for the same respective detuning values as figure 4.5a,b given the coupling value. We observe an excellent match between theoretical and experimental optical response. The energy position of the peaks obtained from the model as a function of Δ are shown as solid lines in figure 4.5e. A comparison between experimental differential reflectance spectra and extinction response from the model across further detunings is presented in figure 4.6, again showing agreement between the experiment and the model across a wide range of detuning. After achieving an understanding of the optical response in the metasurface, we utilize the valley degree of monolayer excitons

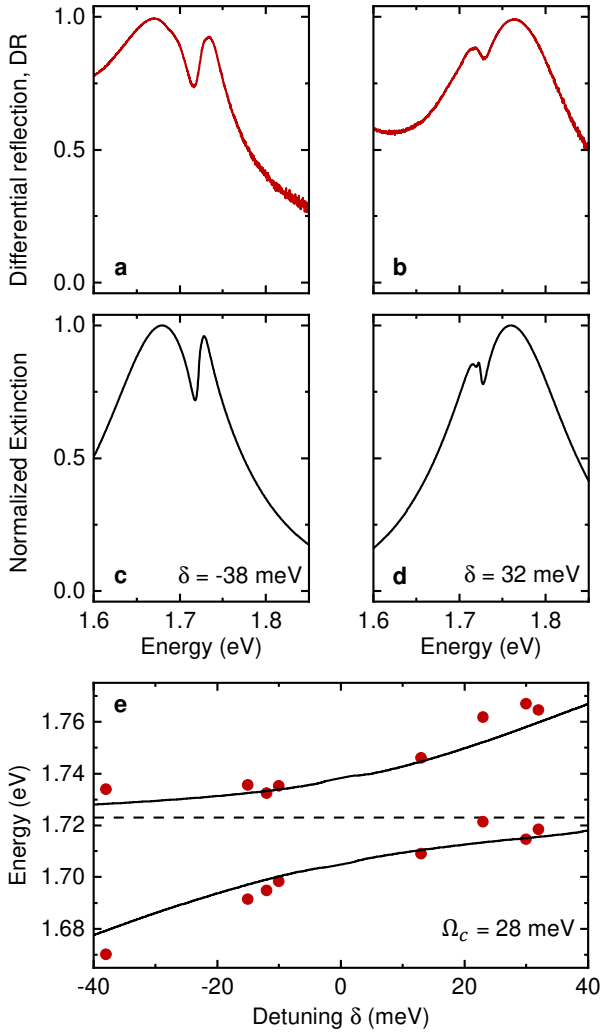

Figure 4.5.: Exciton-plasmon Fano interference as a function of resonance detuning in experiment and theory. **a** and **b**, Differential reflectance spectra of the coupled system for −38 and 32 meV detunings $\delta = \omega_{pg} - \omega_{eg}$ from the exciton-plasmon spectral resonance condition. The spectra were recorded on two spatial area with different plasmon frequencies ω_{pg} (as determined from Lorentzian fits) for a weakly varying exciton frequency $\omega_{eg} \simeq$ 1.723 eV. **c** and **d**, Normalized extinction from coupled model with respective detuning δ and exciton-plasmon coupling strength $\Omega_c = 28$ meV. **e**, Optical response as a function of resonance detuning δ, with red data points corresponding to the peaks in the differential reflection spectra obtained for different ω_{pg} and corresponding coupled model results (black lines) obtained with the bare exciton energy $\hbar\omega_{eg} = 1.723$ eV (grey line) and $\Omega_c = 28$ meV.

in the next section.

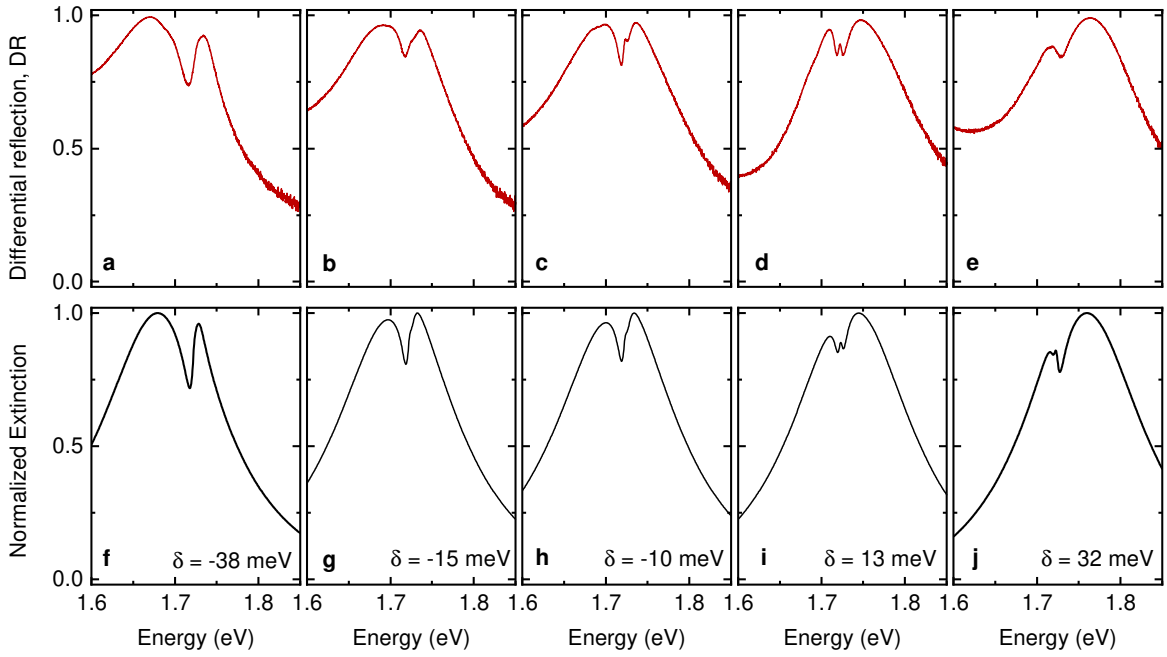

Figure 4.6.: **a-e**, Differential reflectance spectra of the coupled system for various detunings $\delta = \omega_{pg} - \omega_{eg}$. The spectra were recorded on different spatial positions with different plasmon frequencies ω_{pg} for a weakly varying exciton frequency ω_{eg}. **f-j** Respective Fano model optical response with exciton-plasmon coupling strength $\Omega_c = 28$ meV.

4.3. Magneto-induced circular dichroism

Due to the valley-dependent optical transition for excitons in WSe_2 monolayer, we can selectively excite in K (K') valley with σ^+ (σ^-) polarization of light (see section 2.1 for the details on optical properties of TMDs). The presence of an out-of-plane magnetic field induces valley Zeeman splitting in monolayer TMDs that separates the neutral exciton resonance in K and K' valley [67]. First, we demonstrate this valley-Zeeman effect by investigating only monolayer region in our device. We break the valley degeneracy by applying an out-of-plane magnetic field and perform polarization-dependent differential reflection spectroscopy. We excite with a linearly polarized broadband white light source and detect the reflected light in one of the two circular polarizations.

Figure 4.7a (c) shows the differential reflection response of monolayer WSe_2 in magnetic field of 9 T detected under σ^+ (σ^-) polarization. We observe an absorption due to X^0 in K (K') valley with different resonance energy ω_{eg} due to the valley Zeeman effect [67]. To quantify the chiral reflection of light, we define the circular dichroism (CD) of the system as:

$$CD = \frac{DR^+ - DR^-}{DR^+ + DR^-} \tag{4.3}$$

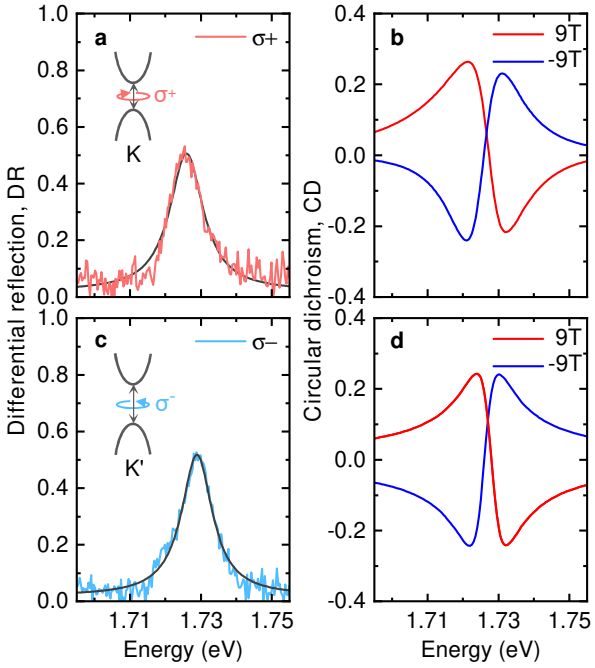

Figure 4.7.: Valley-Zeeman effect of the monolayer excitons in magnetic field. Differential reflectance spectra of the monolayer excitons under **a** σ^+, and **c** σ^- polarization at 9 T. **b** and **d**, Experimental and theoretical CD spectra at 9 and −9 T of the monolayer excitons.

where DR^+ (DR^-) = $\triangle R/R$, i.e. differential reflection spectrum under σ^+ (σ^-) polarization. Figure 4.7c shows the CD measurements at 9 T and −9 T for the monolayer. CD at 9 T shows a maximum CD value of more than 20 % and a sign reversal at the zero field resonance energy of X^0, while the shape of CD at −9 T is reversed compared to 9 T. We also extract the model CD from the extinction of simple two-level exciton system based on the valley g-factor [259]. The optical response for σ^+ and σ^- polarization is normalized by the sum of two optical responses in the calculation of CD, leading to the cancellation of the terms due to various reflecting surfaces in the device. Therefore, the calculated model CD values shown here are quantitative. Figure 4.7d shows the model CD that recreates with high accuracy the behavior of the experimental CD.

In our metasurface device, we use now the valley Zeeman effect to couple valley excitons to plasmons such that the Fano dip in optical response occurs at different energies depending on the spectral position of different valley excitons in the presence of a magnetic field. In principle, this enables to obtain reflection/transmission for σ^+ polarized light while complete absorption for σ^- polarized light at the resonance energy of a K valley exciton and vice versa for a K' valley exciton, when K and K' valley exciton are energetically completely separated.

The spectrally resolved CD is tracked as the magnetic field is ramped from 0 to 9 T and

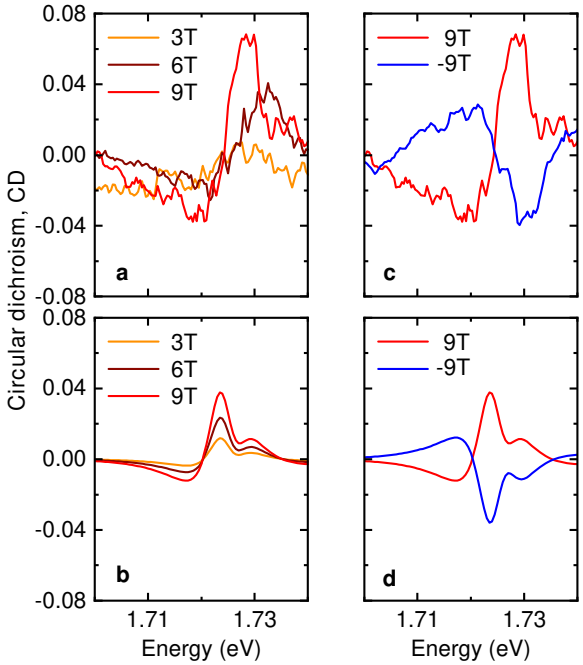

Figure 4.8.: Circular dichroism of the coupled exciton-plasmon system in magnetic field. **a** and **b**, Experimental and theoretical circular dichroism (CD) spectra of the coupled exciton-plasmon system in perpendicular magnetic field of 3, 6 and 9 T. **c** and **d**, Experimental and theoretical CD spectra at 9 and −9 T.

is shown in figure 4.8a. The evolution of negative (and positive) dichroism at lower (and higher) energy is observed as higher magnetic field leads to separated valley excitons. We compare the experimentally observed CD with the expected value from the coupled model extinction. The expected CD is shown in figure 4.8b, where the overall behavior of the CD in our device agrees well with the theoretical model. Due to the competing nature of the Zeeman split energy of the valley excitons and the linewidth of an exciton that defines the linewidth of the Fano dip, the CD value is minimal at 3 T but increases upto 7 % at 9 T which is also predicted by our model.

To demonstrate the switch of chirality of the reflected light, we apply a magnetic field in opposite direction. Figure 4.8c shows the CD at -9 T along with comparison at +9 T, demonstrating the reversal of signs in CD in the entire spectral region. At +9 T, the CD is negative at lower energies and switches to positive CD at higher energies while at -9 T, the CD is positive at lower energy and switches to negative in the higher energy range. The behavior is corroborated excellently by our model as shown in figure 4.8d. Therefore, we demonstrate the control of CD with a magnetic field and its sign reversal by changing the direction of the field in the metasurface device.

4.4. Conclusions

In this chapter, we developed a hybrid system of plasmons in metal nanodisks and excitons in monolayer WSe_2. After the brief introduction to plasmon resonance, we experimentally demonstrated coherent interference. This interference results in Fano line-shapes in optical response. The optical line-shape was confirmed by the three-level quantum system whose dynamics are derived using master equation in chapter 2 and leads to coherent coupling strength $g = 28$ meV. Subsequently, valley Zeeman effect was utilized using external magnetic field to show circular dichroism on the hybrid device of up to 7 %, which is also confirmed with the three-level model.

Our nanophotonic device is a preliminary example of a switchable polarization band-pass filter that could pave the way to an integrable basic element in quantum information processing allowing uni-directional flow of classical and quantum information. This can lead to complex quantum networks and platform to study cascaded open quantum systems [215, 216, 221, 222].

With that prospect, the functionality and performance of our system can be improved in several ways. One obvious way to create a chiral device without an external magnetic field is to create van-der-Waals heterostructures combining monolayer TMDs and magnetic two-dimensional materials that leads to a permanent valley-Zeeman splitting of excitons in TMDs [260]. An improvement towards fully absorptive metamaterials can enable complete absorption over a long spectral range with the Fano dip that leads to chiral reflection or transmission in a narrow spectral window. On the other hand, the improvement in fabrication techniques can lead to narrow exciton resonances in monolayer TMDs limited only by radiative processes. This will lead to narrow Fano transmission dip in our devices.

5 Cryogenic open micro-cavity system

Solid-state systems combined with an optical resonator is an excellent prospect for quantum optics and quantum information applications. This chapter addresses the technological gap encountered in the field of a suitable experimental platform for cryogenic tunable cavity experiments. We present a tunable open Fabry-Pérot cavity in a closed-cycle cryostat and we demonstrate excellent control of light-matter interaction with monolayer WSe_2 in high cooperativity regime.

First, a broad-picture overview of light-matter interaction is given and a motivation to pursue a tunable and open cavity setup at cryogenic temperature is discussed in section 5.1. The challenges in realizing an experimental Fabry-Pérot cavity platform at low temperature that fulfills a set of essential criteria are discussed and the design of the platform is presented in section 5.2. The development and characterization of the setup are addressed in section 5.3. As explained in chapter 3, one outstanding challenge for the operation of an open cavity at cryogenic temperature is mechanical vibration. We report the chronological development of the mechanically stable setup using a combination of vibration isolation techniques. At the end, the state-of-the-art results are demonstrated for a cavity setup with high mechanical stability while maintaining tunability over several millimeter. In section 5.4, the investigation of the coherent interaction between photons trapped in the cavity platform and excitons in TMD is experimentally and theoretically performed. We observe exciton-polaritons with significant Rabi splitting in the system at low temperature with controlled energy detuning between excitons and photons.

5.1. Motivation

Photons are one of the most important ingredient in the rapidly rising quantum technologies. It is thus necessary to be able to manipulate and interact with photons in a controlled environment. However, due to the nature of photons, it makes the manipulation a highly

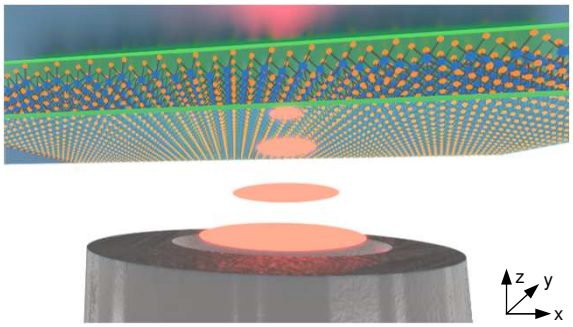

Figure 5.1.: **Open Fabry-Pérot cavity.** An illustration of the cavity composed of a concave-profiled fiber mirror and a macroscopic mirror with a WSe_2 monolayer.

non-trivial and complex task. An introduction of an optical resonator can confine the photon in a small volume leading to enhanced light-matter interaction in the field known as cavity-QED [35, 217, 261].

There are variety of optical resonators ranging from planar micro-cavities, whispering-gallery modes in ring resonators, plasmonic structures and photonic crystal cavities. The goal of an optical cavity is to increase the interaction between photons and a quantum emitter (or an atom in AMO physics), this can be achieved by two main parameters: long confinement time (high finesse) and low confinement volume. There are also several other factors that determines the usability of the resonator, namely: the ease of fabrication with the right characteristics, integration of quantum emitter in solid-state experiments and the in- and out-coupling efficiency of the light in the resonator.

Few years ago, a fiber-based Fabry-Pérot open and tunable cavity platform has been introduced [58, 59]. The open cavity is made of two separate mirror components made either of fiber tip or a macroscopic mirror, with the emitter either suspended between the mirrors or typically integrated on one of the mirrors. It has been shown that high-reflectivity dielectric coating can be deposited on both macroscopic mirror substrate and fiber tip to achieve finesse up to 10^6 [58]. In addition, the fiber has a laser-machined or etched concave curvature with a small radius of curvature (few microns) that enables extremely small mode volume of the order of λ^3. The open nature of the cavity allows for mirrors to be moved with respect to each other during the experiment, thus cavity resonance can be tuned as well as spatial tuning on macroscopic mirror can enable selectivity of different emitters. This tunability feature offers the possibility to adjust experimental parameters in real time which is a particularly huge advantage in present time when the quantum technology applications is still in exploration and development phase. A sketch of the open cavity with a monolayer semiconductor on macroscopic mirror is shown in figure 5.1.

There are several advantages of an open cavity compared to the other optical resonators

listed above. First, the open nature allows an easy integration of solid-state emitters inside the cavity, this relaxes the requirements on fabrication and integration of quantum matter. Second, it allows one mirror of the cavity to be moved with respect to the other mirror enabling in-situ spectral tuning of cavity resonance as well as spatial tuning which is advantageous to select the most suitable emitter on the macroscopic mirror. Third, the use of a fiber as a micromirror for the cavity provides excellent light coupling efficiency [59]. Thus, the fiber-based tunable Fabry-Pérot cavity is an ideal platform to achieve high interaction between photon and matter.

Fiber-based tunable Fabry-Pérot cavities were first used with a cloud of atoms or ions, such as the demonstration of strongly coupled BEC with cavity photons [262–265]. The tunable cavity has also been combined with nanoscale optomechanical system [266], coherent control of ions [267] and biological molecules and polymers [268, 269]. Moreover, it has been utilized as an extremely-sensitive absorption microscope [270]. It has subsequently been coupled with variety of solid-state based quantum emitters. For example, it has been used to demonstrate the Purcell enhancement with solid-state emitters such as quantum dots [271], NV and other defect centers [272–279], rare-earth ions [280–283], carbon nanotubes [284, 285] and interlayer exciton in TMDs [119]. By tuning the interaction parameters, the interaction strength can be increased sufficiently to enter the strong-coupling regime leading to the formation of exciton-polaritons in quantum dots [141, 142, 286–288] and TMDs [127, 136, 289–293].

Despite several pioneering experiments to combine solid-state emitter with the cavity platform, an outstanding challenge is to operate tunable cavity platform with high-finesse in a closed-cycle cryostat. Cryogenic temperature is essential to isolate solid-state quantum emitter from the environment and enhance coherence times. Using a closed-cycle cryostat to reach that regime is an important step on the road towards quantum technologies as it guarantees independence from finite supply of liquid helium, ease of use and long runtime without human intervention, which are all necessary for practicability of the scalable quantum technologies. The primary challenge with a cavity platform in a closed-cycle cryostat is mechanical vibrations that were introduced in chapter 3.

In this chapter, we will present the steps undertaken to implement a stable cavity platform on a closed-cycle cryostat by combining various vibration isolation techniques. The cavity platform achieved in this manner provides tunability over several millimeter in all three translational directions by using commercial nanopositioners along with the ability to tune the objective with respect to the cavity for efficient coupling in transmission towards free-space.

The high stability and wide tunability makes the concept presented here an excellent platform to explore the physics of strong-coupling in TMDs, including several collective polaritonic effects such as condensation and lasing with valley-spin manipulation via quantum matter [56, 294–296]. Here, we will present the first observation of exciton-polaritons with

TMD plus cavity in a closed-cycle cryostat that unlocks wide range of future experiments.

5.2. Requirements for tunable cavity at low-temperatures

The platform studied here, as introduced in section 5.1, is an open Fabry-Pérot cavity where one mirror is a fiber-based micromirror with a concave shape while the other part is a macroscopic mirror hosting a solid-state quantum emitter that enables the formation of a zero-dimensional cavity with high finesse and extremely small mode volume [58, 59].

Solid-state emitters usually require operation at cryogenic temperature to reduce environmental disturbance in order to achieve long coherence times. We decided to use a closed-cycle cryostat (attocube attoDRY800) as the choice of low temperature system for the open cavity setup. However, as shown in chapter 3, the operation of a closed-cycled cryostat leads to significant mechanical vibration that can be a challenge for a stable operation of the open cavity.

The way to estimate the stability requirement for our purposes is as follows. The mechanical stability required for the open cavity is directly connected with the cavity parameter finesse shown in equation 2.7. The finesse $\mathcal{F}$ determines the linewidth of the cavity resonance at a given wavelength. The linewidth will be 0.39 nm for the relatively high finesse of $\mathcal{F} = 10^3$ for the wavelength $\lambda = 780$ nm. Thus, in order to resolve this resonance linewidth in an experiment, the mechanical vibrations need to be much smaller than 0.4 nm. If we assume that a minimal signal-to-noise ratio (SNR) of ~ 10 is desirable, this puts the mechanical stability requirement in the 10 pm range. The state-of-the-art reflective coating allows to reach the finesse $\mathcal{F} \sim 10^6$ and an ongoing improvements in the coating technology suggests that the mechanical stability will have to aim for femtometer range for more demanding applications.

We identify three criteria to characterize the performance of the tunable open cavity platform: 1) Temperature, most solid-state emitters require temperature below 10 K. 2) Tunability, degrees-of freedom and range of tunability to tune the distance between two mirror. And 3) Mechanical stability, mechanical displacement between two mirrors should be minimized.

While a great progress has been made in open Fabry-Pérot cavity experiments, in most cases, a trade-off has to be made regarding at least one of the above criteria. The first demonstrations with tunability and high mechanical stability has been shown at room-temperature [270–272]. It followed with experiments at cryogenic temperature in liquid helium bath cryostat [119, 274, 286, 287]. While high mechanical stability is possible along with large range of in-situ tuning in these experiments, a constant Helium supply and human resources makes them sub-optimal choice for large scale quantum applications. In more recent experiments, cavity platform is used in a closed-cycle cryostat. However, due to

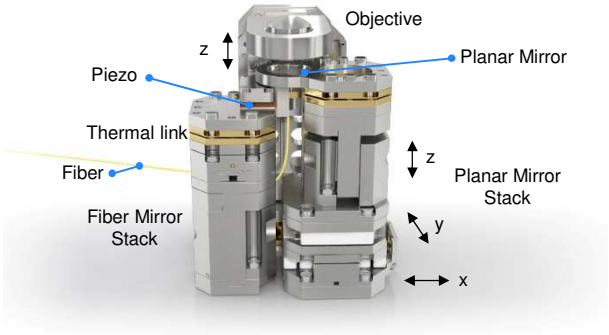

Figure 5.2.: Sketch of the tunable cavity assembly on the closed-cycle cryostat. The planar mirror stack on the right side consists of xyz-nanopositioner with a thermal link below the planar mirror to thermalize it to cryogenic temperature. The fiber mirror stack on the left consists of a piezo element, thermal link and metal blocks to reach the same height as the right stack. The objective is mounted via another metal piece at the back with an additional nanopositioner to adjust the focal spot in z direction.

high mechanical vibrations in closed-cycle cryostat, the experiments so far have achieved only limited mechanical stability, even in highly customized systems, at the cost of none or limited in-situ tunability in various degrees of freedom [275, 277, 281, 282]. The latter two criteria are particularly difficult to achieve as they are in direct contradiction to each other.

We have developed a fully-tunable open Fabry-Pérot cavity platform in a closed-cycle cryostat with a large range of lateral displacement on the sample surface. The cavity platform with quantum emitter reaches less than 5 K temperature and provides tuning range of relative mirror position in 3 spatial directions over several mm along with a free-space access to the cavity through an objective that can be focused with tuning range of 6 mm, where all coarse tuning capabilities are provided with off-the-shelf nanopositioners. Additionally, we show that with the combination of passive and active vibration reduction techniques, the mechanical stability of the rms displacement of less than 90 pm is achieved at the integration bandwidth of 100 kHz.

The two mirrors of Fabry-Pérot cavity are a fiber end with a dimple and a macroscopic mirror which host a solid-state quantum emitter as shown in figure 5.1. The dimple is produced on the fiber tip using CO_2 laser ablation technique [58]. The mirror and fiber tip are both coated with either a silver (Ag) metal thin film or a distributed Bragg reflector (DBR) coating in the experiments shown below.

The mechanical setup that stands on the vibration isolation stage is shown in figure 5.2. The macroscopic mirror is mounted on a commercial xyz-nanopositioner (attocube 2 x ANPx311, ANPz102) to enable coarse cavity tuning in z direction over 4.8 mm and to place the quantum emitter on the mirror at the desired position to couple with the cavity mode

in the xy plane over the area of 36 mm^2. The fiber is mounted on an additional piezo for the precise cavity detuning and active feedback. The axis of the cavity mode is fixed in the xy-plane by the fiber so an independent coarse xyz-tuning of fiber is not required. The objective (ThorLabs AL1210, NA = 0.55) is mounted on another z-nanopositioner (attocube ANPx311HL in vertical direction) providing free-space optical access to the cavity. The characterization of the setup is described in the following section.

5.3. Development and characterization

As discussed in the previous section, an open tunable cavity at cryogenic temperature has two non-complementary requirements: one is multiple degree-of-freedom to tune the cavity length and spatial selection of quantum emitter over millimeter range while the other is the cavity length to be stable in picometer scale. Based on the mechanical vibration performance of the cryostat presented in chapter 3, it is clear that the level of vibrations has to be reduced by orders of magnitude to operate a high-finesse cavity. To reduce the mechanical vibration, we employ a variety of passive and active techniques that were discussed in Chapter 3.

First, I provide a short overview of the method used to characterize the mechanical vibrations in the optical cavity. Then, I will present the characterization of vibrations as different vibration isolation techniques are employed in the cavity setup. The characterization measurements are divided in to two main rounds of measurements called phase one and two.

Phase one covers the exploratory phase of passive vibration reduction techniques for the cavity setup. We implement a simple spring-based vibration isolation stage without separate thermal connection links to enable efficient cooling of cavity mirrors. Furthermore, we explore other passive vibration reduction techniques such as viscous damping via Eddy current, differential motion reduction by introducing a link. In addition, the setup is characterized at low temperature after introducing the thermal links. Moreover, the robustness of the setup in terms of mechanical stability is demonstrated. Phase two of measurements covers active cancellation of mechanical vibration. Furthermore, the performance reproducibility is studied. Latest and most advanced mechanically stable cavity results are summarized to conclude the section.

5.3.1. Methods

Before moving to the evolution of the cavity setup and quantifying its performance, let us first discuss the measurement procedure. The fluctuations in the length in a Fabry-Pérot cavity can be measured with the cavity itself by monitoring the change of phase in the cavity reflection or transmission signal.

The required length stability in the cavity length for finesse $\mathcal{F} = 1000$ is ≈ 40 pm for the

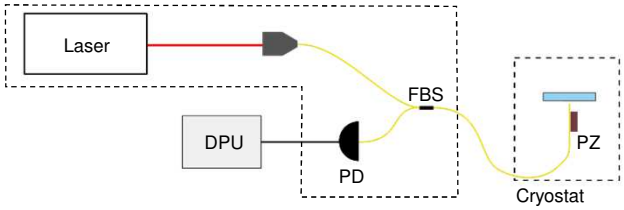

Figure 5.3.: Reflection Setup. A sketch of the experimental setup used for the cavity stability characterization in the first and second phase. Assignment of abbreviations: FBS (Fiber Beamsplitter), PD (Photodiode), DPU (Data Processing Unit).

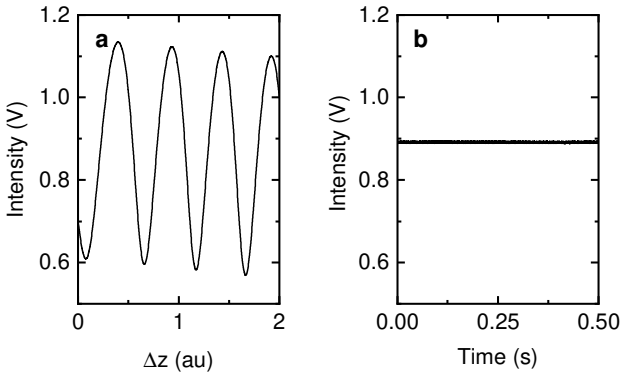

Figure 5.4.: **a** The solid black line is the Reflection data obtained from a cavity length sweep by applying a voltage to the piezo below the fiber. Here, the finesse is very low so the reflection is a sinusoidal curve with period of $\lambda/4$. **b** Timetrace of the reflection signal at the slope to monitor phase fluctuations which are then converted to cavity length fluctuations. The measurement bandwidth is 100 kHz.

SNR of 10 as discussed in the last section. The direct way to check if a cavity of given (high) finesse is sufficiently stable for the operation is to use the mirror with appropriate coating and measure finesse experimentally. However, if the mechanical vibrations are higher, it might be difficult to achieve stability or even estimate how far off the system is from the target stability. Therefore, we take the approach to start with a low to moderate finesse ($\mathcal{F} <$ 10) cavity. This provides us with a high dynamic range such that the length fluctuations over several orders of magnitude can be measured simultaneously. The resolution of the length fluctuations is still limited by the laser and detector noise, which will be discussed in later. The maximum finesse that can be achieved in the system is then estimated based on the length fluctuations and the required SNR for the actual experiment.

In the phase one of the measurements, the fiber used as a micromirror is without any

coating and profile curvature. The uncoated flat fiber is perfectly suitable for the vibration measurements as the mode volume doesn't need to be minimized and the fabrication process involves only a simple step of cleaving the tip of a bare fiber. The other mirror of the cavity is a standard Ag-coated mirror. The glass fiber tip has a reflection of roughly 4 % without coating, yielding a finesse of $\mathcal{F} \approx 1$. The fluctuations can then be monitored through the reflection signal as shown in figure 5.3. The input light is provided by a laser detector module (attocube LDM600) with wavelength λ = 650 nm. The advantage of using a module is that it has an in-built fiber beam splitter and a Si-based photodetector as illustrated, which combines the whole apparatus for the reflection measurement and simplifies the procedure. In the reflection signal, the interference due to two arms of the cavity in the limit of low finesse forms a sine-like wave as the function of displacement Δz (figure 5.4). We bring the cavity to a position where the slope of the reflection signal is highest such that the displacement fluctuations which leads to fluctuations of reflection signal is most sensitive. Then we monitor the reflection fluctuations around this position and convert it to the displacement values.

In the phase two of the measurements, we switch from the flat uncoated fiber tip to a concave-profile fiber tip with either metal or dielectric coating. The macroscopic mirror has the Ag coating, leading to a finesse in the range of $\mathcal{F} \approx$ 10-100, depending on the exact thickness of the coating. Figure 5.5 shows the measurement setup. Due to the change of the fiber tip, the concave-planar cavity implies the need for mode-matching between the fiber and the cavity mode. This can lead to a complex dispersive interference in reflection signal [297], thus the measurement in the phase two are performed with the transmission signal. Additionally, the laser module is replaced with a low noise Ti:Sapphire laser (M Squared SolsTis) with λ = 780 nm. The transmission signal is captured with Silicon photodetector (BPW34) with charge preamplifier (Ithaco Preamplifier 1211). To determine the cavity length, a white light source (NKT SuperContinuum Extreme with Varia filter) is guided to the fiber instead of Ti:Sapphire laser and the transmission signal is spectrally dispersed by a monochromator (Acton SpectraPro-275) and detected by a CCD camera (Princeton Instruments Spec-10). A part of transmission signal is optionally also guided to another photodetector (BPW34) which can be used for the feedback loop to lock the cavity.

For the characterization measurement in this phase, first, the transmission signal across a cavity resonance is logged while sweeping the voltage applied to the piezo below the fiber. For the conversion of the piezo voltage in the units displacement of cavity length, we monitor two consecutive longitudinal TEM_{00} modes across the sweep which are separated by the well defined FSR = $\lambda/2$. The finesse of the cavity resonance is determined from the transmission signal as the function of the change in cavity length Δz as shown in figure 5.6a. The transmission as a function of cavity length is given by [298]:

$$T(z) = \frac{T_0}{1 + g^2 sin(\Phi(z))^2} \tag{5.1}$$

where T_0 corresponds to the transmission signal on resonance, $\Phi(z) = 2\pi(z - L)/\lambda$ where L is the cavity length on resonance and λ is the wavelength of the light and g is related to the finesse by $g = 2\mathcal{F}/\pi$. The derivative of the transmission function (equation 5.1) with respect to the cavity length is given by:

$$\frac{dT}{dz} = -\frac{4g^2\pi}{\lambda} \frac{\sin(\phi)\cos(\phi)}{(1 + g^2 \sin(\phi)^2)^2} \tag{5.2}$$

Fluctuations in the transmission signal as a function of time are converted to the cavity length fluctuations using equation 5.2, assuming a linear approximation for small fluctuations around the half-maximum position. The transmission signal is measured with a photodiode and a current preamplifier with an analog-digital channel with time resolution of 10 μs.

It is important to note that the cavity length fluctuations should be measured with an appropriate dynamic range defined by the finesse of the cavity. For example, the measurements (carried in phase two) are performed with $\mathcal{F} = 110$ leading to a cavity linewidth of $\Delta\lambda \approx 3.5$ nm. Thus the maximum displacement obtained at the vibration kick of 0.7 nm is ensured to be still well within the measurement range of the cavity as an interferometer as illustrated in figure 5.6b.

As a general methodology, we will show the plots of cavity length fluctuations as a function of time and as a function of frequency. The fluctuation time trace covers several seconds i.e. several cycles of the cold head demonstrating full vibration impact of cryostat cooling. The bandwidth of the time trace is 100 kHz unless specified otherwise. The fluctuations are converted to Fourier space, using the Welch method [299], to calculate the power spectral density with the Hamming window and the frequency resolution is set to 1 Hz. Two key numbers used as a figure-of-merit are the peak-to-peak fluctuation and root-mean-square (rms) fluctuation over the period of cryocooler cycle at full measurement bandwidth of 100 kHz. The peak-to-peak displacement in cavity fluctuations is dominated by the pulse kicks (similar to the vibrations on the cold plate in chapter 3). While this can damp within fraction of a second to smaller value, a high peak-to-peak number can kick the active lock out of the stability. The rms displacement, on the other hand, represents the average fluctuations over the entire cycle and thus, it gives an overview on the overall vibration level over a cooling cycle. We will also use the analysis of rms or cumulative amplitude vibration as a function of bandwidth to facilitate and extract the performance difference between various isolation techniques.

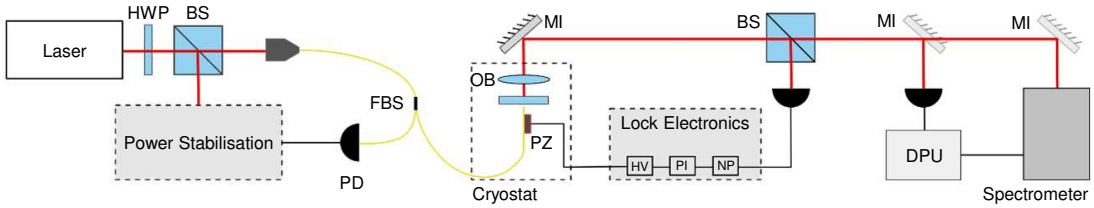

Figure 5.5.: Transmission Setup. A sketch of the experimental setup on the optical table used for the cavity stability characterization in the third phase and study of light-matter coupling with monolayer semiconductor in the cavity. Assignment of abbreviations: HWP ($\lambda/2$-Waveplate), BS (Beamsplitter), FBS (Fiber Beamsplitter), PD (Photodiode), OB (Objective), PZ (Piezo Nanopositioner), MI (Mirror), DPU (Data Processing Unit), Lock Electronics: HV (High Voltage Amplifier, ANM 200), PI (Proportional-Integral control electronics), NP (Notch Pass).

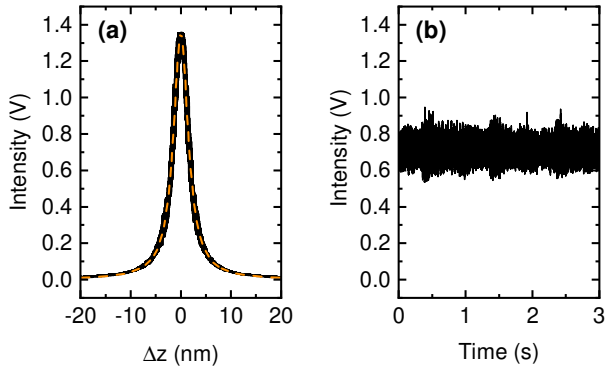

Figure 5.6.: **a** The solid black line is the Transmission data around a cavity resonance obtained from a cavity length sweep by applying voltage to the piezo below the fiber. The yellow dotted line shows the corresponding fit to the Fabry Pérot Transmission function (equation 5.2). Here, the finesse obtained from the fit is $\mathcal{F} = 110$. **b** Timetrace of the transmission signal through the cavity measured at the slope of the cavity resonance shown in **a** at low temperature ($T = 6.5$ K) with active stabilization. The measurement bandwidth is 100 kHz.

5.3.2. Passive vibration reduction techniques

As a starting point, let's recall that the mechanical vibration on the cold plate (figure 3.10) are of the order of a few nm and on the xyz-positioner stack (figure 3.13) of a few 10s of nm in vertical direction. In order to reduce the vibrations, we decide to use a low frequency spring stage as a base vibration isolation platform, as there is a frequency-dependent vibration isolation at frequencies higher than the resonance frequency of the stage as shown in figure 3.19. The spring stage is based on four springs that mechanically isolates the cavity

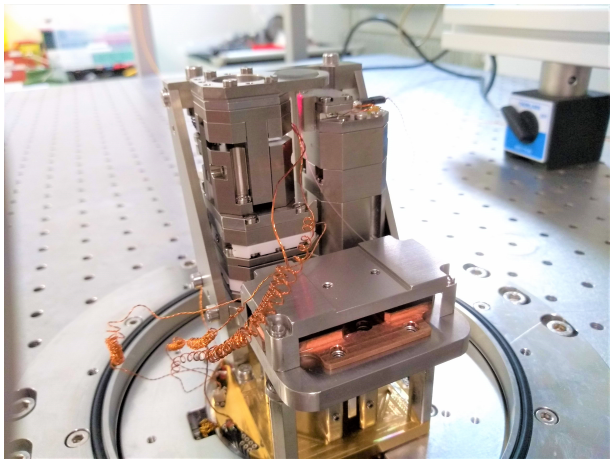

Figure 5.7.: Picture of the first assembly of cavity setup. The two stacks holds two different mirrors of the cavity, the entire structure is on a spring-based vibration isolation stage.

platform from the cold plate in vertical direction. The four springs are divided into group of two which are on different horizontal plane such that the cavity platform on top is in stable position from tilting motion even if the isolation is primarily in vertical direction.

The spring isolation stage holds the cavity setup, a preliminary version similar to the one shown in figure 5.2. This preliminary cavity setup on the spring stage consists of two tower stacks holding mirror and fiber forming the microcavity. The tower stack with the mirror has an ANPxy312 positioner for xy-movement and an ANPz102 positioner for z-movement. The choice of the positioner was made to achieve the highest resonance frequency possible, the ANPxy312 positioner used here was the prototype that was being developed by attocube at the time. The fiber tower stack on the other hand is mounted with dummies with same dimension as 2 x ANPx101 and ANPz102. In principle, the dummies can be replaced with actual xyz-nanopositioner if translation of the fiber independent of the mirror is desired. Here, we decide to keep it fixed as translation of the mirror in 3 spatial direction with respect to fiber is enough, in addition to the objective mounted on an additional nanopositioner, to focus and optimize cavity mode transmission to free space detection and perform experiments. The option to replace the dummies with positioner, however, can be advantageous if a macroscopic mirror with multiple concave profile, with same or different radius of curvature, is used instead of the fiber. This allows more freedom in in-situ tunability and could provide access to multiple 0-D cavities simultaneously [127, 271, 281].

First assembly of the setup did not include thermal links which are required for an efficient thermalization of the microcavity with the cold plate, also the objective was not included at this point. A picture of the first assembly is shown in figure 5.7. We began by measuring the cavity fluctuations by monitoring the reflection signal as explained in the previous section.

Figure 5.8 shows the amplitude fluctuations as a function of time and frequency when

the compressor is running at room temperature. We see the characteristic shape of the amplitude fluctuations is repeated every cooling cycle with some variation. The peak-to-peak vibration amplitude is ≈ 6 nm. This is due to the impact generated by cold head when He-pressure suddenly changes (referred as pulse or pulse-shock). The other criterion calculated from the time plot is rms fluctuations over an entire cooling cycle. The rms fluctuations are averaged over 10 cycles to account for the variation in impact of pulses. Here, the rms fluctuations are 390 ± 25 pm. The Fourier transform plot provides information on resonance frequencies, their respective amplitude as well as Q-factor in the system that are excited. While a detailed analysis and understanding of each peak in the Fourier transform is a non-trivial task, I will point out important or interesting peaks at every stage such that their evolution will be tracked. This will provide useful information on the origin of various internal resonance of the system and can give an insight on tackling them.

In figure 5.8b, we define the first family of peaks as the one around 20 - 35 Hz. These are ascribed to the spring isolation stage as it can be calculated from the stiffness of the spring and the mass of the setup on the spring isolation stage. The reason that there are multiple peaks is because different springs have different mass load on them due to asymmetric mechanical design, leading to different resonance frequencies.

There are also several peaks between 100 and 1000 Hz with high amplitude as well as one peak at around 1200 Hz. The origin of these are not immediately clear. A mechanical resonance with possibly low frequency is the mirror tower stack consisting of ANPxy312 and ANPz102 positioners. The estimated resonance frequency is less than 1000 Hz based on the analysis of similar positioner stack in section 3.3.1. However, the fiber tower is made of dummies and the resonance frequency is expected to be a few kHz.

As an additional way to obtain an insight into the behavior of the various mechanical resonance of the system, we perform an impact test. Upon providing an impact to the optical table that is connected to the cold plate, it excites a broad band of mechanical frequencies in the system. We monitor the time evolution of the cavity length after such excitation to get better understanding of the eigenresonances of the system, without the presence of background noise from sources such as pumps, compressor, fans, etc. The impact is provided by hitting the optical table next to the cold plate with the "same" force (practically it was done by dropping a screwdriver from a small fixed height). This test is particularly helpful in checking the Q-factor and efficiency of the spring isolation stage. The results of the impact test on the first assembly are shown in figure 5.9. We see that the amplitude of the impact is ≈ 100 nm, which is higher than a typical amplitude of the pulse-shock from the compressor. It takes roughly 3 seconds to go back to pre-impact amplitude level. The FFT plot shows that the primary resonance excited by the impact is around 20 Hz which are due to the spring isolation stage. In addition, the few resonances above 100 Hz, particularly 650 Hz and 1200 Hz, that are excited by the cryocooler are also seen in the impact test. Their amplitude is albeit lower than the amplitude of the spring stage in the impact test. This

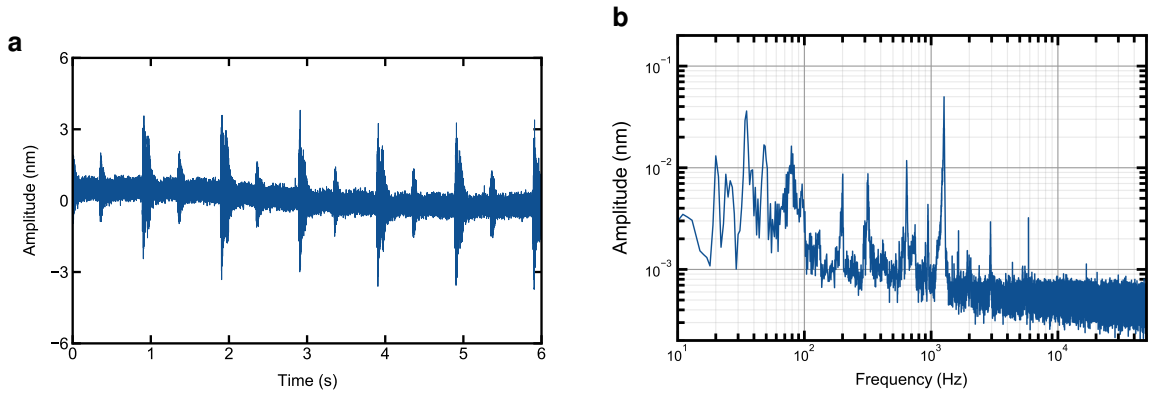

Figure 5.8.: Initial cavity stability characterization of the setup at room temperature. **a** Time plot, the typical pulses are seen every one second with peak-to-peak height of 4 nm, due to the cryocooler. This damps down quickly and the rest of the time period has much smaller length fluctuations. **b** FFT plot shows major frequency contributions to the vibrations. The cryostat excites a wide range of frequencies below 10 kHz.

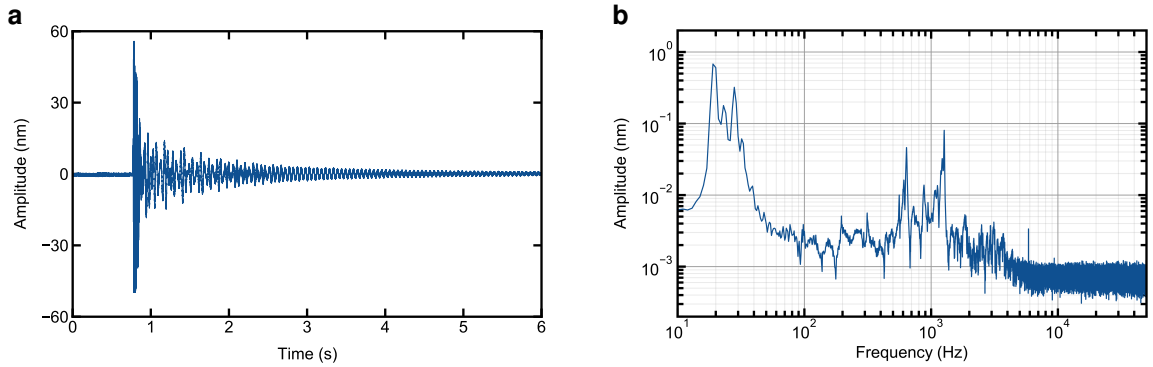

Figure 5.9.: Impact test results of the first assembly showing **a** Time plot and **b** FFT plot. An impact is generated in the steady state to excite the broad band frequency without any other external factor. Spring isolation stage shows the primary excitation by such impact, as confirmed by the FFT plot showing a domination by 20-30 Hz peaks. Typical decay time of the impact in the time plot suggests the Q-factor of this excitation.

indicates that in such broad band excitation, the whole spring stage is excited with a high Q-factor and dominates the dynamics. In the next part, we investigate the method to reduce the Q-factor of such harmonic oscillator with damping based on Eddy current.

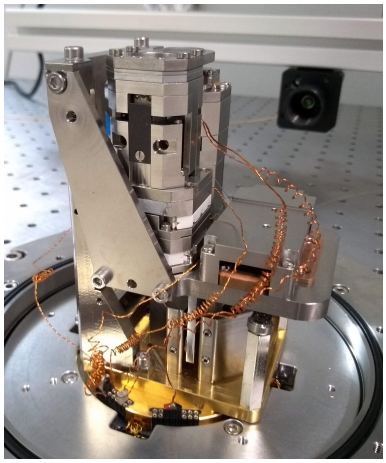

Figure 5.10.: Viscous damping is introduced via 8 pairs of magnets mounted on the cold plate and a piece of metal, connected to the spring isolation stage, positioned between each pair to generate the Eddy current

Magnetic Damping

After the first characterization of the cavity setup including the spring isolation stage, we introduce few pair of magnets in parallel to the spring isolation stage in the setup as shown in figure 5.10. There is an aluminum metal piece attached to the setup which creates a viscous force based on Eddy current generated by moving this metal conductor in the presence of the magnetic field that decreases the Q-factor of the isolation stage. The effect of Eddy current-based viscous damping is discussed theoretically in section 3.3.2. The cavity length fluctuations measured, while the cryocooler is on, are shown in figure 5.11. The peak-to-peak vibration amplitude is ≈ 4 nm and the rms fluctuations are 381 ± 61 pm. There is a slight improvement over the results without Eddy current damping shown in figure 5.8.

To compare the two sets of results in more detail, we plot the FFT plots of both data sets: with and without Eddy current damping in the same plot. Additionally, we also plot the cumulative amplitude of both data sets by summing up the frequency dependent contributions to the power spectral density. This yields the so-called cumulative spectral density. The cumulative plot provides an alternative visualization tool to compare contribution of each frequency to the total vibrations. However, it is important to note that the cumulative amplitude does not include the phase information between frequencies. Therefore, it does not correspond to the total peak-to-peak vibrations as observed in the time plot. The comparison of the two data sets is shown in figure 5.12. There is no clear evidence of a significant decrease in amplitude and Q-factor of the spring stage resonance in the Fourier transform comparison. Due to a low frequency length fluctuations, the cumulative amplitude in the case of the Eddy current damping starts at a higher value at 10 Hz. The contributions of the spring isolation stage and other higher frequency peaks do not show a clear advantage of

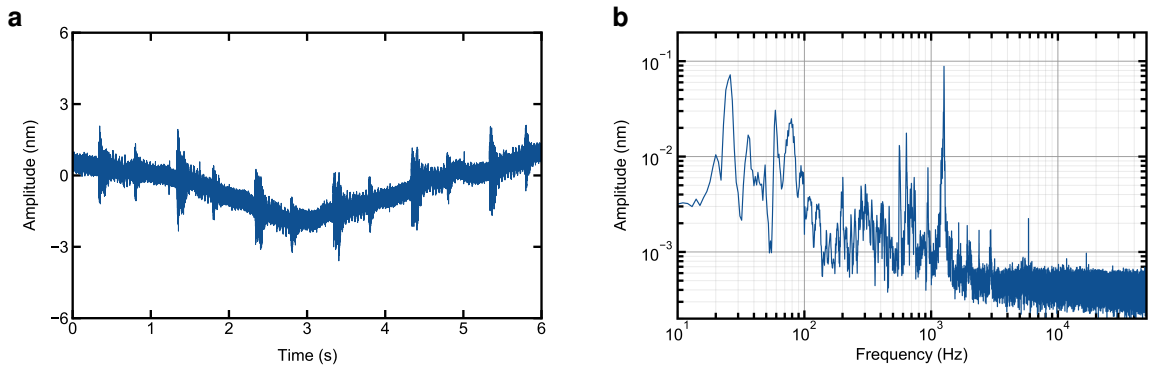

Figure 5.11.: Cavity stability characterization after the implementation of Eddy current damping at room temperature. **a** Time plot shows the peak-to-peak vibrations of 4 nm. **b** FFT plot shows that the spring isolation stage eigenfrequencies still dominates the overall excitation response.

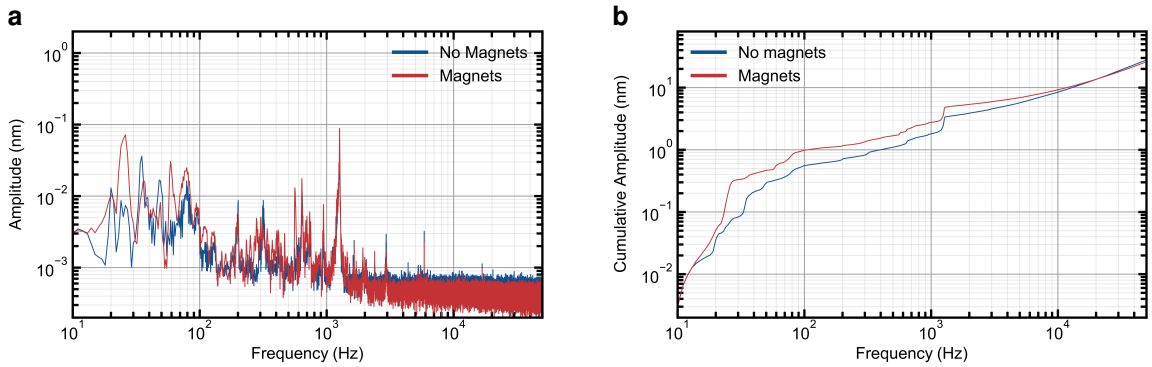

Figure 5.12.: Comparison of the Eddy current damping in the first cavity assembly. **a** FFT plot shows that the reduction of amplitude of peaks around 20-30 Hz is not significant. **b** Cumulative amplitude due to the frequency range below 100 Hz confirms that the effect of Eddy current damping is small.

introducing Eddy current damping.

We also performed the impact test in the presence of magnets. Figure 5.13 shows the results. The impact amplitude is again at ≈ 100 nm. However, here it is damped to pre-impact level within one second. The Fourier transform confirms that the spring stage resonance has been broadened (compared to the results in figure 5.9) leading to faster damping as expected by introducing Eddy currents. For an alternative comparison of impact test with and without magnets, the Fourier transform and cumulative amplitude are shown in figure 5.14.

While the result of the impact test shows that the Q-factor is decreased via the quick

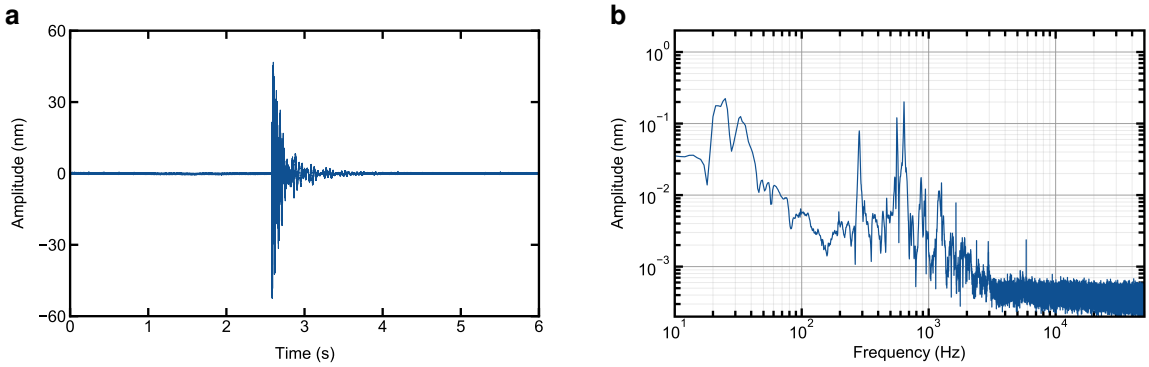

Figure 5.13.: Impact test in the presence of Eddy current damping in terms of **a** Time plot and **b** FFT plot. The fluctuations goes to quiet level within one second in the time plot.

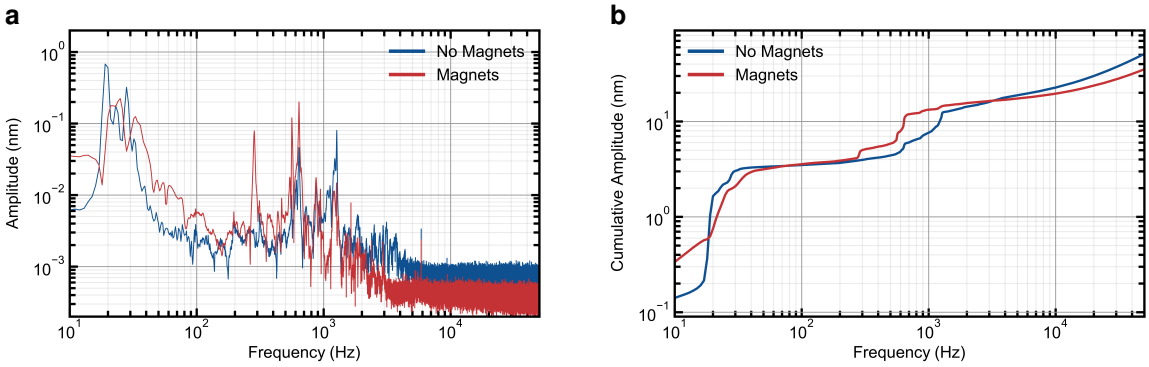

Figure 5.14.: Comparison of the impact test with and without Eddy current damping. Reduction in the Q-factor of the spring stage resonances is visible in both **a** FFT plot and **b** cumulative amplitude contribution.

damping of the impact in case of Eddy current damping compared to the case without such damping. However, the effect of magnets were too weak during the cooling cycle to show a significant improvement in the vibration level.

To increase the effect of Eddy current damping, we decided to change the material of the metal piece attached to the spring stage from aluminum to copper which changes the generated Eddy current and therefore, the viscous force. Also it should be noted that the total mass of the spring stage changes as the mass of the metal piece was changed from ~ 32 g for aluminum to ~ 105 g for copper.

Now, we measured the stability of the cavity during the operation of the cryocooler with magnets and the copper piece to generate Eddy current. Figure 5.15 shows the time and FFT plots. The peak-to-peak vibration amplitude is ≈ 8 nm and the rms fluctuations are 439 ± 45 pm. We achieve similar performance as the one obtained for the aluminum cross with

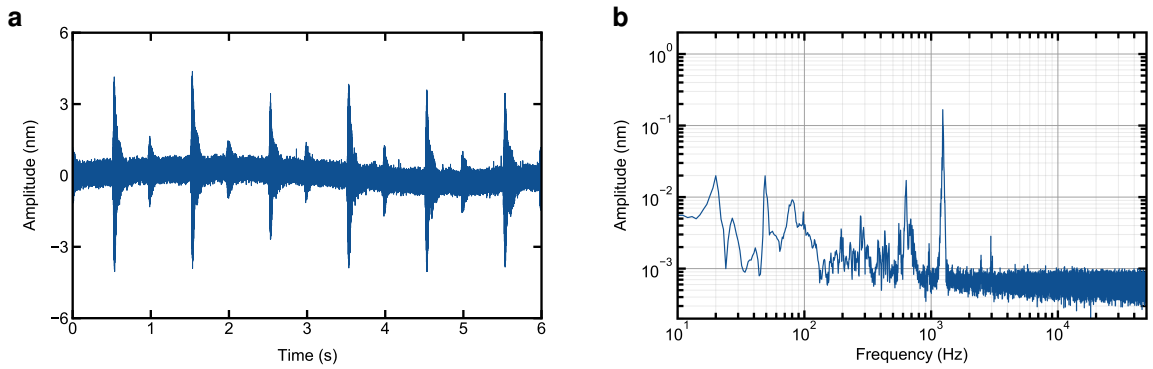

Figure 5.15.: Cavity stability measurement in presence of Eddy current damping after changing the metal used to generate Eddy currents from aluminum to copper. **a** Time plot shows peak-to-peak vibrations are about 6 nm with a characteristic shape of the fluctuations due to the cryocooler cycle. **b** FFT plot shows the characteristic frequencies excited by the cryostat.

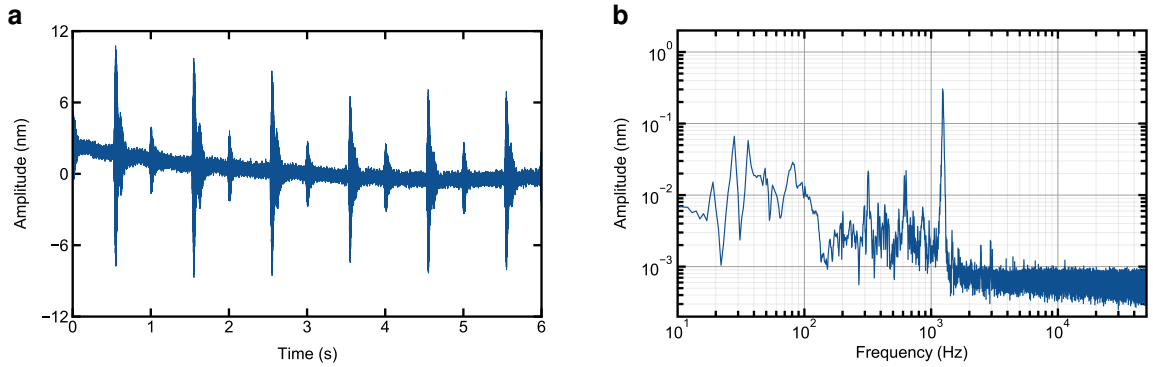

Figure 5.16.: Vibration measurement without Eddy current damping but with copper part still attached. This data set is without damping but differs in the mass of the spring stage to the previous measurement shown in figure 5.8. Peak-to-peak vibrations in **a** time plot and amplitude of various resonances in **b** FFT plot are higher compared to the one with Eddy current damping.

magnet as well as without magnet (shown in figure 5.8 and figure 5.11). For verification, we also perform the test with copper piece but without magnets, this should essentially be the same as the one with aluminum, only difference is the slight change in mass of the total spring stage that can lead to a different resonance frequency. The results of the measurement are shown in figure 5.16, the peak-to-peak vibration amplitude however is surprisingly high at ≈ 18 nm and the rms fluctuations are 1015 ± 112 pm

The comparison of performance with both metallic pieces with and without Eddy current is done in figure 5.17, FFT plot is only shown for the frequency range of 10 - 1000 Hz for

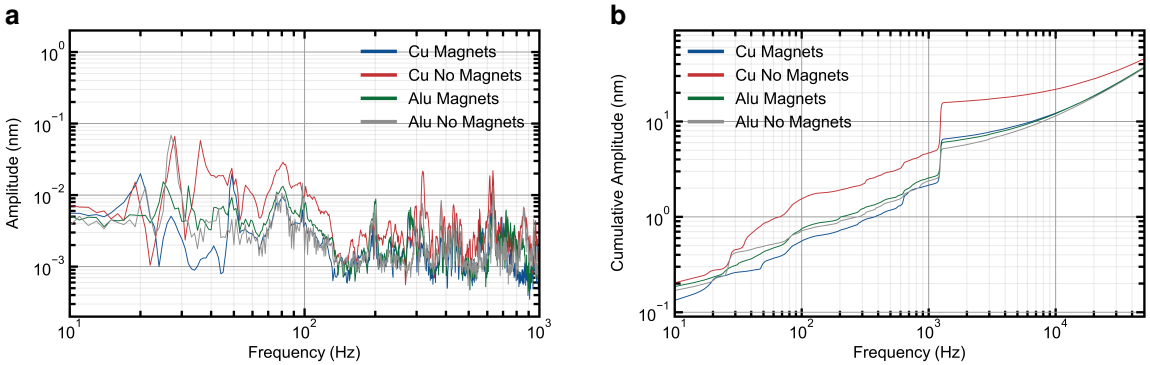

Figure 5.17.: Comparison of the cavity length fluctuations with and without magnets and different weights of the spring stage as **a** FFT plot and **b** cumulative amplitude as a function of bandwidth. Eddy current damping with copper shows the best performance, but data sets with and without Eddy current with aluminum piece shows a very similar cavity stability.

better comparison. The peak-to-peak amplitude and rms fluctuations are the same for all but the date set with copper piece without magnet. However, FFT and cumulative amplitude shows that the data with Eddy current damping by copper piece are slightly improved.

The out-liar performance is the result with copper piece and without magnet shown in figure 5.16. The reason for this set of measurement being so different from the one with aluminum piece (figure 5.8) is perplexing since we expected it to be same as there is no Eddy current damping. The possible reason for the higher vibration could be an external influence e.g. environmental disturbance, sub-optimal optical table floating or high impact by the cold head during cooling cycle due to some error. Another reason could be the problem with the spring isolation stage in mounting. However, we did not pursue further investigation to understand this anomaly, we continued with the further exploration of vibration reduction techniques.

In conclusion, the change in the vibration fluctuations during a cooling cycle due to the Eddy current damping are not significant. However, we demonstrated a reduction of Q-factor in impact test with both aluminum and copper metal piece in the presence of magnets. Therefore, introducing Eddy current damping based on pairs of magnets and electric conductor metal piece can be a useful tool when the contribution from the low frequency spring isolation stage with a high Q-factor is the dominant feature in vibrations during the operation of cryostat.

Reduction of differential motion with copper wool

Next, we consider methods to reduce the excess motion on top of the spring isolation stage. An important fact to consider here is that the goal in a stable Fabry-Pérot cavity is to reduce

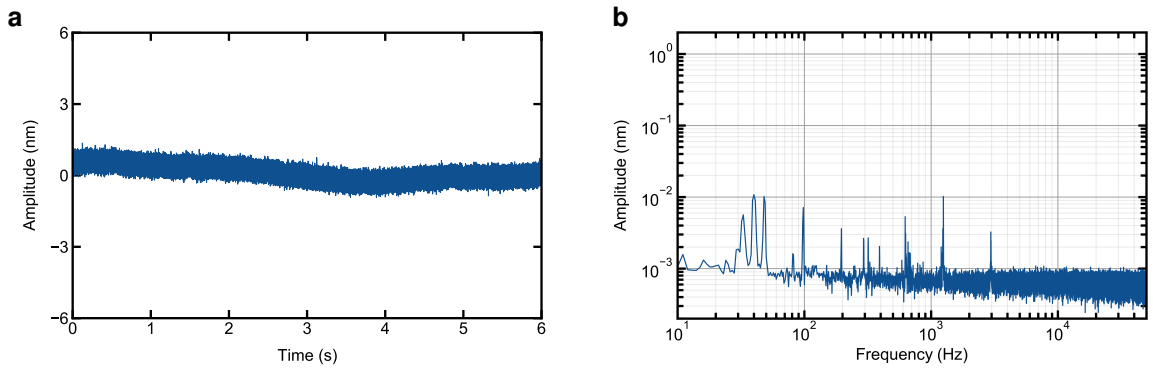

Figure 5.18.: Cavity length characterization in the 'quiet state' at room temperature showing **a** length as a function of time and **b** FFT of the length fluctuations. In the absence of cryocooler operation and other external disturbances, the cavity length shows an almost white-noise behavior in FFT.

the relative displacement of two mirrors with respect to each other. Thus, any excess mechanical vibrations on the spring isolation stage are an issue only if they cause differential motion between the mirror and fiber towers, and it does not need to be eliminated if they cause displacement with same phase and amplitude (we refer to it as common-mode motion). The same idea also applies for many scanning-probe techniques such as AFM, SNOM or STM where the relative motion between the tip and the sample has to be minimized.

One idea to reduce the differential motion between two positioner towers in cavity setup is to introduce some copper wool in contact with both towers. The copper wool is a fine-meshed copper wire bundle that can absorb kinetic energy of a moving object due to the high friction coefficient offered by the geometry of the wire bundle, hence they are used as a material for acoustic damper [300, 301].

Before trying this idea, the amplitude fluctuations of the cavity was measured again to serve as a benchmark for reduction using the copper wool. The following measurement are done with the copper metal piece mounted on the spring isolation stage but without magnets and Eddy current damping. Since the measurements shown are all performed at room temperature, we measure the cavity length fluctuations in the so-called 'quiet state' when the cryocooler is not in operation. This indicates the base vibration of the system without any external disturbance. Figure 5.18 shows the amplitude fluctuations in the 'quiet state', the peak-to-peak vibration amplitude is $\approx$ 1 nm and the rms fluctuations are 180 $\pm$ 20 pm. The power spectral density shows some resonance frequencies that are excited even in the 'quiet state'. Now the cryocooler is switched on, the results are shown in figure 5.19. The peak-to-peak vibration amplitude is $\approx$ 18 nm and the rms fluctuations are 988 $\pm$ 65 pm, similar to the measurement shown in figure 5.16. To analyze the effect of the cold head, the comparison of 'quiet state' with the effect of the cryocooler is shown in figure 5.20. We

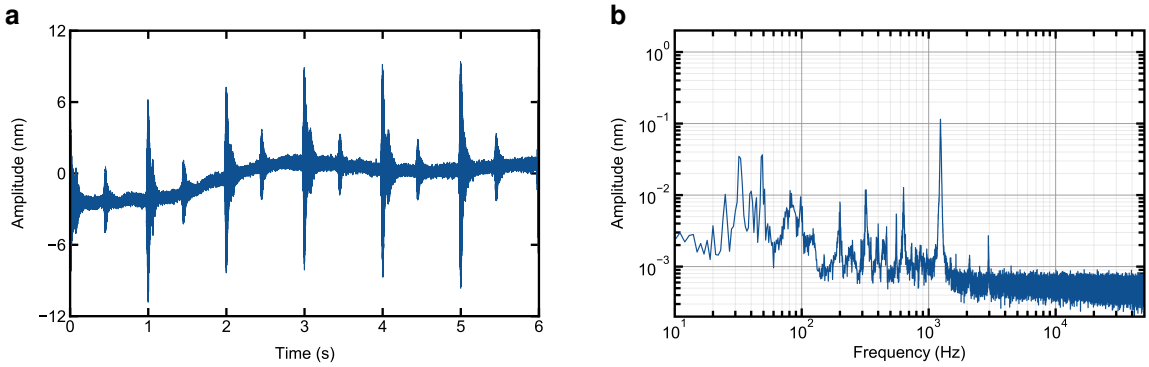

Figure 5.19.: Cavity stability during the cooling cycle at room temperature showing **a** cavity stability as a function of time and **b** FFT plot. Benchmark the cavity stability before introducing a differential motion reduction technique using copper wool.

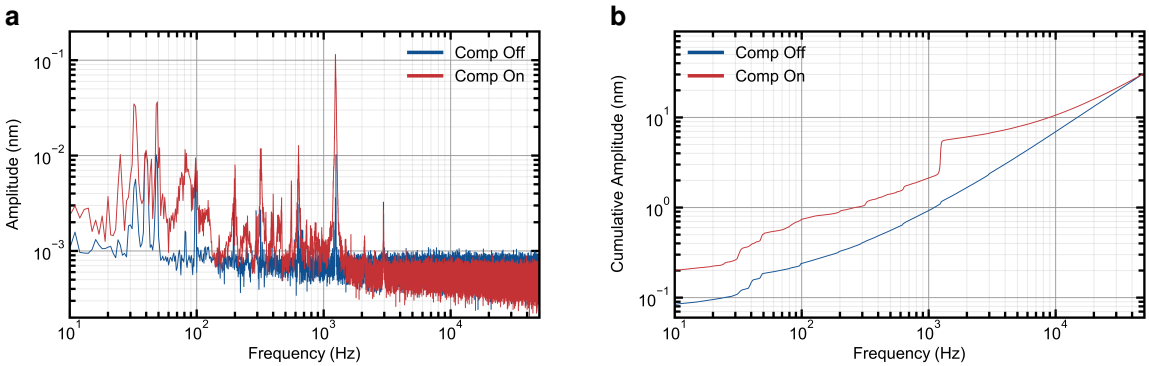

Figure 5.20.: Effect of the cryocooler on the cavity stability. **a** FFT shows that the amplitude of several peaks is enhanced due to the cryocooler while some new resonances are also excited by the operation, the most significant is the resonance at 1200 Hz. **b** Cumulative amplitude shows respective contribution of the eigenresonances.

observe several resonance frequencies of the system are further excited during the cooling cycle, the most prominent is the resonance at 1200 Hz. The impact test was also repeated to identify mechanical resonance and their damping efficiency, the results are displayed in figure 5.21. We see that the impact excites the resonances around 20 - 30 Hz, and they are damped within two seconds.

Now we introduce a small piece of copper wool mesh (fine copper wool from Copper Garden) between the mirror and the fiber stack to establish a mechanical link that intends to decrease the differential motion. The picture of the setup with the copper wool is shown in figure 5.22. The measurement of the vibration amplitude during the operation of cryocooler is displayed in figure 5.23. The peak-to-peak vibration amplitude is $\approx$ 10 nm and the rms

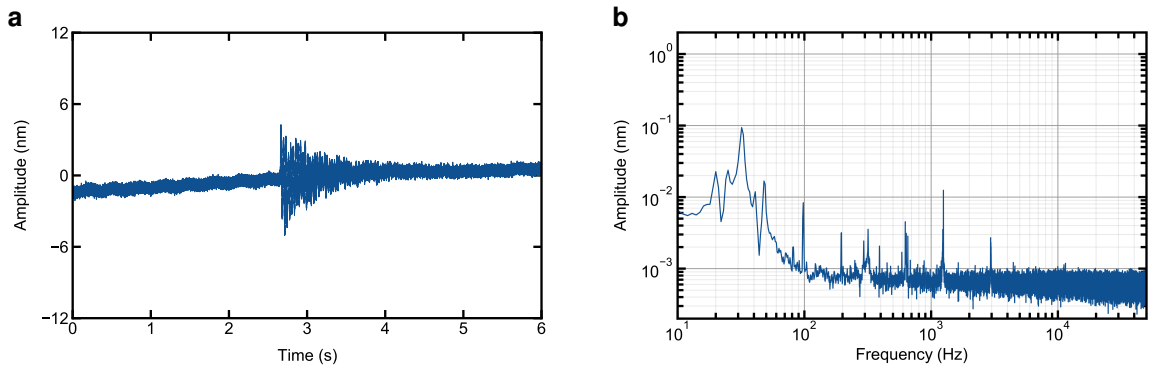

Figure 5.21.: Impact test benchmarking at room temperature, **a** cavity length as a function of time and **b** FFT of the length fluctuations. Excitation of spring isolation stage takes roughly two seconds to decay to the quiet level.

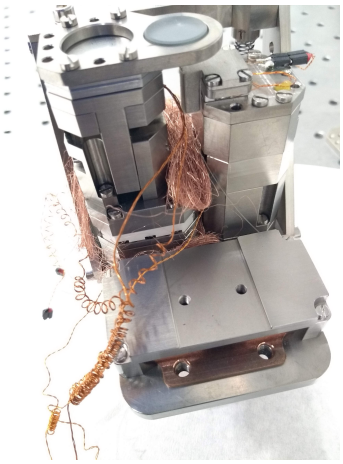

Figure 5.22.: Copper wool is added between the two stacks of the cavity setup to introduce a friction-based differential motion reduction.

fluctuations are 572 ± 36 pm. We see an improvement of a factor of two compared to the results without copper wool (figure 5.19). The comparison of the FFT and the cumulative amplitude is plotted in figure 5.24. While some low frequency peaks have broadened upon introduction of copper wool, the effect on the amplitudes of higher frequencies peaks and in the cumulative amplitude seem to be negligible or worse, which is opposite to the reduction of peak amplitude during the pulse shock as seen in the time plot.

We inferred that the introduction of the copper wool brings improvement of up to factor 2 in peak-to-peak and rms vibration during a cooling cycle. In this attempt, the wool was added to the setup in an indefinite way and due to the nature of the absorbance of mechanical energy based on the friction inside wool, it is a difficult task to completely understand or model the damping mechanism. We also performed the impact test in the presence of cop-

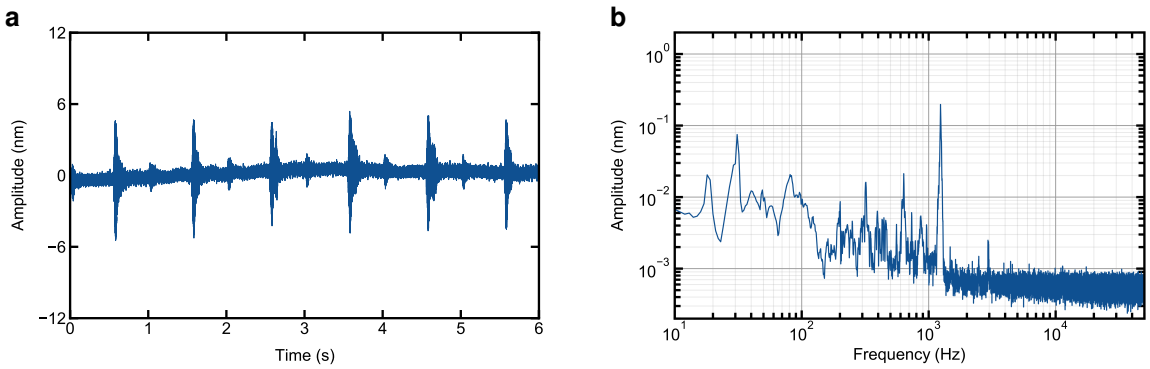

Figure 5.23.: Vibration characterization in presence of copper wool during the cryocooler operation. **a** Fluctuations over time and their **b** FFT plot. Peak-to-peak vibrations are reduced by factor of two compared to the benchmark measurement before the introduction of copper wool.

per wool, however the analysis was inconclusive in terms of understanding the frequency range or the mechanism of the vibration reduction by copper wool. Nevertheless, the idea to reduce differential motion is promising.

Reduction of differential motion with spring-loaded pin

To explore the idea of increasing stability by reducing differential motion, we developed a new approach to introduce a mechanical connection between mirror and fiber using a spring-loaded pin called pogo pin. It is known for the open cavity that the stability is highest when the fiber or mirror, with radius of curvature, makes physical contact with the other mirror of the cavity [302]. However, this method of increasing stability only allow operation at a specific cavity length or perhaps with a very limited tuning capability.

The task to introduce a rigid connection while allowing the cavity length tuning over a millimeter is challenging. We decided to use the pogo pin to fulfill this task. The pogo pin are spring-loaded pin, resembling the shape of a pogo-stick, that are used as the electrical connectors, especially in the electronic testing industry as they provide durable contact resistant to mechanical vibrations. In our case, we decided to employ them as a physical connector between two arms of the cavity right next to the mirrors. These pins are soft enough to allow tuning with positioner or a piezo but prevents unwanted drift between two cavity mirrors due to the spring inside the pogo pin. The mechanism of the pogo pin is discussed in section 3.3.2.

The hypothesis to introduce a spring-based physical link to improve the mechanical stability was tested. The pogo pin (N& H SVPC-F-N005M2) is glued to the mirror holder (UHU Plus Sofortfest glue) such that the tip gets in contact with the fiber holder when the

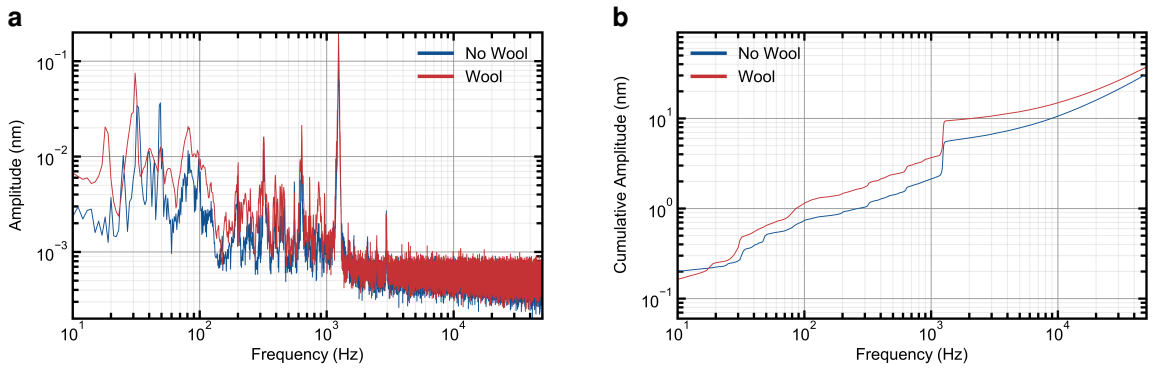

Figure 5.24.: **a** Frequency analysis of the effect of the copper wool during the cooling cycle on the cavity fluctuations. It shows broadening of the resonance peaks, especially at low frequencies. **b** Cumulative amplitude show no improvement due to copper wool, unlike the reduction observed in the peak-to-peak vibration level in length fluctuations over time.

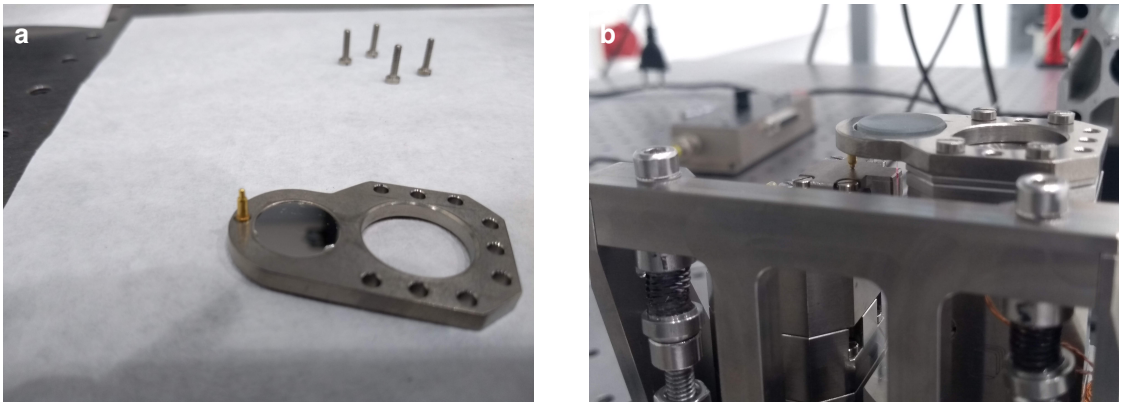

Figure 5.25.: Pogo pin as a differential motion reduction technique between mirror holder and fiber holder in the cavity setup. **a** Pogo pin glued to the cavity mirror holder and **b** the mirror holder installed in the setup.

cavity length is reduced below a certain length. The picture of the setup with the pogo pin is shown in figure 5.25.

The fluctuations during the operation of cryocooler are measured while there is a close mechanical connection between the two cavity mirrors via the pogo pin is shown in figure 5.26. The peak-to-peak vibration amplitude is ≈ 2 nm and the rms fluctuations are 206 ± 36 pm. The cavity length fluctuations are improved greatly compared to the results obtained without the pogo pin (figure 5.19), the peak-to-peak vibrations are improved by factor of 9 while the rms fluctuations are improved by factor of 5. This set of results indicates that we have achieved the most stable cavity length so far.

At this point, we also measure the fluctuations in the 'quiet' state without a running

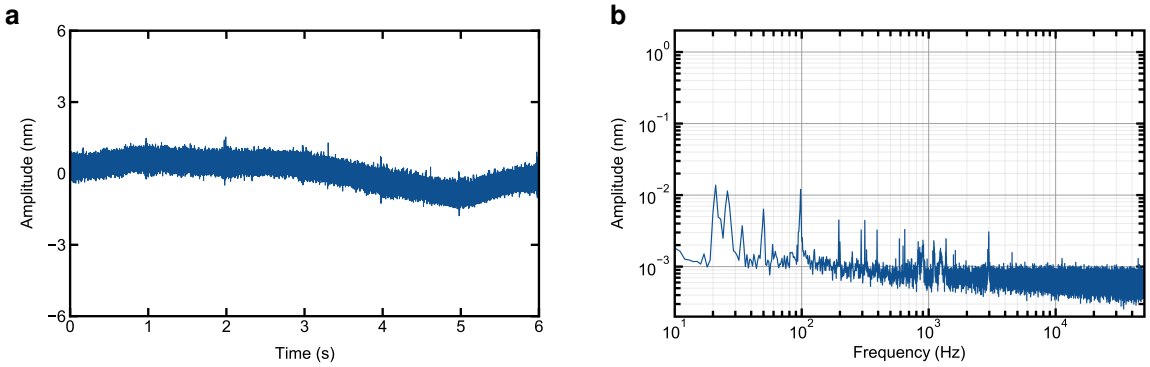

Figure 5.26.: Characterization of the cavity stability after implementing the common mode link between cavity mirrors via the pogo pin. **a** Fluctuations over time and their **b** FFT plot. Peak-to-peak vibration levels are down to 1 nm.

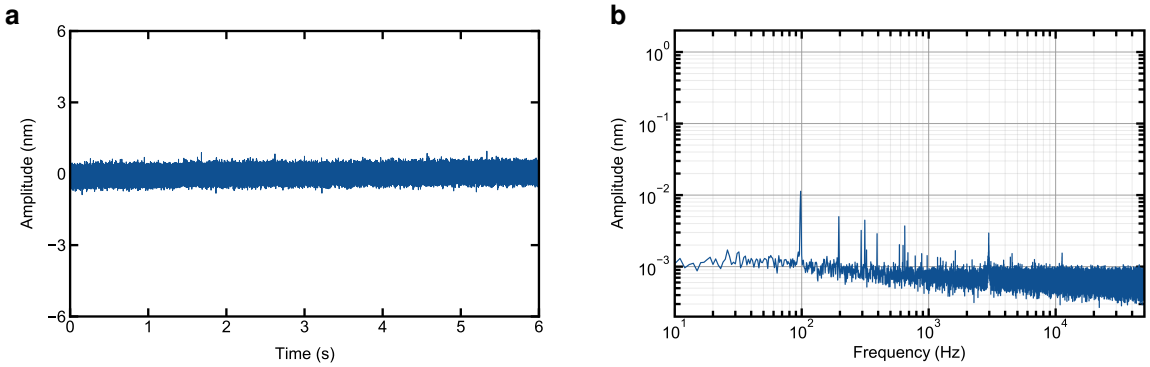

Figure 5.27.: Cavity length fluctuations with the pogo pin in the quiet state without external disturbances. **a** Time plot is very similar to the measurement with the cryocooler operation except small peaks visible due to pulse shocks. **b** FFT plot also shows a flat spectrum except a resonance at 100 Hz and harmonics. This indicates that the length fluctuations measured here are limited by the laser or detector noise.

cryocooler or any external impact. Figure 5.27 shows the time plot and the Fourier transform. The peak-to-peak vibration amplitude is $\approx$ 1 nm and the rms fluctuations are 165 $\pm$ 1 pm. The FFT suggests that, apart from the few sharp peaks (such as 98 Hz and its higher harmonics), the rest of the spectrum is a white noise spectrum with a base level of $approx$ 1 pm. Therefore, the fluctuation in the 'quiet' state is attributed to the base laser noise plus detector noise of our measurement setup. This was verified by measuring the same noise level (not shown) at the cavity minimum instead of the slope to not account for any phase fluctuations i.e. mechanical displacement fluctuations.

We also note that the pulse shocks during the cooling cycle is visible in figure 5.26 but

quickly damps below the noise level of the setup. Therefore, the vibration results shown during the operation of the cryocooler are already limited by the setup noise during the majority of the cooling cycle. In the next section, we analyze the setup noise by changing the laser and the detector.

Laser noise comparison

After the improvements in the vibration reduction design of the cavity setup, we demonstrated that the setup noise is a limiting factor for the measurement of the cavity fluctuations. The requirement for a sensitive interferometry for the vibration measurements includes a laser with low amplitude and frequency noise as well as low noise photodetector. The laser and detector combination used so far was the laser inspection module (LDM 600) which is not designed for the purpose of a high resolution vibration measurement. Here, we try two other lasers to check whether their noise performance exceeds the performance of the LDM 600.

First, we change to another laser detection module (attocube LDM 1300) with wavelength λ = 1310 nm. This module, at an infrared wavelength, is primarily used for interferometric AFM readout. So it suggested to offer a better resolution. After changing the laser inspection module and also the fiber with an appropriate wavelength as the cavity micromirror, the cavity length fluctuations are measured. Figure 5.28 shows the cavity length fluctuations in the 'quiet' state, the cryocooler is not turned on because we want to compare the base setup noise. The peak-to-peak vibration amplitude is $\approx$ 1.5 nm and the rms fluctuations are 292 $\pm$ 8 pm. This is worse than the results using the LDM 600 by about 50 %.

Second laser we tried was distributed feedback (DFB) laser (ThorLabs WDM Source) also in the infrared range. The laser wavelength was λ = 1549.32 nm and it requires a frequency modulation to stabilize laser frequency. The detector used was a commercial photodetector with in-built pre-amplifier (Femto Si Photodetector). The results are shown in figure 5.29. The 'quite state' fluctuations are quite high due to the frequency modulation of the laser. The peak-to-peak vibration amplitude is $\approx$ 12 nm and the rms fluctuations are 2126 $\pm$ 89 pm, clearly suggesting that the noise of DFB laser is far worse than the laser inspection module.

The comparison of the two lasers with the LDM 600 is done in figure 5.30. The lowest level is clearly offered by the LDM 600 but it has some sharp peaks that might origin from the detector electronics inside the module. While LDM 1300 has less sharp peaks, the base level is slightly higher. On the other hand, the DFB laser showed not only sharp features due to frequency modulation but also has higher base white noise. This behavior didn't match previous laser noise measurement [303, 304] performed with the same laser, this might be due to a defect in the device during this measurement. We note here that another device of the same LDM 600 model was also tested. It showed the variation of noise level in the range of 1 - 5 pm depending on the device and laser power. Therefore, LDM 600 is the lowest noise

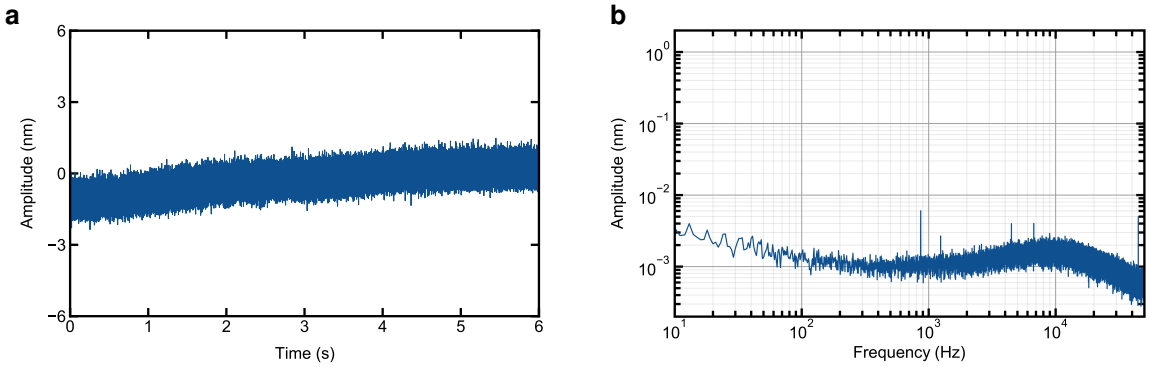

Figure 5.28.: Stability measurements after changing the laser and detector module to LDM 1300. **a** Fluctuations over time and their **b** FFT plot. Base vibration level of 2 nm suggests that the noise level is higher than the one in LDM 600.

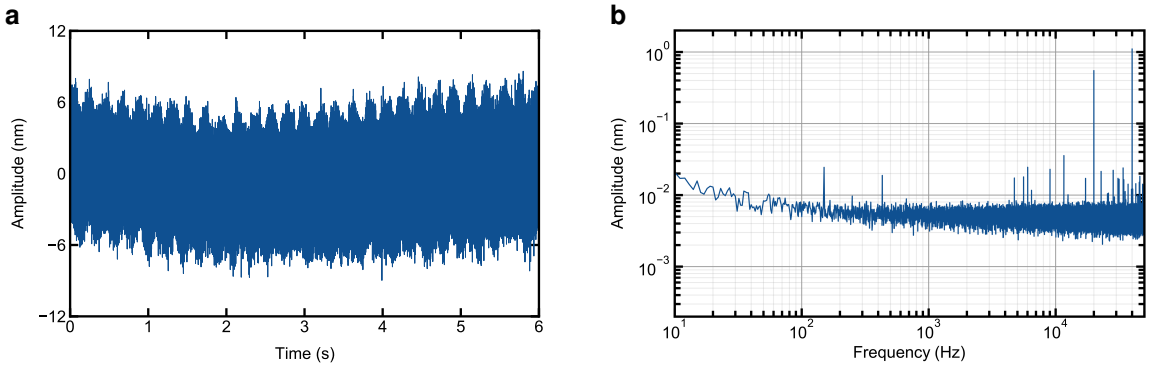

Figure 5.29.: Stability measurements with the DFB laser and external photodetector. **a** Fluctuations over time and their **b** FFT plot. Due to the modulation of laser diode at 40 kHz, the peak-to-peak shows a huge amplitude modulated noise.

laser and detector module among all of the above. However, we will switch to a M Squared Titanium:Sapphire laser and separate photodetectors in the phase two to reduce the noise.

The implementation of vibration reduction techniques so far have been done at room temperature with the assumption that the results are same upon going from the room temperature to the low temperature measurements. The measurement at room temperature doesn't require time-consuming cycles of cool down and warm up every time. This provides the motivation to perform the measurement at room temperature to receive fast feedback enabling changes in the setup design. However, the mechanical properties of materials changes at low temperature, most notably the mechanical resonance of a component shows higher amplitude and an increase in Q-factor. Next, we investigate the cavity performance at low temperature.

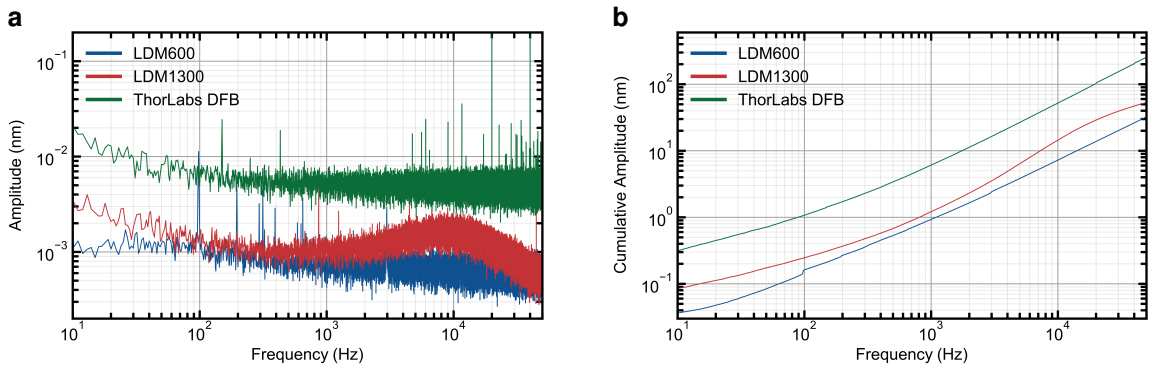

Figure 5.30.: Comparison of laser and detector noise in laser detection modules LDM 600 and LDM 1300, and DFB laser in terms of **a** FFT plot and **b** cumulative noise as a function of bandwidth. LDM 600 has the lowest base noise level, however, it has some sharp peaks that might originate from electronic noise in the module.

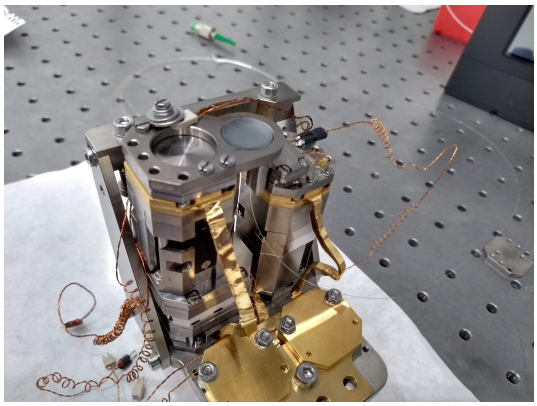

Figure 5.31.: Thermal links (golden color) between the cold plate and the cavity mirrors, via spring isolation stage, are introduced to ensure efficient cool down to cryogenic temperature.

Low Temperature Measurements

As we have discussed, the cavity setup is designed for a closed-cycle cryostat. The cooling to low temperature in attoDRY800 is done via contact cooling, so the cavity components need an efficient thermal connection to the cold plate. We have designed thermal links that serves as such an efficient channel, it also ensures minimal transmission of mechanical motion as the cavity has to remain mechanically isolated from the cold plate with the spring isolation stage.

We examine the effect of adding thermal link components to the cavity setup. The picture of cavity setup after the introduction of thermal links is shown in figure 5.31.

The measurements are done in reflection with laser module LDM 600. The other parameters are same as previous measurements, we have a pogo pin as a differential motion

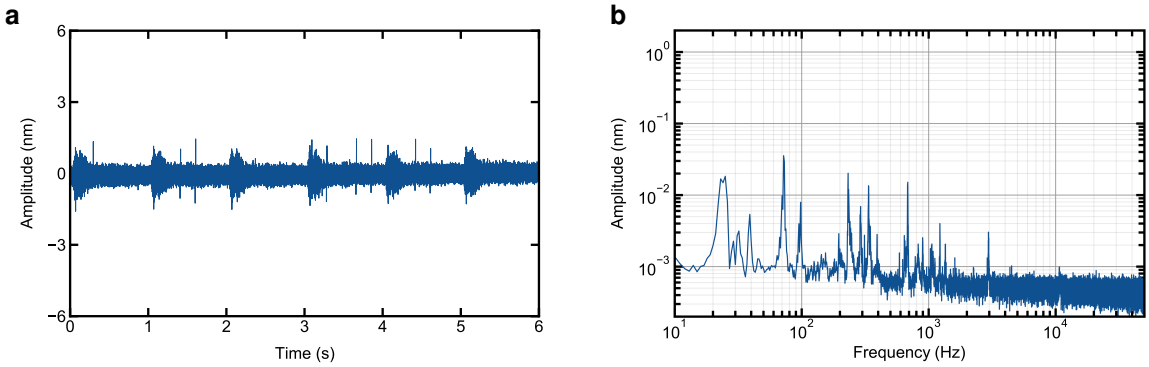

Figure 5.32.: Stability measurements after the introduction of thermal links at room temperature. Fluctuations as a function of **a** time and **b** frequency. Peak-to-peak vibrations of 1.5 nm indicates that thermal link does not introduce an additional channel parallel to the spring isolation stage for the mechanical vibrations.

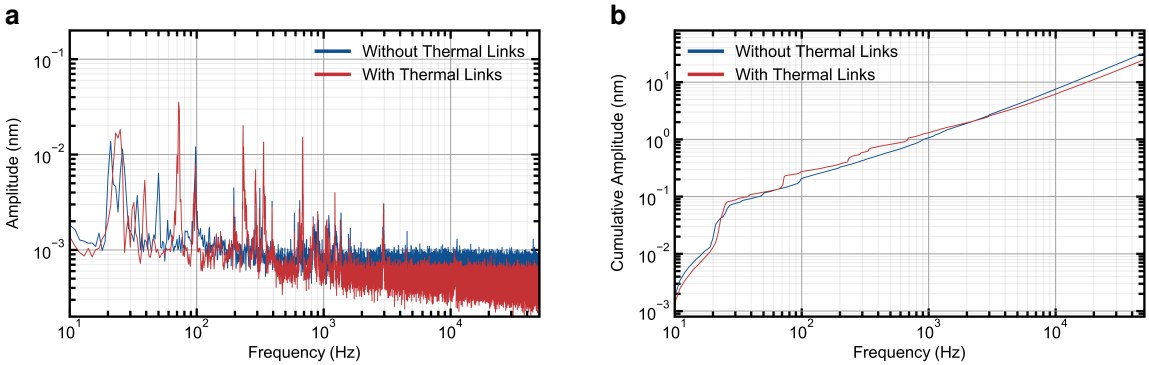

Figure 5.33.: Effect of thermal link components on the cavity fluctuations. **a** FFT shows some resonance peaks appearing or shifting upon introducing the thermal links. However, **b** cumulative amplitude shows no additional vibrations, similar to the time plot values.

reduction tool and there is no Eddy current damping. Figure 5.32 shows the cavity length fluctuations at room temperature after the addition of the thermal links during the operation of the cryocooler. The peak-to-peak vibration amplitude is ≈ 1.5 nm and the rms fluctuations are 178 ± 3 pm, it has slightly higher peak-to-peak amplitude than the measurement without thermal link but same rms fluctuations (figure 5.26). The comparison of Fourier transform is done in figure 5.33. There are few additional peaks that appears with thermal link addition, such as 250 Hz and 700 Hz.

Now, we cool down the cavity setup in the cryostat. The temperature reached was $T = 4.5$ K at cold plate (it was not measured at the cavity mirror during this measurement). Figure 5.34 shows the vibration measurements of the cavity length were performed at low temperature.

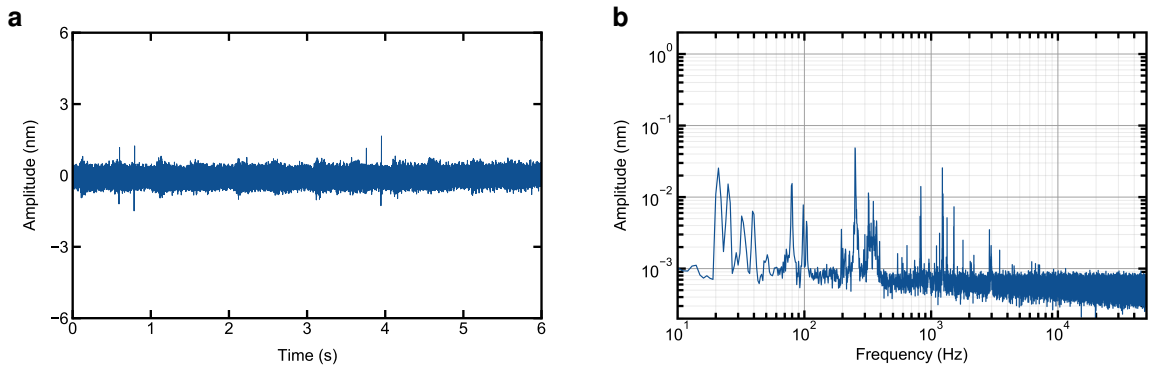

Figure 5.34.: Cavity stability characterization at low temperature as a function of **a** time and **b** frequency. First measurements at low temperature indicates no significant change in vibrations upon cool down.

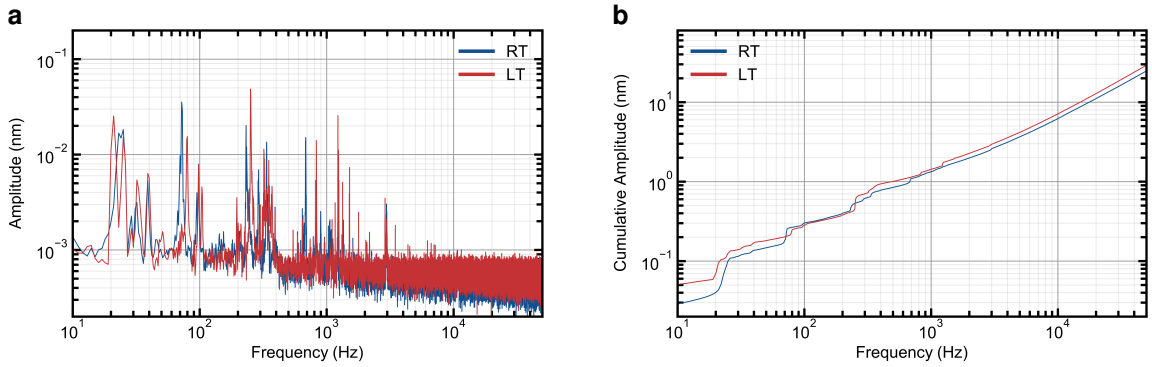

Figure 5.35.: Comparison of vibration fluctuations at cryogenic vs room temperature. **a** FFT shows that several resonances shifts to higher frequencies and have narrower linewidth. **b** Cumulative amplitude shows that the effect of the changes is minimal, as verified by the comparison of peak-to-peak and rms fluctuations.

The peak-to-peak vibration amplitude is ≈ 1.5 nm and the rms fluctuations are 181 ± 3 pm, both quantitatively similar to the results at room temperature. It demonstrates that despite the change in mechanical properties, our design leads to no significant addition in mechanical vibration at cryogenic temperature. The detailed comparison of FFT (figure 5.35) shows that several resonances have shifted to higher frequencies and became narrower, such as the peaks at 230 Hz -> 260 Hz and 700 Hz -> 800 Hz. The spring isolation stage resonance remains similar in frequency and amplitude. The cumulative amplitude comparison shows the relative contribution of different resonance and the overall increase in vibration amplitude at low temperature.

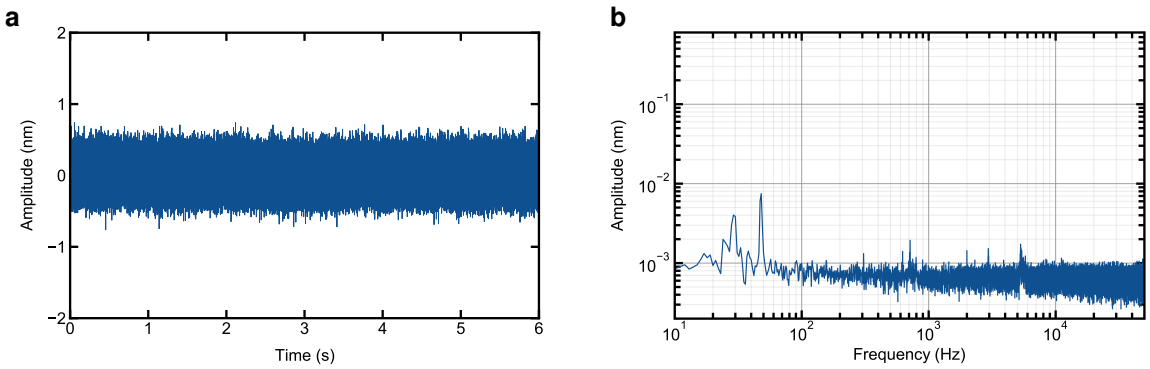

Figure 5.36.: Characterization of cavity stability in 'quiet' state after the move of cavity setup to LMU as a function of **a** time and **b** frequency. Peak-to-peak and rms values suggests that length fluctuation values are limited by the system noise and there is no additional external disturbances.

Robustness of the Setup

After the characterization of the cavity stability at low temperature, the open cavity setup was moved to the new attoDRY800 at a university lab in LMU. This move of the prototype setup provided two key benefits.

First, it helped check the validity of the design principle behind the setup. The idea behind a modular tunable cavity using standard nanopositioners is the ease of assembly, usability and robust low vibration performance. Thus, moving the setup to another cryostat in another building is a perfect validation exercise. Second, the lab at LMU provided an access to the low noise laser and detectors. This will be utilized in the phase two characterization measurements with a better length fluctuation resolution, as well as, when the cavity will be combined with TMD monolayer to study light-matter interaction discussed in section 5.4.

However, we first characterized the robustness of the cavity stability in reflection measurement. Figure 5.36 shows the result at room temperature in 'quiet' state without the operation of cryocooler. The peak-to-peak vibration amplitude is ≈ 1 nm and the rms fluctuations are 162 ± 1 pm. The fluctuations during the operation of cryocooler are shown in figure 5.37. The peak-to-peak vibration amplitude is ≈ 1.5 nm and the rms fluctuations are 172 ± 1 pm. The results at room temperature are similar to the previous measurement (figure 5.26) so the system is cooled down to the cryogenic temperature.

The stability of the cavity length at low temperature is displayed in figure 5.38. The peak-to-peak vibration amplitude is ≈ 1 nm and the rms fluctuations are 145 ± 11 pm. It is hard to clearly distinguish pulse shocks at low temperature. We see that the stability achieved here is similar to the stability at room temperature during (and even without) the operation of cryocooler. Figure 5.39 shows the comparison of the FFT and the cumulative amplitude that

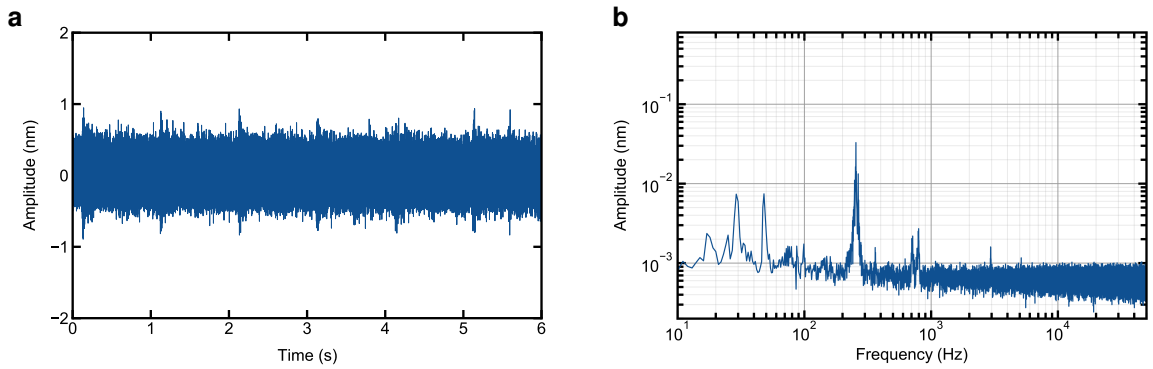

Figure 5.37.: Cavity length stability at room temperature during the operation of cryocooler as a function of **a** time and **b** frequency. This measurement verifies that the effect of the cryocooler on cavity length stability is same as measured previously, indicating the robustness of the cavity setup and vibration levels across different cryostats.

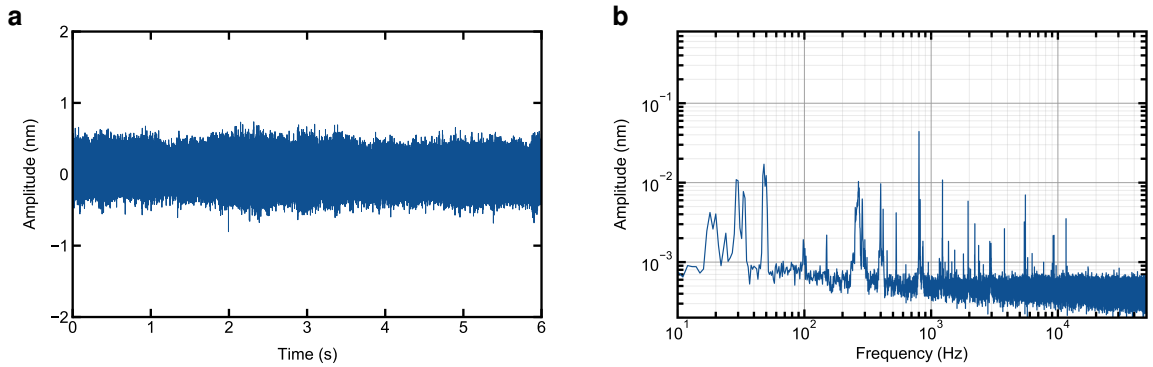

Figure 5.38.: Cavity length fluctuations at low temperature, as a function of **a** time and **b** frequency, demonstrating the robustness and reproducibility of cavity stability. FFT plot gives insight on the resonance peaks that appears in the new location, for example the resonance at 50 Hz.

confirm that the results obtained at both temperatures are comparable.

This results demonstrates the most stable cavity achieved so far with the peak-to-peak fluctuations of 1 nm and rms fluctuations of 145 ± 11 pm. Moreover, the cavity length fluctuations are limited by the setup noise as discussed earlier.

In conclusion of the phase one, we explored and implemented several passive vibration reduction techniques at room temperature to improve the mechanical stability of open cavity. Particularly, we have implemented vibration isolation stage using springs which hosts the tunable cavity components. This can be complemented with additional magnets and metal piece to generate Eddy currents based damping to reduce the Q-factor of the

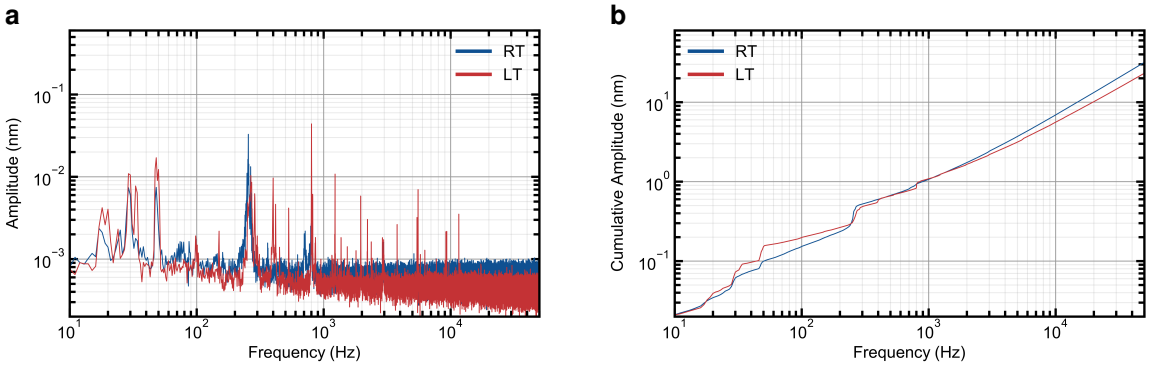

Figure 5.39.: Comparison of measurements at different temperature. **a** FFT and **b** cumulative amplitude suggests no major changes in the stability at cryogenic temperature.

spring isolation stage. We also explored two mechanisms to decrease the differential motion between two cavity mirrors, using either the copper wool or the pogo pin. The vibration reduction achieved by spring isolation stage and pogo pin was subsequently verified at the low temperature. Their robustness is shown with measurements of the cavity across different locations. We also showed that this results are limited by the setup noise. In the next set of measurements, we implement a transmission measurement technique with high finesse cavity. Furthermore, we will implement the active vibration cancellation.

5.3.3. High finesse and active vibration feedback

The implementation of several passive vibration reduction technique has led to the stability of cavity length that is limited by the setup noise rather than the inherent mechanical fluctuations. In this phase, first we will implement transmission-based detection setup (see methods for experimental details) to measure the length fluctuations. Another degree of control that has not been employed yet is active feedback to one of the cavity mirror to reduce vibration. We will employ an analog feedback servo loop and study the system properties for active cancellation.

Implementation of high finesse cavity

As a first step with the measurement setup for transmission through macroscopic cavity mirror is to replicate the cavity stability results done via reflection signal measurement. An optical objective is introduced with an additional nanopositioner (ANPx311 HL) to collimate the light coming from the cavity. Figure 5.40 shows the complete setup with the objective above the cavity mirrors.

At this stage, the cleaved uncoated fiber is replaced with a laser-machined concave fiber

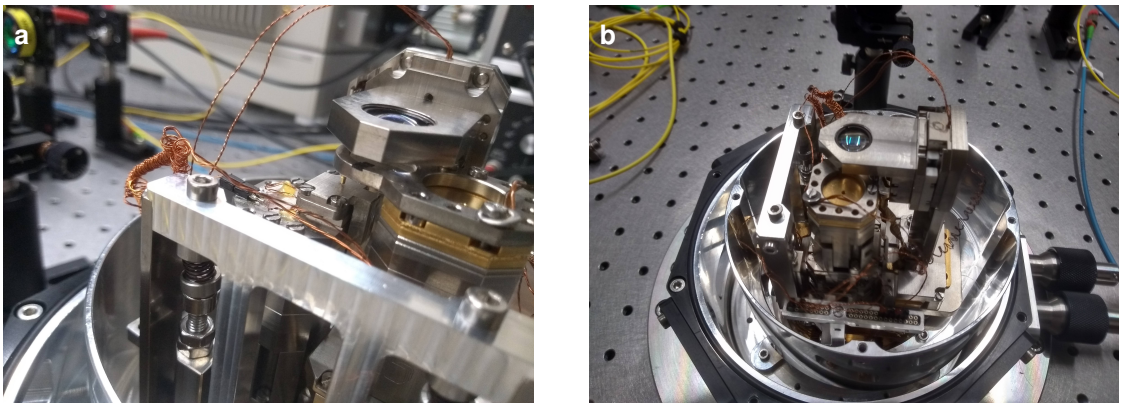

Figure 5.40.: Pictures of the final setup including spring isolation stage, two positioner stacks holding macroscopic mirror and fiber micromirror, thermal links and objective on top to efficiently out-couple the light. **a** Setup showing cavity mirrors, objective, pogo pin and piezo. **b** Top view of complete cavity setup on the cold plate.

with a Ag coating to increase the finesse to ≈ 30. We begin with measuring the cavity length fluctuations at low temperature, the time and Fourier transform are shown in 5.41. The peak-to-peak vibration amplitude is around 18 nm, much higher than the last reported measurement in reflection setup (figure 5.38). And due to higher finesse, the measurement dynamic range here is roughly 18 nm, therefore the fluctuations appears to be at the limit of dynamic range and clipped on both sides and are possibly higher than the one measured here. We subsequently warmed up the cavity setup and verified that the vibration fluctuations shows high amplitude also at room temperature so the issues were not specific to cryogenic temperature.

After a thorough investigation, we found few issues that were contributing to the higher vibration level. While none of the issue were fundamental design flaw or problem with experimental method, I list them here as a guide on avoiding common mistakes and for troubleshooting. The issues were: 1) Broken 40 K link of the cryostat, similar to the problem seen in chapter 3, solved by replacing with a new generation link. 2) Mechanical contact between positioner on spring isolation stage and support stage connected to cold plate that bypasses the vibration isolation for the cavity. 3) The contact between electric contacts and cold shield due to mistake in assembly leading to higher height of the spring isolation stage. The biggest contribution to vibration was due to the mechanical contact, thus it demands a careful assembly and control of all components in the setup including electric wires.

The cavity length fluctuations were measured after fixing all the issues. The room temperature results are shown in figure 5.42. The peak-to-peak vibration amplitude is ≈ 1 nm and the rms fluctuations are 86 ± 6 pm, the numbers are better than the previous phase measurement as it is no longer limited by the setup noise. Subsequently, the cavity setup is

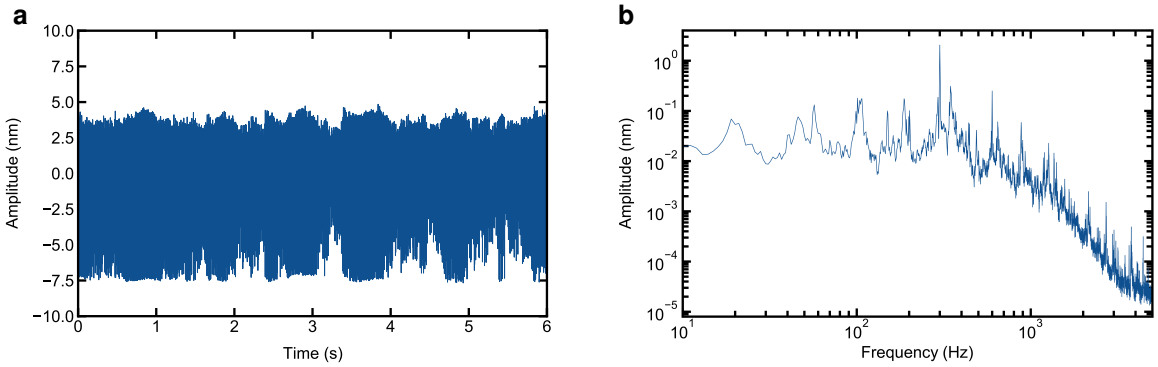

Figure 5.41.: Stability measurement results in transmission after changing the finesse and measurement setup. **a** Length fluctuations as a function of time suggests that the stability results are significantly worse than the previous measurement in reflection setup. It is also limited by the linewidth of the cavity. **b** FFT plot shows that the noise level at high frequencies reaches 10 fm range demonstrating that the laser and detector noise is significantly improved.

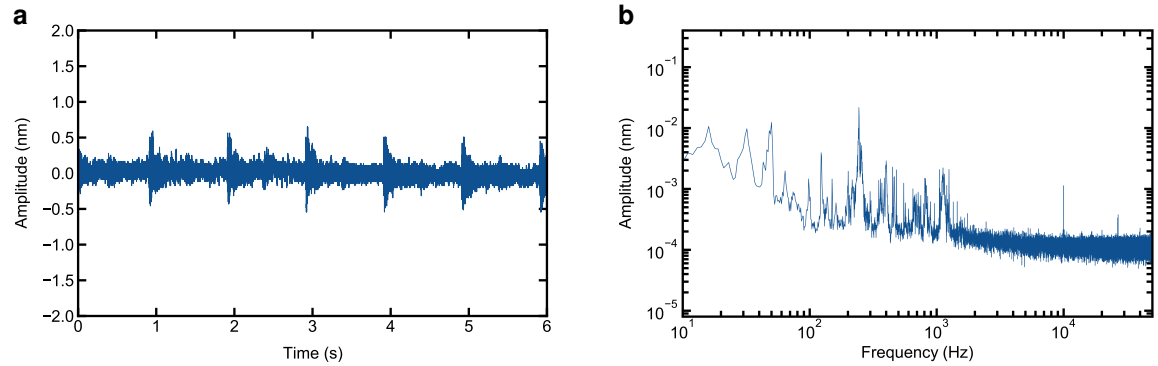

Figure 5.42.: Cavity stability results in transmission at room temperature, after troubleshooting the mechanical contact issues upon implementing high finesse cavity, as a function of **a** time and **b** frequency. Results shows an improvement over the results in reflection setup as the system noise is reduced.

cooled down. The temperature reached was $T \approx 4.5$ K at cold plate and $T \approx 7$ K on the cavity mirror. Figure 5.43 shows the stability characterization results. The peak-to-peak vibration amplitude is ≈ 2.5 nm and the rms fluctuations are 291 ± 25 pm. There are several mechanical resonance with contribution to mechanical fluctuations below 1 kHz, this can be potentially reduced by an active feedback scheme. This will be the focus of the next section.

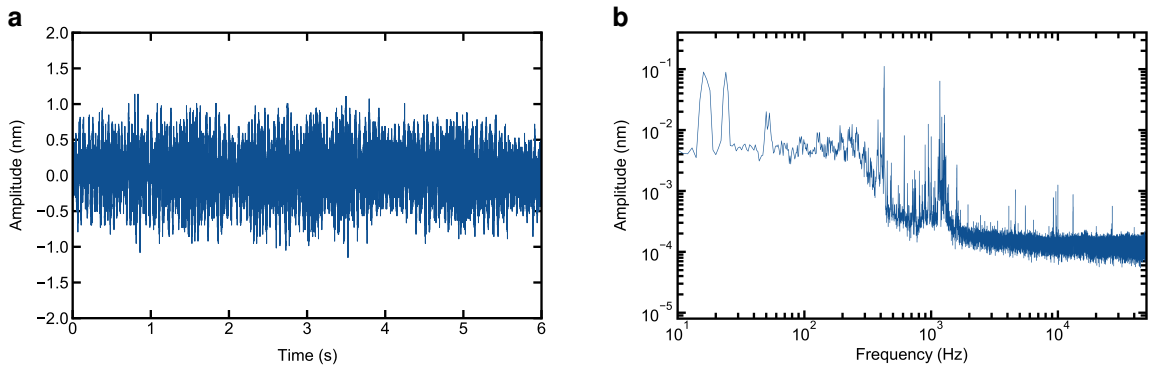

Figure 5.43.: Cavity stability results at low temperature, after troubleshooting the mechanical contact issues upon implementing high finesse cavity, as a function of **a** time and **b** frequency. Length fluctuations show higher vibrations at low temperature compared to the room temperature results.

Active vibration cancellation

The tunable cavity setup offers the advantage to stabilize the cavity resonance frequency i.e. cavity length in an active feedback loop where change in resonance frequency (referred as error signal) is measured and then a correction signal is applied to an actuator. There are several methods to obtain the error signal from the cavity such as on-slope of transmission signal or Pound-Drever-Hall technique [305, 306].

After the optimization of the cavity stability with passive methods, we implement an active feedback circuit with the piezo element below the fiber serving as an actuator. For the first implementation, we divide the transmission signal on the slope with a beam-splitter and use one photodetector to measure the cavity length fluctuations while the other photodetector is used as the error signal. The error signal is feed into a home-made analog servo box based on the design of reference [307].

The reason to place the piezo actuator just below the fiber is to have the maximum resonance frequency of the actuator that allows for the largest feedback bandwidth. However, there are several other mechanical resonance in the cavity setup that might have a phase difference between two cavity mirror that can limit the real bandwidth of the active feedback. Therefore, we use the method discussed in section 3.3.2 to determine the transfer function of the cavity length fluctuations. Figure 5.44a shows the system-detector transfer function. The gain magnitude (blue) shows the various mechanical resonance frequencies of the system with corresponding phase shift (red). The first few resonances are peaks around 20 Hz (vibration isolation stage), 49 Hz, 250 Hz, 450 Hz, 900 Hz and 1.2 kHz, which have been observed before in the cavity length fluctuation measurements. However, we see that most of these resonances are associated with a phase shift in the system. This is surprising

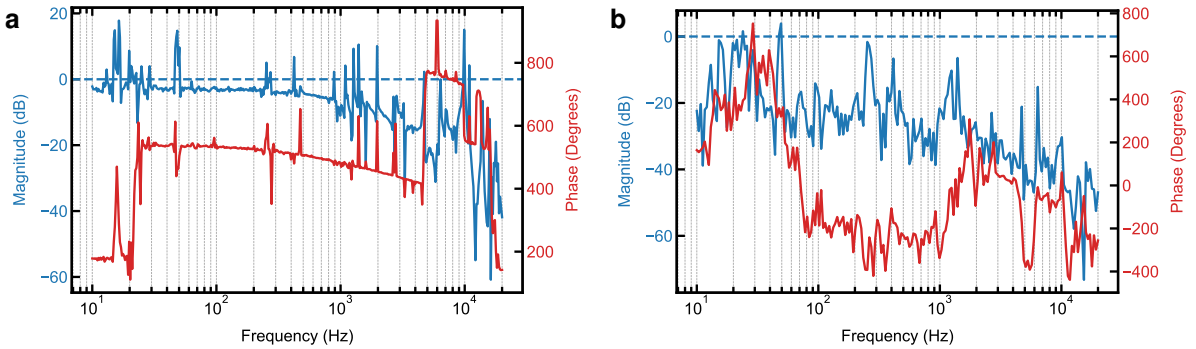

Figure 5.44.: Characterization of the cavity setup with active feedback. **a** System-detector transfer function with gain (blue) and phase (red). **b** Open-loop transfer function with cavity actively stabilized on the transmission slope. System-detection transfer function shows a phase change at the resonances of the spring isolation stage suggesting that the lock bandwidth will be limited.

particularly for the resonance peaks of the spring isolation stage as one would not expect the spring stage to induce a motion between two cavity mirrors which is out-of-phase. The resonance with a non-zero phase shift in the transfer function is difficult to be compensated with an active feedback scheme due to a complex phase response required as an input to the actuator.

We implement an active feedback scheme where part of the transmission signal is guided to a photodiode which is fed into an home-made servo that is used to determine the input signal for the piezo actuator. The servo equips a PI-based feedback with a low-pass filter and 2 notch-pass filters. Due to the simple phase response of servo plus filters, the bandwidth of the feedback was limited. The overall transfer function of controller-system-detector after the optimization is shown in figure 5.44b. We see that the feedback gain due to the active loop is positive only in few frequency gaps and a further increase in gain is not possible as system enters a 'self-oscillation' mode at some frequency which has an out-of-phase phase response.

The cavity length fluctuations in the presence of active feedback at low temperature are shown in figure 5.45. The peak-to-peak vibration amplitude is $\approx$ 1 nm and the rms fluctuations are 123 $\pm$ 9 pm. By looking at the FFT of the fluctuations, it is clear that most dominant contribution comes from the resonances due to vibration isolation stage. The comparison to the fluctuations without active feedback is done in figure 5.46. The effect of active feedback is clear for resonances below 50 Hz in both FFT and cumulative amplitude, thus the feedback bandwidth is certainly in the range of 50-100 Hz.

We should note here that this measurements are done without viscous damping through Eddy current that was explored in phase one. Since the most dominant contribution in the

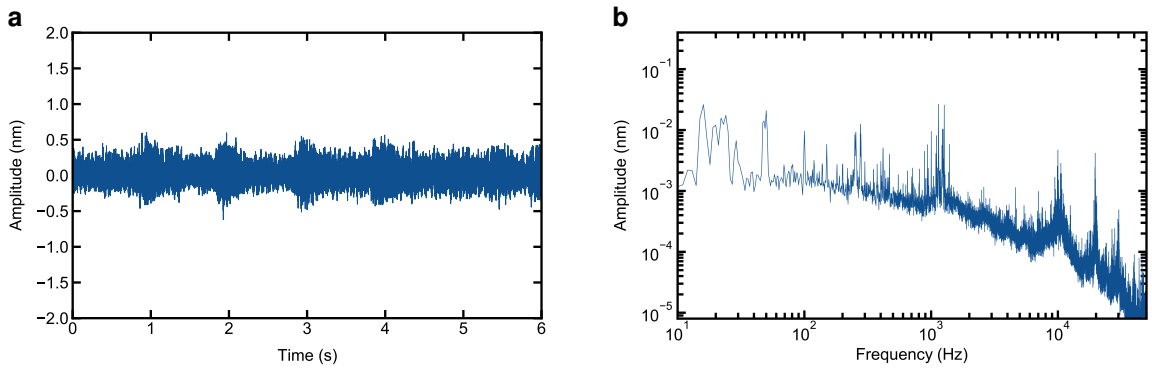

Figure 5.45.: Characterization of cavity stability with active locking at low temperature as a function of **a** time and **b** frequency. An improvement in cavity length fluctuations is seen by using the active lock. A dominant contribution to the vibrations is the resonances of spring isolation stage.

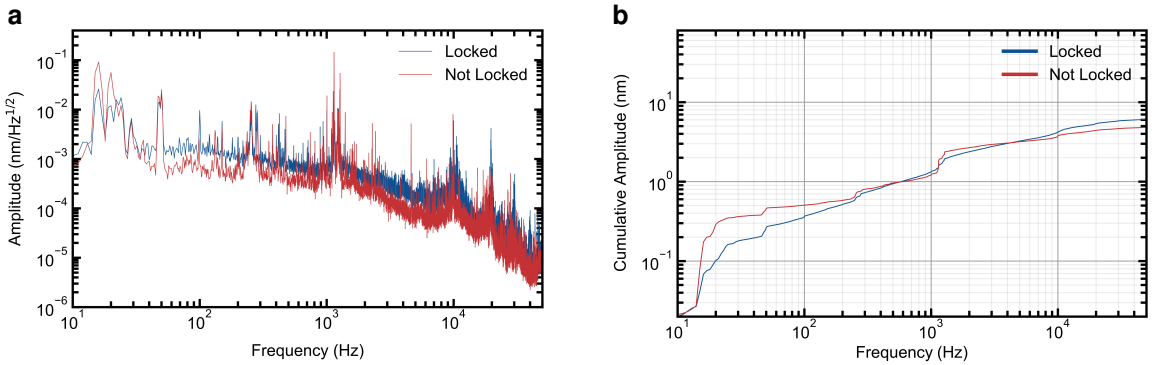

Figure 5.46.: Comparison of stability results due to active feedback. A clear reduction in the vibration level below 100 Hz is observable both in the **a** FFT plot and **b** cumulative amplitude as a function of frequency.

FFT is from the spring isolation stage, as a next step, magnets were reintroduced to the setup to decrease the Q-factor of eigenresonances of the spring stage. First, we check the fluctuations of cavity length at room temperature. The active feedback is optimized and active at this step. Figure 5.47 shows the time and FFT plots. The peak-to-peak vibration amplitude is ≈ 0.3 nm and the rms fluctuations are 31 ± 0.5 pm.

Subsequently, the cavity setup is cooled down and the fluctuations at low temperature are measured (figure 5.48). The peak-to-peak vibration amplitude is ≈ 0.7 nm and the rms fluctuations are 88 ± 4 pm. First, we compare the results at low temperature with room temperature result as shown in figure 5.49. All mechanical resonances, from 20 Hz to 1.2 kHz, demonstrates higher Q-factors and higher amplitudes as expected from the change of

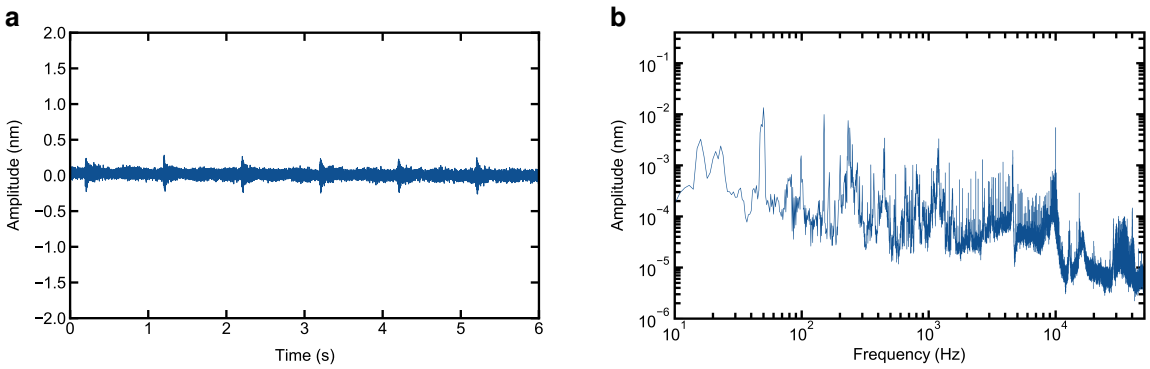

Figure 5.47.: Cavity length stability after introducing the Eddy current damping at room temperature and with active feedback as a function of **a** time and **b** frequency. Stability results shows an improvement due to the introduction of Eddy current damping. Peak-to-peak vibration of 0.3 nm and rms stability of 30 pm are observed.

mechanical properties of materials at cryogenic temperature. Subsequently, we compare the stability result after introducing viscous damping compared to the one before in figure 5.50. The intended effect of reducing the Q-factor of 20 Hz resonance due to vibration isolation stage is clearly observed.

Thus, we demonstrate an improvement by introducing viscous damping and obtain the highest stability so far in the cavity setup with active feedback using home-made servo. In the next part, I summarize the results of the mechanical stability characterization of tunable open cavity setup and present key results.

5.3.4. Progress results

The key challenge with a fully tunable open Fabry-Pérot cavity setup in a closed-cycle cryostat is the mechanical stability. In terms of the starting point, the displacement of the cold plate is brought down to few nm level as detailed in chapter 3. The displacement of the cold plate is less than 10 nm as shown in figure 5.51a. The mechanical vibration is exacerbated by the addition of nanopositioners that are necessary to provide the motion in spatial axes to tune the cavity. The displacement amplitude of a xyz-nanopositioner (2 x ANPx101, ANPz102) mounted on the cold plate are shown in figure 5.51b, it shows that the peak-to-peak displacement reaches maximum of around 30 nm at an interval of 1 s due to the vibration kick. Therefore, the addition of each degree-of-tunability leads to an increase in mechanical vibration and the requirement for the stability of open cavity is at odds with the tuning advantage of the cavity.

We explored various vibration isolation and reduction techniques to improve mechanical stability. In our final setup, we combine a spring-based passive vibration isolation stage

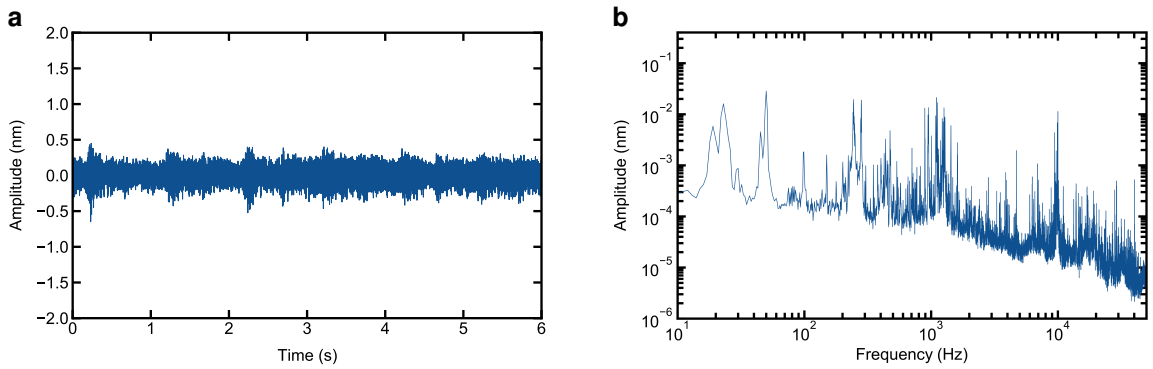

Figure 5.48.: Cavity stability measurements at low temperature with Eddy current damping and active feedback. **a** Time plot results shows the most stable cavity length so far with peak-to-peak vibration level of 0.7 nm and rms fluctuations of 89 pm. **b** FFT plot shows that the dominant frequency contribution peaks are 20 Hz (spring isolation stage), 250 Hz and 1 kHz.

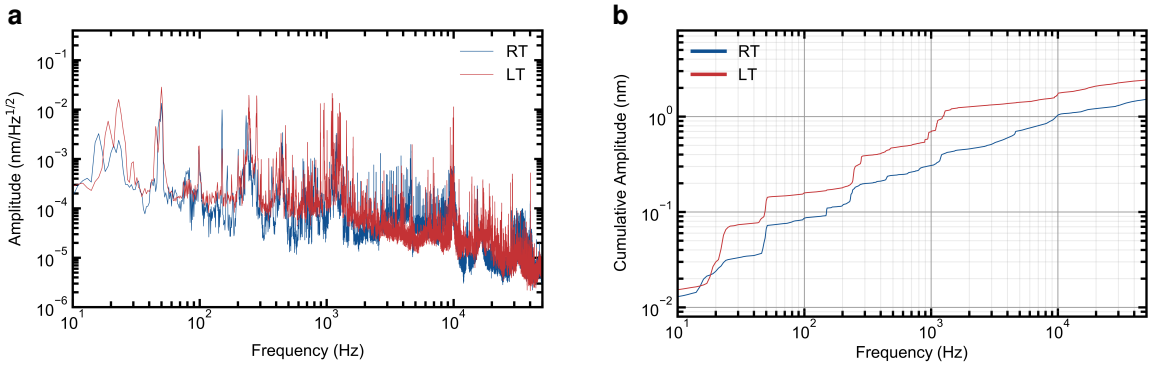

Figure 5.49.: Comparison between low temperature and room temperature cavity fluctuations with Eddy current damping and active feedback. **a** FFT shows the change of eigenresonances to higher amplitude, Q-factor and frequencies at cryogenic temperature. **b** shows the increase in cumulative amplitude for low temperature is clearly higher than for room temperature.

with viscous damping and an additional pogo pin as a common mode vibration reduction technique plus the active cancellation of fluctuations to improve the mechanical stability of the open cavity setup.

Figure 5.51c demonstrates the cavity length fluctuations as a function of time with measurement bandwidth of 100 kHz. The displacement due to vibration is improved by a huge margin and is invisible at the same scale compared to the positioner stack on the cold sample space without the damping stage (Fig. 5.51b). The inset on the right shows the data with

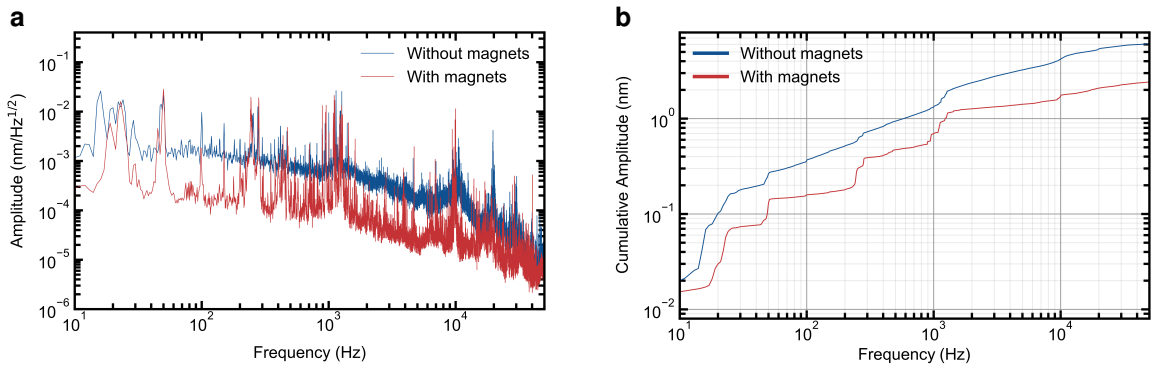

Figure 5.50.: Characterization of the effect of Eddy current damping. An improvement in the contribution of vibration from spring isolation stage at 20 Hz is visible in **a** FFT plot and **b** cumulative amplitude.

a 20x magnification, which shows the vibration kick at interval of 1 s albeit with a much smaller amplitude. The peak-to-peak amplitude is ≈ 0.3 nm and the root-mean-square (rms) length fluctuations is 31.6 ± 0.5 pm. The comparison of the vibration level of the tunable cavity platform to the cold plate and upon introducing tunability via nanopositioner is done in terms of rms fluctuations in figure 5.51d. The improvement due to the implementation of vibration isolation technique is 100x. In addition, the fourier transform of the displacement fluctuations to identify the source of remaining vibrations. Figure 5.51e) shows the fourier transform of the cavity fluctuations, the resonance peaks around 20 Hz are due to the vibration isolation stage while the resonance peaks starting from 250 Hz are due to the various components in the setup. There are also several sharp resonance peaks, these are the higher harmonics of 50 Hz. We note here that all the measurements shown in figure 5.51 are performed at room temperature by turning on the compressor to simulate the vibration kicks without complete cool-down to cryogenic temperature. This has been a useful tool for a quick characterization of the vibration performance throughout this work, especially during the development stage of the setup. However, it is necessary to characterize the actual performance at cryogenic temperature where mechanical properties of various components might change leading to different fluctuation level.

Therefore, the cavity setup is cooled down to cryogenic temperature (T = 6.5 K) to characterize the cavity operation at low temperature. The low temperature results are shown in figure 5.52. Here, we evaluate the effect of the active feedback scheme. Figure 5.52a shows the length fluctuations without active stabilization scheme. The peak-to-peak amplitude is ≈ 0.7 nm while rms fluctuations is 117 ± 7 pm. Upon turning on the active feedback, the length fluctuations shows a small improvement (Fig. 5.52b). The peak-to-peak amplitude is still ≈ 0.7 nm while the rms fluctuations is reduced to 89 ± 5 pm. The improvement is visualized by taking a projection of the fluctuations to number of occurrence of cavity length

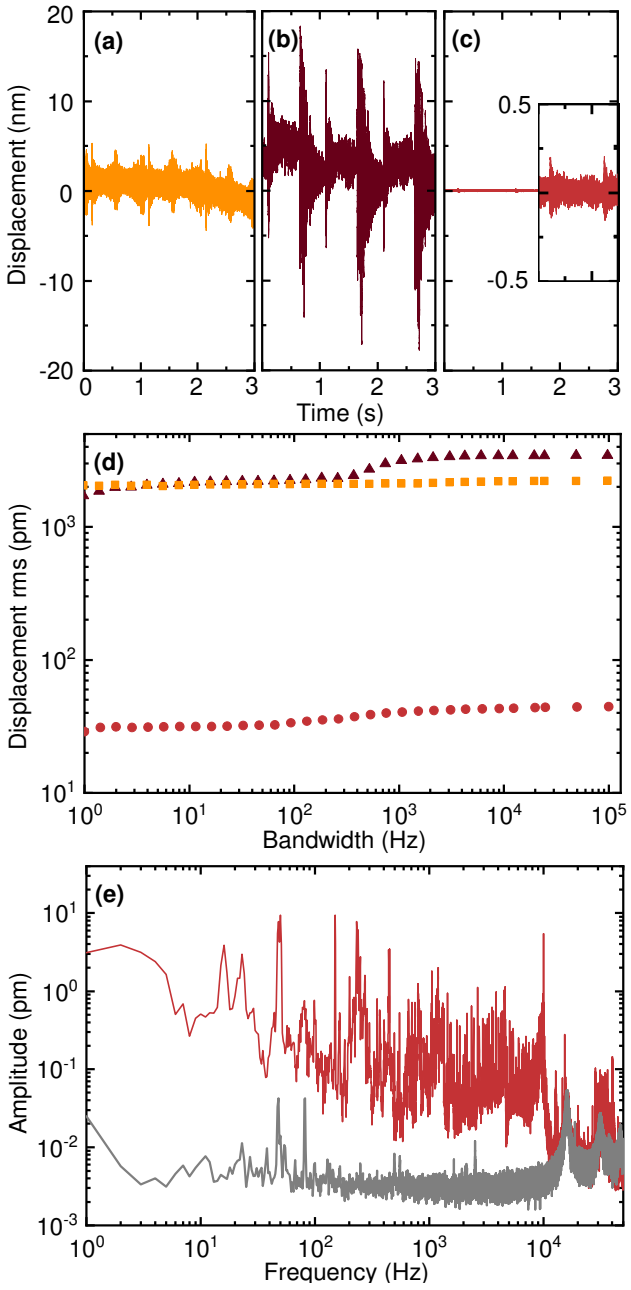

Figure 5.51.: **Mechanical vibration of a closed-cycle cryostat. a**, The displacement of the cold sample space of the cryostat. **b**, The displacement of a xyz-nanopositioner stack on the cold sample space. **c**, The cavity length fluctuations of the open cavity on the vibration damping stage on the cold sample space. **d** The rms displacement for cold sample space (square, **a**), nanopositioner stack (triangle, **b**) and open cavity (circle, **c**). **e** The Fourier transform of cavity length fluctuations (red) and noise floor (grey)

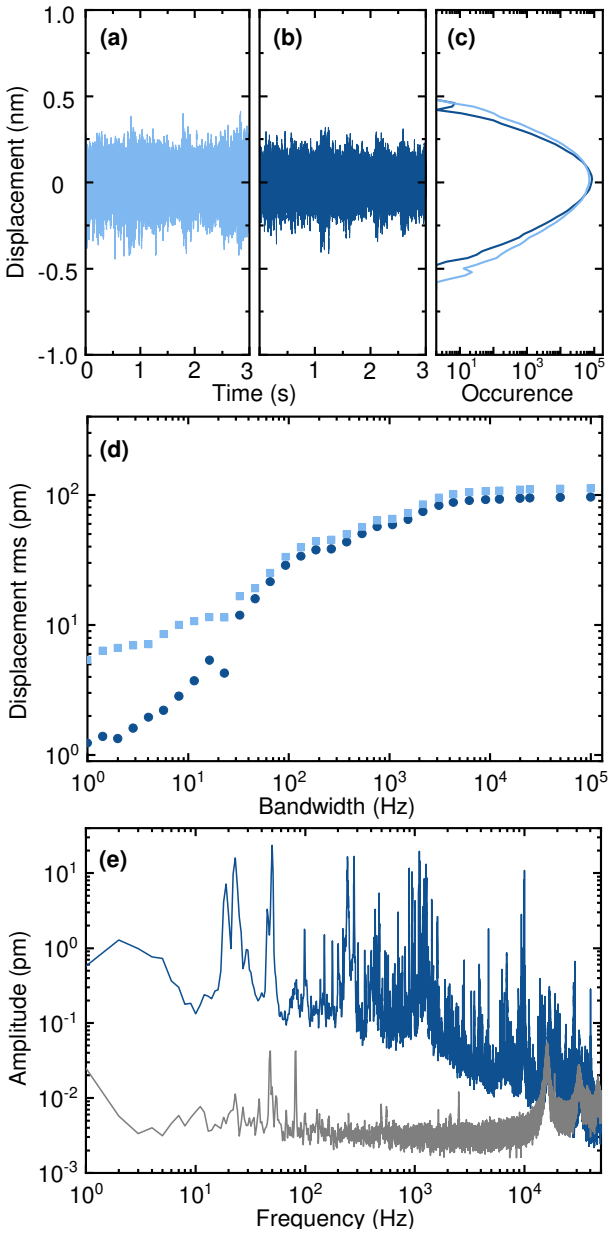

Figure 5.52.: **Cavity Characterization at cryogenic temperature.** The vibration displacement of the tunable cavity at T = 6.5 K **a** without lock and **b** with lock at bandwidth of 100 kHz. **c** The occurrence of cavity length values over 10 s, and **d** the rms displacement of cavity fluctuation as function of integration bandwidth for without lock (square) (**a**) and with lock (circle) (**b**). **e** The Fourier transform of cavity fluctuation with lock (blue) and noise floor (grey) with frequency resolution of 1 Hz.

as shown in figure 5.52c, we see that the tail of the peak shape is curtailed i.e. there is a reduction in occurrence of high amplitude away from the center.

The comparison of the rms fluctuations are done in figure 5.52d. We clearly see that the effect of active feedback loop is pronounced until ≈ 50 Hz so the bandwidth of the feedback achieved is rather limited. However, the analysis of rms fluctuations as a function of bandwidth shows that the mechanical stability of around 1 pm is possible with small measurement integration bandwidth. The FFT of the cavity fluctuations (figure 5.51b) are shown in figure 5.52e, where we can identify the regions that corresponds to the clear increase in rms fluctuations, such as region between 10-100 Hz where there is the resonance of vibration isolation stage. There are two prominent higher frequencies regions that can be assigned to mechanical resonance of the components: ~ 200-500 Hz and ~ 1-2 kHz which shows a clear increase in rms fluctuations plot.

In conclusion, we demonstrate the rms mechanical stability of 89 ± 5 pm at cryogenic temperature (T = 6.5 K) in a tunable open cavity setup. The finesse of few 10^2-10^3 can be realized with the setup depending on the required signal-to-noise ratio. The further improvement in the vibration isolation is possible, particularly it is possible to improve the active feedback gain and bandwidth with more sophisticated feedback technique.

5.4. Strong coupling with excitons in monolayer semiconductor

Monolayer transition-metal dichalcogenides (TMDs) exhibit strong oscillator strength making them an exciting candidate for cavity-QED experiments [308]. There have been wide range of experiments studying light-matter interaction between excitons in TMDs and photons in various optical resonators such as monolithic and open Fabry-Përot cavity, photonic crystal cavity and plasmonics [126–128, 132, 133, 136, 242, 308]. Here, we investigate monolayer WSe_2 in the tunable open cavity setup and demonstrate a controlled interaction in the strong-coupling regime with the observation of exciton-polaritons.

We investigate a device with a monolayer WSe_2 encapsulated in hexagonal boron nitride (hBN) which is exfoliated on a silver mirror. The monolayer was first characterized in an independent setup with confocal microscopy at cryogenic temperature. The monolayer WSe_2 is characterized by the neutral exciton X^0 at the direct band gap with high oscillator strength. The exciton X^0 are identified in differential reflection spectrum with energy E_X = 1.723 eV and the linewidth of $\hbar\gamma$ = 6.1 meV.

The device under study is a monolayer WSe_2 encapsulated in hBN on a silver mirror. The characterization of optical properties of the monolayer were done in a bath cryostat (T = 4.2 K) with a home-built confocal microscope. For the white-light reflection spectroscopy measurements a Halogen lamp or NKT SuperContinuum Extreme laser were used as broadband excitation source with illumination focus area ~ 1 μm (attocube LT-APO objective, NA = 0.82). The reflected light was spectrally dispersed and detected by a CCD. The differential reflection spectrum at the monolayer position is shown in figure 5.53. A single resonance

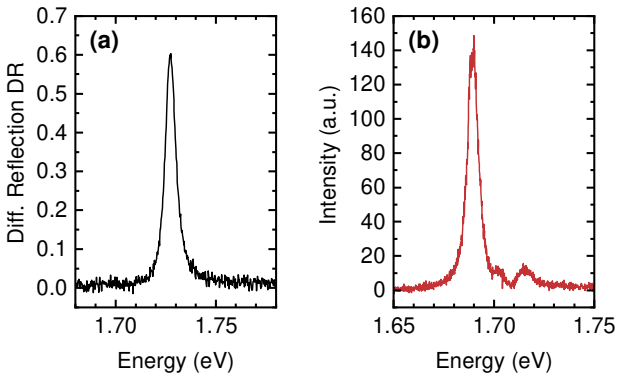

Figure 5.53.: **a** Differential reflection spectrum of the WSe_2 monolayer measured in a confocal microscope setup at low temperature (T = 4 K). **b** Transmission spectrum of the cavity detuned from the exciton resonance.

peak is obtained which is denoted to a neutral exciton X^0 at energy E_X = 1.723 eV with the linewidth of $\hbar\gamma$ = 6.1 meV. This neutral exciton has a high oscillator strength and it is used for the light-matter interaction inside the open cavity. For completeness, Figure 5.53b shows the cavity resonance detuned from the X^0 resonance at energy E_C = 1.69 eV and the linewidth of the cavity resonance is $\hbar\kappa$ = 6.3 meV.

After the characterization, the silver mirror with WSe_2 was introduced in the tunable cavity setup in closed-cycle cryostat. The fiber is now changed to one with a radius of curvature ROC = 14 µm and silver-coating (T = 1%). The finesse of the cavity was measured to be $\mathcal{F}$ = 30. The setup was then cooled down to cryogenic temperature (T = 30 K). We identified the monolayer region by performing a differential absorption xy-scan across the sample using white-light excitation (NKT SuperContinuum Laser) through the fiber and record the spectrally-dispersed transmission signal. The cavity length for the lateral scan was set at around $l_c \approx 50\,\mu m$.

The tuning capabilities of the open cavity setup allows to locate the monolayer region in the macroscopic region. An xy-scan in transmission with white light excitation and detection with a CCD in free-space provides a comprehensive overview of the optical properties of the macroscopic mirror and the solid state emitter placed on the former. Similar to differential reflection spectroscopy above, here we confirm the presence of WSe_2 by differential transmission signal where transmission across entire wavelength range is obtained by sweeping the cavity length at spatial position corresponding to on and off the monolayer. The transmission spectra at three different cavity length is shown in figure 5.54a, apparent from the respective shift of the cavity resonances. The reduced transmission between 1.7 eV and 1.75 eV is a clear signature of the X^0 in the monolayer. By extracting the resonance peak positions at different cavity length on and off the monolayer position, the differential trans-

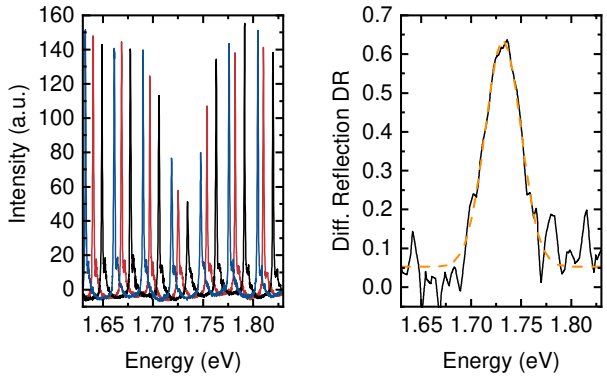

Figure 5.54.: **a** Cavity transmission spectra for varying cavity length by small steps (L_{red} > L_{black} > L_{blue}). The overall cavity length L is large (mode number q > 50). **b** Differential transmission spectrum of the WSe_2 neutral exciton inside the cavity obtained from interpolating the intensity values of all cavity mode maxima of a cavity length sweep on (as shown in **a**) and off the monolayer position. The yellow dashed line shows a Gaussian fit to the processed data.

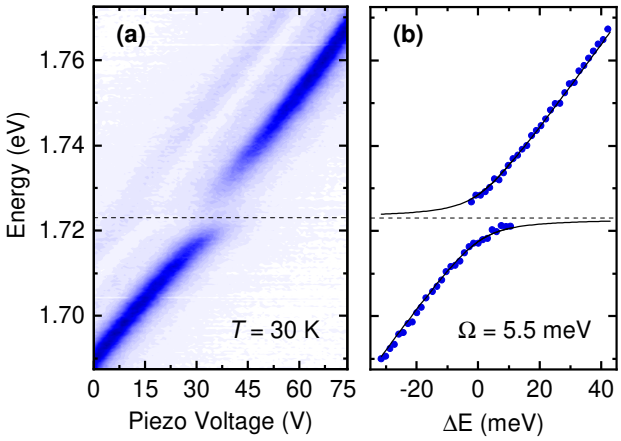

Figure 5.55.: **Strong coupling of monolayer WSe_2 at cryogenic temperature**. **a**, A map showing transmission through the cavity as function of actuator piezo voltage tuning the photonic resonance energy. The avoided crossing behavior is observed as photonic resonance is tuned across the exciton resonance. **b**, The exciton-polariton peak position derived from the left plot as the function of energy detuning, the calculated Rabi splitting is 12 meV.

mission spectrum is obtained (figure 5.54b).

Once the monolayer is found inside the cavity, to study photon-exciton interaction, the cavity length was reduced to bring the effective cavity mode volume to a small value. At the cavity length $l_c \approx 2.9\ \mu$m, the cavity resonance energy is tuned around $E_C \approx 1.72$ eV and the linewidth of the cavity resonance for the given finesse is $\hbar\kappa = 6.3$ meV. We monitor the

cavity resonance mode as it is tuned closer to the X_0 resonance of WSe_2. The corresponding transmission signal as a function of voltage applied on the piezo actuator is shown in figure 5.55a for the cavity mode q = 8. We observe an avoided-crossing behavior as the photonic resonance is tuned through the exciton resonance. At a small energy detuning between photon and exciton resonance energy $\Delta E = E_C - E_X$, there are two peaks in the transmission spectrum which are denoted to the lower and upper exciton-polariton peaks. The peak positions of exciton-polaritons are plotted in figure 5.55b as the function of detuning along with the expected polariton energy based on the coupled oscillator model. Based on this coupled model, the calculated Rabi splitting is $\hbar\Omega_c = 5.5$ meV (see Supplementary Information). Using the photonic decay rate $\hbar\kappa = 6.3$ meV and excitonic decay rate $\hbar\gamma = 6.1$ meV, the Cooperativity of the system is $C = 2\Omega_c^2/(\kappa\gamma) = 1.57$ putting it in the regime of a strongly-coupled exciton-photon system.

5.5. Conclusions

In this chapter, we introduce the open Fabry-Pérot cavity platform as a versatile tool for quantum optics experiments. Firstly, the advantages of open tunable cavity are discussed, followed by a brief introduction to the common terms and properties of Fabry-Pérot cavity. After introducing the main challenges of implementing such cavity at low temperature, the development and characterization of the cavity platform is discussed. We used several passive vibration reduction techniques in conjunction to achieve a reduction of peak-to-peak and rms length fluctuations by a factor of 50. The most stable cavity results are presented, showing rms stability of less than 100 pm. This will enable the operation of high finesse cavity at cryogenic temperature in a powerful and modular platform, which could easily integrate variety of solid-state quantum systems to form quantum network nodes and study novel many-body physics phenomena.

To demonstrate this functionality, we integrated monolayer WSe_2 in the cavity platform to study light-matter interaction. With controlled tuning of the cavity resonance, we observed exciton-polaritons in the strong-coupling regime. This opens the possibility to study polaritonic physics such as the polariton lasing or polariton-based quantum simulations in the TMDs.

6 Summary and Outlook

The overarching goal of this work was to engineer light-matter interaction with novel two-dimensional semiconductors. Van der Waals heterostructures of semiconductor TMDs promise to open novel application directions in the area of quantum information processing. This work focused on two experiments studying coherent coupling between excitons in TMDs and photons in different systems.

In the first experiment, we demonstrated a device showing non-reciprocal chiral reflectivity based on coherent Fano interference of an exciton-plasmon system. A device hosting monolayer WSe_2 and an array of gold nanodisks was used to study the coherent coupling of excitons with localized plasmons. With the motivation to develop chiral optical devices, experimental observation of the Fano interference was presented with an excellent agreement to the analytic spectral line shape modeling based on a three-level open system with a master equation approach and Lindblad dynamics. Furthermore, the valley-Zeeman effect in TMD monolayer in the presence of an external magnetic field was utilized to demonstrate circular dichroism of up to 7% in the energetically narrow reflection window.

The coherent exciton-plasmon interference was used for a proof-of-principle demonstration of chiral non-reciprocal reflectivity. It cab enable future integrated photonic devices towards a switchable polarization-dependent band-pass filter that will allow a uni-directional flow of classical and quantum information. Such devices promise to be the basic building blocks of complex quantum networks and a platform to study cascaded open quantum systems [215, 216, 221, 222]. A special case of the Fano interference is electromagnetically induced transparency (EIT). The EIT phenomenon has been successfully used to slow down and store light [309–312]. Our results present the possibility to utilize the valley-properties of TMDs to generate chiral slow light and chiral information storage.

In the second experiment, we implemented a high finesse tunable open Fabry-Pérot cavity setup in a closed-cycle cryostat. The development of the platform and investigation of the exciton-photon coupling in a high cooperativity regime ($C > 1$) with deterministic control of the coupling parameters was demonstrated. We focused, to this end, on a thorough under-

standing of the thermal and mechanical performance of a closed-cycle cryostat as a specific platform for low-temperature cavity experiments. A reduction of the base temperature of the cryostat by ~ 0.8 K was achieved. Furthermore, a method to reduce the base temperature oscillations was presented with the demonstration of oscillation reduction of up to factor of 25. In terms of mechanical performance, the base vibrations of the cryostat were measured with an optical interferometer in the order of 10 nm. While this level of vibrations is enough for optical microscopy experiments, an improvement by several orders of magnitude is necessary for the operation of high finesse cavities.

With that background, a versatile platform for cavity QED experiments was established. The development and characterization of the setup are described in detail. We achieved a vibration reduction of factor of 100 over the entire bandwidth by combining spring-based vibration isolation with viscous damping using eddy currents, establishing a link to turn cavity mirrors into a coupled oscillator and applying active feedback. The vibration levels were brought down to a peak-to-peak value of 0.7 nm and rms value of 89 pm. In addition, the platform was combined with WSe_2 monolayer to study the coherent interaction of excitons and photons in the strong coupling regime. The strong coupling is substantiated with the observation of exciton-polaritons with a vacuum Rabi splitting of 6 meV at cryogenic temperatures in a controlled setting of our versatile platform.

The development of a tunable open Fabry-Pérot cavity in a closed cycle cryostat opens a plethora of opportunities for future scientific exploration and applications. The incorporation of van der Waals heterostructures inside the cavity will pave the path towards a controllable system to study polaritonic physics with atomically thin semiconductors. One possible direction for exploration is investigatation of polariton condensation and polariton lasing with the TMDs in a high polariton density regime [137–139]. Due to high exciton binding energy, polariton lasing at different energies can be possible in variety of TMDs at room temperature, which remains an outstanding goal in the research community [313–316]. The presence of valley degree offers an additional knob to control the polarization of the polariton emission [291, 293, 317–321].

Another direction will be utilizing the cavity-TMD platform for quantum simulations. Polariton gases in TMDs can serve as a condensed-matter simulation platform to study many-body quantum models and realize topological systems, similar to cold atoms in optical lattices [144–147, 296, 322–324]. The interaction dynamics for exciton-polaritons can be controlled and manipulated via their excitonic or photonic part, e.g. using local strain, electrostatic traps, etched micropillar lattices and many other techniques [325]. One appealing way to engineer polariton-polariton interaction is by designing the optical excitation beam using a spatial light modulator [326–329].

Another obvious approach includes van der Waals heterostructures with two or more TMD monolayers which host interlayer excitons and also lead to a moiré pattern [294, 330–334]. Interlayer excitons have a permanent dipole moment which makes them an

attractive candidate for dipolar polaritons in the strong-coupling regime. The long-range interaction strength of dipolar excitons can enable the study of strongly-correlated systems. Furthermore, the moiré superlattice provides an inherent potential landscape for electrons that has recently been used to study the Hubbard model and to demonstrate novel phases of matter [335–343]. Dipolar polaritons based on TMD excitons also provide a platform to reach the non-linear optical regime at a single particle level and observe long elusive polariton blockade in a strongly quantum-correlated regime [140–143, 166].

The open cavity developed here is an appealing platform at cryogenic temperatures to host a variety of solid-state quantum emitters in TMDs as well as quantum dots or NV centers, amongst others. The coupled system can serve as a deterministic and controllable single-photon source via Purcell enhancement [109–114] or can be used to generate complex cluster states in the future [344–348]. An effective photon-matter mediator is also essential for quantum networks and provide promising novel qubit architectures such as rare-earth ions leading to applications in quantum communication and quantum computing [216, 349–352].

The tunability feature makes cavity a versatile tool to perform absorption spectroscopy and microscopy. In direct extension to the polaritonic physics, the cavity can be used to perform scanning absorption microscopy with TMDs to study other excitonic species, apart from the well-understood neutral exciton, and provide an insight on their origin and properties, e.g. the measurement of the oscillator strength of the lower energy dark exciton in WSe_2. A sensitive absorption microscope is necessary for novel material characterization with applications in chemistry and biology [270, 353–356].

The technological expertise and the development of low-vibration cryogenics presented in this work is significant for different areas of physics. The detailed understanding of cryogenic systems is important for low temperature experiments in solid-state physics, cryo-electron microscopy and quantum technologies. In particular, the low vibration platform developed here is crucial for the implementation of any sensitive microscopy technique where the unwanted distance fluctuations between a tip and a sample has to be minimized, such as atomic-force microscopy (AFM) or scattering near-field optical microscopy (SNOM) at cryogenic temperatures [357–363]. Low vibration cryogenics can also provide a better frequency-reference platforms to create more accurate atomic clocks and to enrich fundamental physics by the detection of dark matter [364–366].

A Appendix: Elastic metamaterial

This chapter introduces the idea of elastic metamaterial for vibration isolation and studying novel physics such as topological phenomena.

A.1. Introduction

A metamaterial is an artificial material engineered to demonstrate characteristics or features that can not be easily found in a natural material. The concept of engineering material properties started over a century ago with early work on negative phase velocity of wave and artificial chiral media [367–369]. The seminal theoretical proposal on negative-index metamaterial was done by Veselago in 1967 [370]. Since 1990s, the realization of metamaterials have seen remarkable progress in electromagnetic domain due to advances in technology.

Photonic metamaterial in various frequency ranges has been shown with either negative permeability or permittivity and thus, negative effective refractive index [371–373]. The negative refractive index can be used to design a super lens with focusing resolution below diffraction limit [374, 375]. Another interesting experiment involves demonstration of optical cloaking [376–378]. The set of material with same periodicity as the wavelength of electromagnetic field are called photonic crystals [379–381]. This photonic crystals have applications in highly-reflective coatings or photonic crystal based fibers [381]. By introduction of an asymmetry in photonic crystal, it is possible to introduce an optical resonator with ultra-small confinement volume. The photonic crystal cavities has been used in cavity QED experiments with a great success [382–384].

More recently, the design of artificial metamaterials has also been extended to the other waves such as acoustic or elastic waves, referred to as phononic metamaterials [193, 385, 386]. Phononic metamaterials shows similar intriguing phenomena as their counterparts in the electromagnetic domain. The demonstration of effective negative bulk modulus and negative effective mass density in such materials has been achieved [385, 387–389].

Acoustic and elastic metamaterials have also been used for sub-wavelength imaging, negative refraction and cloaking [385, 390–394]. Another potential application is to design a frequency-dependent absorbers or reflectors for phononic waves with practical use-cases, such as sound noise mitigation or shock absorbers for the automotives, space instruments and even seismic waves [192, 194, 395]. In the next section, we discuss the physical origin of the intriguing properties of the metamaterials.

A.2. Types of phononic metamaterials

There are two primary techniques to modify the wave properties: Bragg scattering and locally resonant structures. Here, I briefly describe this two phenomena.

Bragg scattering

Bragg diffraction occurs when a wave is incident on a periodic array of scattering objects where the period of the objects is comparable to the wavelength of the incident wave [396, 397]. For example, let us consider a simple wave propagating in one direction of the form:

$$i(x,t) = \cos(\omega t - kx) \tag{A.1}$$

where ω is the angular frequency, $k = 2\pi/\lambda$ is the wave number and λ is the wavelength. The scattered waves by two identical objects separated by the distance l can be written as:

$$\begin{aligned} s_1(x,t) &= \cos\left(kx - \omega t + \Delta\varphi\right), \\ s_2(x,t) &= \cos\left(kx - \omega t + \Delta\varphi + kL\right) \end{aligned} \tag{A.2}$$

where $\Delta\varphi$ is the phase change between incident and scattered wave. There can be a complete destructive interference between two scattered waves, i.e. there is a band gap for the wave of the given wavelength, when the following condition is satisfied:

$$L = \frac{\lambda}{2} \tag{A.3}$$

This condition is known as the Bragg condition. It was first discovered in the X-rays reflected by crystalline solids by Lawrence Bragg and William Bragg in 1913 [397]. This effect is used in both photonic and phononic crystals where an artificial pattern of scatterers can be fabricated to manipulate or stop the wave propagation [381, 385].

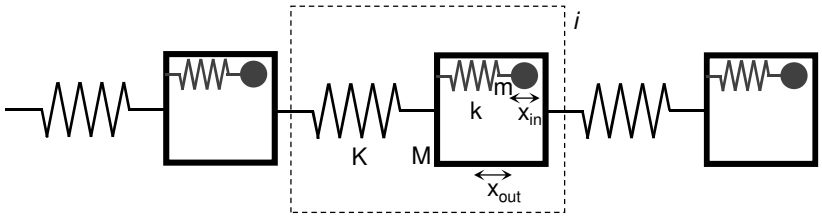

Figure A.1.: Lattice of a mass-in-mass system. A unit cell, dashed rectangle, consists of two masses. An external mass is connected to other unit cell with a spring, while an internal mass is connected with another spring to external mass and acts as a local resonant structure.

Locally resonant structures

Propagation of waves can also be manipulated with an artificial lattice which relies on the resonance of a local oscillator in the unit cell instead of the spacing of the cells leading to Bragg scattering like above. A simple example of such a local oscillator in a unit cell is a mass-in-mass system. Let us look at the one-dimensional lattice of mass-in-mass system.

The unit cell of the system is sketched in figure A.1. It consists of a block of mass M which is connected to the block in next unit cell with spring constant K. The block is hollow such that it contains an additional block of mass m inside which is connected to the outer block with spring which has a spring constant k. The equation of motion of the two masses in the unit cell can be written as:

$$\begin{aligned} M\ddot{x}_{out}^{(i)} + K\left(2x_{out}^{(i)} - x_{out}^{(i-1)} - x_{out}^{(i+1)}\right) + k\left(x_{out}^{(i)} - x_{in}^{(i)}\right) = 0 \\ m\ddot{x}_{in}^{(i)} + k\left(x_{in}^{(i)} - x_{out}^{(i)}\right) = 0 \end{aligned} \tag{A.4}$$

We assume that the solution to the displacement of blocks in unit cell j is of the following form:

$$x_{\gamma}^{(j+n)} = A_{\gamma} e^{i(qx+nqL-\omega t)} \tag{A.5}$$

where A is the amplitude, q is the wave-vector, L is the distance between two unit cells and γ denotes either in or out block. The dispersion relation can be written from the equation of motion as:

$$mM\omega^4 - \left[(m+M)\,k + 2mK(1-\cos(qL))\right]\omega^2 + 2kK(1-\cos(qL)) = 0 \tag{A.6}$$

The solution to the wave-vector can be written in terms of effective mass as:

$$\cos(qL) = 1 - \frac{m_{\text{eff}}\omega^2}{2K} \tag{A.7}$$

where the effective mass is:

$$m_{\text{eff}} = m_{\text{tot}} + \frac{m\,(\omega/\omega_{in})^2}{1-(\omega/\omega_{in})^2} \tag{A.8}$$

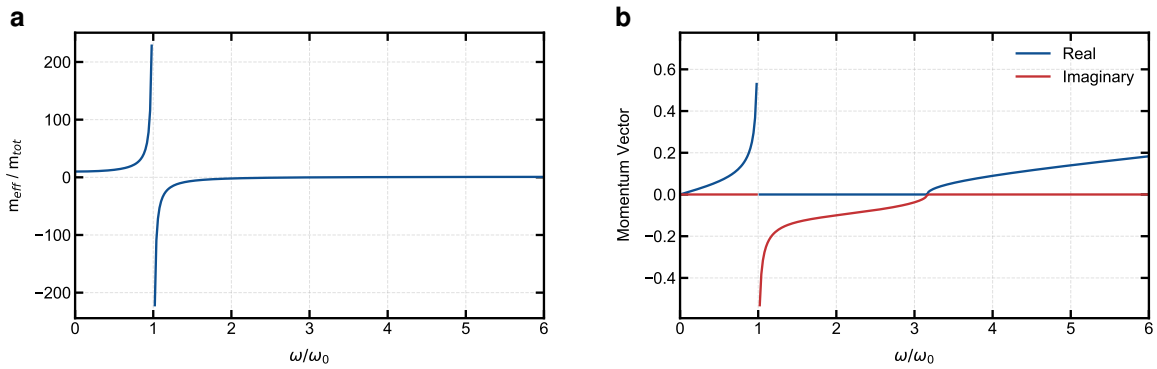

Figure A.2.: Mass in mass model. **a** Effective mass as a function of frequency normalized to the resonance frequency of inner mass. Effective mass shows a dispersive behavior around resonance frequency and it has a negative value for a frequency region above the inner block's resonance frequency. **b** Real and imaginary component of wave-vector. In the region where the effective mass is negative, the wave-vector only has imaginary solution.

where $m_{\text{tot}} = m + M$ is total mass, $\omega_{in} = \sqrt{k/m}$ is the resonance frequency of the internal block. The mass-in-mass model is effectively described by a simple chain of blocks of mass m_{eff} connected by springs. We plot the negative mass and the corresponding wave-vector as a function of frequency in figure A.2.

The frequency-dependent wave-vector in figure A.2b shows a frequency region where there is no real solution. This leads to a decay term in the displacement leading to a frequency band gap after the resonance frequency of the internal mass block. Thus, the local resonant structure enables wave manipulation at frequencies much smaller than the unit cell of the structure. Next, we discuss the practical applications of using locally resonant structures for vibration isolation.

A.3. Vibration isolation using phononic metamaterials

Elastic waves at low frequencies have long wavelength. For example, acoustic waves in Titanium have speed of 6070 m/s, therefore, the wavelength of sub-kHz waves that are mainly responsible for mechanical vibrations have wavelength longer than 6 m. While vibration isolation experiment using Bragg condition has been demonstrated [192, 395], it is not practical to design metamaterial structures with such length scales for most applications, especially in confined environments such as vacuum and cryogenic conditions.

With the use of locally resonant structure, first remarkable demonstration was a sonic metamaterial, with silicone outer mass and lead balls as inner mass, with acoustic attenuation at 400 Hz [194]. Thereafter, a variety of systems have been used to demonstrate acoustic

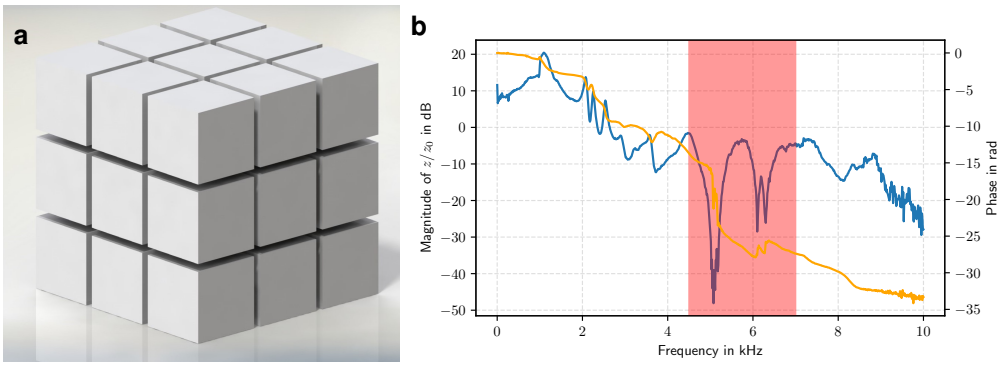

Figure A.3.: **a** Initial design of 3D vibration isolation of stage. This is 3x3 simple cubic unit cell without an internal resonant structure to validate the design and manufacturing process. **b** Displacement (blue) and phase (orange) response of vibration isolation stage. Displacement shows resonances below 3 kHz and a pronounce dip between 4 and 7 kHz. Result from [398].

or elastic wave attenuation [385, 399–416]. The experiments includes hierarchical resonant structures [412], active tuning of frequency band-gap [405, 413] and a single material design [414].

Proof-of-concept design

Within the context of this thesis on vibration reduction in the cryogenic environment, a three-dimensional locally resonant metamaterial is a promising technique. A 3D unit cell with a mass inside another mass is required to achieve vibration reduction in all three translational axes. Even a simple cubic unit cell enables variety of geometrical design to achieve a locally resonant structure in the desired frequency range from 10 Hz to 10 kHz. Few possible geometries includes: springs to inner mass from unit cell faces, springs to inner mass from unit cell vertices, multiple inner mass in parallel or series. In addition, the geometry should be optimized to maximize the inner mass and reduce the spring constant.

The additive manufacturing and 3D printing provides a high degree of flexibility to design such metamaterials [417]. To check the feasibility of 3D printing, we designed a simple prototype device as shown in figure A.3a. It is a simple mass-spring unit cell without a locally resonant structure [398]. Two lowest eigenfrequency of the unit cell for the chosen material (PA12) were calculated analytically to be ~ 700 Hz and ~ 1400 Hz. The motivation for the structure design was to analyze the response close to the eigenfrequency of the unit cell and establish a measurement methodology. The structure with 3x3 units was 3D printed, however, the design parameters were too small to be accurately manufactured in the first iteration.

The structure was placed on a piezo shaker plate and the response was measured with an

optical interferometer [398]. The response is plotted in figure A.3b. We see that the displacement shows two pronounced transmission dips at 5 kHz and 6.2 kHz. While this is a promising early result, the origin of these dips requires further analysis and an accurate numerical simulation of phonon propagation. It is important to note that there is also an enhancement of transmission at smaller frequencies. This suggests that vibration attenuation at one frequency range can lead to an enhancement at other frequencies. Therefore, the metamaterial needs to be carefully designed for an effective vibration reduction in the desired frequency range. Therefore, this preliminary study with a simple geometry demonstrates encouraging results and promises to be an exciting approach of using artificial materials for vibration reduction techniques.

A.4. Outlook

The approach to engineer novel materials with desired properties is highly promising. In terms of the vibration reduction, the continuous advances in manufacturing, and particularly 3D printing, will enable complex geometries to address mechanical vibrations at specific frequencies with *mechanical band pass filter*. The metamaterials are particularly attractive for vibration isolation at cryogenic temperature and other harsh environments, where the requirement complexity can be tackled by the suitable design criteria in advance. Metamaterial also provides an avenue to study novel topological physics [418, 419]. The recent demonstrations in acoustic or mechanical metamaterials includes topological boundary modes [420–422], band inversion [196] and one-way transport [423–425].

Bibliography

1. Deutsch, I. H. Harnessing the Power of the Second Quantum Revolution. *PRX Quantum* **1,** 020101 (2 2020).
2. Acín, A., Bloch, I., Buhrman, H., *et al.* The quantum technologies roadmap: a European community view. *New J. Phys.* **20,** 080201 (2018).
3. Dowling, J. P. & Milburn, G. J. Quantum technology: the second quantum revolution. *Philos. T. Roy. Soc. A* **361,** 1655–1674 (2003).
4. Alexeev, Y., Bacon, D., Brown, K. R., *et al.* Quantum Computer Systems for Scientific Discovery. *PRX Quantum* **2,** 017001 (1 2021).
5. Altman, E., Brown, K. R., Carleo, G., *et al.* Quantum Simulators: Architectures and Opportunities. *PRX Quantum* **2,** 017003 (1 2021).
6. Awschalom, D., Berggren, K. K., Bernien, H., *et al.* Development of Quantum Interconnects (QuICs) for Next-Generation Information Technologies. *PRX Quantum* **2,** 017002 (1 2021).
7. Lange, W., Turchette, Q., Hood, C., *et al.* in *Coherence and Quantum Optics VII* 345–346 (Springer, 1996).
8. Duan, L.-M., Lukin, M. D., Cirac, J. I., *et al.* Long-distance quantum communication with atomic ensembles and linear optics. *Nature* **414,** 413–418 (2001).
9. Gisin, N. & Thew, R. Quantum communication. *Nat. Photonics* **1,** 165–171 (2007).
10. Nielsen, M. A. & Chuang, I. *Quantum computation and quantum information* (American Association of Physics Teachers, 2002).
11. Shor, P. W. Polynomial-time algorithms for prime factorization and discrete logarithms on a quantum computer. *SIAM review* **41,** 303–332 (1999).
12. Grover, L. K. Quantum mechanics helps in searching for a needle in a haystack. *Phys. Rev. Lett.* **79,** 325 (1997).
13. Preskill, J. Quantum Computing in the NISQ era and beyond. *Quantum* **2,** 79 (2018).
14. Levine, I. N., Busch, D. H. & Shull, H. *Quantum chemistry* (Pearson Prentice Hall Upper Saddle River, NJ, 2009).

15. Farhi, E., Goldstone, J. & Gutmann, S. A quantum approximate optimization algorithm. *arXiv:1411.4028* (2014).

16. Kandala, A., Mezzacapo, A., Temme, K., *et al.* Hardware-efficient variational quantum eigensolver for small molecules and quantum magnets. *Nature* **549,** 242–246 (2017).

17. Devoret, M. H., Wallraff, A. & Martinis, J. M. Superconducting qubits: A short review. *arXiv: cond-mat/0411174* (2004).

18. Arute, F., Arya, K., Babbush, R., *et al.* Quantum supremacy using a programmable superconducting processor. *Nature* **574,** 505–510 (2019).

19. Cirac, J. I. & Zoller, P. Quantum computations with cold trapped ions. *Phys. Rev. Lett.* **74,** 4091 (1995).

20. Leibfried, D., Blatt, R., Monroe, C., *et al.* Quantum dynamics of single trapped ions. *Rev. Mod. Phys.* **75,** 281 (2003).

21. Koppens, F. H., Buizert, C., Tielrooij, K.-J., *et al.* Driven coherent oscillations of a single electron spin in a quantum dot. *Nature* **442,** 766–771 (2006).

22. Watson, T., Philips, S., Kawakami, E., *et al.* A programmable two-qubit quantum processor in silicon. *Nature* **555,** 633–637 (2018).

23. Childress, L., Dutt, M. G., Taylor, J., *et al.* Coherent dynamics of coupled electron and nuclear spin qubits in diamond. *Science* **314,** 281–285 (2006).

24. Bertaina, S., Gambarelli, S., Tkachuk, A., *et al.* Rare-earth solid-state qubits. *Nat. Nanotechnol.* **2,** 39–42 (2007).

25. Kok, P., Munro, W. J., Nemoto, K., *et al.* Linear optical quantum computing with photonic qubits. *Rev. Mod. Phys.* **79,** 135 (2007).

26. O'brien, J. L., Furusawa, A. & Vučković, J. Photonic quantum technologies. *Nat. Photonics* **3,** 687–695 (2009).

27. Wang, J., Sciarrino, F., Laing, A., *et al.* Integrated photonic quantum technologies. *Nat. Photonics* **14,** 273–284 (2020).

28. Degen, C. L., Reinhard, F. & Cappellaro, P. Quantum sensing. *Rev. Mod. Phys.* **89,** 035002 (3 2017).

29. Abbott, B. P., Abbott, R., Abbott, T. D., *et al.* Observation of Gravitational Waves from a Binary Black Hole Merger. *Phys. Rev. Lett.* **116,** 061102 (6 2016).

30. Georgescu, I. M., Ashhab, S. & Nori, F. Quantum simulation. *Rev. Mod. Phys.* **86,** 153 (2014).

31. Cirac, J. I. & Zoller, P. Goals and opportunities in quantum simulation. *Nat. Phys.* **8,** 264–266 (2012).

32. Haroche, S. Nobel Lecture: Controlling photons in a box and exploring the quantum to classical boundary. *Rev. Mod. Phys.* **85,** 1083 (2013).

33. Kimble, H. J. Strong interactions of single atoms and photons in cavity QED. *Phys. Scripta* **1998,** 127 (1998).

34. Ye, J., Vernooy, D. & Kimble, H. Trapping of single atoms in cavity QED. *Phys. Rev. Lett.* **83,** 4987 (1999).

35. Imamoglu, A., Awschalom, D. D., Burkard, G., *et al.* Quantum information processing using quantum dot spins and cavity QED. *Phys. Rev. Lett.* **83,** 4204 (1999).

36. Goy, P., Raimond, J., Gross, M., *et al.* Observation of cavity-enhanced single-atom spontaneous emission. *Phys. Rev. Lett.* **50,** 1903 (1983).

37. Kleppner, D. Inhibited spontaneous emission. *Phys. Rev. Lett.* **47,** 233 (1981).

38. Hulet, R. G., Hilfer, E. S. & Kleppner, D. Inhibited spontaneous emission by a Rydberg atom. *Phys. Rev. Lett.* **55,** 2137 (1985).

39. Gabrielse, G. & Dehmelt, H. Observation of inhibited spontaneous emission. *Phys. Rev. Lett.* **55,** 67 (1985).

40. Purcell, E. M., Torrey, H. C. & Pound, R. V. Resonance absorption by nuclear magnetic moments in a solid. *Phys. Rev.* **69,** 37 (1946).

41. Meschede, D., Walther, H. & Müller, G. One-atom maser. *Phys. Rev. Lett.* **54,** 551 (1985).

42. Meystre, P., Rempe, G. & Walther, H. Very-low-temperature behavior of a micromaser. *Opt. Lett.* **13,** 1078–1080 (1988).

43. Rempe, G., Schmidt-Kaler, F. & Walther, H. Observation of sub-Poissonian photon statistics in a micromaser. *Phys. Rev. Lett.* **64,** 2783 (1990).

44. Scully, M. O., Englert, B.-G. & Walther, H. Quantum optical tests of complementarity. *Nature* **351,** 111–116 (1991).

45. Weisbuch, C., Nishioka, M., Ishikawa, A., *et al.* Observation of the coupled exciton-photon mode splitting in a semiconductor quantum microcavity. *Phys. Rev. Lett.* **69,** 3314 (1992).

46. Houdré, R., Weisbuch, C., Stanley, R., *et al.* Measurement of cavity-polariton dispersion curve from angle-resolved photoluminescence experiments. *Phys. Rev. Lett.* **73,** 2043 (1994).

47. Norris, T., Rhee, J.-K., Sung, C.-Y., *et al.* Time-resolved vacuum Rabi oscillations in a semiconductor quantum microcavity. *Phys. Rev. B* **50,** 14663 (1994).

48. Jacobson, J., Pau, S., Cao, H., *et al.* Observation of exciton-polariton oscillating emission in a single-quantum-well semiconductor microcavity. *Phys. Rev. A* **51,** 2542 (1995).

49. Novoselov, K. S., Geim, A. K., Morozov, S. V., *et al.* Electric field effect in atomically thin carbon films. *Science* **306,** 666–669 (2004).

50. Novoselov, K. S., Jiang, D., Schedin, F., *et al.* Two-dimensional atomic crystals. *P. Natl. Acad. Sci.* **102,** 10451–10453 (2005).

51. Novoselov, K. Nobel lecture: Graphene: Materials in the flatland. *Rev. Mod. Phys.* **83,** 837 (2011).

52. Mak, K. F., Lee, C., Hone, J., *et al.* Atomically Thin MoS_2: A New Direct-Gap Semiconductor. *Phys. Rev. Lett.* **105,** 136805 (13 2010).

53. Splendiani, A., Sun, L., Zhang, Y., *et al.* Emerging photoluminescence in monolayer MoS_2. *Nano Lett.* **10,** 1271–1275 (2010).

54. Geim, A. K. & Grigorieva, I. V. Van der Waals heterostructures. *Nature* **499,** 419–425 (2013).

55. Wang, Q. H., Kalantar-Zadeh, K., Kis, A., *et al.* Electronics and optoelectronics of two-dimensional transition metal dichalcogenides. *Nat. Nanotechnol.* **7,** 699–712 (2012).

56. Mak, K. F. & Shan, J. Photonics and optoelectronics of 2D semiconductor transition metal dichalcogenides. *Nat. Photon.* **10,** 216–226 (2016).

57. Wang, G., Chernikov, A., Glazov, M. M., *et al.* Colloquium: Excitons in atomically thin transition metal dichalcogenides. *Rev. Mod. Phys.* **90,** 021001 (2 2018).

58. Steinmetz, T., Colombe, Y., Hunger, D., *et al.* Stable fiber-based Fabry-Perot cavity. *Appl. Phys. Lett.* **89,** 111110 (2006).

59. Hunger, D., Steinmetz, T., Colombe, Y., *et al.* Fiber Fabry-Perot cavity with high finesse. *New J. Phys.* **12,** 065038 (2010).

60. Liu, Y., Weiss, N. O., Duan, X., *et al.* Van der Waals heterostructures and devices. *Nat. Rev. Mat.* **1,** 1–17 (2016).

61. Novoselov, K., Mishchenko, o. A., Carvalho, o. A., *et al.* 2D Mater. and van der Waals heterostructures. *Science* **353** (2016).

62. Wilson, J. A. & Yoffe, A. The transition metal dichalcogenides discussion and interpretation of the observed optical, electrical and structural properties. *Adv. Phys.* **18,** 193–335 (1969).

63. Chernikov, A., Berkelbach, T. C., Hill, H. M., *et al.* Exciton binding energy and nonhydrogenic Rydberg series in monolayer WS_2. *Phys. Rev. Lett.* **113,** 076802 (2014).

64. He, K., Kumar, N., Zhao, L., *et al.* Tightly bound excitons in monolayer WSe_2. *Phys. Rev. Lett.* **113,** 026803 (2014).

65. Ye, Z., Cao, T., O?brien, K., *et al.* Probing excitonic dark states in single-layer tungsten disulphide. *Nature* **513,** 214–218 (2014).

66. Wang, G., Marie, X., Gerber, I., *et al.* Giant enhancement of the optical second-harmonic emission of WSe_2 monolayers by laser excitation at exciton resonances. *Phys. Rev. Lett.* **114,** 097403 (2015).

67. Srivastava, A., Sidler, M., Allain, A. V., *et al.* Valley Zeeman effect in elementary optical excitations of monolayer WSe 2. *Nat. Phys.* **11,** 141 (2015).

68. Dery, H. & Song, Y. Polarization analysis of excitons in monolayer and bilayer transition-metal dichalcogenides. *Phys. Rev. B* **92,** 125431 (2015).

69. Wang, G., Robert, C., Glazov, M., *et al.* In-plane propagation of light in transition metal dichalcogenide monolayers: optical selection rules. *Phys. Rev. Lett.* **119,** 047401 (2017).

70. Lindlau, J., Robert, C., Funk, V., *et al.* Identifying optical signatures of momentum-dark excitons in transition metal dichalcogenide monolayers. *arXiv:1710.00988* (2017).

71. Lindlau, J., Selig, M., Neumann, A., *et al.* The role of momentum-dark excitons in the elementary optical response of bilayer WSe_2. *Nat. Commun.* **9,** 1–7 (2018).

72. Selig, M., Berghäuser, G., Richter, M., *et al.* Dark and bright exciton formation, thermalization, and photoluminescence in monolayer transition metal dichalcogenides. *2D Mater.* **5,** 035017 (2018).

73. You, Y., Zhang, X.-X., Berkelbach, T. C., *et al.* Observation of biexcitons in monolayer WSe_2. *Nat. Phys.* **11,** 477–481 (2015).

74. Barbone, M., Montblanch, A. R.-P., Kara, D. M., *et al.* Charge-tuneable biexciton complexes in monolayer WSe_2. *Nat. Commun.* **9,** 1–6 (2018).

75. Steinhoff, A., Florian, M., Singh, A., *et al.* Biexciton fine structure in monolayer transition metal dichalcogenides. *Nat. Phys.* **14,** 1199–1204 (2018).

76. Förste, J., Tepliakov, N. V., Kruchinin, S. Y., *et al.* Exciton g-factors in monolayer and bilayer WSe_2 from experiment and theory. *Nat. Commun.* **11,** 1–8 (2020).

77. He, M., Rivera, P., Van Tuan, D., *et al.* Valley phonons and exciton complexes in a monolayer semiconductor. *Nat. Commun.* **11,** 1–7 (2020).

78. Zhang, X.-X., You, Y., Zhao, S. Y. F., *et al.* Experimental evidence for dark excitons in monolayer WSe_2. *Phys. Rev. Lett.* **115,** 257403 (2015).

79. Zhou, Y., Scuri, G., Wild, D. S., *et al.* Probing dark excitons in atomically thin semiconductors via near-field coupling to surface plasmon polaritons. *Nat. Nanotechnol.* **12,** 856 (2017).

80. Zhang, X.-X., Cao, T., Lu, Z., *et al.* Magnetic brightening and control of dark excitons in monolayer WSe_2. *Nat. Nanotechnol.* **12,** 883–888 (2017).

81. Molas, M. R., Faugeras, C., Slobodeniuk, A., *et al.* Brightening of dark excitons in monolayers of semiconducting transition metal dichalcogenides. *2D Mater.* **4,** 021003 (2017).

82. Molas, M., Slobodeniuk, A., Kazimierczuk, T., *et al.* Probing and manipulating valley coherence of dark excitons in monolayer WSe_2. *Phys. Rev. Lett.* **123,** 096803 (2019).

83. Tang, Y., Mak, K. F. & Shan, J. Long valley lifetime of dark excitons in single-layer WSe_2. *Nat. Commun.* **10,** 1–7 (2019).

84. Manzeli, S., Ovchinnikov, D., Pasquier, D., *et al.* 2D transition metal dichalcogenides. *Nat. Rev. Mat.* **2,** 1–15 (2017).

85. Akinwande, D., Petrone, N. & Hone, J. Two-dimensional flexible nanoelectronics. *Nat. Commun.* **5,** 1–12 (2014).

86. Choi, W., Choudhary, N., Han, G. H., *et al.* Recent development of two-dimensional transition metal dichalcogenides and their applications. *Mater. Today* **20,** 116–130 (2017).

87. Jin, C., Ma, E. Y., Karni, O., *et al.* Ultrafast dynamics in van der Waals heterostructures. *Nat. Nanotechnol.* **13,** 994–1003 (2018).

88. Rivera, P., Yu, H., Seyler, K. L., *et al.* Interlayer valley excitons in heterobilayers of transition metal dichalcogenides. *Nat. Nanotechnol.* **13,** 1004–1015 (2018).

89. Mueller, T. & Malic, E. Exciton physics and device application of two-dimensional transition metal dichalcogenide semiconductors. *2D Mater.* **2,** 1–12 (2018).

90. Liu, X. & Hersam, M. C. 2D Mater. for quantum information science. *Nat. Rev. Mat.* **4,** 669–684 (2019).

91. Liu, C., Chen, H., Wang, S., *et al.* Two-dimensional materials for next-generation computing technologies. *Nat. Nanotechnol.* **15,** 545–557 (2020).

92. Pu, J., Yomogida, Y., Liu, K.-K., *et al.* Highly flexible MoS_2 thin-film transistors with ion gel dielectrics. *Nano Lett.* **12,** 4013–4017 (2012).

93. Chang, H.-Y., Yang, S., Lee, J., *et al.* High-performance, highly bendable MoS_2 transistors with high-k dielectrics for flexible low-power systems. *ACS Nano* **7,** 5446–5452 (2013).

94. Lee, G.-H., Yu, Y.-J., Cui, X., *et al.* Flexible and transparent MoS_2 field-effect transistors on hexagonal boron nitride-graphene heterostructures. *ACS Nano* **7,** 7931–7936 (2013).

95. Sundaram, R., Engel, M., Lombardo, A., *et al.* Electroluminescence in single layer MoS_2. *Nano Lett.* **13,** 1416–1421 (2013).

96. Cheng, R., Li, D., Zhou, H., *et al.* Electroluminescence and photocurrent generation from atomically sharp WSe_2/MoS_2 heterojunction p–n diodes. *Nano Lett.* **14,** 5590–5597 (2014).

97. Ross, J. S., Klement, P., Jones, A. M., *et al.* Electrically tunable excitonic light-emitting diodes based on monolayer WSe_2 p–n junctions. *Nat. Nanotechnol.* **9,** 268–272 (2014).

98. Withers, F., Del Pozo-Zamudio, O., Mishchenko, A., *et al.* Light-emitting diodes by band-structure engineering in van der Waals heterostructures. *Nat. Mater.* **14,** 301–306 (2015).

99. Zhang, Y., Oka, T., Suzuki, R., *et al.* Electrically switchable chiral light-emitting transistor. *Science* **344,** 725–728 (2014).

100. Lopez-Sanchez, O., Lembke, D., Kayci, M., *et al.* Ultrasensitive photodetectors based on monolayer MoS_2. *Nat. Nanotechnol.* **8,** 497–501 (2013).

101. Tsai, D.-S., Liu, K.-K., Lien, D.-H., *et al.* Few-layer MoS_2 with high broadband photogain and fast optical switching for use in harsh environments. *ACS Nano* **7,** 3905–3911 (2013).

102. Lee, C.-H., Lee, G.-H., Van Der Zande, A. M., *et al.* Atomically thin p–n junctions with van der Waals heterointerfaces. *Nat. Nanotechnol.* **9,** 676 (2014).

103. Baugher, B. W., Churchill, H. O., Yang, Y., *et al.* Optoelectronic devices based on electrically tunable p–n diodes in a monolayer dichalcogenide. *Nat. Nanotechnol.* **9,** 262–267 (2014).

104. Furchi, M. M., Pospischil, A., Libisch, F., *et al.* Photovoltaic effect in an electrically tunable van der Waals heterojunction. *Nano Lett.* **14,** 4785–4791 (2014).

105. Mak, K. F., McGill, K. L., Park, J., *et al.* The valley Hall effect in MoS_2 transistors. *Science* **344,** 1489–1492 (2014).

106. Yuan, H., Wang, X., Lian, B., *et al.* Generation and electric control of spin–valley-coupled circular photogalvanic current in WSe_2. *Nat. Nanotechnol.* **9,** 851–857 (2014).

107. Chakraborty, C., Kinnischtzke, L., Goodfellow, K. M., *et al.* Voltage-controlled quantum light from an atomically thin semiconductor. *Nat. Nanotechnol.* **10,** 507–511 (2015).

108. He, Y.-M., Clark, G., Schaibley, J. R., *et al.* Single quantum emitters in monolayer semiconductors. *Nat. Nanotechnol.* **10,** 497–502 (2015).

109. Koperski, M., Nogajewski, K., Arora, A., *et al.* Single photon emitters in exfoliated WSe_2 structures. *Nat. Nanotechnol.* **10,** 503–506 (2015).

110. Srivastava, A., Sidler, M., Allain, A. V., *et al.* Optically active quantum dots in monolayer WSe_2. *Nat. Nanotechnol.* **10,** 491 (2015).

111. Lodahl, P., Mahmoodian, S. & Stobbe, S. Interfacing single photons and single quantum dots with photonic nanostructures. *Rev. Mod. Phys.* **87,** 347–400 (2 2015).

112. Palacios-Berraquero, C., Kara, D. M., Montblanch, A. R.-P., *et al.* Large-scale quantum-emitter arrays in atomically thin semiconductors. *Nat. Commun.* **8,** 1–6 (2017).

113. Klein, J., Lorke, M., Florian, M., *et al.* Site-selectively generated photon emitters in monolayer MoS_2 via local helium ion irradiation. *Nat. Commun.* **10,** 1–8 (2019).

114. Peng, L., Chan, H., Choo, P., *et al.* Creation of Single-Photon Emitters in WSe_2 Monolayers Using Nanometer-Sized Gold Tips. *Nano Lett.* **20,** 5866–5872 (2020).

115. Gan, X., Gao, Y., Fai Mak, K., *et al.* Controlling the spontaneous emission rate of monolayer MoS_2 in a photonic crystal nanocavity. *Appl. Phys. Lett.* **103,** 181119 (2013).

116. Wu, S., Buckley, S., Jones, A. M., *et al.* Control of two-dimensional excitonic light emission via photonic crystal. *2D Mater.* **1,** 011001 (2014).

117. Wu, S., Buckley, S., Schaibley, J. R., *et al.* Monolayer semiconductor nanocavity lasers with ultralow thresholds. *Nature* **520,** 69–72 (2015).

118. Ye, Y., Wong, Z. J., Lu, X., *et al.* Monolayer excitonic laser. *Nat. Photonics* **9,** 733–737 (2015).

119. Förg, M., Colombier, L., Patel, R. K., *et al.* Cavity-control of interlayer excitons in van der Waals heterostructures. *Nat. Commun.* **10,** 3697 (2019).

120. Kern, J., Tru?gler, A., Niehues, I., *et al.* Nanoantenna-enhanced light–matter interaction in atomically thin WS_2. *ACS Photonics* **2,** 1260–1265 (2015).

121. Lee, B., Park, J., Han, G. H., *et al.* Fano resonance and spectrally modified photoluminescence enhancement in monolayer MoS_2 integrated with plasmonic nanoantenna array. *Nano Lett.* **15,** 3646–3653 (2015).

122. Butun, S., Tongay, S. & Aydin, K. Enhanced light emission from large-area monolayer MoS_2 using plasmonic nanodisc arrays. *Nano Lett.* **15,** 2700–2704 (2015).

123. Wang, Z., Dong, Z., Gu, Y., *et al.* Giant photoluminescence enhancement in tungsten-diselenide–gold plasmonic hybrid structures. *Nat. Commun.* **7,** 1–8 (2016).

124. Tahersima, M. H., Birowosuto, M. D., Ma, Z., *et al.* Testbeds for transition metal dichalcogenide photonics: efficacy of light emission enhancement in monomer vs dimer nanoscale antennae. *ACS Photonics* **4,** 1713–1721 (2017).

125. Cheng, F., Johnson, A. D., Tsai, Y., *et al.* Enhanced photoluminescence of monolayer WS_2 on Ag films and nanowire–WS_2–film composites. *ACS Photonics* **4,** 1421–1430 (2017).

126. Liu, X., Galfsky, T., Sun, Z., *et al.* Strong Light-Matter Coupling in Two-Dimensional Atomic Crystals. *Nat. Photonics* **9,** 30 (Jan. 2015).

127. Dufferwiel, S., Schwarz, S., Withers, F., *et al.* Exciton-polaritons in van der Waals heterostructures embedded in tunable microcavities. *Nat. Commun.* **6,** 1 (2015).

128. Lundt, N., Klembt, S., Cherotchenko, E., *et al.* Room-temperature Tamm-plasmon exciton-polaritons with a WSe_2 monolayer. *Nat. Commun.* **7** (2016).

129. Zheng, D., Zhang, S., Deng, Q., *et al.* Manipulating coherent plasmon–exciton interaction in a single silver nanorod on monolayer WSe_2. *Nano Lett.* **17,** 3809–3814 (2017).

130. Kleemann, M.-E., Chikkaraddy, R., Alexeev, E. M., *et al.* Strong-coupling of WSe_2 in ultra-compact plasmonic nanocavities at room temperature. *Nat. Commun.* **8,** 1–7 (2017).

131. Liu, R., Zhou, Z.-K., Yu, Y.-C., *et al.* Strong light-matter interactions in single open plasmonic nanocavities at the quantum optics limit. *Phys. Rev. Lett.* **118,** 237401 (2017).

132. Zhang, L., Gogna, R., Burg, W., *et al.* Photonic-crystal exciton-polaritons in monolayer semiconductors. *Nat. Commun.* **9,** 713 (2018).

133. Wang, S., Li, S., Chervy, T., *et al.* Coherent Coupling of WS_2 Monolayers with Metallic Photonic Nanostructures at Room Temperature. *Nano Lett.* **16,** 4368–4374 (2016).

134. Flatten, L. C., He, Z., Coles, D. M., *et al.* Room-temperature exciton-polaritons with two-dimensional WS_2. *Sci. Rep.* **6,** 1–7 (2016).

135. Hu, T., Wang, Y., Wu, L., *et al.* Strong coupling between Tamm plasmon polariton and two dimensional semiconductor excitons. *Appl. Phys. Lett.* **110,** 051101 (2017).

136. Sidler, M., Back, P., Cotlet, O., *et al.* Fermi polaron-polaritons in charge-tunable atomically thin semiconductors. *Nat. Phys.* **13,** 255–261 (2017).

137. Deng, H., Weihs, G., Santori, C., *et al.* Condensation of semiconductor microcavity exciton polaritons. *Science* **298,** 199–202 (2002).

138. Kasprzak, J., Richard, M., Kundermann, S., *et al.* Bose–Einstein condensation of exciton polaritons. *Nature* **443,** 409–414 (2006).

139. Deng, H., Haug, H. & Yamamoto, Y. Exciton-polariton bose-einstein condensation. *Rev. Mod. Phys.* **82,** 1489 (2010).

140. Verger, A., Ciuti, C. & Carusotto, I. Polariton quantum blockade in a photonic dot. *Phys. Rev. B* **73,** 193306 (2006).

141. Muñoz-Matutano, G., Wood, A., Johnsson, M., *et al.* Emergence of quantum correlations from interacting fibre-cavity polaritons. *Nat. Mater.* **18,** 213–218 (2019).

142. Delteil, A., Fink, T., Schade, A., *et al.* Towards polariton blockade of confined exciton–polaritons. *Nat. Mater.* **18,** 219–222 (2019).

143. Kyriienko, O., Krizhanovskii, D. & Shelykh, I. Nonlinear Quantum Optics with Trion Polaritons in 2D Monolayers: Conventional and Unconventional Photon Blockade. *Phys. Rev. Lett.* **125,** 197402 (2020).

144. Carusotto, I. & Ciuti, C. Quantum fluids of light. *Rev. Mod. Phys.* **85,** 299 (2013).

145. Berloff, N. G., Silva, M., Kalinin, K., *et al.* Realizing the classical XY Hamiltonian in polariton simulators. *Nat. Mater.* **16,** 1120–1126 (2017).

146. Lagoudakis, P. G. & Berloff, N. G. A polariton graph simulator. *New J. Phys.* **19,** 125008 (2017).

147. Ashida, Y., İmamoğlu, A., Faist, J., *et al.* Quantum electrodynamic control of matter: Cavity-enhanced ferroelectric phase transition. *Phys. Rev. X* **10,** 041027 (2020).

148. Ozbay, E. Plasmonics: merging photonics and electronics at nanoscale dimensions. *Science* **311,** 189–193 (2006).

149. Atwater, H. A. The promise of plasmonics. *Sci. Am.* **296,** 56–63 (2007).

150. Gramotnev, D. K. & Bozhevolnyi, S. I. Plasmonics beyond the diffraction limit. *Nat. Photonics* **4,** 83–91 (2010).

151. Kawata, S., Inouye, Y. & Verma, P. Plasmonics for near-field nano-imaging and superlensing. *Nat. Photonics* **3,** 388–394 (2009).

152. Schuller, J. A., Barnard, E. S., Cai, W., *et al.* Plasmonics for extreme light concentration and manipulation. *Nat. Mater.* **9,** 193–204 (2010).

153. Fox, M. *Optical properties of solids* (American Association of Physics Teachers, 2002).

154. Maier, S. A. *Plasmonics: fundamentals and applications* (Springer Science & Business Media, 2007).

155. Scherzer, J. *Building Light-Matter Hybrid Systems from Plasmonic Nanostructures and Monolayer Semiconductors* Master Thesis (Ludwig-Maximilians-Universität München, 2020).

156. Mie, G. Beiträge zur Optik trüber Medien, speziell kolloidaler Metallösungen. *Ann. Phys.* **330,** 377–445 (1908).

157. Link, S. & El-Sayed, M. A. Shape and size dependence of radiative, non-radiative and photothermal properties of gold nanocrystals. *Int. Rev. Phys. Chem.* **19,** 409–453 (2000).

158. Sönnichsen, C., Franzl, T., Wilk, T., *et al.* Drastic reduction of plasmon damping in gold nanorods. *Phys. Rev. Lett.* **88,** 774021 (2002).

159. Fabry, C. & Pérot, A. On the fringes of thin silver plates 'a and their application 'a the measurement of small é air thicknesses. *Ann. Chim. Phys* **12** (1897).

160. Hernández, G. *Fabry-Pérot interferometers* **3** (Cambridge University Press, 1988).

161. Siegman, A. E. *Lasers* **208** (Mill Valley, CA, 1986).

162. Grynberg, G., Aspect, A. & Fabre, C. *Introduction to quantum optics: from the semi-classical approach to quantized light* (Cambridge university press, 2010).

163. Loudon, R. *The quantum theory of light* (Oxford University Press, 2000).

164. Weisskopf, V. F. & Wigner, E. P. Calculation of the natural brightness of spectral lines on the basis of Dirac's theory. *Z. Phys.* **63,** 54–73 (1930).

165. Scully, M. O. & Zubairy, M. S. *Quantum optics* (American Association of Physics Teachers, 1999).

166. Kavokin, A., Baumberg, J. J., Malpuech, G., *et al. Microcavities* (Oxford University Press, 2017).

167. Rand, S. *Lectures on Light: Nonlinear and Quantum Optics using the Density Matrix* (OUP Oxford, 2016).

168. Gerardot, B. D., Brunner, D., Dalgarno, P. A., *et al.* Optical pumping of a single hole spin in a quantum dot. *Nature* **451,** 441 (2008).

169. Karrai, K. & Warburton, R. J. Optical transmission and reflection spectroscopy of single quantum dots. *Superlattices Microst.* **33,** 311 (2003).

170. Bowman, D. M. J. S., Balch, J. K., Artaxo, P., *et al.* Fire in the Earth System. *Science* **324,** 481–484 (2009).

171. ONNES, H. K. The Condensation of Helium. *Nature* **77,** 581–581 (1908).

172. Onnes, H. K. *Nobel Prize in Physics 1913*

173. Zhao, Z. & Wang, C. *Cryogenic Engineering and Technologies: Principles and Applications of Cryogen-free Systems* (CRC Press, 2019).

174. Wang, C. & Gifford, P. E. A Single-Stage Pulse Tube Cryocooler for Horizontally Cooling HTS MRI Probe. *AIP Conference Proceedings* **710,** 1805–1811 (2004).

175. Haft, D., Otto, F., Dal Savio, C., *et al. Optical table* US Patent App. 15/518,646.

176. Dal Savio, C. & Karrai, K. *Cooled table* US Patent App. 15/528,853.

177. Duthil, P. Material properties at low temperature. *arXiv preprint arXiv:1501.07100* (2015).

178. Tomaru, T., Suzuki, T., Haruyama, T., *et al.* Vibration analysis of cryocoolers. *Cryogenics* **44,** 309–317 (2004).

179. Thurner, K. *Position sensing using a fiber-optic Fabry-Pérot interferometer* Dissertation (Technische Universität München, 2018).

180. Shieh, J., Huber, J., Fleck, N., *et al.* The selection of sensors. *Prog. Mater. Sci.* **46,** 461–504 (2001).

181. Fleming, A. J. A review of nanometer resolution position sensors: Operation and performance. *Sensors Actuat. A-Phys.* **190,** 106–126 (2013).

182. Thurner, K., Braun, P.-F. & Karraï, K. Fabry-Pérot interferometry for long range displacement sensing. *Rev. Sci. Instrum.* **84,** 095005 (2013).

183. Thurner, K., Braun, P.-F. & Karrai, K. Absolute distance sensing by two laser optical interferometry. *Rev. Sci. Instrum.* **84,** 115002 (2013).

184. Thurner, K., Karrai, K. & Braun, P.-F. *Absolute distance laser interferometer* US Patent 9,829,306. 2017.

185. Hua, W. *Low frequency vibration isolation and alignment system for advanced LIGO* Dissertation (Caltech, 2005).

186. Martynov, D. *Lock Acquisition and Sensitivity Analysis of Advanced LIGO Interferometers* Dissertation (Caltech, 2015).

187. Rivin, E. *Passive Vibration Isolation* (ASME Press, 2003).

188. Amr, B. M. *Active and Passive Vibration Damping* (Wiley, 2018).

189. Ledezma-Ramírez, D. F., Tapia-González, P. E., Ferguson, N., *et al.* Recent advances in shock vibration isolation: An overview and future possibilities. *Appl. Mech. Rev.* **71** (2019).

190. Fiorillo, F. *Measurement and characterization of magnetic materials* (North-Holland, 2004).

191. Kushwaha, M. S., Halevi, P., Dobrzynski, L., *et al.* Acoustic band structure of periodic elastic composites. *Phys. Rev. Lett.* **71,** 2022–2025 (13 1993).

192. Liu, Z., Chan, C. T., Sheng, P., *et al.* Elastic wave scattering by periodic structures of spherical objects: Theory and experiment. *Phys. Rev. B* **62,** 2446–2457 (4 2000).

193. Deymier, P. A. *Acoustic metamaterials and phononic crystals* (Springer Science & Business Media, 2013).

194. Liu, Z., Zhang, X., Mao, Y., *et al.* Locally Resonant Sonic Materials. *Science* **289,** 1734–1736 (2000).

195. Zhou, X., Liu, X. & Hu, G. Elastic metamaterials with local resonances: an overview. *Theor. Appl.* **2,** 041001 (2012).

196. Xiao, M., Ma, G., Yang, Z., *et al.* Geometric phase and band inversion in periodic acoustic systems. *Nat. Phys.* **11,** 240 (2015).

197. Nash, L. M., Kleckner, D., Read, A., *et al.* Topological mechanics of gyroscopic metamaterials. *P. Natl. Acad. Sci.* **112,** 14495–14500 (2015).

198. Wang, P., Lu, L. & Bertoldi, K. Topological Phononic Crystals with One-Way Elastic Edge Waves. *Phys. Rev. Lett.* **115,** 104302 (10 2015).

199. Süsstrunk, R. & Huber, S. D. Classification of topological phonons in linear mechanical metamaterials. *P. Natl. Acad. Sci.* **113,** E4767–E4775 (2016).

200. Ibrahim, R. Recent advances in nonlinear passive vibration isolators. *J. Sound Vib.* **314,** 371–452 (2008).

201. Platus, D. L. *Negative-stiffness-mechanism vibration isolation systems* in *Optomechanical Engineering and Vibration Control* **3786** (SPIE, 1999), 98–105.

202. Frizenschaf, Y., Giles, S., Miller, J., *et al. Development of a magnetic levitation vibration isolator using inclined permanent magnet springs* in *Proc. Acoustics* (2011).

203. Mizuno, T., Takasaki, M., Kishita, D., *et al.* Vibration isolation system combining zero-power magnetic suspension with springs. *Control Eng. Pract.* **15,** 187–196 (2007).

204. Zhu, T., Cazzolato, B., Robertson, W. S., *et al.* Vibration isolation using six degree-of-freedom quasi-zero stiffness magnetic levitation. *J. Sound Vib.* **358,** 48–73 (2015).

205. Gong, Z., Ding, L., Yue, H., *et al.* System integration and control design of a maglev platform for space vibration isolation. *J. Vib. Control* **25,** 1720–1736 (2019).

206. Bennett, S. A brief history of automatic control. *IEEE Contr. Syst. Mag.* **16,** 17–25 (1996).

207. Valavanis, K. P., Vachtsevanos, G. J. & Antsaklis, P. J. Technology and Autonomous Mechanisms in the Mediterranean: From Ancient Greece to Byzantium [Historical Perspectives]. *IEEE Contr. Syst. Mag.* **34,** 110–119 (2014).

208. Assig, M., Koch, A., Stiepany, W., *et al.* Miniature active damping stage for scanning probe applications in ultra high vacuum. *Rev. Sci. Instrum.* **83,** 033701 (2012).

209. Bechhoefer, J. Feedback for physicists: A tutorial essay on control. *Rev. Mod. Phys.* **77,** 783 (2005).

210. Åström, K. & Murray, R. *Feedback Systems: An Introduction for Scientists and Engineers* (Princeton University Press, 2010).

211. Dorf, R. C. & Bishop, R. H. *Modern control systems* (Pearson, 2011).

212. Franklin, G. F., Powell, J. D., Emami-Naeini, A., *et al. Feedback control of dynamic systems* (Prentice hall Upper Saddle River, NJ, 2002).

213. Ryou, A. & Simon, J. Active cancellation of acoustical resonances with an FPGA FIR filter. *Rev. Sci. Instrum.* **88,** 013101 (2017).

214. Okada, M., Serikawa, T., Dannatt, J., *et al.* Extending the piezoelectric transducer bandwidth of an optical interferometer by suppressing resonance using a high dimensional IIR filter implemented on an FPGA. *Rev. Sci. Instrum.* **91,** 055102 (2020).

215. Kimble, H. J. The quantum internet. *Nature* **453,** 1023 (2008).

216. Reiserer, A. & Rempe, G. Cavity-based quantum networks with single atoms and optical photons. *Rev. Mod. Phys.* **87,** 1379 (2015).

217. Chang, D. E., Vuletić, V. & Lukin, M. D. Quantum nonlinear optics: photon by photon. *Nat. Photonics* **8,** 685–694 (2014).

218. Söllner, I., Mahmoodian, S., Hansen, S. L., *et al.* Deterministic photon–emitter coupling in chiral photonic circuits. *Nat. Nanotechnol.* **10,** 775–778 (2015).

219. Sayrin, C., Junge, C., Mitsch, R., *et al.* Nanophotonic Optical Isolator Controlled by the Internal State of Cold Atoms. *Phys. Rev. X* **5,** 041036 (4 2015).

220. Scheucher, M., Hilico, A., Will, E., *et al.* Quantum optical circulator controlled by a single chirally coupled atom. *Science* **354,** 1577–1580 (2016).

221. Carmichael, H. J. Quantum trajectory theory for cascaded open systems. *Phys. Rev. Lett.* **70,** 2273 (1993).

222. Gardiner, C. W. Driving a quantum system with the output field from another driven quantum system. *Phys. Rev. Lett.* **70,** 2269 (1993).

223. Stannigel, K., Rabl, P. & Zoller, P. Driven-dissipative preparation of entangled states in cascaded quantum-optical networks. *New J. Phys.* **14,** 063014 (2012).

224. Lodahl, P., Mahmoodian, S., Stobbe, S., *et al.* Chiral quantum optics. *Nature* **541,** 473 (2017).

225. Anker, J. N., Hall, W. P., Lyandres, O., *et al.* Biosensing with plasmonic nanosensors. *Nat. Mater.* **7,** 442–453 (2008).

226. Nam, J.-M., Thaxton, C. S. & Mirkin, C. A. Nanoparticle-based bio-bar codes for the ultrasensitive detection of proteins. *Science* **301,** 1884–1886 (2003).

227. Elghanian, R., Storhoff, J. J., Mucic, R. C., *et al.* Selective colorimetric detection of polynucleotides based on the distance-dependent optical properties of gold nanoparticles. *Science* **277,** 1078–1081 (1997).

228. Catchpole, K. & Polman, A. Plasmonic solar cells. *Opt. Expr.* **16,** 21793–21800 (2008).

229. Ferry, V. E., Verschuuren, M. A., Li, H. B., *et al.* Light trapping in ultrathin plasmonic solar cells. *Opt. Expr.* **18,** A237–A245 (2010).

230. Jang, Y. H., Jang, Y. J., Kim, S., *et al.* Plasmonic solar cells: from rational design to mechanism overview. *Chem. Rev.* **116,** 14982–15034 (2016).

231. Willets, K. A. & Van Duyne, R. P. Localized surface plasmon resonance spectroscopy and sensing. *Annu. Rev. Phys. Chem.* **58,** 267–297 (2007).

232. Lee, S. J., Guan, Z., Xu, H., *et al.* Surface-enhanced Raman spectroscopy and nanogeometry: The plasmonic origin of SERS. *J. Phys. Chem. C* **111,** 17985–17988 (2007).

233. Vo-Dinh, T., Wang, H.-N. & Scaffidi, J. Plasmonic nanoprobes for SERS biosensing and bioimaging. *J. Biophotonics* **3,** 89–102 (2010).

234. Jacob, Z. & Shalaev, V. M. Plasmonics goes quantum. *Science* **334,** 463–464 (2011).

235. Russell, K. J., Liu, T.-L., Cui, S., *et al.* Large spontaneous emission enhancement in plasmonic nanocavities. *Nat. Photonics* **6,** 459–462 (2012).

236. De Leon, N. P., Lukin, M. D. & Park, H. Quantum plasmonic circuits. *IEEE J. Sel. Top. Quant.* **18,** 1781–1791 (2012).

237. Tame, M. S., McEnery, K., Özdemir, Ş., *et al.* Quantum plasmonics. *Nat. Phys.* **9,** 329–340 (2013).

238. Bozhevolnyi, S. I. & Mortensen, N. A. Plasmonics for emerging quantum technologies. *Nanophotonics* **6,** 1185–1188 (2017).

239. Cotrufo, M., Sun, L., Choi, J., *et al.* Enhancing functionalities of atomically thin semiconductors with plasmonic nanostructures. *Nanophotonics* **8,** 577–598 (2019).

240. Sriram, P., Manikandan, A., Chuang, F. C., *et al.* Hybridizing Plasmonic Materials with 2D-Transition Metal Dichalcogenides toward Functional Applications. *Small* **16,** 1–27 (2020).

241. Wen, J., Wang, H., Wang, W., *et al.* Room temperature strong light–matter interaction with active control in single plasmonic nanorod coupled with two-dimensional atomic crystals. *Nano Lett.* **17,** 4689–4697 (2017).

242. Cuadra, J., Baranov, D. G., Wersall, M., *et al.* Observation of tunable charged exciton polaritons in hybrid monolayer WS2- plasmonic nanoantenna system. *Nano Lett.* **18,** 1777–1785 (2018).

243. Park, K.-D., Jiang, T., Clark, G., *et al.* Radiative control of dark excitons at room temperature by nano-optical antenna-tip Purcell effect. *Nat. Nanotechnol.* **13,** 59–64 (2018).

244. Luo, Y., Shepard, G. D., Ardelean, J. V., *et al.* Deterministic coupling of site-controlled quantum emitters in monolayer WSe_2 to plasmonic nanocavities. *Nat. Nanotechnol.* **13,** 1137–1142 (2018).

245. Cai, T., Kim, J.-H., Yang, Z., *et al.* Radiative enhancement of single quantum emitters in WSe_2 monolayers using site-controlled metallic nanopillars. *ACS Photonics* **5,** 3466–3471 (2018).

246. Sortino, L., Zotev, P., Mignuzzi, S., *et al.* Enhanced light-matter interaction in an atomically thin semiconductor coupled with dielectric nano-antennas. *Nat. Commun.* **10,** 1–8 (2019).

247. Chervy, T., Azzini, S., Lorchat, E., *et al.* Room temperature chiral coupling of valley excitons with spin-momentum locked surface plasmons. *ACS Photonics* **5,** 1281–1287 (2018).

248. Gong, S.-H., Alpeggiani, F., Sciacca, B., *et al.* Nanoscale chiral valley-photon interface through optical spin-orbit coupling. *Science* **359,** 443–447 (2018).

249. Sun, L., Wang, C.-Y., Krasnok, A., *et al.* Separation of valley excitons in a MoS_2 monolayer using a subwavelength asymmetric groove array. *Nat. Photonics* **13,** 180–184 (2019).

250. Li, Z., Liu, C., Rong, X., *et al.* Tailoring MoS_2 valley-polarized photoluminescence with super chiral near-field. *Adv. Mater.* **30,** 1801908 (2018).

251. Fano, U. Effects of configuration interaction on intensities and phase shifts. *Phys. Rev.* **124,** 1866 (1961).

252. Luk'yanchuk, B., Zheludev, N. I., Maier, S. A., *et al.* The Fano resonance in plasmonic nanostructures and metamaterials. *Nat. Mater.* **9,** 707 (2010).

253. Limonov, M. F., Rybin, M. V., Poddubny, A. N., *et al.* Fano resonances in photonics. *Nat. Photonics* **11,** 543 (2017).

254. Jakubczyk, T., Delmonte, V., Koperski, M., *et al.* Radiatively Limited Dephasing and Exciton Dynamics in $MoSe_2$ Monolayers Revealed with Four-Wave Mixing Microscopy. *Nano Lett.* **16,** 5333 (2016).

255. Cadiz, F., Courtade, E., Robert, C., *et al.* Excitonic Linewidth Approaching the Homogeneous Limit in MoS_2-Based van der Waals Heterostructures. *Phys. Rev. X* **7,** 021026 (2017).

256. Branny, A., Kumar, S., Proux, R., *et al.* Deterministic strain-induced arrays of quantum emitters in a two-dimensional semiconductor. *Nat. Commun.* **8,** 1–7 (2017).

257. Glazov, M. M., Amand, T., Marie, X., *et al.* Exciton fine structure and spin decoherence in monolayers of transition metal dichalcogenides. *Phys. Rev. B* **89,** 201302 (20 2014).

258. Moody, G., Kavir Dass, C., Hao, K., *et al.* Intrinsic homogeneous linewidth and broadening mechanisms of excitons in monolayer transition metal dichalcogenides. *Nat. Commun.* **6,** 1 (2015).

259. Li, Y., Ludwig, J., Low, T., *et al.* Valley Splitting and Polarization by the Zeeman Effect in Monolayer $MoSe_2$. *Phys. Rev. Lett.* **113,** 266804 (26 2014).

260. Norden, T., Zhao, C., Zhang, P., *et al.* Giant valley splitting in monolayer WS2 by magnetic proximity effect. *Nat. Commun.* **10** (2019).

261. Zheng, S.-B. & Guo, G.-C. Efficient Scheme for Two-Atom Entanglement and Quantum Information Processing in Cavity QED. *Phys. Rev. Lett.* **85,** 2392–2395 (11 2000).

262. Colombe, Y., Steinmetz, T., Dubois, G., *et al.* Strong atom–field coupling for Bose–Einstein condensates in an optical cavity on a chip. *Nature* **450,** 272–276 (2007).

263. Steiner, M., Meyer, H. M., Deutsch, C., *et al.* Single ion coupled to an optical fiber cavity. *Phys. Rev. Lett.* **110,** 043003 (2013).

264. Brandstätter, B., McClung, A., Schüppert, K., *et al.* Integrated fiber-mirror ion trap for strong ion-cavity coupling. *Rev. Sci. Instrum.* **84,** 123104 (2013).

265. Haas, F., Volz, J., Gehr, R., *et al.* Entangled states of more than 40 atoms in an optical fiber cavity. *Science* **344,** 180–183 (2014).

266. Favero, I., Stapfner, S., Hunger, D., *et al.* Fluctuating nanomechanical system in a high finesse optical microcavity. *Opt. Expr.* **17,** 12813–12820 (2009).

267. Lee, M., Lee, M., Hong, S., *et al.* Microelectromechanical-System-Based Design of a High-Finesse Fiber Cavity Integrated with an Ion Trap. *Phys. Rev. Appl.* **12,** 044052 (2019).

268. Wang, D., Kelkar, H., Martin-Cano, D., *et al.* Turning a molecule into a coherent two-level quantum system. *Nat. Phys.* **15,** 483–489 (2019).

269. Scafirimuto, F., Urbonas, D., Scherf, U., *et al.* Room-temperature exciton-polariton condensation in a tunable zero-dimensional microcavity. *ACS Photonics* **5,** 85–89 (2018).

270. Mader, M., Reichel, J., Hänsch, T. W., *et al.* A scanning cavity microscope. *Nat. Commun.* **6,** 1–7 (2015).

271. Barbour, R. J., Dalgarno, P. A., Curran, A., *et al.* A tunable microcavity. *J. Appl. Phys.* **110,** 053107 (2011).

272. Albrecht, R., Bommer, A., Deutsch, C., *et al.* Coupling of a Single Nitrogen-Vacancy Center in Diamond to a Fiber-Based Microcavity. *Phys. Rev. Lett.* **110,** 243602 (24 2013).

273. Janitz, E., Ruf, M., Dimock, M., *et al.* Fabry-Perot microcavity for diamond-based photonics. *Phys. Rev. A* **92,** 043844 (2015).

274. Riedel, D., Söllner, I., Shields, B. J., *et al.* Deterministic Enhancement of Coherent Photon Generation from a Nitrogen-Vacancy Center in Ultrapure Diamond. *Phys. Rev. X* **7,** 031040 (2017).

275. Bogdanović, S., van Dam, S. B., Bonato, C., *et al.* Design and low-temperature characterization of a tunable microcavity for diamond-based quantum networks. *Appl. Phys. Lett.* **110,** 171103 (2017).

276. Benedikter, J., Kaupp, H., Hümmer, T., *et al.* Cavity-enhanced single-photon source based on the silicon-vacancy center in diamond. *Phys. Rev. Appl.* **7,** 024031 (2017).

277. Salz, M., Herrmann, Y., Nadarajah, A., *et al.* Cryogenic platform for coupling color centers in diamond membranes to a fiber-based microcavity. *Appl. Phys. B* **126,** 131 (2020).

278. Ruf, M., Weaver, M. J., van Dam, S. B., *et al.* Resonant Excitation and Purcell Enhancement of Coherent Nitrogen-Vacancy Centers Coupled to a Fabry-Pérot Micro-Cavity. *arXiv:2009.08204* (2020).

279. Nair, S. R., Rogers, L. J., Vidal, X., *et al.* Amplification by stimulated emission of nitrogen-vacancy centres in a diamond-loaded fibre cavity. *Nanophotonics* **1** (2020).

280. Casabone, B., Benedikter, J., Hümmer, T., *et al.* Cavity-enhanced spectroscopy of a few-ion ensemble in $Eu^{3+} : Y_2O_3$. *New J. Phys.* **20,** 095006 (2018).

281. Merkel, B., Ulanowski, A. & Reiserer, A. Coherent and Purcell-Enhanced Emission from Erbium Dopants in a Cryogenic High-Q Resonator. *Phys. Rev. X* **10,** 041025 (2020).

282. Casabone, B., Deshmukh, C., Liu, S., *et al.* Dynamic control of Purcell enhanced emission of erbium ions in nanoparticles (2020).

283. Jensen, R. H., Janitz, E., Fontana, Y., *et al.* Cavity-enhanced photon emission from a single germanium-vacancy center in a diamond membrane. *Phys. Rev. Appl.* **13,** 064016 (2020).

284. Hümmer, T., Noe, J., Hofmann, M. S., *et al.* Cavity-enhanced Raman microscopy of individual carbon nanotubes. *Nat. Commun.* **7,** 1–7 (2016).

285. Jeantet, A., Chassagneux, Y., Claude, T., *et al.* Exploiting one-dimensional exciton–phonon coupling for tunable and efficient single-photon generation with a carbon nanotube. *Nano Lett.* **17,** 4184–4188 (2017).

286. Besga, B., Vaneph, C., Reichel, J., *et al.* Polariton boxes in a tunable fiber cavity. *Phys. Rev. Appl.* **3,** 1–8 (2015).

287. Najer, D., Söllner, I., Sekatski, P., *et al.* A gated quantum dot strongly coupled to an optical microcavity. *Nature* **575,** 622–627 (2019).

288. Giriunas, L., Li, F., Sich, M., *et al.* Formation of a macroscopically occupied polariton state in a tunable open-access microcavity under resonant excitation. *J. Appl. Phys.* **124,** 025703 (2018).

289. Gebhardt, C., Förg, M., Yamaguchi, H., *et al.* Polariton hyperspectral imaging of two-dimensional semiconductor crystals. *Sci. Rep.* **9,** 1–9 (2019).

290. Dufferwiel, S., Li, F., Cancellieri, E., *et al.* Spin textures of exciton-polaritons in a tunable microcavity with large TE-TM splitting. *Phys. Rev. Lett.* **115,** 246401 (2015).

291. Dufferwiel, S., Lyons, T., Solnyshkov, D., *et al.* Valley coherent exciton-polaritons in a monolayer semiconductor. *Nat. Commun.* **9,** 1–7 (2018).

292. Fernandez, H. A., Withers, F., Russo, S., *et al.* Electrically Tuneable Exciton-Polaritons through Free Electron Doping in Monolayer WS_2 Microcavities. *Adv. Opt. Mater.* **7,** 1900484 (2019).

293. Król, M., Lekenta, K., Mirek, R., *et al.* Valley polarization of exciton–polaritons in monolayer WSe_2 in a tunable microcavity. *Nanoscale* **11,** 9574–9579 (2019).

294. Fogler, M., Butov, L. & Novoselov, K. High-temperature superfluidity with indirect excitons in van der Waals heterostructures. *Nat. Commun.* **5,** 1–5 (2014).

295. Waldherr, M., Lundt, N., Klaas, M., *et al.* Observation of bosonic condensation in a hybrid monolayer $MoSe_2$-GaAs microcavity. *Nat. Commun.* **9,** 1–6 (2018).

296. Klembt, S., Harder, T., Egorov, O., *et al.* Exciton-polariton topological insulator. *Nature* **562,** 552–556 (2018).

297. Gallego, J., Ghosh, S., Alavi, S. K., *et al.* High-finesse fiber Fabry–Perot cavities: stabilization and mode matching analysis. *Appl. Phys. B* **122,** 47 (2016).

298. Saleh, B. & Teich, M. *Fundamental of Photonics* (Wiley).

299. Welch, P. The use of fast Fourier transform for the estimation of power spectra: a method based on time averaging over short, modified periodograms. *IEEE T. Acoust. Speech.* **15,** 70–73 (1967).

300. Ertas, B., Luo, H. & Hallman, D. *Dynamic characteristics of shape memory alloy metal mesh dampers* in *50th AIAA/ASME/ASCE/AHS/ASC Structures, Structural Dynamics, and Materials Conference 17th AIAA/ASME/AHS Adaptive Structures Conference 11th AIAA No* (2009), 2521.

301. San Andrés, L., Chirathadam, T. A. & Kim, T.-H. Measurement of structural stiffness and damping coefficients in a metal mesh foil bearing. *J. Eng. Gas Turb. Power* **132** (2010).

302. Warburton, R., Hunger, D. & van Dam, S. Private Communication. 2017.

303. Rugar, D., Mamin, H. & Guethner, P. Improved fiber-optic interferometer for atomic force microscopy. *Appl. Phys. Lett.* **55,** 2588–2590 (1989).

304. Karrai, K. *Detection limits and nise issues in laser interferometry position readout* attocube Research Notes. 2008.

305. Drever, R., Hall, J. L., Kowalski, F., *et al.* Laser phase and frequency stabilization using an optical resonator. *Appl. Phys. B* **31,** 97–105 (1983).

306. Black, E. D. An introduction to Pound–Drever–Hall laser frequency stabilization. *Am. J. Phys.* **69,** 79–87 (2001).

307. Schäfermeier, C. *Quantum enhanced optical sensing* PhD thesis (2016).

308. Schneider, C., Glazov, M. M., Korn, T., *et al.* Two-dimensional semiconductors in the regime of strong light-matter coupling. *Nat. Commun.* **9,** 2695 (2018).

309. Boller, K.-J., Imamoglu, A. & Harris, S. E. Observation of electromagnetically induced transparency. *Phys. Rev. Lett.* **66,** 2593 (1991).

310. Lukin, M. D. & Imamoglu, A. Controlling photons using electromagnetically induced transparency. *Nature* **413,** 273 (2001).

311. Zhang, S., Genov, D. A., Wang, Y., *et al.* Plasmon-induced transparency in metamaterials. *Phys. Rev. Lett.* **101,** 1 (2008).

312. Hau, L. V., Harris, S. E., Dutton, Z., *et al.* Light speed reduction to 17 meters per second in ultracold atomic gases. *Nature* **397,** 594 (1999).

313. Kéna-Cohen, S. & Forrest, S. Room-temperature polariton lasing in an organic single-crystal microcavity. *Nat. Photonics* **4,** 371 (2010).

314. Lu, T.-C., Lai, Y.-Y., Lan, Y.-P., *et al.* Room temperature polariton lasing vs. photon lasing in a ZnO-based hybrid microcavity. *Opt. Expr.* **20,** 5530–5537 (2012).

315. Daskalakis, K., Maier, S., Murray, R., *et al.* Nonlinear interactions in an organic polariton condensate. *Nat. Mater.* **13,** 271–278 (2014).

316. Plumhof, J. D., Stöferle, T., Mai, L., *et al.* Room-temperature Bose–Einstein condensation of cavity exciton–polaritons in a polymer. *Nat. Mater.* **13,** 247–252 (2014).

317. Zeng, H., Dai, J., Yao, W., *et al.* Valley polarization in MoS 2 monolayers by optical pumping. *Nat. Nanotechnol.* **7,** 490–493 (2012).

318. Cao, T., Wang, G., Han, W., *et al.* Valley-selective circular dichroism of monolayer molybdenum disulphide. *Nat. Commun.* **3** (2012).

319. Xiao, D., Liu, G. B., Feng, W., *et al.* Coupled spin and valley physics in monolayers of MoS 2 and other group-VI dichalcogenides. *Phys. Rev. Lett.* **108,** 1 (2012).

320. Jones, A. M., Yu, H., Ghimire, N. J., *et al.* Optical generation of excitonic valley coherence in monolayer WSe_2. *Nat. Nanotechnol.* **8,** 634–638 (2013).

321. Xu, X., Yao, W., Xiao, D., *et al.* Spin and pseudospins in layered transition metal dichalcogenides. *Nat. Phys.* **10,** 343 (2014).

322. Hartmann, M. J., Brandao, F. G. & Plenio, M. B. Strongly interacting polaritons in coupled arrays of cavities. *Nat. Phys.* **2,** 849–855 (2006).

323. Karzig, T., Bardyn, C.-E., Lindner, N. H., *et al.* Topological polaritons. *Phys. Rev. X* **5,** 031001 (2015).

324. Nalitov, A., Solnyshkov, D. & Malpuech, G. Polariton Z topological insulator. *Phys. Rev. Lett.* **114,** 116401 (2015).

325. Schneider, C., Winkler, K., Fraser, M., *et al.* Exciton-polariton trapping and potential landscape engineering. *Rep. Prog. Phys.* **80,** 016503 (2016).

326. Zupancic, P., Preiss, P. M., Ma, R., *et al.* Ultra-precise holographic beam shaping for microscopic quantum control. *Opt. Expr.* **24,** 13881–13893 (2016).

327. Sun, Y., Wen, P., Yoon, Y., *et al.* Bose-Einstein condensation of long-lifetime polaritons in thermal equilibrium. *Phys. Rev. Lett.* **118,** 016602 (2017).

328. Sun, Y., Yoon, Y., Steger, M., *et al.* Direct measurement of polariton–polariton interaction strength. *Nat. Phys.* **13,** 870–875 (2017).

329. Clark, L. W., Schine, N., Baum, C., *et al.* Observation of Laughlin states made of light. *Nature* **582,** 41–45 (2020).

330. Zhang, C., Chuu, C.-P., Ren, X., *et al.* Interlayer couplings, Moiré patterns, and 2D electronic superlattices in MoS_2/WSe_2 hetero-bilayers. *Sci. Adv.* **3,** e1601459 (2017).

331. Tran, K., Moody, G., Wu, F., *et al.* Evidence for moiré excitons in van der Waals heterostructures. *Nature* **567,** 71–75 (2019).

332. Alexeev, E. M., Ruiz-Tijerina, D. A., Danovich, M., *et al.* Resonantly hybridized excitons in moiré superlattices in van der Waals heterostructures. *Nature* **567,** 81–86 (2019).

333. Jin, C., Regan, E. C., Yan, A., *et al.* Observation of moiré excitons in WSe_2/WS_2 heterostructure superlattices. *Nature* **567,** 76 (Mar. 2019).

334. Seyler, K. L., Rivera, P., Yu, H., *et al.* Signatures of moiré-trapped valley excitons in $MoSe_2$ /WSe_2 heterobilayers. *Nature* **567,** 66 (Mar. 2019).

335. Yu, H., Liu, G.-B., Tang, J., *et al.* Moiré excitons: From programmable quantum emitter arrays to spin-orbit–coupled artificial lattices. *Sci. Adv.* **3,** e1701696 (2017).

336. Wu, F., Lovorn, T. & MacDonald, A. H. Topological exciton bands in moiré heterojunctions. *Phys. Rev. Lett.* **118,** 147401 (2017).

337. Tong, Q., Yu, H., Zhu, Q., *et al.* Topological mosaics in moiré superlattices of van der Waals heterobilayers. *Nat. Phys.* **13,** 356–362 (2017).

338. Wu, F., Lovorn, T., Tutuc, E., *et al.* Hubbard model physics in transition metal dichalcogenide moiré bands. *Phys. Rev. Lett.* **121,** 026402 (2018).

339. Wang, Z., Rhodes, D. A., Watanabe, K., *et al.* Evidence of high-temperature exciton condensation in two-dimensional atomic double layers. *Nature* **574,** 76–80 (2019).

340. Regan, E. C., Wang, D., Jin, C., *et al.* Mott and generalized Wigner crystal states in WSe 2/WS 2 moiré superlattices. *Nature* **579,** 359–363 (2020).

341. Tang, Y., Li, L., Li, T., *et al.* Simulation of Hubbard model physics in WSe 2/WS 2 moiré superlattices. *Nature* **579,** 353–358 (2020).

342. Shimazaki, Y., Schwartz, I., Watanabe, K., *et al.* Strongly correlated electrons and hybrid excitons in a moiré heterostructure. *Nature* **580,** 472–477 (2020).

343. Kennes, D. M., Claassen, M., Xian, L., *et al.* Moiré heterostructures as a condensed-matter quantum simulator. *Nat. Phys.*, 1–9 (2021).

344. Buterakos, D., Barnes, E. & Economou, S. E. Deterministic Generation of All-Photonic Quantum Repeaters from Solid-State Emitters. *Phys. Rev. X* **7,** 041023 (4 2017).

345. Schwartz, I., Cogan, D., Schmidgall, E. R., *et al.* Deterministic generation of a cluster state of entangled photons. *Science* **354,** 434–437 (2016).

346. Li, Z.-D., Zhang, R., Yin, X.-F., *et al.* Experimental quantum repeater without quantum memory. *Nat. Photonics* **13,** 644–648 (2019).

347. Pilnyak, Y., Aharon, N., Istrati, D., *et al.* Simple source for large linear cluster photonic states. *Phys. Rev. A* **95,** 022304 (2017).

348. Russo, A., Barnes, E. & Economou, S. E. Generation of arbitrary all-photonic graph states from quantum emitters. *New J. Phys.* **21,** 055002 (2019).

349. Wesenberg, J. H., Mølmer, K., Rippe, L., *et al.* Scalable designs for quantum computing with rare-earth-ion-doped crystals. *Phys. Rev. A* **75,** 012304 (1 2007).

350. De Riedmatten, H., Afzelius, M., Staudt, M. U., *et al.* A solid-state light-matter interface at the single-photon level. *Nature* **456,** 773–777 (2008).

351. Kolesov, R., Xia, K., Reuter, R., *et al.* Optical detection of a single rare-earth ion in a crystal. *Nat. Commun.* **3** (2012).

352. Kindem, J. M., Ruskuc, A., Bartholomew, J. G., *et al.* Control and single-shot readout of an ion embedded in a nanophotonic cavity. *Nature* **580,** 201–204 (2020).

353. O?Keefe, A. & Deacon, D. A. Cavity ring-down optical spectrometer for absorption measurements using pulsed laser sources. *Rev. Sci. Instrum.* **59,** 2544–2551 (1988).

354. Engeln, R., Berden, G., Peeters, R., *et al.* Cavity enhanced absorption and cavity enhanced magnetic rotation spectroscopy. *Rev. Sci. Instrum.* **69,** 3763–3769 (1998).

355. Dolan, P. R., Hughes, G. M., Grazioso, F., *et al.* Femtoliter tunable optical cavity arrays. *Opt. Lett.* **35,** 3556–3558 (2010).

356. Vollmer, F. & Yang, L. Label-free detection with high-Q microcavities: a review of biosensing mechanisms for integrated devices. *Nanophotonics* **1,** 267 (2012).

357. Pan, S., Hudson, E. W. & Davis, J. 3 He refrigerator based very low temperature scanning tunneling microscope. *Rev. Sci. Instrum.* **70,** 1459–1463 (1999).

358. Kirk, M., Albrecht, T. & Quate, C. Low-temperature atomic force microscopy. *Rev. Sci. Instrum.* **59,** 833–835 (1988).

359. Giessibl, F. J. Advances in atomic force microscopy. *Rev. Mod. Phys.* **75,** 949 (2003).

360. Hillenbrand, R., Taubner, T. & Keilmann, F. Phonon-enhanced light–matter interaction at the nanometre scale. *Nature* **418,** 159–162 (2002).

361. Qazilbash, M. M., Brehm, M., Chae, B.-G., *et al.* Mott transition in VO2 revealed by infrared spectroscopy and nano-imaging. *Science* **318,** 1750–1753 (2007).

362. Yang, H. U., Hebestreit, E., Josberger, E. E., *et al.* A cryogenic scattering-type scanning near-field optical microscope. *Rev. Sci. Instrum.* **84,** 023701 (2013).

363. Luo, W., Boselli, M., Poumirol, J.-M., *et al.* High sensitivity variable-temperature infrared nanoscopy of conducting oxide interfaces. *Nat. Commun.* **10,** 1–8 (2019).

364. Zhang, W., Robinson, J., Sonderhouse, L., *et al.* Ultrastable silicon cavity in a continuously operating closed-cycle cryostat at 4 K. *Phys. Rev. Lett.* **119,** 243601 (2017).

365. Robinson, J. M., Oelker, E., Milner, W. R., *et al.* Crystalline optical cavity at 4 K with thermal-noise-limited instability and ultralow drift. *Optica* **6,** 240–243 (2019).

366. Kennedy, C. J., Oelker, E., Robinson, J. M., *et al.* Precision metrology meets cosmology: improved constraints on ultralight dark matter from atom-cavity frequency comparisons. *Phys. Rev. Lett.* **125,** 201302 (2020).

367. Lamb, H. On Group-Velocity. *Proc. Lond. Math. Soc.* **2,** 473–479 (1904).

368. Pocklington, H. Growth of a wave-group when the group velocity is negative. *Nature* **71,** 607–608 (1905).

369. Bose, J. C. On the rotation of plane of polarisation of electric wave by a twisted structure. *P. R. Soc. London* **63,** 146–152 (1898).

370. Veselago, V. G. Electrodynamics of substances with simultaneously negative values of permittivity and permeability. *Usp. Fiz. Nauk* **92,** 517 (1967).

371. Shalaev, V. M. Optical negative-index metamaterials. *Nat. Photon.* **1,** 41 (2007).

372. Soukoulis, C. M. & Wegener, M. Past achievements and future challenges in the development of three-dimensional photonic metamaterials. *Nat. Photon.* **5,** 523 (2011).

373. Liberal, I. & Engheta, N. Near-zero refractive index photonics. *Nat. Photon.* **11,** 149 (2017).

374. Pendry, J. B. Negative refraction makes a perfect lens. *Phys. Rev. Lett.* **85,** 3966 (2000).

375. Fang, N., Lee, H., Sun, C., *et al.* Sub–diffraction-limited optical imaging with a silver superlens. *Science* **308,** 534 (2005).

376. Alù, A. & Engheta, N. Achieving transparency with plasmonic and metamaterial coatings. *Phys. Rev. E* **72,** 016623 (2005).

377. Pendry, J. B., Schurig, D. & Smith, D. R. Controlling electromagnetic fields. *Science* **312,** 1780–1782 (2006).

378. Schurig, D., Mock, J. J., Justice, B., *et al.* Metamaterial electromagnetic cloak at microwave frequencies. *Science* **314,** 977–980 (2006).

379. Yablonovitch, E. Inhibited spontaneous emission in solid-state physics and electronics. *Phys. Rev. Lett.* **58,** 2059 (1987).

380. John, S. Strong localization of photons in certain disordered dielectric superlattices. *Phys. Rev. Lett.* **58,** 2486 (1987).

381. Joannopoulos, J. D., Johnson, S. G., Winn, J. N., *et al. Photonic crystals* (Princeton university press, 2011).

382. Painter, O., Lee, R., Scherer, A., *et al.* Two-dimensional photonic band-gap defect mode laser. *Science* **284,** 1819–1821 (1999).

383. Noda, S., Chutinan, A. & Imada, M. Trapping and emission of photons by a single defect in a photonic bandgap structure. *Nature* **407,** 608–610 (2000).

384. Qi, M., Lidorikis, E., Rakich, P. T., *et al.* A three-dimensional optical photonic crystal with designed point defects. *Nature* **429,** 538–542 (2004).

385. Ma, G. & Sheng, P. Acoustic metamaterials: From local resonances to broad horizons. *Sci. Adv.* **2,** e1501595 (2016).

386. Cummer, S. A., Christensen, J. & Alù, A. Controlling sound with acoustic metamaterials. *Nat. Rev. Mat.* **1,** 1 (2016).

387. Li, J. & Chan, C. T. Double-negative acoustic metamaterial. *Phys. Rev. E* **70,** 055602 (2004).

388. Wu, Y., Lai, Y. & Zhang, Z.-Q. Elastic metamaterials with simultaneously negative effective shear modulus and mass density. *Phys. Rev. Lett.* **107,** 105506 (2011).

389. Ding, Y., Liu, Z., Qiu, C., *et al.* Metamaterial with simultaneously negative bulk modulus and mass density. *Phys. Rev. Lett.* **99,** 093904 (2007).

390. Kaina, N., Lemoult, F., Fink, M., *et al.* Negative refractive index and acoustic superlens from multiple scattering in single negative metamaterials. *Nature* **525,** 77 (2015).

391. Park, J. J., Lee, K., Wright, O. B., *et al.* Giant acoustic concentration by extraordinary transmission in zero-mass metamaterials. *Phys. Rev. Lett.* **110,** 244302 (2013).

392. Lemoult, F., Kaina, N., Fink, M., *et al.* Wave propagation control at the deep subwavelength scale in metamaterials. *Nat. Phys.* **9,** 55 (2013).

393. Norris, A. N. Acoustic cloaking. *Acoust. Today* **11,** 38 (2015).

394. Liang, Z. & Li, J. Extreme acoustic metamaterial by coiling up space. *Phys> Rev. Lett.* **108,** 114301 (2012).

395. Brûlé, S., Javelaud, E., Enoch, S., *et al.* Experiments on seismic metamaterials: molding surface waves. *Phys. Rev. Lett.* **112,** 133901 (2014).

396. Lipson, A., Lipson, S. G. & Lipson, H. *Optical physics* (Cambridge University Press, 2010).

397. Bragg, W. H. & Bragg, W. L. The reflection of X-rays by crystals. *Proc. R. Soc. Lond. A* **88,** 428 (1913).

398. Vosshage, P. *An acoustic metamaterial study* Bachelor Thesis (Ludwig-Maximilians-Universität München, 2021).

399. Lazarov, B. S. & Jensen, J. S. Low-frequency band gaps in chains with attached nonlinear oscillators. *Int. J. NonLin. Mech.* **42,** 1186–1193 (2007).

400. Yao, S., Zhou, X. & Hu, G. Experimental study on negative effective mass in a 1D mass–spring system. *New J. Phys.* **10,** 043020 (2008).

401. Huang, H., Sun, C. & Huang, G. On the negative effective mass density in acoustic metamaterials. *Int. J. Eng. Sci.* **47,** 610–617 (2009).

402. Huang, H. & Sun, C. Wave attenuation mechanism in an acoustic metamaterial with negative effective mass density. *New J. Phys.* **11,** 013003 (2009).

403. Pai, P. F. Metamaterial-based broadband elastic wave absorber. *J. Intel. Mat. Syst. Str.* **21,** 517–528 (2010).

404. Yang, Z., Dai, H., Chan, N., *et al.* Acoustic metamaterial panels for sound attenuation in the 50–1000 Hz regime. *Appl. Phys. Lett.* **96,** 041906 (2010).

405. Boechler, N., Yang, J., Theocharis, G., *et al.* Tunable vibrational band gaps in one-dimensional diatomic granular crystals with three-particle unit cells. *J. Appl. Phys.* **109,** 074906 (2011).

406. Mei, J., Ma, G., Yang, M., *et al.* Dark acoustic metamaterials as super absorbers for low-frequency sound. *Nat. Commun.* **3,** 1–7 (2012).

407. Zhu, R., Liu, X., Hu, G., *et al.* A chiral elastic metamaterial beam for broadband vibration suppression. *J. Sound Vib.* **333,** 2759–2773 (2014).

408. Fleury, R., Sounas, D. L., Sieck, C. F., *et al.* Sound isolation and giant linear nonreciprocity in a compact acoustic circulator. *Science* **343,** 516–519 (2014).

409. Matlack, K. H., Bauhofer, A., Krödel, S., *et al.* Composite 3D-printed metastructures for low-frequency and broadband vibration absorption. *P. Natl. Acad. Sci. USA* **113,** 8386–8390 (2016).

410. Sugino, C., Leadenham, S., Ruzzene, M., *et al.* On the mechanism of bandgap formation in locally resonant finite elastic metamaterials. *J. Appl. Phys.* **120,** 134501 (2016).

411. Sugino, C., Xia, Y., Leadenham, S., *et al.* A general theory for bandgap estimation in locally resonant metastructures. *J. Sound Vib.* **406,** 104–123 (2017).

412. Xu, X., Barnhart, M. V., Li, X., *et al.* Tailoring vibration suppression bands with hierarchical metamaterials containing local resonators. *J. Sound Vib.* **442,** 237 (2019).

413. Gao, P., Climente, A., Sánchez-Dehesa, J., *et al.* Single-phase metamaterial plates for broadband vibration suppression at low frequencies. *J. Sound Vib.* **444,** 108–126 (2019).

414. Li, X., Chen, Y., Hu, G., *et al.* A self-adaptive metamaterial beam with digitally controlled resonators for subwavelength broadband flexural wave attenuation. *Smart Mater. Struct.* **27,** 045015 (2018).

415. Bilal, O. R., Ballagi, D. & Daraio, C. Architected lattices for simultaneous broadband attenuation of airborne sound and mechanical vibrations in all directions. *Phys. Rev. Appl.* **10,** 054060 (2018).

416. Barnhart, M. V., Xu, X., Chen, Y., *et al.* Experimental demonstration of a dissipative multi-resonator metamaterial for broadband elastic wave attenuation. *J. Sound Vib.* **438,** 1–12 (2019).

417. Gibson, I., Rosen, D., Stucker, B., *et al. Additive manufacturing technologies* (Springer, 2014).

418. Yang, Z., Gao, F., Shi, X., *et al.* Topological acoustics. *Phys. Rev. Lett.* **114,** 114301 (2015).

419. Huber, S. D. Topological mechanics. *Nat. Phys.* **12,** 621 (2016).

420. Kane, C. & Lubensky, T. Topological boundary modes in isostatic lattices. *Nat. Phys.* **10,** 39 (2014).

421. Paulose, J., Chen, B. G.-g. & Vitelli, V. Topological modes bound to dislocations in mechanical metamaterials. *Nat. Phys.* **11,** 153 (2015).

422. Wen, X., Qiu, C., Qi, Y., *et al.* Acoustic Landau quantization and quantum-Hall-like edge states. *Nat. Phys.* **15,** 352 (2019).

423. He, C., Ni, X., Ge, H., *et al.* Acoustic topological insulator and robust one-way sound transport. *Nat. Phys.* **12,** 1124 (2016).

424. Lu, J., Qiu, C., Ye, L., *et al.* Observation of topological valley transport of sound in sonic crystals. *Nat. Phys.* **13,** 369 (2017).

425. Süsstrunk, R. & Huber, S. D. Observation of phononic helical edge states in a mechanical topological insulator. *Science* **349,** 47 (2015).

Acknowledgments

The past few years has been an intense journey with enormous scientific and personal growth for me. Doing research is certainly not a solo task and I am indebted to many people who supported me during this journey. I begin with thanking the two people who gave me the opportunity to work with them: Alexander Högele and Khaled Karraï. It was a privilege to be mentored by two brilliant and compassionate scientists. It is hard to put into words all the things I have learned from them over the years, I owe them the deepest sense of gratitude for shaping my research and general identity.

Thank you Alex for letting me be the part of your group. I am grateful for fostering a nurturing academic environment and providing a constant source of support and motivation during the last years. I will carry with me your passion to understand and unveil new concepts in great detail as well as how to pursue a problem and research topic. Khaled, thank you for entrusting me with such a fun challenging project and providing the right environment within attocube with the InnoVision team. Your energy, ability to think on your feet across the wide breadth of physics and engineering topics and creativity were all remarkable, I will try my utmost best to remember and follow the countless advise that you directly or indirectly imprinted on me.

I have to thank all the members of the Nano Photonics group for creating a cohesive and scientifically enriching environment. I thank the two more-experienced PhD students when I joined the lab, Manuel Nutz and Michael Förg, you guys were excellent colleagues and office-mates, as well as friends and mentors. Manuel, thank you for solving every question and problem that I bothered you with on a daily basis over the years and teaching me great many stuff in the lab. Michi, thank you for being the cavity guru. Having you working also on light-matter interaction was a great source of motivation and wisdom, I am grateful for that. I also thank two contemporary PhDs, with whom I spent the most time, Victor Funk and Jonathan Förste. I enjoyed being in the lab and in the office with you guys, brain-storming about solving physics and technical problems, our many scientific and non-scientific discussions over conferences and everyday lunch. A special thanks goes to Johannes Scherzer. It was fun to work with you in a team, to solve all technical problems, to perform experiments and discuss the underlying physics. I am glad that you will carry on the amazing work with the setup. Thank you for the great zussamenarbeit. I also thank Anna Rupp and Christian Mohl for working on a fun project together.

I want to thank all members of the group for many scientific discussions and social activi-

ties together: André Neumann, Anvar Baimuratov, Borislav Polovnikov, Farsane Tabataba-Vakili, Franziska Haslinger, Ismail Bilgin, Jessica Lindlau, Jiaxiang Zhang, Jonas Göser, Jonathan Noé, Leo Colombier, Lukas Husel, Lukas Krelle, Robin Patel, Shen Zhao, Xin Huang and Zhijie Li. I am especially excited about the new cohort, their enthusiasm and ability is enthralling and I am sure that many interesting work will be coming out of the group in coming years. Also a warm thank you to the other members in the Lehrstuhl, Bert Lorenz, Dayse Ferreira e Silva and Martina Edenhofer for the constant help and making life easier. Thank you Anton Heindl, Christian Obermayer, Philipp Altpeter and Stephan Manus for the various help with technical challenges in lab and in cleanroom. I also want to thank the team in the mechanical workshop including Jürgen Aust and Thomas Grosshauser for making the crucial mechanical parts for us.

It was a unique opportunity that I was able to do a great part of my PhD work at attocube. Working in an industrial setting gave me a great insight on the inner workings of a company and simultaneously see attocube grow at a rapid pace. I am thankful to each and everyone at attocube. Let me start with the InnoVision team. Being part of the InnoVision team was an exceptional experience, it is a uniquely agile and innovative research team within industrial setting and I can't imagine a better place to do a PhD. First of all, thanks to Claudio Dal Savio. Claudio's expertise in cryogenics and designing products was valuable. Thank you Meryem Benelajla for sharing the PhD journey, it was great to have another person in the company who was undergoing the same experiences. Thank you Clemens Schäfermeier who is both a great mentor and friend. Your broad expertise in cavity and various other topics were immensely helpful in progressing the experiment and I cherish all the different discussions. Thank you Holger Thierschmann who has provided a fresh impetus and scientific vigor to the cavity project since joining attocube. I am thankful, Holger, for many scientific and technological discussions and brain-storming we did, your ability to ask the right questions and find the actual underlying principles taught me a lot. I am sure you'll take the project to the next level with your brilliant ideas in the next years. I am also thankful to other members in Inno team for creating a friendly environment and providing support in innumerable ways: Chris Kelvin von Grundherr, Dominik Irber, Gunter Wüst, Katinka von Grafenstein, Pablo Kühnemann and Paul Vosshage.

During the course of various projects, I worked quite closely with almost every department in the company, my sincere thanks to people in R & D, Systems, Product Management, Production, Purchasing, Sales, Marketing and neaSpec. A special thanks to Luca Gragnaniello, I really enjoyed our collaboration on all the projects in my first year. Several people who needs a special mention for helping me over the years: Alex Watananbe, Andreas Rusche, Andreas Räpke, Armin Schöning, Constanze Metzger, Dieter Andres, Florian Brenken, Florian Otto, Paul Müller, Martin Seiz, Tobias Lesnicar and Thomas Sieben. I also thank the People and Office team for taking care of the administrative issues and our well-being.

Modern day research is truly a collaborative effort and I had the chance to interact and

work with some extremely smart and friendly people. First of all, I want to thank David Hunger. David was a supporter for the cavity project from day one and his expertise, feedback and fibers were crucial to make the project success. Also a big thanks to his team both in Munich and Karlsruhe, particularly Thomas Hümmer. Being able to join a Marie-Curie ITN was a wonderful opportunity for my scientific and personal development. It was great to travel every half a year to different places with a cohort of fellow PhD researchers going through the similar experiences as you. We not only had an interesting exchange on science, the interactions through workshops and discovering new cities were highly appreciated. I want to thank European Commission for Marie-Curie Actions, Alexander Tartakovskii for making Spin-Nano possible and all the fellow Spin-Nano ITN researchers.

During the course of the PhD, I was fortunate to maintain the crucial work-life balance. I managed to pursue my hobbies and discover some new ones, particularly I enjoyed working on meaningful causes close to my heart. I want to thank my team at 'Munich for SDGs' for coming together on creating awareness on sustainability. It was also a great experience to organize an outreach on quantum technologies with the Spin-Nano team as a part of European Researchers' Night in Brussels. I am also thankful to the team of 'Soapbox Science Munich' for letting me contribute to organize an awesome event to promote women in science and the MCQST team to organize Tag der Offenen Tür at LMU. A strong support structure was necessary to remind me of the things outside of science and make life enjoyable and eventful. I cherish the friends that I made and had during this time, for hanging out together many evenings, doing sports, eating great food and spending holidays together. A shout-out to my friends: Ajay, Angela, Aniket, Cristina, Enrico, Karan, Komron, Luca, Markus, Matteo, Megs, Naina, Nora, Payal, Sumit, Vedant, Vinayak, Viraj and Wilhelm.

Finally, I want to thank and dedicate this work to my family. My sister, Rucha, thank you so much for being a constant support who has motivated and helped me follow my dreams since childhood. And my parents, Vandana and Mahendra, for providing me with all the opportunities and giving an unwavering support to pursue my own path. You are the greatest parents anyone can ask for, I owe you everything and this thesis is dedicated to you.